

UNIVERSITY OF LIVERPOOL

Atomic Structure, Chemical Composition, and Oxidation Behaviour of the Low Index Surfaces of the In_3Ni_2 Intermetallic Catalyst

Thesis submitted in accordance with the requirements of the University of Liverpool for the degree of Doctor in Philosophy by

Ahowd Yousef Alfahad

Department of Physics
University of Liverpool

01/10/2025

Acknowledgments

I am deeply grateful to my supervisors, Dr. Hem Raj Sharma and Prof. Ronan McGrath, for their invaluable guidance, continuous support, and encouragement throughout my research. Their insightful feedback and patience were instrumental in the successful completion of this thesis.

I also extend my sincere appreciation to Dr. Julian Ledieu and Dr. Vincent Fournee for their collaboration in shared experiments and for fostering a collegial and supportive environment that greatly enriched this research journey. I am particularly grateful to Dr. Adrian Gardner, Dr. Sam Haq, and Dr. Matthew Bilton for their expert guidance and collaboration throughout the experimental work.

I owe profound gratitude to my mother for her sacrifices, encouragement, and unwavering belief in me, and to my brothers and sisters, whose patience and understanding provided strength during the most challenging times. I also wish to acknowledge my colleagues during the study period, whose support and camaraderie contributed meaningfully to this journey.

I gratefully acknowledge King Abdulrahman bin Faisal University and the Saudi Arabian Cultural Bureau in London for their financial support and for providing me with the opportunity to undertake doctoral studies at the University of Liverpool. I also extend my sincere thanks to ECMetAC for facilitating the experimental research trips.

The completion of this thesis would not have been possible without the contributions of these individuals and institutions, to all of whom I express my heartfelt gratitude.

Abstract

Intermetallic compounds have become promising candidates for heterogeneous catalysis because of their structural stability and variable electronic properties. This study investigates how crystallographic orientation affects the surface characteristics of the intermetallic compound In_3Ni_2, focusing specifically on the (001), $(2\bar{1}0)$ and (100) surfaces. It examines key properties: surface structure, chemical composition and oxidation behaviour, using a range of surface sensitive techniques, including X-ray Photoelectron Spectroscopy (XPS), Low Energy Ion Scattering (LEIS), Scanning Tunnelling Microscopy (STM) and Low Energy Electron Diffraction (LEED).

This study demonstrates that the surface properties and reactivity of In_3Ni_2 are dependent on crystallographic orientation. The (001) and (100) surfaces are characterised by indium (In)-terminated layers, with In atoms bonded to subsurface Ni. In contrast, the $(2\bar{1}0)$ surface is terminated by In atoms bonded to Ni atoms within the same layer.

XPS and LEIS analyses reveal preferential sputtering of In, with the effect being most distinct on the (001) and (100) surfaces due to their weaker Ni–In bonds. Upon annealing, In segregates to the surface, with the extent of enrichment depending on surface geometry; the more open $(2\bar{1}0)$ surface exhibits the highest degree of In segregation, whereas the compact (001) and (100) surfaces partially shield subsurface In, thereby limiting its segregation to the outermost layer. The observed preferential sputtering and segregation are attributed to the lower surface free energy of In compared to Ni.

LEED and STM show that the (001) surface undergoes a c($2\sqrt{3} \times 4$) reconstruction upon hydrogen (H) exposure, whereas the (100) and ($2\bar{1}0$) surfaces remain unreconstructed under the same conditions. Reactivity studies indicate that the ($2\bar{1}0$) surface exhibits the highest reactivity toward oxygen (O), attributable to its increased density of In atoms, while the (001) surface is more reactive toward H due to its greater Ni content. In contrast, the (100) surface displays minimal oxidation under the same conditions.

This work provides fundamental insight into the surface structure of the intermetallic compound In_3Ni_2, showing how crystallographic orientation governs atomic arrangement and surface stability. The results reveal that In–Ni bonding plays a key role in stabilising the surface, while the presence of Ni atoms at the outermost layer forms isolated sites that may influence chemical interactions.

Contents

Contents **iv**

1 Introduction **1**

2 Surface Science and Catalysis **5**

2.1 Introduction 5

2.2 A Brief History of Catalysis 7

2.3 A Brief Introduction to Alloys and Intermetallic Compounds 10

2.3.1 Principles of Heterogeneous Catalyst 12

2.3.2 Intermetallic Compounds as Heterogeneous Catalysis 13

2.4 Structure and Properties of Intermetallic Catalysts 15

2.5 Applications of Intermetallic Compounds in Catalysis 17

2.6 Surface Studies of Intermetallic Catalysts 18

2.7 Phase Diagram, Growth and Crystal Structure of In_3Ni_2 25

3 Experimental Methods and Techniques **31**

3.1 Introduction 31

3.2 Basic Principles and Design of Ultra High Vacuum (UHV) 32

3.2.1 UHV Pumps 36

3.2.2 Pressure Gauges 40

3.2.3 Laboratory Equipment 41

3.2.4 Venting and Baking the System . . . 42
3.2.5 Mass Spectrometry . . . 43
3.3 Surface Preparation . . . 44
3.3.1 Sputtering the Surface (Ion Bombardment) . . . 48
3.3.2 Annealing the Surface (High Temperature Treatment) . . . 49
3.4 Experimental Techniques . . . 49
3.4.1 X-ray Photo Electron Spectroscopy (XPS) . . . 49
3.4.2 Low Energy Ion Spectroscopy (LEIS) . . . 55
3.4.3 Low Energy Electron Diffraction (LEED) . . . 58
3.4.4 Scanning Tunnelling Microscopy (STM) . . . 64

4 In_3Ni_2(001) Surface 72
4.1 Introduction . . . 72
4.2 In_3Ni_2(001) Model Structure . . . 73
4.3 Experimental Methods . . . 74
4.4 Results and Discussion . . . 76
4.4.1 Chemical Composition Studied by XPS . . . 76
4.4.2 Elemental Information Studied by LEIS . . . 82
4.4.3 Atomic Structure Studied by LEED and STM . . . 86
4.4.4 Identification of Surface Termination . . . 96
4.4.5 Oxidation Behaviour . . . 98
4.5 Summary . . . 103

5 $In_3Ni_2(2\bar{1}0)$ Surface 105
5.1 Introduction . . . 105
5.2 $In_3Ni_2(2\bar{1}0)$ Model Structure . . . 106
5.3 Experimental Methods . . . 106
5.4 Results and Discussion . . . 109

5.4.1 Chemical Composition Studied by XPS . . . 109
5.4.2 Elemental Information Studied by LEIS . . . 114
5.4.3 Atomic Structure Studied by LEED and STM . . . 117
5.4.4 Oxidation Behaviour . . . 128
5.5 Summary . . . 136

6 In_3Ni_2 (100) Surface **137**
6.1 Introduction . . . 137
6.2 In_3Ni_2 (100) Model Structure . . . 138
6.3 Experimental Methods . . . 139
6.4 Results and Discussion . . . 140
6.4.1 Chemical Composition Studied by XPS . . . 140
6.4.2 Elemental Information Studied by LEIS . . . 146
6.4.3 Atomic Structure Studied by LEED and STM . . . 149
6.4.4 Identification of Surface + . . . 157
6.4.5 Oxidation Behaviour . . . 159
6.5 Summary . . . 166

7 Comparative Study of In_3Ni_2 (001), (2$\bar{1}$0) and (100) Surfaces **167**
7.1 Introduction . . . 167
7.2 Surface Orientation Dependent Chemical Composition . . . 169
7.2.1 XPS Study . . . 170
7.2.2 LEIS Study . . . 172
7.3 Reactivity of Crystallographic Surfaces . . . 174
7.3.1 Surface Reactivity with Oxygen . . . 175
7.3.2 Surface Reactivity with Hydrogen . . . 177
7.4 Summary . . . 178

8 Conclusions and Outlook **180**

Bibliography **183**

List of Figures **197**

List of Tables **215**

Appendix: Publications, Conferences, Research Visits and Awards **217**

1 Introduction

Intermetallic compounds (IMCs) are materials composed of two or more elements in defined stoichiometric ratios, with each element occupying specific positions within the crystal lattice [1]. Their unique structural arrangement gives rise to a range of distinctive properties, making them highly suitable for various applications, including heterogeneous catalysis [2, 3, 4]. Compared to metal catalysts, IMCs offer cost-effective and environmentally friendly alternatives, which are particularly advantageous in reducing reliance on expensive and rare metals [5].

For instance, the $Al_{13}Fe_4$ intermetallic compound has been demonstrated to be an effective replacement for palladium (Pd) catalysts in semi-hydrogenation reactions [5]. A key advantage of IMCs lies in their tunable electronic properties, which can be adjusted through modifications in chemical composition [6, 7]. This tunability enables the optimisation of their catalytic performance, rendering them versatile candidates for a wide range of catalytic processes. Furthermore, IMCs often exhibit site isolation, wherein catalytically active sites are spatially separated within the crystal structure. This feature has been shown to enhance both selectivity and thermal stability compared with metallic catalysts. The spatial separation of active sites minimises undesired side reactions and facilitates more controlled catalytic activity [8].

The In–Ni intermetallic compounds (IMCs), which are the focus of the present study, have shown considerable potential as environmental catalysts [9]. These materials are particularly suited to the dry reforming of methane, a process that simultaneously utilises two

major greenhouse gases, carbon dioxide (CO_2) and methane (CH_4), to produce valuable chemical products [10]. This reaction represents a significant step towards mitigating the environmental effects of these gases. Moreover, In–Ni IMCs have demonstrated potential as effective catalysts for the hydrogenation of carbonyl compounds, further emphasising their versatile catalytic capabilities [11]. However, real-world catalysts are often highly complex, which makes it challenging to obtain a fundamental understanding of their catalytic behaviour. Consequently, catalytic activity is typically optimised through trial-and-error approaches. To address this challenge, simpler and well-defined model systems are commonly employed to investigate the underlying physical parameters that govern catalytic activity. In particular, single-crystal samples, with surfaces prepared along well-defined crystallographic planes, are used as model catalysts. These systems allow precise control and characterisation of atomic and electronic properties. Surface science techniques, typically conducted under ultra-high vacuum (UHV) conditions, are then used to analyse the behaviour of these model catalysts in response to reactants in various chemical reactions [12].

Surface science plays a foundational role in the investigation and optimisation of catalysts, as catalytic reactions predominantly occur at the material surface. The efficiency, selectivity, and stability of a catalyst are closely linked to its surface properties, including atomic structure, defects, and the spatial arrangement of active sites. These features are crucial in determining not only the catalyst's reactivity but also its durability and resistance to deactivation [13]. Therefore, a comprehensive understanding of these surface characteristics is essential for the development of more efficient and stable catalysts capable of operating under a variety of industrial conditions.

To achieve this understanding, advanced surface analysis techniques such as X-ray Photoelectron Spectroscopy (XPS), Low Energy Ion Scattering (LEIS), Scanning Tunnelling Microscopy (STM), and Low Energy Electron Diffraction (LEED) have been employed in this thesis. XPS allows for the examination of the chemical composition and oxidation

behaviour of elements on the surface [14], LEIS offers information on the surface structure and elemental distribution [15], while STM provides high-resolution imaging of surface morphology and atomic arrangements [16]. These methods collectively enable a detailed characterisation of the catalyst surface, providing the necessary data to inform the design of more efficient catalytic materials.

Thesis Structure

Chapter Two offers a comprehensive overview of the historical development of catalysis, tracing the evolution of catalytic processes through different periods. This chapter highlights significant advancements and key achievements in the field, with a particular focus on the various types of catalysis. Special emphasis is placed on heterogeneous catalysis, exploring its fundamental principles and applications in modern science. The chapter concludes with a discussion of phase diagrams and a brief outline of the methodology employed for the growth of In∗3Ni∗2 crystals, providing the basis for the subsequent experimental work.

Chapter Three details the experimental methodologies utilised in this study. This includes an in-depth description of the UHV system and the associated sample preparation techniques. Furthermore, the chapter introduces the surface analysis methods employed, such as XPS, LEIS, STM, and LEED, providing an overview of their applications and relevance in characterising surface properties.

Chapters Four, Five, and Six present the experimental results obtained from the study of high-symmetry surfaces of In∗3Ni∗2, specifically the (001), $(2\bar{1}0)$, and (100) surfaces. These chapters describe ~~the~~ characterisation of the atomic and chemical structure of these surfaces, using a combination of surface science techniques including XPS, LEIS, STM, and LEED. The surface atomic structures of the three orientations were investigated primarily using LEED and STM, while XPS and LEIS were employed to analyse their chemical composition. Additionally, the oxidation behaviour of these surfaces was examined through

XPS, offering insights into the surface reactivity under various conditions.

Chapter Seven presents a comparison of the low-index surfaces, (001), ($2\bar{1}0$), and (100), to reveal how crystallographic orientation influences surface termination, atomic composition, segregation, and chemical reactivity.

Chapter Eight summarises the key findings of the thesis and discusses the implications of the results. The chapter also provides suggestions for potential future studies, outlining areas where further research could build upon the findings presented.

2 Surface Science and Catalysis

2.1 Introduction

This chapter provides a comprehensive overview of the historical development of catalysis and its various types, with a particular focus on intermetallic compounds as heterogeneous catalysts. Catalysis plays an essential role in numerous chemical processes, both in industrial applications and in the fundamental understanding of reaction mechanisms [17, 18]. The objective of this chapter is to outline the evolution of catalysis, highlighting key milestones in its development and exploring the significance of surface science in advancing catalytic research.

The study of surface phenomena is fundamental in understanding the behaviour of materials in catalysis and various other processes, such as relaxation, segregation and reconstruction. Surface physics and surface chemistry, as sub-disciplines, examine the properties and dynamics of solid surfaces, including the arrangement and interactions of atoms and molecules. These investigations are essential for the development of more efficient and selective catalytic systems, particularly when considering materials at the atomic level.

A key aspect of surface science is the identification and characterisation of surface atoms, the chemical composition of surfaces and their atomic structure. Understanding how atoms are arranged on the surface, the electronic properties of the surface and the nature of interactions with adsorbed elements is fundamental for designing materials with

optimal catalytic performance. In the case of heterogeneous catalysis, these interactions often dictate the reaction pathways and overall efficiency of the catalyst.

To gain a comprehensive understanding of surface properties, a variety of surface analysis techniques are employed. Techniques such as X-ray photoelectron spectroscopy (XPS) and low-energy ion scattering (LEIS) provide insight into the chemical composition of surfaces, revealing information about surface elements and their oxidation behaviour. Additionally, scanning tunnelling microscopy (STM) and low-energy electron diffraction (LEED) are powerful methods to determine surface structure at the atomic scale. These techniques enable the study of atomic arrangements and the chemical composition of the surface. The importance of these surface characterisation methods, which are integral to this thesis, will be explained in detail in the following sections.

Furthermore, this chapter will explore the role of intermetallic compounds in heterogeneous catalysis, specifically the In3Ni2 system. Intermetallic compounds, with their unique electronic structures and well-defined stoichiometries, have demonstrated catalytic activity in a wide range of reactions. The phase diagram and crystal structure of In3Ni2, which are essential for understanding its catalytic properties, will be discussed alongside its surface characteristics, thereby providing a foundation for the experimental work presented later in the thesis.

By integrating principles from surface science with the study of intermetallic catalysts, this chapter develops the theoretical and experimental basis for the research presented in subsequent chapters. Furthermore, it highlights the significance of surface characterisation techniques in advancing our understanding of catalytic mechanisms at the atomic level.

2.2 A Brief History of Catalysis

Catalysis is an essential topic of investigation across various scientific fields, including chemical engineering, physics, and chemistry [19]. This technique, in which a material (the catalyst) facilitates chemical reactions at significantly lower temperatures and pressures without being consumed during the reaction, boasts a long and distinguished history that extends back centuries [2]. The term *catalysis* was first introduced in the early 19^{th} century by the Swedish chemist Jöns Jacob Berzelius in 1836 [20]. Nevertheless, the phenomenon of catalysis was documented long before its formal definition, with early evidence of catalytic reactions observed in the contributions of chemists such as Louis Pasteur (1860). [21]

In the early 19^{th} century, Berzelius described the catalytic effects of certain substances in reactions such as the oxidation of alcohol. However, it was not until the 19^{th} century that the foundational principles of catalysis began to be comprehensively understood [22]. During the late 19^{th} and early 20^{th} centuries, significant progress was made in the study of catalysis, particularly with the introduction of the concept of surface catalysis by Sir William Ostwald. He expanded upon the understanding of how reactions occur at the surface of a catalyst [20, 21].

The discovery of industrial catalytic processes, such as the Haber–Bosch process for ammonia synthesis in the early 20^{th} century, revolutionised both chemistry and industry. This advancement was achieved by Fritz Haber and Carl Bosch, who developed a process that utilised iron as a catalyst to fix nitrogen from the air, a key breakthrough for agriculture and the development of fertilisers [22].

In the 20^{th} century, the field of catalysis expanded into areas such as heterogeneous, homogeneous, and enzymatic catalysis [20]. The emergence of X-ray diffraction techniques in the 1930s allowed scientists to begin studying the atomic structure of catalysts, and the development of new catalytic materials, such as zeolites and palladium catalysts, paved

the way for numerous chemical advancements [23]. Today, catalysis remains an essential field of study with applications in industrial chemistry, energy production, environmental protection, and biological processes.

The fundamental principle of catalysis involves reactants bonding to a catalyst, as illustrated in Figure 2.1. The interaction between reactants A and B occurs while they are bound to the catalyst surface, allowing for the subsequent separation of the product from the catalytic surface. Consequently, the formation of this compound is exothermic, resulting in a reduction in free energy. Finally, the endothermic process of detaching product P from the catalyst occurs. Catalysts operate as substances that facilitate the breaking of bonds and the formation of new ones. Catalysis can be categorised into three distinct subdisciplines: homogeneous, heterogeneous, and biocatalysis [24].

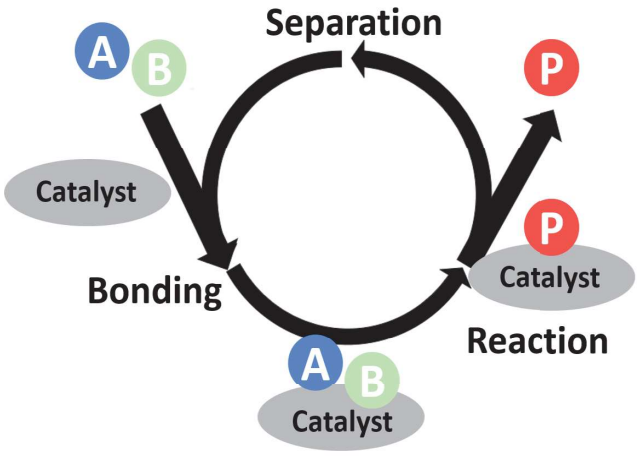


Figure 2.1: Cyclic catalytic reaction: in a catalytic reaction, reactant molecules bind to the catalyst, where molecules A and B react, and the product P then separates from the catalyst, releasing it for use in the next cycle. Reproduced and modified from [25].

In homogeneous catalysis, both the catalyst and the reactants exist in the same phase, typically in a liquid solution. This uniformity facilitates efficient molecular interaction and often results in high reaction selectivity. Conversely, heterogeneous catalysis involves multiple phases, most commonly a solid catalyst interacting with liquid or gas reactants, where the catalytic activity occurs at the surface interface.

The reaction pathways in heterogeneous catalysis are commonly described by the Langmuir–Hinshelwood and Eley–Rideal mechanisms, as illustrated schematically in Figure 2.2. In the Langmuir–Hinshelwood mechanism, both reactant species are first adsorbed onto the catalyst surface before reacting to form products. Consequently, the reaction occurs between two adsorbed species, making surface coverage, adsorption strength, and the availability of active sites important factors governing catalytic activity and selectivity. This mechanism is widely used to describe reactions occurring on metallic and intermetallic catalyst surfaces.

In contrast, the Eley–Rideal mechanism involves a direct reaction between a gas-phase species and a reactant already adsorbed onto the catalyst surface. In this pathway, only one reactant is adsorbed prior to the reaction, while the second interacts directly from the gas phase. Such behaviour is commonly associated with systems in which one reactant exhibits relatively weak adsorption or under conditions of low surface coverage.

Together, these mechanisms provide a fundamental framework for understanding heterogeneous catalytic reactions and emphasise the critical role of surface atomic structure, adsorption geometry, and active surface sites in determining catalytic performance.[25]

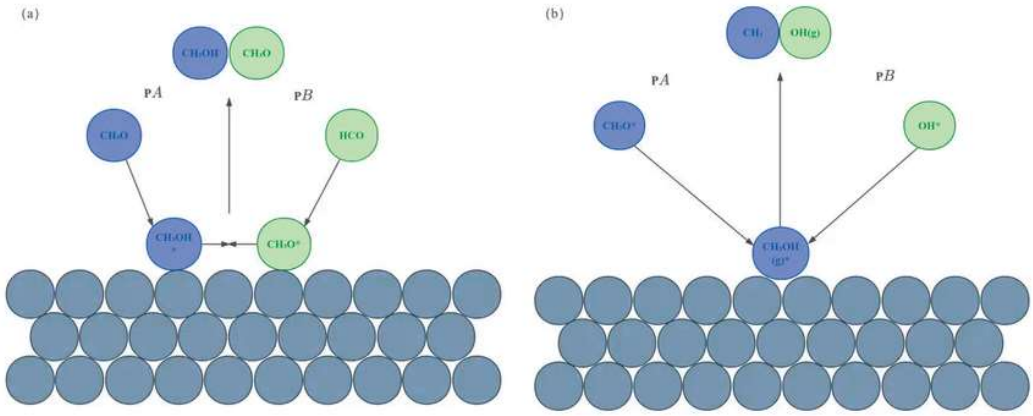


Figure 2.2: Schematic representation of the Langmuir–Hinshelwood and Eley–Rideal mechanisms in heterogeneous catalysis. In the Langmuir–Hinshelwood pathway (a), both reactants are adsorbed onto the catalyst surface before reacting to form products. In the Eley–Rideal pathway (b), a gas-phase species reacts directly with an adsorbed surface species. The grey spheres represent catalyst surface atoms, whereas the coloured spheres indicate reactant species and intermediates [26].

Biocatalysis, on the other hand, utilises naturally occurring catalysts such as enzymes or whole cells to accelerate chemical reactions, often under mild and environmentally friendly conditions [24].

2.3 A Brief Introduction to Alloys and Intermetallic Compounds

The term "intermetallic" has only recently been used in its technically accurate sense, moving away from its former use as a synonym for "alloy." An intermetallic compound refers to a solid phase formed by at least two metals, characterised by a well-defined crystal structure where atoms occupy fixed positions and exhibit long-range order [27]. For example, the PdZn intermetallic structure has (P4/mmm), with palladium (Pd) atoms located at (0, 0, 0) and zinc (Zn) atoms at (0.5, 0.5, 0.5) [28]. In contrast, an alloy is a solid solution composed of at least two metals, but with a random distribution of atoms across the lattice sites, where the arrangement of constituent elements is not fixed, as shown in Figure 2.3 (a–b) [29]. The atomic site distribution in alloys is generally governed by statistical factors that depend on the stoichiometry of the mixture [30].

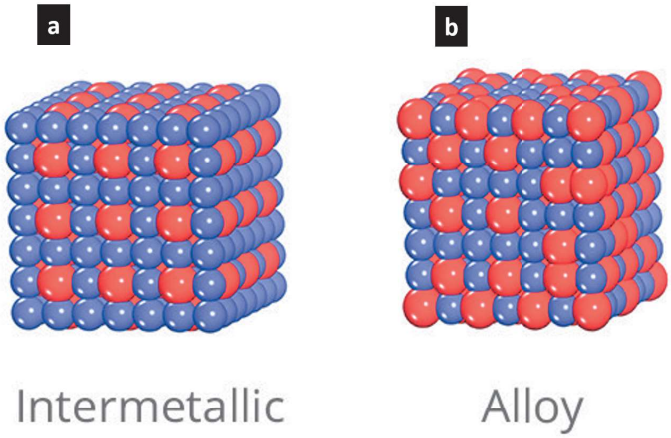


Figure 2.3: (a) An ordered intermetallic structure. (b) An alloy that lacks periodic order or well-defined site occupation [29].

A key factor contributing to the well-defined periodicity observed in intermetallic compounds is the strong ionic and electronic interactions between their constituent elements. These interactions facilitate the development of unique and often complex crystal structures that differ significantly from those of the individual parent metals. In contrast, alloys typically preserve the crystal structure of the more abundant component, commonly referred to as the solvent. The advantage of intermetallic compounds over alloys for catalysis is succinctly demonstrated by Armbruster *et al.* [31].

IMCs frequently demonstrate superior catalytic performance compared to conventional alloys, primarily due to their unique crystal structures and long-range atomic ordering. These structural characteristics enable greater precision in controlling the morphology of active sites and improve the overall rationality of catalyst design. In contrast to alloys, where atomic site occupancy is typically random and composition dependent, IMCs display a well-defined atomic arrangement that, in principle, guarantees homogeneous and reproducible catalytic surfaces. This distinction has established intermetallics as ideal candidates for model catalyst systems.

Although it must be acknowledged that surface composition may deviate from the bulk under varying reaction temperatures or chemical environments, intermetallic compounds display a greater resistance to surface segregation than alloys. This behaviour is attributed to their intrinsic "enthalpy driving force" to preserve structural order, as suggested by Meyer *et al.* [32] and corroborated by Kovnir *et al.* [30], thereby promoting stability during catalytic reactions. Furthermore, intermetallics can adopt distinct crystal phases such as the γ-brass structure observed in certain Ni–Zn systems, which are uncommon in pure metals or conventional alloys. These unique structures often yield specific coordination geometries that enhance both electronic and geometric catalytic effects, contributing to their improved performance in heterogeneous catalysis [33].

2.3.1 Principles of Heterogeneous Catalyst

Heterogeneous catalysis is a process in which a solid catalyst facilitates chemical reactions between reactants in different phases, typically gaseous or liquid, without being consumed in the reaction [34]. The catalytic cycle comprises three main steps: adsorption, reaction, and desorption. Initially, reactant molecules adsorb onto the catalyst surface, often through chemisorption, forming stronger interactions such as covalent or ionic bonds. This step activates the reactants, rendering them more reactive. Following adsorption, the catalyst surface facilitates the chemical transformation of the reactants by lowering the activation energy. Finally, the products are desorbed from the surface, regenerating the catalyst for subsequent cycles [35].

The efficiency of the process is largely influenced by the catalyst's surface properties, such as the nature and distribution of active sites, its electronic structure, and the presence of defects. The strength of the interaction between the catalyst and the reactant is also crucial; weak interactions may result in insufficient adsorption, while excessively strong interactions can hinder further reactions. In addition, the catalyst must remain stable under reaction conditions to avoid deactivation due to sintering, poisoning, or leaching. The design of heterogeneous catalysts requires a balance of these factors to optimise reaction rates, selectivity, and long-term performance, making them essential for a wide array of industrial applications, from petrochemical refining to environmental protection [36].

Figure 2.4 illustrates the process of heterogeneous catalysis. The reactants first diffuse to the catalyst surface, where they make contact with the external surface. Some molecules then overcome the surface barrier, entering the interior, including pathways and cracks. These molecules adhere to available adsorption sites, increasing the likelihood of interactions between the reactants.

This results in the formation of an intermediate compound. Following this, the intermediate is desorbed from the surface, making the adsorption sites available for additional reactants. The intermediate then decomposes to form the final products, which diffuse

out through both the internal pores and the external surface of the catalyst [37].

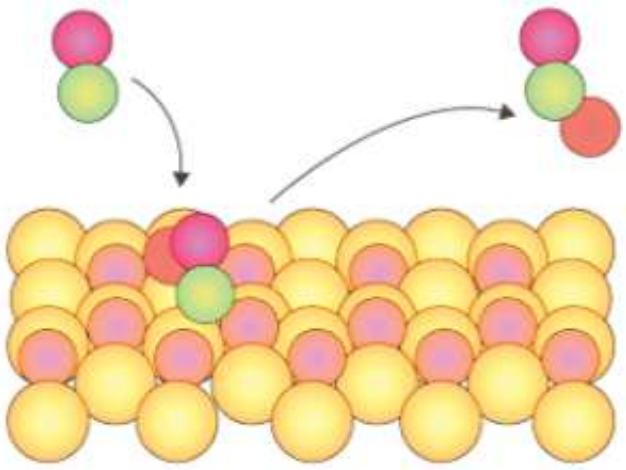


Figure 2.4: A schematic diagram
of heterogeneous catalysis process [37].

2.3.2 Intermetallic Compounds as Heterogeneous Catalysis

Intermetallic compounds (IMCs) have gained considerable attention as candidates for heterogeneous catalysis due to their unique structural and electronic properties. Unlike conventional alloys, IMCs exhibit a well defined atomic arrangement and long range ordering, which enable precise control over the morphology of active sites and enhance catalyst design [1].

The distinct crystal structures of IMCs result in the formation of specific electronic environments at the surface, which can facilitate selective adsorption and activation of reactants. This structural regularity makes IMCs particularly advantageous over traditional catalysts, as they tend to exhibit enhanced catalytic stability, reproducibility, and improved resistance to surface segregation under reaction conditions. Moreover, the interaction between the constituent metals in IMCs often leads to a synergistic effect, modifying the *d* band centre and thereby optimising adsorption energies and reactions [38].

These properties make IMCs suitable for a range of catalytic applications, including selective hydrogenation, oxidation, and methane reforming. The superior performance of IMCs is, however, contingent on maintaining phase purity and surface stability, which remains a challenge during their synthesis and under operating conditions. Despite these challenges, ongoing research continues to highlight the potential of IMCs as highly efficient catalysts for industrial processes [39].

The concept of site isolation has been experimentally investigated in intermetallic Pd–Ga compounds, such as Pd_3Ga_7, PdGa, and Pd_2Ga, for their role in hydrogenation reactions [6, 40, 41, 42]. In these Pd–Ga intermetallics, palladium (Pd) atoms are surrounded by gallium (Ga), effectively isolating the Pd atoms from one another within the crystal structure. This spatial isolation not only prevents direct Pd–Pd interactions but also results in significant modifications to the electronic structure of Pd near the Fermi level, distinguishing it from that of elemental Pd. These structural and electronic changes are believed to contribute to the enhanced catalytic performance of Pd–Ga intermetallics, which exhibit catalytic properties superior to those of their pure metal counterparts [43].

Similarly, Tsai *et al.* investigated the correlation between catalytic activity and the valence electron density of states in isostructural compounds such as PdZn, PtZn, and ZnNi [44]. They observed that the valence electron density of states in PdZn closely resembles that of elemental copper (Cu), in contrast to the valence electron density of the other two compounds. On the basis of this finding, it was proposed that PdZn could potentially replace copper catalysts in the steam reforming of methanol. The study further suggested that Zn–Pd bonds, which form on the catalyst surface, play a crucial role in the excellent catalytic properties exhibited by PdZn [45].

In addition to hydrogenation reactions, Ni-based catalysts are extensively used in a variety of oxidation reactions, such as carbon monoxide oxidation [46], methane conversion to syngas [47, 48, 49], and synthesis of essential industrial chemicals [50]. These versatile catalysts are crucial in various industrial processes, highlighting their broad utility in cat-

alytic applications.

2.4 Structure and Properties of Intermetallic Catalysts

Segregation is a crucial phenomenon that can significantly influence the properties and performance of intermetallic compounds (IMCs) and catalysts [2]. It refers to the redistribution of constituent elements within a material, often occurring at the surface or grain boundaries, which can lead to the formation of non-stoichiometric phases or the exposure of less active sites [51]. In the case of IMCs, segregation is typically observed under reaction conditions, particularly at high temperatures or in reactive environments [52].

This phenomenon can alter the ideal atomic ordering of the catalyst, leading to changes in the electronic structure and, consequently, in catalytic activity. For example, in bimetallic catalysts, surface segregation can cause a metal to accumulate on the surface, potentially disrupting the interaction between the metals and impairing the stability and efficiency of the catalyst. Although some degree of segregation may be beneficial in promoting the formation of active sites, excessive segregation often leads to the loss of catalytic properties or catalyst deactivation. Therefore, understanding and controlling segregation processes is essential for the design of stable, high-performance intermetallic catalysts, particularly for reactions such as hydrogenation, oxidation, and carbon monoxide removal [30].

Segregation influences the properties and performance of IMCs, particularly under catalytic and high-temperature conditions. In the study of ZrNiAl, YNiAl, and UNiAl IMCs, segregation behaviour was found to significantly alter the surface composition and stability of these materials [53]. In these compounds, surface segregation of the more electropositive element, such as Ni in the case of ZrNiAl and YNiAl, was observed at high temperatures. This segregation occurs due to the lower surface energy of Ni, which tends to accumulate at the surface, leaving the less electropositive elements, such as Zr, Y, and

U, in the bulk of the material. This behaviour aligns with the findings of this research, in which a comparable segregation of In was observed, driven by its lower surface energy.

Segregation can modify the electronic structure and the catalytic properties of the surface, potentially leading to changes in reactivity and selectivity [53]. For example, in the ZrNiAl system, the segregation of Ni at the surface enhanced its catalytic performance in hydrogenation reactions due to the exposure of the Ni-rich surface, which is more active for such processes. However, excessive segregation can also lead to catalyst deactivation, as the exposed metal may suffer from sintering or poisoning effects. The segregation behaviour of these IMCs is therefore a crucial factor that must be carefully controlled for effective catalytic applications. This study underscores the importance of understanding the segregation phenomena in designing more stable and efficient catalysts based on IMCs [39, 54].

Relaxation in IMCs refers to the process by which these materials undergo atomic rearrangements to relieve internal stresses that may arise due to differences in atomic size, composition, or external environmental conditions. Such relaxation is a crucial aspect of the stability and performance of IMCs, especially under operational conditions where temperature fluctuations or mechanical stress can induce strain in the crystal lattice. For instance, in Pd-based intermetallics, atomic rearrangements at the surface can lead to a reduction in surface energy, which, in turn, enhances the material's catalytic activity by exposing more active sites for reactions. The extent of relaxation depends on the specific IMC, its crystal structure, and the nature of the atomic interactions within the material. Additionally, relaxation can influence the electronic structure of IMCs, thereby affecting their reactivity and stability.

In the case of the PdGa system, surface relaxation leads to the exposure of Pd-rich sites, which are beneficial for selective hydrogenation reactions. However, relaxation may also cause deviations from the ideal stoichiometry, potentially resulting in surface segregation or deactivation over time. Therefore, understanding relaxation mechanisms in IMCs is

essential for optimising their use in catalytic applications, as these processes directly affect both the material performance and its long-term durability [32, 55].

2.5 Applications of Intermetallic Compounds in Catalysis

The distinct atomic arrangement and bonding characteristics of IMCs often result in superior catalytic performance, including enhanced activity, selectivity, and stability, compared to conventional monometallic catalysts. These materials possess the ability to modify the electronic structure of active sites, which optimises the adsorption energies and facilitates the tailoring of reaction pathways. This feature is particularly advantageous in reactions that require precise control over product distribution, such as selective hydrogenation and methanol steam reforming. Moreover, IMCs are capable of mitigating the overbinding of intermediates, a common issue observed in monometallic catalysts, thereby enabling higher reaction rates and improved selectivity for the desired products. However, despite these benefits, significant challenges persist in the synthesis, surface characterisation, and preservation of the phase purity of IMCs under operational conditions. Despite these obstacles, ongoing research continues to emphasise the potential of IMCs in advancing sustainable and efficient catalytic processes for a range of industrial applications, such as fuel reform and CO_2 reduction.

For instance, PdGa and PdZ intermetallic compounds have demonstrated exceptional performance in selective hydrogenation, steam reforming of methanol and CO_2 reduction, providing enhanced catalytic activity while addressing the overbinding of intermediates commonly encountered in monometallic systems [39, 56]. The electronic synergy between the constituent metals within these IMCs leads to modifications in the *d*-band centres, which play a critical role in governing the adsorption energies and reaction pathways. However, challenges remain with respect to the precise synthesis and surface characterisation of these materials, particularly with regard to maintaining phase purity and surface

termination under catalytic conditions. Despite these issues, the inherent structural regularity and thermodynamic stability of IMCs position them as a promising class of catalysts for both fundamental research and industrial applications, particularly as efforts are intensifying to design more sustainable and efficient catalytic processes [28].

Table 2.1 provides a comprehensive summary of various intermetallic compounds and the catalytic reactions they facilitate, highlighting instances where they outperform conventional monometallic catalysts in terms of activity, selectivity, and stability.

Reaction Chemistry	Intermetallic Compound	Advantage
Hydrogenation Reactions	PdZn [39], Ni_5Zn_{21} [57], PdIn [55], Pd_2Ga [56], PdGa [56], Pd_3Ga_7 [40], $Al_{13}Fe_4$ [5]	Higher ethylene selectivity.
Methanol Steam Reforming	PdZn [58]	Higher resistance to sintering and higher CO_2 selectivity.
CO_2 Reduction	Ni_5Ga_3 [59]	Operated at ambient pressure instead of 50–100 bar.

Table 2.1: Summary of chemical reactions catalysed and key advantages of selected intermetallic compounds.

2.6 Surface Studies of Intermetallic Catalysts

Recent developments in the field of intermetallic catalysts have underscored their significant potential in heterogeneous catalysis, primarily due to their well defined crystal structures, tunable electronic properties and exceptional thermal and chemical stability under various reaction environments. These materials exhibit site specific reactivity that arises from their ordered atomic arrangements and compositional precision, making them particularly attractive for selective catalytic transformations. IMCs such as PdGa, PdZn, InPd, $Al_{13}Co_4$ and $Al_{13}Fe_4$ have been extensively studied as model systems to understand

structure reactivity relationships [40, 56]. To probe the surface characteristics of these catalysts, surface sensitive techniques have been widely employed, including XPS, STM and LEED, providing detailed insights into their atomic structure, surface terminations, reconstructions and chemical compositions.

A critical parameter influencing catalytic performance in intermetallic systems is the nature of surface termination, which defines the atomic configuration of the outermost layer. Surface terminations often distinct from bulk structures as a result of surface relaxation, reconstruction, or segregation phenomena, which can significantly influence the adsorption behaviour, reactivity and selectivity of a catalyst. As catalytic reactions are inherently surface dependent, understanding and controlling surface terminations is essential for the rational design of active and selective catalysts. Moreover, these surface structures are sensitive to environmental conditions such as temperature, pressure and reactant atmosphere, necessitating in depth investigation under ultra high vacuum (UHV) to accurately predict catalytic behaviour.

Despite their promising catalytic properties, characterising the surface structure and composition of IMCs remains a significant challenge due to their complex surface behaviour, including preferential sputtering, segregation and temperature dependent reconstructions. For example, Pd-based intermetallic such as PdGa, InPd and PdZn have demonstrated unique catalytic activity for hydrogenation and CO_2 conversion, yet their surface structures are often distinct from their bulk terminations. Studies employing LEED and STM have revealed a range of surface reconstructions and order-disorder transitions that depend sensitively on preparation conditions. XPS and LEIS have further shown that surface compositions can vary significantly with annealing, indicating surface segregation of the constituent elements. These findings highlight the necessity of employing multiple complementary surface sensitive techniques to accurately resolve the atomic and chemical structure of intermetallic surfaces. Such an integrated approach is essential not only for understanding catalytic mechanisms but also for guiding the design of inter-

metallic materials with tailored surface properties for specific reactions.

Comparative analysis of the PdGa ($\bar{1}\bar{1}\bar{1}$) and InPd surfaces reveals distinct differences in structural stability, surface ordering and response to thermal and chemical treatments, despite the fact that both are Pd based IMCs of interest in heterogeneous catalysis [38, 60]. The surface of PdGa($\bar{1}\bar{1}\bar{1}$) exhibits a well ordered, unreconstructed (1×1) hexagonal structure, characterised by atomically flat terraces and uniform step heights, as evidenced by LEED and STM analyses (Figure 2.5 (a–d)) [38]. This morphology reflects a stable, bulk terminated surface that remains free from contamination or reconstruction under UHV conditions. Furthermore, the low background intensity observed in the LEED patterns suggests that there is no surface segregation.

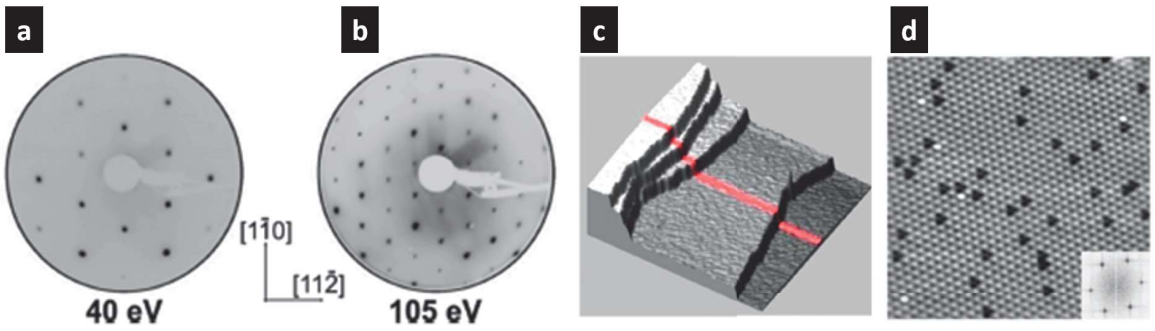


Figure 2.5: (1×1) LEED patterns after annealing the PdGa($\bar{1}\bar{1}\bar{1}$) surface with different beam energies (a) 40 eV. (b) 105 eV [38]. (c) STM images of the PdGa($\bar{1}\bar{1}\bar{1}$) surface after sputtering and annealing show (c) A highly terraced surface area (1000 Å × 1000 Å, −1 V, 0.5 nA). (d) atomic resolution of a smaller region (200 Å × 200 Å, −2.5 V, 0.5 nA), with the FFT [38].

The corresponding XPS measurements further corroborate the structural stability of the PdGa($\bar{1}\bar{1}\bar{1}$) surface, as indicated by the STM and LEED analyses, showing minimal surface contamination and no significant segregation of Pd or Ga after sputtering and annealing. However, surface terminations are observed to vary depending on the annealing temperature, highlighting the critical role of thermal treatment in stabilising particular surface structures and compositions. TDS and high resolution STM data suggest that the Pd_1 termination is favoured at a preparation temperature of 870 K, while the terminations

of Ga_3 and Pd_3 are more prevalent at lower preparation temperatures. A substantial positive shift of approximately 1.2 eV in the Pd $3d_{5/2}$ binding energy is observed, indicative of strong Pd–Ga interactions, whereas the Ga $2p_{3/2}$ signal remains unshifted [38].

In contrast, the InPd system demonstrates more complex and dynamic surface behaviour in its low index surfaces, with sensitivity to temperature and surface orientation [60]. On the (100) surface, low temperature LEED measurements revealed a diffuse (4×4) pattern, indicative of a surface reconstruction. Upon annealing, this pattern evolved into a sharp superstructure $c(3\sqrt{2} \times \sqrt{2})R45°$, which was also noted on polycrystalline grains at 970 K, suggesting its thermodynamic stability at high temperatures [60]. The (111) surface, in contrast, undergoes a transformation from Pd- to In-rich termination, accompanied by a transient $(\sqrt{3} \times \sqrt{3})R30°$ superstructure and increased surface disorder (Figure 2.6 (a-e)).

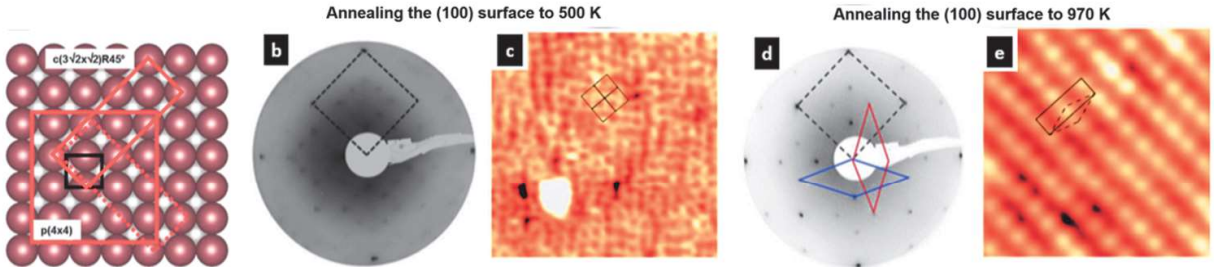


Figure 2.6: (a) Bulk terminated structural models of the InPd(100) surface, illustrating terminations at either a pure In or pure Pd atomic plane. (b) LEED pattern of the InPd(100) surface exhibiting the p(4×4) reconstruction, recorded at a primary beam energy of 50 eV. The (1×1) reciprocal unit cell is outlined with a dashed line for reference. (c) STM image of the same p(4×4) structure, revealing quasi ordered square surface features (scan area, 15×15 nm^2, +1.8 V, 0.09 nA). (d) LEED pattern of the $c(3\sqrt{2} \times \sqrt{2})R45°$ superstructure recorded at beam energy of 46 eV. (c) STM image (5×5 nm^2, +1.4 V, 0.25 nA) showing a single domain of the $c(3\sqrt{2} \times \sqrt{2})R45°$ reconstruction, with both rectangular (solid line) and primitive (dashed line) unit cells superimposed [60].

The (110) surface displays the most significant reconstruction behaviour, remaining disordered at lower temperatures and adopting c(4×2) and p(2×1) structures with increase temperature from 675 °C to 875 °C, along with the formation of faceted craters and buckled surface terminations (Figure 2.7). DFT calculations and STM imaging suggest a

protrusion of In atoms by 0.26 Å above Pd atoms, with theoretical work indicating that strong In–Pd bonding inhibits significant segregation, although anti-site defects can appear under non stoichiometric conditions [60].

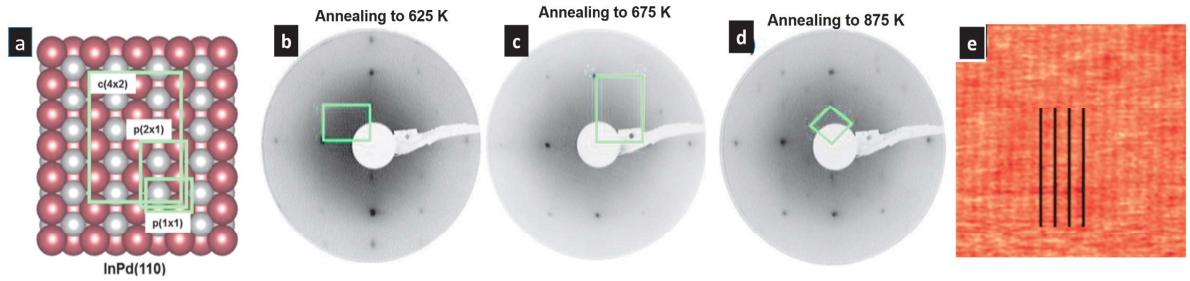


Figure 2.7: (a) Bulk terminated structure models of the InPd(110) surface, the unit cells corresponding to (110) surface reconstructions observed during sample preparation are illustrated and labelled. LEED patterns of the (b) (1×1), (c) (2×1), (d) c(4×2) phases observed on the InPd(110) surface, recorded at a consistent electron beam energy of 63 eV. The primitive reciprocal space unit cells for each surface phase are indicated by green solid lines. (e) STM image of the same surface, revealing linear atomic rows attributed to either In or Pa (9.4×9.4 nm^2, -1.5 V, 0.08 nA) [60].

In additional evidence of the reactive nature of InPd surfaces, poor LEED order and rough topography on the InPd(111) surface was observed after annealing to 1070 K. A well ordered c$(3\sqrt{2} \times 3\sqrt{2})$R45° phase was found after oxygen exposure at 750 K, highlighting oxygen induced restructuring (Figure 2.8) [60].

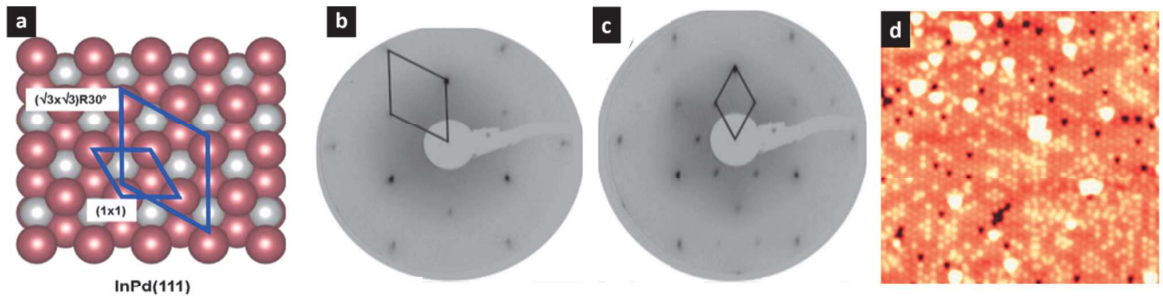


Figure 2.8: (a) Bulk terminated structural models of the (111) surface. LEED images, both taken at a primary beam energy of 50 eV, showing (b) the (1×1) phase and (c) the $(\sqrt{3} \times \sqrt{3})$R30° superstructure on the InPd(111) surface. The reciprocal unit cells are marked by solid lines. (d) STM image (30×30 nm^2, +1.8 V, 0.09 nA) of the InPd(111)-$(\sqrt{3} \times \sqrt{3})$R30° phase [60].

During surface preparation, preferential sputtering results in a depletion of indium (In) within the topmost layers of the three low index InPd surfaces ((100), (110) and (111)). The near surface region remains slightly Pd rich until it is annealed to approximately 580 K. A compositional transition occurs between 580 K and 660 K, where In segregates to the surface, rendering the near surface region slightly In-rich above 660 K [60].

Across all three surfaces, this transition reflects a systematic change from In-depleted to In-enriched surface compositions. The In rich limit is more significant on the (100) and (111) surfaces (60 at.% In) compared to the (110) surface (55 at.%), attributed to the exposure of pure In atomic planes on (100) and (111), while the (110) surface terminates in stoichiometric planes [60].

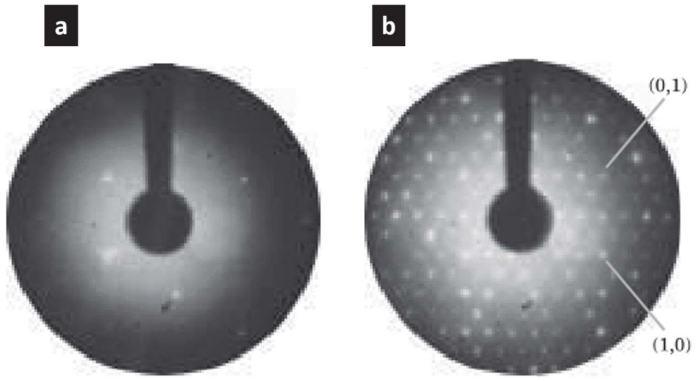


Figure 2.9: (a) LEED pattern of the clean InPd(111) surface recorded at beam energy of 68eV, exhibiting a (1×1) surface symmetry indicative of an unreconstructed termination under UHV conditions. (b) LEED pattern of the c$(3\sqrt{2} \times 3\sqrt{2})$R45° oxygen overlayer formed on the InPd(111) surface following exposure to 20 L of O_2 at 750 K, recorded at beam energy of 69 eV [60].

The surface behaviour of PdZn has been investigated through a combination of XPS, STM, μLEED, LEEM, PEEM and DFT based modelling, establishing its structural and compositional stability under UHV conditions [45]. XPS identified ZnO formation on air exposed surfaces and preferential Zn sputtering, which led to Pd surface enrichment. However, subsequent annealing restored near bulk stoichiometry, demonstrating the thermodynamic stability of the surface.

LEED analyses confirmed that surface orientations correspond to bulk truncations, with the (114) surface, which demonstrates long range order. DFT calculations indicated that the (101) and (110) surfaces are thermodynamically favourable but kinetically less stable upon annealing, whereas (111) and (114) surfaces remain stable, reflecting a balance between thermodynamic and kinetic influences. Notably, the stabilising function of Zn–Pd interactions is highlighted by the absence of the (001) surface, which would result in a single element termination [45].

STM investigations revealed stepped surface morphologies dominated by the (101) surface, with less frequent occurrence of (110), (111) and (114) orientations. High resolution imaging of the (114) and (111) surfaces showed well ordered atomic lattices, whereas (110) facets appeared too narrow for atomic contrast. Bias dependent STM contrast analysis, supported by DFT, demonstrated that Pd atoms dominate the tunnelling current due to their 4d states near the Fermi level, which strongly contribute to the local DOS. At negative bias, filled Pd 4d states appear prominently, enhancing Pd contrast, while at positive bias, unoccupied Zn-derived states contribute modestly, resulting in reduced atomic corrugation. This clear link between bias dependent imaging and the calculated DOS confirms that the tunnelling current is highly sensitive to Pd electronic contributions, which govern the apparent topography [45].

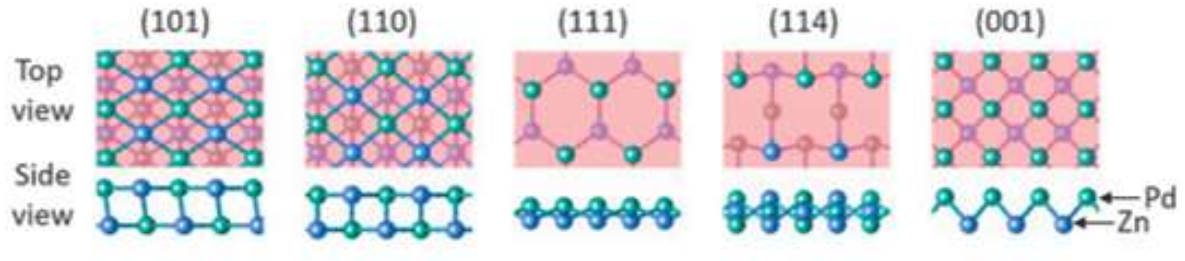


Figure 2.10: Schematic of various PdZn surfaces. The (110), (101), (111) and (114) surfaces, observed by STM, contain both Zn and Pd atoms in or near the top surface layer. The (001) surface, which has not been observed, shows single element termination [45].

The NiAl(110) surface exhibits a stoichiometric termination with equal proportions of Ni and Al (50% Ni, 50% Al) and displays a (1×1) LEED pattern in the clean state. Experiments involving hydrogen exposure have shown that molecular H_2, when dosed at either 115 K or 300 K, does not adsorb onto this surface, as evidenced by thermal desorption spectroscopy (TDS), LEED and vibrational spectroscopy measurements. In contrast, atomic hydrogen readily adsorbs, indicating that the dissociative adsorption of H_2 is an activated process on the rippled NiAl(110) surface. Both experimental and theoretical results confirm that atomic hydrogen adsorption induces a restructuring of the surface [61].

At low atomic hydrogen exposures, the (1×1) LEED pattern remains unchanged. However, at exposures between 10 and 20 L, a weak c(2×2) LEED pattern appears, corresponding to approximately one hydrogen atom per two surface unit cells, as quantified by nuclear reaction analysis (NRA). In this regime, LEED I–V profiles of the (1, 0) and (0, 1) spots differ significantly from those of the clean surface, with peak shifts of up to 7 eV. Theoretical modelling predicts that in the 1 ML (1×1) overlayer, hydrogen atoms preferentially occupy Ni–Ni bridge sites, effectively removing the rippled relaxation characteristic of the clean AlNi(110) surface. The distinct adsorption behaviour compared to pure Ni or Al surfaces reflects the unique electronic structure of AlNi(110), where alloying modifies the chemical reactivity. The presence of an activation barrier for H_2 dissociation, coupled with the restructuring induced by atomic hydrogen, highlights the interplay between surface geometry, electronic structure and adsorption energetics in intermetallic systems [61].

2.7 Phase Diagram, Growth and Crystal Structure of In_3Ni_2

Phase Diagram

The phase diagram acts as a fundamental tool for understanding the thermodynamic behaviour and phase relationships within the binary alloy system In-Ni. This system spans from pure In, which melts at 156 °C, to pure Ni, with a significantly higher melting point

of 1455 °C. The significant decline in the liquidus line from the melting point of pure Ni reflects the strong interactions between the constituent elements, highlighting the complexity of their alloying behaviour.

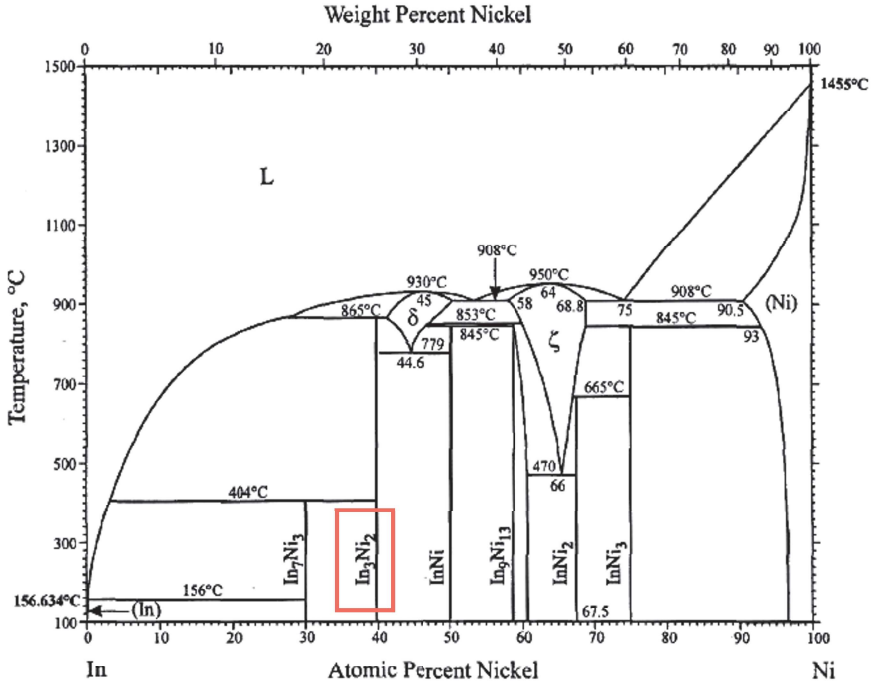


Figure 2.11: Thermodynamic phase diagram for the In–Ni binary system [62].

Within this system, In_3Ni_2 represents a distinct intermetallic phase that forms under specific compositional and thermal conditions. According to the In–Ni binary phase diagram, In_3Ni_2 is thermodynamically stable at intermediate temperatures and typically forms through solid-state diffusion between In-rich and Ni-rich regions [62]. This phase stability is essential when preparing well-defined surfaces for experimental investigation, as it directly influences the surface atomic structure and chemical reactivity.

The surface stability of different crystallographic orientations, such as (001), $(2\bar{1}0)$ and (100), is governed not only by the bulk phase equilibria, but also by surface-specific thermodynamic considerations, including surface energy minimisation and atomic rearrangement, particularly under UHV conditions. Thus, a thorough understanding of the phase diagram is critical for maintaining the structural and compositional integrity of the sur-

face during preparation procedures such as sputtering, annealing and oxidation. Moreover, this thermodynamic insight underpins the interpretation of surface-sensitive measurements and guides the optimisation of experimental procedures for surface characterisation and catalytic applications.

Crystal Growth and Structure Characterisation

The single crystal growth was carried out using the Czochralski process, which is one of the methods that can be used for crystal growth. The samples have been grown and given for examination by Professor Peter Gille [63].

An earlier attempt to obtain In_3Ni_2 from a previously synthesised isostructural Ga_3Ni_2 seed was unsuccessful due to a significant lattice parameter misfit of approximately 8% [63].

The initial stage of the Czochralski method of synthesising In_3Ni_2 single crystals is the preparation of a homogeneous melt. For In–Ni IMCs, starting with an In-rich solution of $In_{72}Ni_{28}$, the mixture is melted to a temperature where the alloy is completely molten, typically ranging from 1000 to 1200 °C, dependent upon the particular alloy composition and its melting-point characteristics. As we see in Figure 2.11, In_3Ni_2 exhibits a peritectic decomposition temperature of 869 °C, around 80 K lower than that of Ga_3Ni_2 [62]. The crystallisation temperature range has correspondingly decreased by the same amount. Then, a [001]-orientated native seed was used to grow a high-quality crystal [64]. It was immersed in the molten alloy and then carefully drawn upward while being rotated. The rate of crystal neck formation began at 0.1 mm/hr, which decreased to 0.05 mm/hr after three days and finally to 0.025 mm/hr, allowing crystal growth for a duration of 22 days. The crucible maintained a continuous rotation of 6.7 rpm, while the crystal was counter-rotated at 70 rpm to assist with the transfer of material at the growth interface [63]. An essential characteristic that determines the size and quality of the growing crystal is the pulling rate.

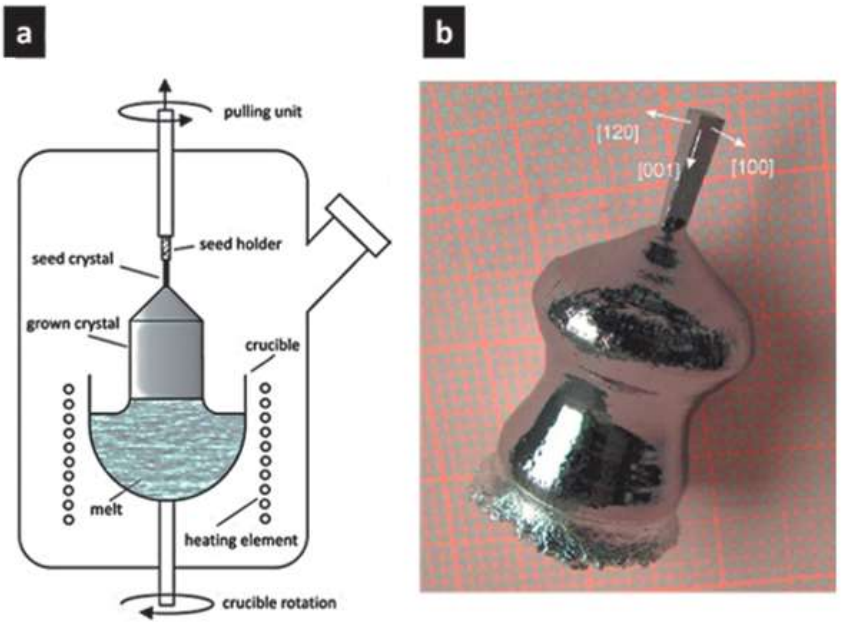


Figure 2.12: (a) A schematic of the Czochralski method [65]. (b) An image of the In_3Ni_2 single crystal that was grown using the Czochralski method, with the $3\bar{3}$ rotating axis pulled along [001] [66].

By gradually reducing the temperature of the alloy below its melting point, which can be controlled using the heating and cooling systems of the crucible, the crystal will grow. The crystal will take on a cylindrical shape as depicted in Figure 2.12 (b).

Following this, cooling must be done gradually and consistently once the crystal has been stretched into 3 samples, each one with a different crystallographic orientation, (001), (100) and $(2\bar{1}0)$. Subsequently, each surface is polished using a diamond grit paste with decreasing grain size, progressing from 6 μm to 0.25 μm, with methanol cleaning performed between each grain in an ultrasonic bath [65].

The quality of the In_3Ni_2 crystal is assessed after its growth by subjecting it to several characterisation procedures, such as back-scattered Laue diffraction, which is a common technique for ensuring the correct crystallographic orientation. The back-scattered Laue diffraction images, shown in Figure 2.13, were taken with the main X-ray beam oriented along the three distinct directions of the point group symmetry $\bar{3}$m [66].

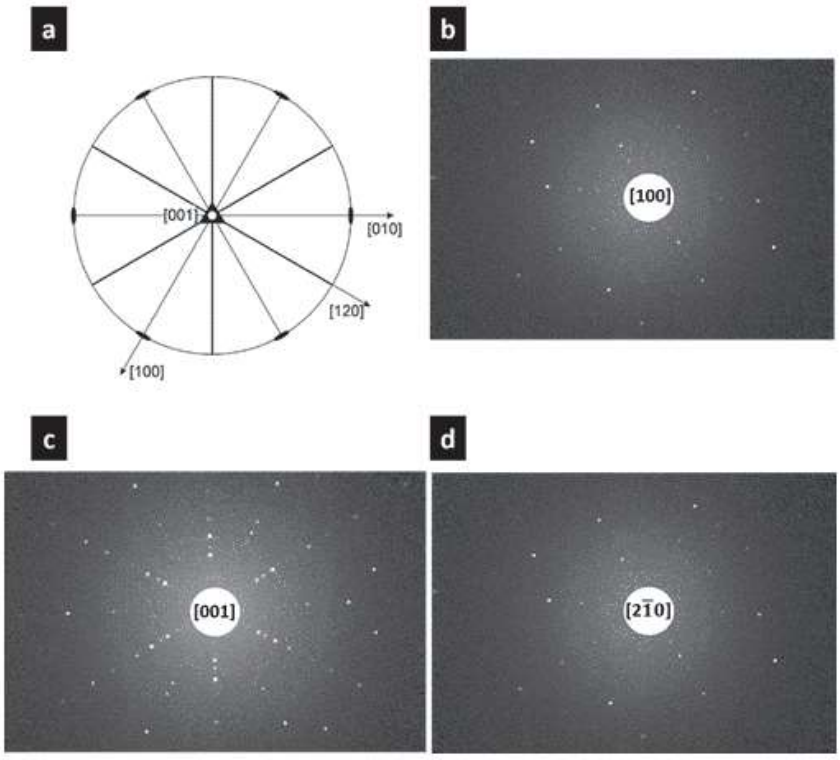


Figure 2.13: Laue diffraction images obtained from the grown In_3Ni_2 crystal with the principal X-ray beam parallel to the three symmetrically different orientations indicated in the stereographic projection: (a) [100], (b) [001], (c) [2$\bar{1}$0].

Crystal Structure

In_3Ni_2 is an intermetallic compound, with a structure identical to the Al_3Ni_2 type, which is trigonal, space group P$\bar{3}$m1 (Figure 2.12 (a)) [65]. The lattice parameters are a = b = 4.387 Å, and c = 5.295 Å, with $\alpha = \beta = 90°$ and $\gamma = 120°$ [65]. The notable selectivity of this intermetallic compound is due to the isolation of the site [9], which is shown in Figure 2.14, as all Ni atoms in grey are surrounded by four In atoms in purple, which isolate Ni atoms from one another.

Although a study has been published on the physical properties (magnetoresistance, electrical resistivity, thermal conductivity, thermoelectric power), the magnetic characteristics, specific heat and electronic density of In_3Ni_2, there are no surface studies reported on single crystals of bulk In_3Ni_2 IMCs[66].

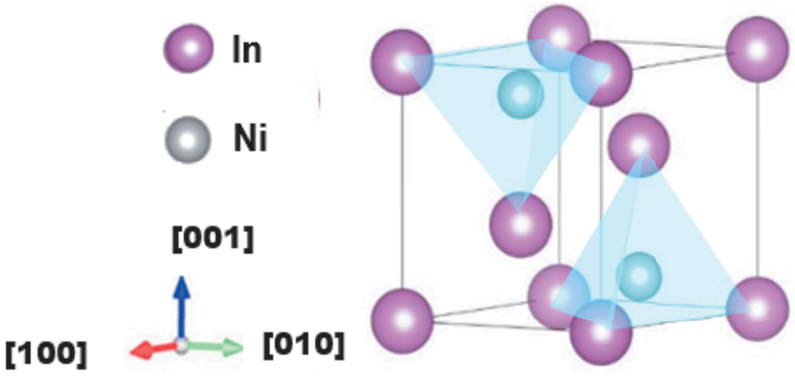


Figure 2.14: The unit cell of the In_3Ni_2 surface. Ni atoms are structurally isolated from each other by In first neighbours.

In summary, this chapter has outlined key concepts in surface science and catalysis, focusing on the role of IMCs in heterogeneous catalysis. The subsequent chapters will explore experimental methodologies and results in more depth, providing a detailed analysis of the catalytic properties of In_3Ni_2 and other intermetallic materials.

3 Experimental Methods and Techniques

3.1 Introduction

This chapter presents the experimental methodologies used to investigate the atomic structure, chemical composition and oxidation behaviour of the In_3Ni_2 intermetallic compound in its three distinct crystallographic orientations. The techniques used in this study include XPS, LEIS, STM and LEED. To ensure the purity of the samples and to minimise potential contamination during these measurements, all experiments were carried out under ultra-high vacuum (UHV) conditions.

The use of UHV is crucial in surface science, as it allows the study of clean, well-defined surfaces, free from adsorbed gases or contaminants from the atmosphere, which could otherwise compromise the accuracy of the results. In this chapter, we first describe the design and operational principles of the UHV system, detailing the necessary equipment and procedures required to achieve and maintain UHV conditions. Following this, each of the surface analysis techniques employed in this research will be discussed, from their theoretical foundations to their practical working principles and experimental setups. The combination of these advanced surface analysis techniques enables a comprehensive characterisation of the In_3Ni_2 surface properties.

3.2 Basic Principles and Design of Ultra High Vacuum (UHV)

Ultra high vacuum plays an essential role in surface science experiments by providing a clean environment. The sample surface is maintained clean, and interaction with foreign materials is minimised, ensuring a stable environment free of contamination [67]. This procedure requires maintaining low pressure to ensure that the surface remains clean throughout the experiment.

There are various vacuum regimes , to understand the difference between them, they can be divided into five regions according to pressure as shown in Table 3.1 [68]. An ultra high vacuum is usually defined as an environment with a pressure below approximately 10^{-9} mbar.

Vacuum Level	Pressure Range
Rough Vacuum	Atmospheric pressure – 10^{-3} mbar
Medium Vacuum	10^{-3} mbar – 10^{-6} mbar
High Vacuum (HV)	10^{-6} mbar – 10^{-9} mbar
Ultra high Vacuum (UHV)	10^{-9} mbar – 10^{-11} mbar
Extremely High Vacuum (XHV)	10^{-11} mbar and below

Table 3.1: Classification of vacuum levels and their corresponding pressure ranges [68].

Gas Flow

The nature of gas flow is a key characteristic that varies across different pressure regions within a vacuum system. The ratio of the mean free path (λ) of gas molecules and the diameter of the vacuum chamber (d) can be used to characterise the type of gas flow [69]. There are three different gas flow regimes that occur as gas passes through a system, which are determined by the pressure region.

At high and ultra high vacuum (UHV) pressures, the gas flow is classified as molecular flow. In this regime, gas molecules flow freely without significant collisions with one another , and they primarily interact with the walls of the vacuum chamber. In molecular flow, the mean free path of the gas molecules is much greater than the diameter of the conducting tube ($\lambda \gg d$), which has important implications for the design and operation of vacuum pumps [69, 70, 71].

The region between rough vacuum and high vacuum is commonly referred to as the medium vacuum range, where the flow regime transitions from continuum flow to molecular flow. In this intermediate regime, known as transitional flow, the mean free path of gas molecules becomes comparable to the characteristic dimension of the system, typically the diameter of the tube ($\lambda \approx d$). Under these conditions, gas molecules undergo collisions both with the chamber walls and with each other, resulting in more complex flow dynamics than those observed in either the continuum or molecular regimes. This transitional behaviour necessitates careful consideration when designing vacuum systems, as neither the assumptions of viscous nor free-molecular flow alone are sufficient to describe the gas transport accurately [69, 70, 71].

In contrast, when the diameter of the tube (d) is much larger than the mean free path (λ) of the gas particles ($\lambda \ll d$), the system operates in the low (rough) vacuum region. In this case, gas molecules undergo frequent intermolecular interactions, leading to a continuum (or viscous) flow regime. The continuum flow can be further classified as either laminar flow or turbulent flow, depending on the behaviour of the gas particles. In laminar flow, the gas flows smoothly in parallel layers, while in turbulent flow, the motion is chaotic, with the appearance of vortices. The specific flow regime is influenced by the interactions between the gas particles and the geometry of the vacuum system [69, 70, 71].

Mean Free Path (λ)

As particles pass through a material, they undergo several collisions that may change their direction of motion or other properties of the particle. The average distance that a particle, atom, molecule, or ion travels in a system before colliding with other particles is referred to as the mean free path [72].

$$\lambda = \frac{K_B T}{\sqrt{2}\epsilon^2 \pi P} \tag{1}$$

where , K_B refers to the Boltzmann constant ($K_B = 1.380 \times 10^{-23}\,\mathrm{J\,K^{-1}}$), T is the temperature in K, ϵ is the diameter of the molecule in m, and P is the gas pressure in $\mathrm{N\,m^{-2}}$ [73].

λ is influenced by factors such as temperature, pressure, and the size of the gas molecules. It plays a crucial role in determining the flow regime of gases, distinguishing between molecular, transitional , and continuum flow regimes.

From Equation 1, the mean free path is inversely proportional to the pressure, which means that high pressure results in a shorter mean free path. This leads to collisions between gas molecules and has an effect on the surface cleanliness. In low pressure regimes, where gas molecules are far apart, the mean free path can be relatively long, allowing molecules to travel substantial distances before colliding with other particles [67, 73].

The Incident Flux (Z**)**

The incident flux is a critical parameter in surface science and vacuum technology, quantifying the rate at which particles, including atoms, ions, or molecules, impact a surface. It is commonly defined as the number of particles striking a unit area of the surface per unit time [74]. Several factors influence the incident flux, including the intensity of the particle source, the configuration of the system , and the spatial separation between the particle source and the surface.

$$Z = \frac{dN}{dt} = \frac{P}{\sqrt{2MT\pi K_B}} \tag{2}$$

or

$$Z = \frac{1}{\sqrt{2\pi K_B}} \times \frac{P}{\sqrt{MT}} = 1.074 \times 10^{11} \frac{P}{\sqrt{MT}} \tag{3}$$

Where , P refers to ambient pressure in N m^{-2}, T is the temperature in K, M is the mass of a molecule in kg, and K_B is the Boltzmann constant ($k_B = 1.380 \times 10^{-23}$ J K^{-1}).

Equation 2 indicates that the incident flux of gas molecules is directly proportional to the pressure, indicating that increased pressure increases the density of particles (molecules, atoms, or ions) impacting the surface. This results in surface contamination [67, 75].

Sticking Coefficient (S)

The sticking coefficient is a parameter that quantifies the probability that a gas-phase particle, upon colliding with a surface, will adsorb rather than reflect or scatter. It is defined as the ratio of the number of particles that adhere to the surface to the total number of particles that impact it.

$$S = \frac{N_{\text{adsorbed}}}{N_{\text{incident}}} \tag{4}$$

where:

- N_{adsorbed} is the number of particles that successfully adsorb onto the surface.
- N_{incident} is the total number of incident particles on the surface.

The value of the sticking coefficient ranges from 0 to 1:

- $S = 1$ indicates that every particle striking the surface is adsorbed.

- $S = 0$ indicates that no particles stick to the surface.

The sticking coefficient is influenced by several variables, including particle kinetic energy, surface coverage, gas composition and surface chemical composition and surface temperature [76, 77].

3.2.1 UHV Pumps

Maintaining a clean surface is essential in surface analysis, as any contamination can significantly affect the accuracy of the results. To ensure surface cleanliness during measurements, analyses are performed under UHV conditions. The UHV system employed for the experimental measurements in this study is illustrated in Figure 3.6.

Various materials are commonly used in the construction of UHV systems, including stainless steel, glass, copper, ceramics, specific plastics, and refractory metals such as tantalum, tungsten, and molybdenum. In contrast, materials with high vapour pressures are unsuitable for UHV environments due to their tendency to evaporate at relatively low temperatures. Alloys containing these elements are also generally avoided, as they can release gases that compromise the vacuum quality [75, 78].

Achieving the extremely low pressures required for UHV systems involves the use of several types of vacuum pumps, each offering distinct operational characteristics such as a rotary pump, a turbo-molecular pump, an ion getter pump , and and a titanium sublimation pump [69]. A detailed explanation of these pumping systems, ion gauges and mass spectrometers is provided in this section. a titanium sublimation pump [69]. A detailed explanation of these pumping systems, ion gauges, and mass spectrometers is provided in this section.

Rotary Pump (Rough Pump)

The rotary vane pump is widely employed due to its effectiveness in serving both roughing and primary pumping. It is used as a first pumping stage to remove bulk gas (air)

from the chamber and create a pre-vacuum for another pump by use of rotors, set off-centre within the chamber [69]. When the pump is intaking gas, there is an expanding volume. As the rotor continues to rotate, the volume is compressed, the valve is opened , and gas molecules are removed from the system, causing the pressure to fall from atmospheric pressure to 10^{-3} mbar. This cycle is repeated several times [69, 75].

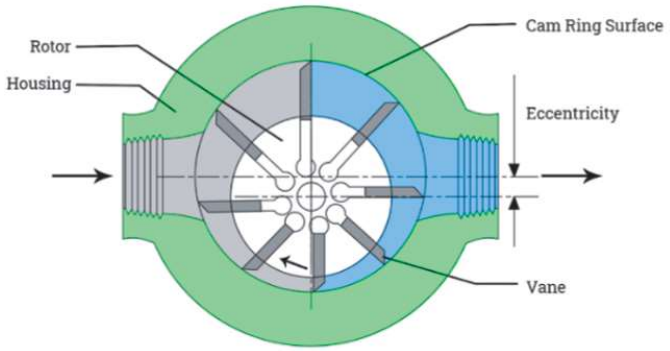


Figure 3.1: Schematic of a rotary pump [79].

Turbo Molecular Pump

turbo molecular pump consists of two blades, the rotors and the stators, oppositely inclined to each other (Figure 3.2) and is used as the second stage of a pumping system to pump the chamber to the UHV range. It operates by spinning up the rotors to 30,000 rpm and transferring momentum to gas molecules that enter from the inlet. The molecules then go straight to the stator's transfer holes. Finally, a pump linked to the bottom removes the molecules.

This pump, which operates in the molecular flow regime, can reduce the pressure from 10^{-3} mbar down to 10^{-10} mbar and therefore must be exhausted to a backing pump, typically a rotary vane pump. For correct operation, the system must be at molecular flow conditions. In other words, the mean free path is larger than the blade spacing [69]. A turbo molecular pump may achieve UHV; however, the vibrations generated are frequently detrimental for vibration-sensitive methods such as scanning tunnelling microscopy.

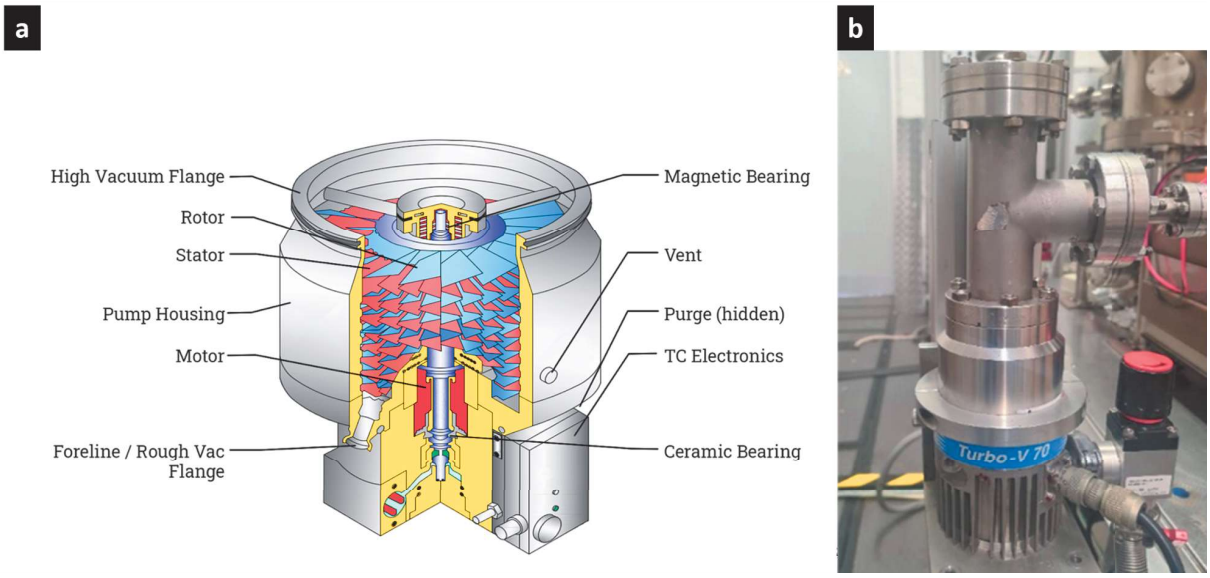


Figure 3.2: (a) Schematic of a turbo molecular pump [79]. (b) Turbo molecular pump at the Surface Science Research Centre of the University of Liverpool.

Ion Pump (UHV Pump)

Ion pumps maintain the pressure low to 10^{-11} mbar [69], by binding residual gas, therefore preventing it from influencing the pressure. The basic components of ion pumps are short cylindrical anodes, made of stainless steel, positioned between two titanium cathodes [77].

The pump works through sorption processes initiated by ionised gas particles following a cold cathode discharge. The significant potential difference (several keV) drives the ionised particles towards the titanium cathode, where they are either collected or chemisorbed. The pumps are surrounded by substantial magnets, which induce the discharge electrons to traverse a helical path, increasing the route length and, consequently, the probability of ionising collisions [77]. The operational concept of this pump type is shown in Figure 3.3.

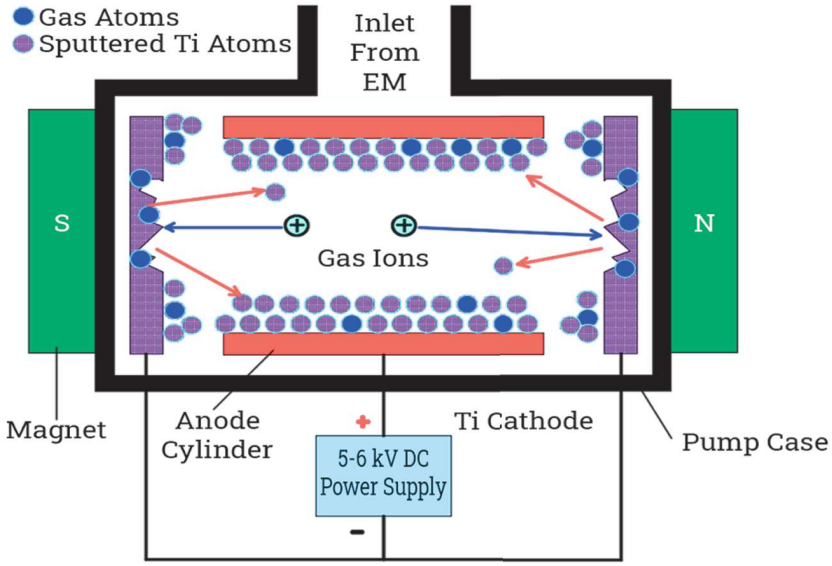


Figure 3.3: Schematic of an ion pump [79].

Titanium Sublimation Pump (TSP)

A titanium sublimation pump is commonly employed as a supplementary pumping device within vacuum chambers, particularly in conjunction with ion pumps. It operates effectively under low pressure conditions.

The mechanism involves heating a titanium filament with a high electric current, causing the metal to sublimate and deposit onto the chamber walls (Figure 3.4). This deposition forms a highly reactive surface that promotes chemisorption, especially of hydrogen, which is otherwise difficult to remove. The pumping efficiency can be significantly enhanced by cooling the chamber walls using a liquid nitrogen trap. However, this cooling technique is not implemented in the experimental systems used in this study [67].

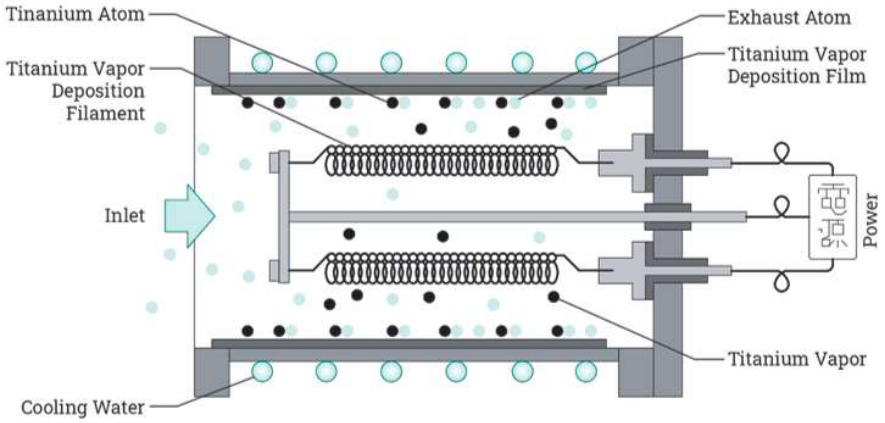


Figure 3.4: Schematic of a titanium sublimation pump [79].

3.2.2 Pressure Gauges

Pressure measurement requires several methods depending on the flow regime. There are two gauges used in UHV systems.

Pirani Gauge

In the higher pressure, viscous flow region, the Pirani gauge is commonly used to measure pressures down to approximately 10^{-3} mbar. This gauge operates based on the thermal conductivity of gases, which varies with pressure. A constant electric current is passed through a filament within the vacuum chamber. The interaction of gas particles impacts the filament's temperature, thus affecting its resistance. At higher pressures, more heat is transferred, leading to a decrease in filament temperature, which in turn alters its electrical resistance. This change in resistance is detected using a Wheatstone bridge circuit, providing a measure of the pressure [67].

However, below 10^{-3} mbar, the decreased frequency of molecular collisions limits the gauge sensitivity, as there are insufficient interactions to cause a measurable change in the filament resistance.

Ion Gauge

The molecular flow regime gauge requires an ionisation gauge for pressure measurement (Figure 3.5). Electrons are pushed over a large potential difference and into a positively biased cage by use of a filament, which enhances thermionic emission. It is common for electrons to go through the cage before returning to the anode, but sometimes an electron will ionise a gas particle inside the cage, which then accelerates into the collector with a negative bias. The pressure can then be calculated the current that is measured from the collector [67].

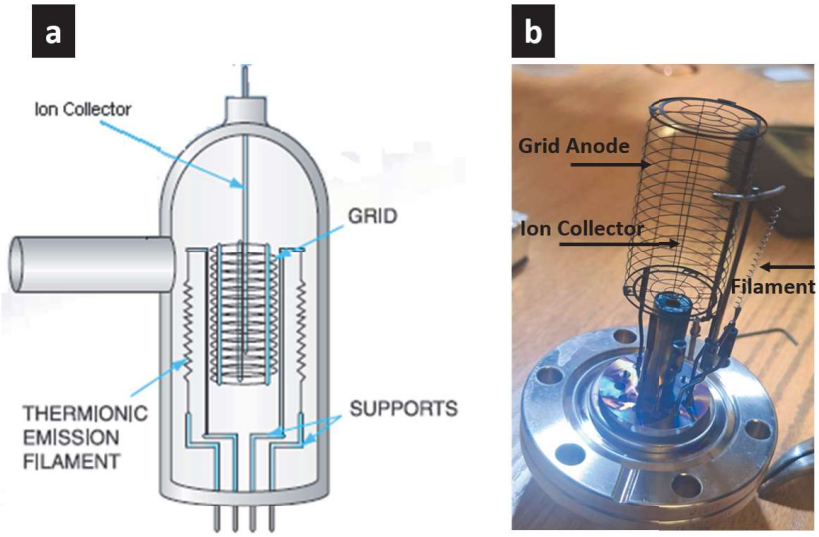


Figure 3.5: (a) Schematic of an ionisation gauge [67]. (b) An ionisation gauge at the Surface Science Research Centre of the University of Liverpool.

3.2.3 Laboratory Equipment

Ultra high vacuum is essential for surface science studies as it ensures a clean environment and minimises interaction with extraneous materials to ensure a stable environment free from contamination [67]. This procedure requires low pressure to maintain surface cleanliness during the experiment. The ultra high vacuum equipment used in this thesis, situated in the Surface Science Research Centre of the University of Liverpool, is shown in Figure 3.6.

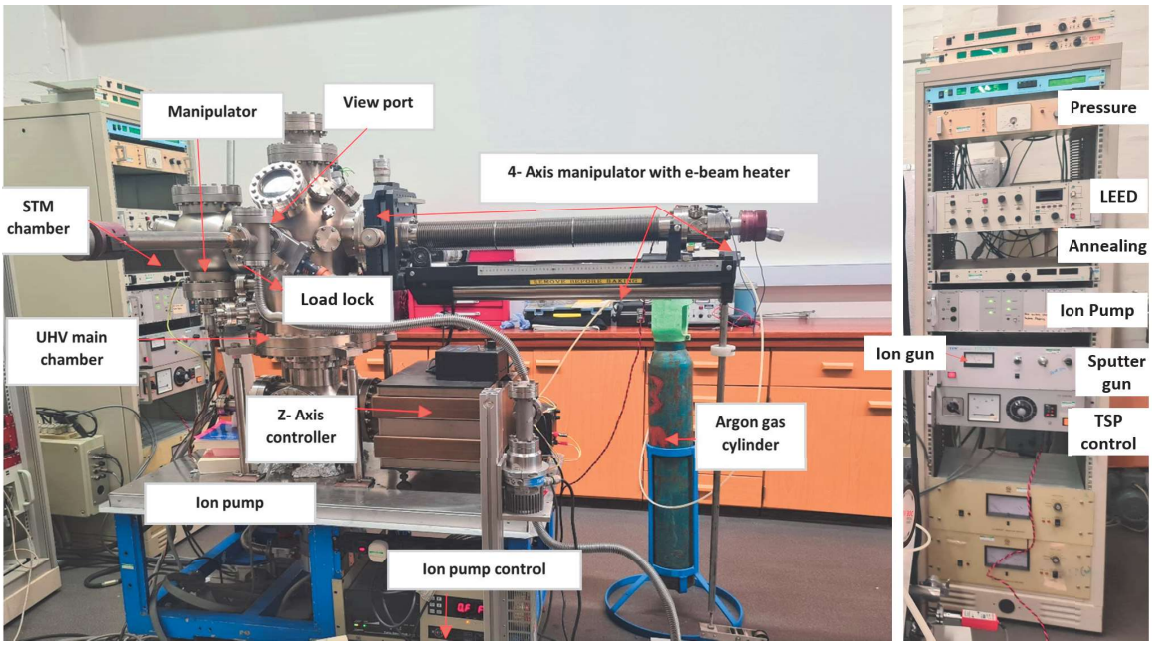


Figure 3.6: Ultra high vacuum chamber at the Surface Science Research Centre of the University of Liverpool used in this thesis.

3.2.4 Venting and Baking the System

Venting the UHV system requires exposing it to atmospheric pressure. It may need opening so that some broken parts, such as the tip in the STM or a leak in the main chamber, can be repaired. To vent a UHV system, all components and pumps must be turned off.

During baking, weakly bonded surface water and hydrocarbon molecules that adhere to the walls of the UHV chamber after venting of the system are eliminated. To begin the baking process, all chamber windows must be covered with aluminium foil to prevent breakage and all electrical connection plugs must be unplugged, as seen in Figure 3.7. This technique is conducted while the turbo molecular pump operates. It entails heating the whole chamber to a temperature range of 120–200 °C with ceramic heaters and insulating panels for a duration of 24 to 48 hours [76].

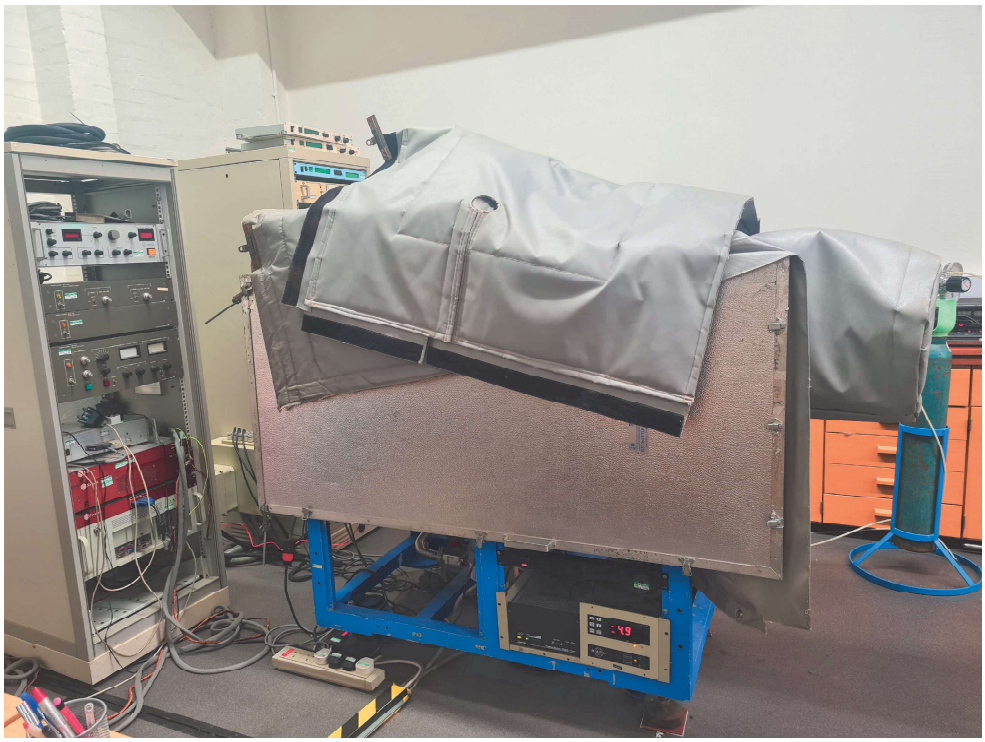


Figure 3.7: Baking ultra high vacuum equipment at the Surface Science Research Centre of the University of Liverpool.

3.2.5 Mass Spectrometry

Mass spectrometry is essential in UHV systems, particularly for the analysis and identification of residual gases at exceedingly low pressures (<10^{-9} mbar).

The mass spectrometer uses quadrupole technology to selectively filter ions before they reach the detector. The primary operations within the mass spectrometer include the ionisation of gas molecules, the filtration of ions via the detector and the subsequent detection of the ions. The spectrometer subsequently amalgamates the findings into a spectrum, displaying the peaks for each identified ion. This enables the user to identify the gases present, accurately measure their concentration, or verify the purity of any manually provided gases.

A heated cathode first experiences thermionic emission, ionising gas molecules and propelling electrons towards the anode. The quadrupole analyser ionises the gas molecules

passing through this region and then propels them along a path. The quadrupole selectively causes resonance in ions with certain mass-to-charge ratios as they move by applying oscillating radio frequency voltages between one pair of rods and another. All other ions move away from the detector and towards the poles. The detector picks up the ions post quadrupole passage and turns it into an intensity that is related to the number of ions that were collected [80].

By analysing the voltage frequencies at the poles, the device examines the mass-to-charge ratios and quantifies the quantity of ions for every period. This approach enables the collection of a spectrum of the present gas molecules.

The high sensitivity and selectivity of mass spectrometry make it an essential instrument for maintaining ultra high vacuum conditions, identifying leaks and ensuring the dependability of high-precision experiments and industrial operations.



Figure 3.8: Mass spectrometer used in the Surface Science Research Centre of the University of Liverpool, which is used to indicate the elements inside the UHV chamber.

3.3 Surface Preparation

It is essential to make sure that the surface is clean before measuring its characteristics. To achieve the required cleanliness, it is necessary to eliminate surface contaminants on both a macroscopic and microscopic level. This section will detail the preparation of each of the three samples before and after their positioning in the UHV chamber.

Ex situ

To prepare In3Ni2 samples for the surface study, we used a standard stainless steel sample holder and cleaned it by placing it in an ultrasonic bath with methanol for 15 minutes to remove residual contamination that could be emitted in the UHV system (Figure 3.9 (a)). The sample holder was then degassed in the UHV system to ensure that the sample holder surface was free of contaminants before placing the sample on it. We placed the sample in the clean holder using a tantalum wire (Ta), a welding instrument and a microscope, as seen in Figure 3.9 (b). Once the sample was mounted, it was put in an ultrasonic bath once again (Figure 3.9 (c)). Then it was placed in the load lock, pumped until the desired pressure was reached and then moved to the main chamber to start the measurements (Figure 3.9 (d)).

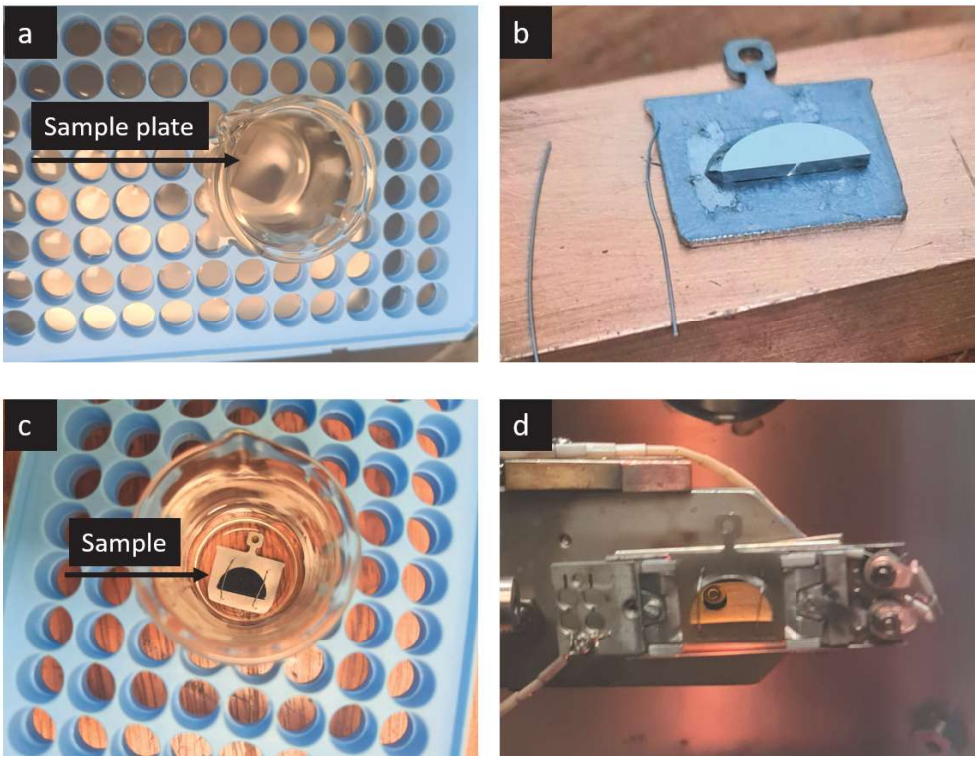


Figure 3.9: (a) Stainless steel sample holder cleaned by immersing it in methanol and an ultrasonic device for 15 minutes. (b) Sample attached to the holder by using tantalum (Ta) wire. (c) Ultrasonic device used to clean sample after being placed on the holder. (d) $In_3Ni_2(001)$ sample inserted into the UHV chamber after cleaning.

In situ

Atomic surface preparation is done within the UHV system using ion bombardment (sputtering) and high temperature treatment (annealing) cycles, which are common techniques used to clean the surface. The degassing was carried out in an ultra high vacuum system with a base pressure around 3.6×10 $^{-}$10 mbar at 560 °C for 30 minutes. This was followed by multiple cycles of sputtering with noble gas ions (Ar^{+}) for 30 minutes at a pressure of approximately 7.4×10 $^{-}$6 mbar, with an average drain current of 7 µA. Subsequently, the sample was annealed at different temperatures ranging from 360 °C to 560 °C for (60–180) minutes to ensure thermal equilibrium, with a base pressure around 6×10 $^{-}$10 mbar.

This process was carried out several times until LEED patterns were seen from the surface or until an XPS analysis revealed no contamination on the surface. One of the highest temperatures used to anneal all the samples was 560 °C. After directly annealing the surface, an optical pyrometer with an emissivity of 0.40 measured all temperatures, while using thermocouples for LEIS experiments.

To determine the appropriate emissivity setting for the optical pyrometer, a thermocouple was used as a reference in the LEIS (Low Energy Ion Scattering) setup. The In_3Ni_2 surface was mounted in such a way that both the optical pyrometer and the thermocouple could accurately measure the temperature of the sample. Temperature readings were recorded from the thermocouple in the LEIS chamber and the emissivity of the optical pyrometer was adjusted until the temperature indicated by the pyrometer corresponded to that measured by the thermocouple. The emissivity value was varied at different temperatures to achieve a match with the thermocouple readings presented in Table 3.2.

Emissivity	Optical Pyrometer	Thermocouple
0.1	389 °C	319 °C
0.2	336 °C	309 °C
0.3	319 °C	306 °C
0.4	286 °C	300 °C
0.5	294 °C	297 °C
0.6	281 °C	293 °C
0.7	255 °C	287 °C
0.8	249 °C	284 °C
0.9	249 °C	275 °C

Table 3.2: Comparison of temperature measurements obtained from the thermocouple and the optical pyrometer at various emissivity settings. Emissivity values between 0.4 and 0.5, highlighted in blue, represent the most accurate correspondence between the two measurement methods.

The emissivity values in the range of 0.4 to 0.5 were found to yield the most accurate temperature readings, with good agreement between the thermocouple and the optical pyrometer measurements. Therefore, subsequent analysis focused on this emissivity range, as summarised in Table 3.3. It was observed that the 0.48 emissivity remained relatively constant over the temperature range.

Emissivity	Optical Pyrometer	Thermocouple
0.4	261 °C	267 °C
0.42	259 °C	264 °C
0.44	259 °C	261 °C
0.46	258 °C	259 °C
0.48	250 °C	250 °C

Table 3.3: Comparison of emissivity values measured using thermocouple and optical pyrometer techniques. The emissivity value of 0.48, highlighted in blue, shows the closest agreement between the optical pyrometer and thermocouple values; therefore, 0.48 is considered the most accurate emissivity.

Experiments to determine the structural and chemical properties of the clean In_3Ni_2 surface were conducted in a UHV chamber with a base pressure around 2×10^{-8} mbar using a four-grid LEED system and XPS, respectively.

3.3.1 Sputtering the Surface (Ion Bombardment)

The sputtering technique requires a high energy process gas (100 - 3000 eV), such as argon gas (Ar^+), produced by a noble gas ion positioned in front of the crystal surface [24]. Second, the electric potential applied to the cathode will cause free electrons to accelerate and move away from the cathode. The moving electrons collide with the neutral argon atoms and an electron is removed from the atom, resulting in an argon ion (Ar^+). These are accelerated towards the cathode and collide at a grazing angle with the target material in the chamber space. The ejected atoms are not charged, so they travel straight to the centre of the chamber [81]. Sputtering produces a negative side effect as it changes the structure of the substrate. The crystals require annealing at high temperatures to eliminate imperfections on the surface caused by sputtering [82].

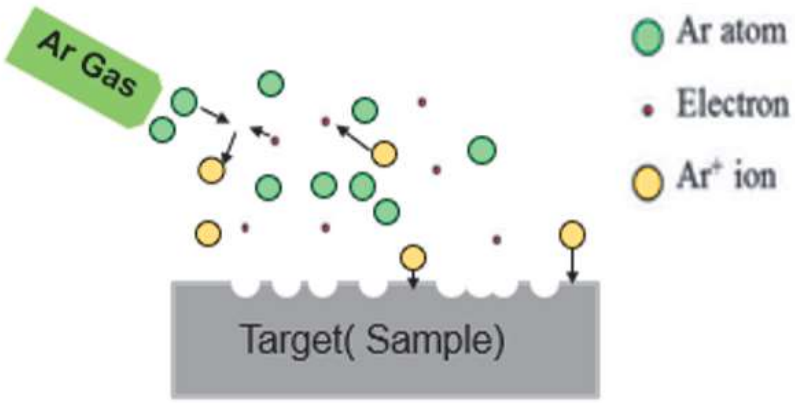


Figure 3.10: Operational setup of an Ar^+ ion gun during the sputtering process. In this configuration, argon ions are accelerated under vacuum conditions and directed towards the target (sample surface), where they induce the controlled removal of surface atoms. This process is commonly used for surface cleaning in surface science.

3.3.2 Annealing the Surface (High Temperature Treatment)

A surface that has been sputtered becomes pitted and rough. Consequently, it is essential to restore it to its original state by annealing the substrate below or near its melting temperature [83]. The binary In–Ni phase diagram shows that the melting temperature for In_3Ni_2 is 865 °C.

To prevent damage to the sample, it must not be annealed to temperatures above 570 °C, which is around $\frac{2}{3}$ of the bulk temperature. This will influence the number of active sites, their geometry and the catalytic activity and selectivity of the surface [10]. In addition, it may take several hours of annealing to produce atomically flat terraces that are sufficiently large and well spaced to allow useful data analysis [74].

3.4 Experimental Techniques

3.4.1 X-ray Photo Electron Spectroscopy (XPS)

X-ray photoelectron spectroscopy (also known as electron spectroscopy for chemical analysis, or ESCA) can provide chemical state information of a sample up to a few nanometres in depth [84].

The sample is exposed to incident X-rays, which cause photoemission. Then, the kinetic energies of the electrons are measured. After that, spectra that contain specific peaks are generated and those peaks may be used to determine which chemical species are present on the surface of the sample. The electrons which are non-scattered from the sample can only reach the detector if the procedure is performed under UHV conditions [85]. Initially proposed by Albert Einstein in 1905, for which he subsequently won the Nobel Prize in 1921 [86], the method was invented and pioneered by Karl Siegbahn, who received the Nobel Prize in 1981 for his groundbreaking work in the development of electron spectroscopy [87].

Physical Basis

The surface atoms of a sample are exposed to bombardment by photons of specific energy, resulting in the excitation of the electronic states within the atoms. This produces electron emission from the surface that corresponds with the photoelectric effect, which can be described by equation 5. The binding energy E_B can be calculated using the kinetic energy of the emitted electron E_k, the energy of the incident radiation $h\nu$, and the energy required to release an electron from the Fermi level to vacuum, known as the work function ϕ.

$$E_B = h\nu - E_K - \phi \tag{5}$$

Equation 5 shows that the binding energy E_B may be calculated by using the kinetic energy of the emitted electron E_K, the energy of the incident radiation $h\nu$, and the work function ϕ. In XPS, the work function of the detector is used rather than the material's work function, which is what the equation above refers to [88]. This occurs because the Fermi levels of the sample and the spectrometer are aligned and there is electrical contact between the two [89].

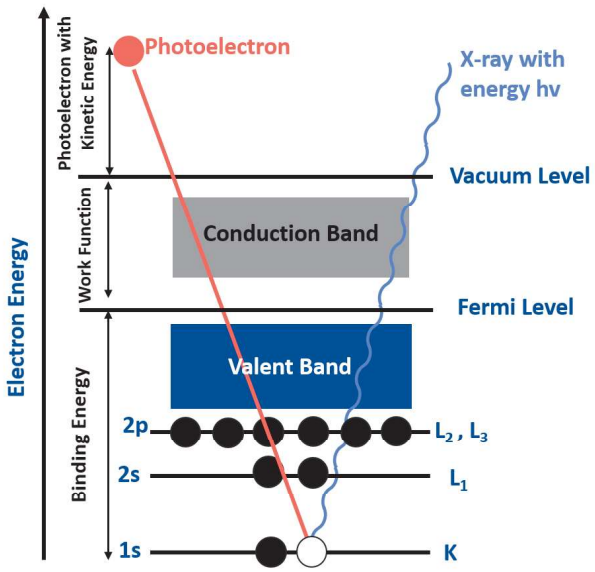


Figure 3.11: Photoemission process in XPS. Reproduced and modified from [89].

In Figure 3.11, we can see an example of the fundamental processes that occur in the atomic electronic states during XPS. XPS is used in the identification of the chemical composition of samples, discussed further in Chapters 6, 7 and 8.

Instrumentation

In a laboratory equipped with XPS, the selection of an incident X-ray beam excites an electron from a sample to a detector. The main sources are Mg and Al, where high energy electrons are accelerated towards a water-cooled Mg and Al anode to produce incident X-rays of defined energy.

The production of this X-ray conforms to a procedure similar to that shown in Figure 3.11. Subsequent to the extraction of the core-level electron, the electrons within the atom undergo rearrangement. Electrons that are less tightly bound move from higher energy levels to the core level, resulting in the emission of a photon.

An X-ray source that comes from Mg or Al in the lab has clear doublet emission peaks. These are caused by electron vacancies in the K shell. This will result in the observation of "satellite" peaks within the spectra where both Kα and Kβ photoelectrons are recorded. Mg and Al possess Kα energies of 1253.6 eV and 1486.6 eV, respectively. By filtering out one of the photons and diffracting the X-ray beam, the Kβ photons are taken out until only the Kα photons are left in the beam. This thesis does not employ a monochromatic XPS system for its research. The following procedure is to focus the electrons on the hemispherical analyser entrance slit after being enhanced using a series of electrostatic lenses.

The electron passes through the analyser inner and outer domes. To create an electromagnetic field that enables only electrons with certain energy levels to pass to the detectors, each hemisphere is set up with a different voltage [90]. To generate an XPS spectrum, one needs to change the voltages and distribute the energy over the spectrum. There are two ways for operating the system: fixed retardation energy mode (FRR) and fixed analyser transmission mode (FAT). All electrons enter the analyser with the same kinetic

energy in FAT mode as the electrostatic lenses either slow them down or speed them up. The energy being measured is identical to the pass energy of the electron energy analyser. In this mode, the lens biases change such that electrons with a certain starting kinetic energy are focused on the entry slit of the analyser and either slowed down or sped up to the pass energy of the analyser. Another thing that is modified in FRR mode is the analyser pass energy such that the initial electron energy divided by the pass energy remains constant. In this study, all measurements were done in FAT mode, which can produce a stronger signal even at low kinetic energies.

The XPS spectra from the In3Ni2(001) surface are shown in Figure 3.12. The spectra are a graph of the number of electrons recorded for each binding energy bin. The energy step range determines the size of the bins. Emission of photoelectrons from core levels occurs when there is enough energy. We can determine the elemental composition of the surface by recording the binding energies of each peak. Figure 3.12 displays core level peaks for In and Ni. The intensity of In and Ni core levels can be fitted by removing the background from the area of each peak to determine the peak position and area under the peak. This topic is further covered in Sections 4.4, 5.4 and 6.4.

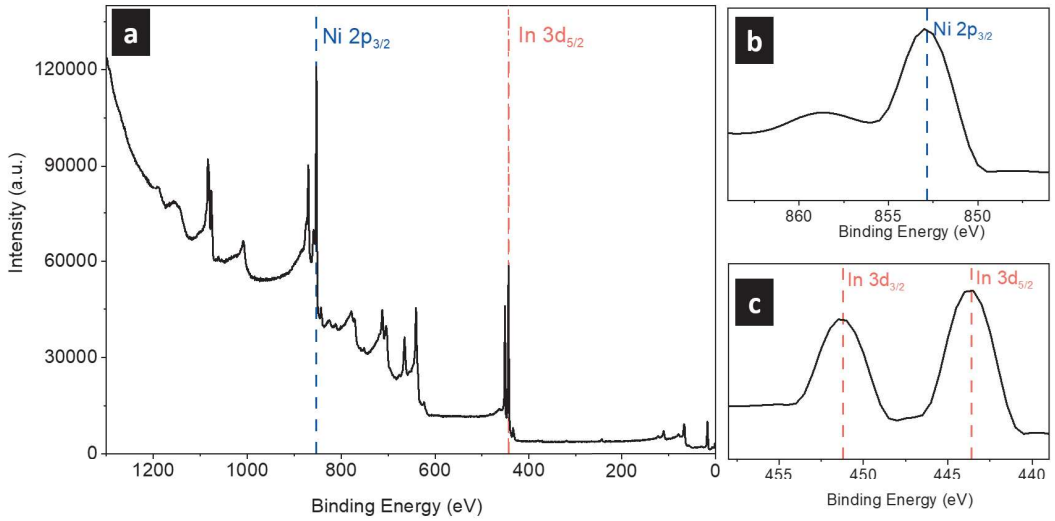


Figure 3.12: (a) An XPS spectrum taken from $In_3Ni_2(001)$ with the largest core level highlighted by a blue line for Ni and red lines for In. (b) Ni 2*p* core level. (c) In 3*d* core level.

Atomic Composition Calculation

The atomic composition of the surface, determined from XPS spectra, involves measuring the relative concentrations of In and Ni elements on the surface of In3Ni2 samples, based on the intensities of the peaks in the XPS spectrum.

The first step in atomic composition calculation is to identify the peaks corresponding to the In and Ni elements. Then, removing a background signal caused by inelastic scattering of photoelectrons from the XPS spectrum using the Shirley-type function [91], which fits a background curve to the spectrum, subtracts it from the total signal and dividing the area by the number of XPS scans used during data acquisition.

After background subtraction, the area under each peak is determined. However, the atomic composition is affected by several instrumental factors, such as the photoionization cross-section (PC), the analyser transmission function (ATF), which corrects for the efficiency of the analyser in detecting photoelectrons and depends on the specific setup of the XPS instrument, and the inelastic mean free path (IMFP) that represents the average distance a photoelectron can travel before losing energy due to inelastic collisions.

To account for differences in the sensitivity of the XPS system to different elements, the corrected peak area (CA) for each element is normalised. The normalisation process generally involves dividing CA by the PC, as obtained from the literature [92], corresponding to the X-ray source used. The IMF IMFP value for In3Ni2 was calculated using the Tanuma, Powell and Penn - Model 2 Modified (TPP2M model) from equation 6 [93].

$$IMF = \frac{538, a, E_k^2}{(E_k^2 + E_g^2)\left[\beta \ln\left(1 + \frac{\gamma E}{E_p^2}\right)\right]} \tag{6}$$

Where, IMF refers to the inelastic mean free path, E_k is the electron kinetic energy of the core level, E_p is the free electron plasmon energy, E_g is the band gap energy, a is a material-dependent constant and (β, γ) are empirical fitting parameters.

The normalised area function (NA) is given by

$$\text{Normalised Area } (NA) = \frac{CA}{PC \times IMF \times ATF} \tag{7}$$

The analyser transmission function (ATF) is defined by

$$ATF = \left(\frac{a^2}{a^2 + \frac{E_K^2}{E_P^2}} \right)^b \tag{8}$$

After normalisation, the relative atomic composition can be calculated by comparing the normalised peak area of each element to the sum of all normalised areas.

$$\text{AC}_i = \frac{NA_i}{\sum_j NA_j} \tag{9}$$

Where j refers to In and Ni elements, NA_i is the normalised peak area corresponding to In and Ni elements, and $\sum_j NA_j$ is the sum of the normalised peak areas for all elements present in the sample.

Depth Profile

For the In3Ni2 surface, XPS measurements are typically performed with the sample positioned normal to the detector, which maximises the photoelectron collection efficiency and reduces statistical error. This configuration ensures that photoelectrons originating from a few nanometres beneath the surface can escape and reach the detector. The profiling depth for the In3Ni2 surface, when oriented normal to the detector, was estimated to be approximately 24 nm. This estimation was derived using the standard approximation of 3λ, where λ represents the inelastic mean free path for the In3Ni2 sample, calculated using the TPP2M formalism (Tennant, Papp and Pannell), which describes the average distance an electron can travel through a material during inelastic scattering events, such as excitations of electrons in the target material [94].

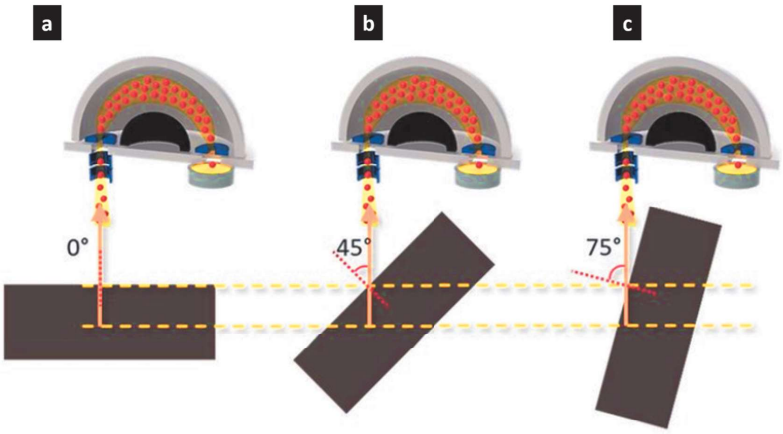


Figure 3.13: The scanning angles between the detector and the X-ray affect the depth of the sample scanned by XPS: (a) at normal angle; (b) at 45°; (c) at 75°. Reproduced and modified from [95].

As the grazing angle increases, the XPS technique becomes more sensitive to the surface [96], as photoelectrons generated closer to the surface have a higher probability of escaping. In contrast, at smaller grazing angles, photoelectrons from deeper regions are less likely to be ejected. However, this increased surface sensitivity is accompanied by a decrease in the overall signal intensity recorded.

To account for this variation, our experimental setup is designed to collect XPS data at multiple grazing angles by rotating the sample, thus providing a more comprehensive surface analysis.

3.4.2 Low Energy Ion Spectroscopy (LEIS)

Low Energy Ion Spectroscopy (LEIS) is an extremely surface-sensitive analytical method employed to investigate the composition of the outermost atomic layers of materials. By the end of the 1960s, advancements in ultra-high vacuum (UHV) systems and ion beam technology enabled the first systematic LEIS experiments, demonstrating its capability to probe only the outermost atomic layer [97]. LEIS has developed into an essential tool for basic science and industrial applications.

Notably, LEIS is different from other surface analysis methods because it can give in-

formation about the very top atomic layer of materials. This is in contrast to methods like X-ray photoelectron spectroscopy (XPS), which probes the very first few nanometres [98].

Physical Basis

The physical principles concerning LEIS are primarily based on classical mechanics, particularly the conservation of energy and momentum during elastic collisions between incoming ions and surface atoms.

In LEIS, a sample is exposed to ions with energy ranging from 0.1 to 10 keV. The sample atoms scatter these ions. He, Ne, Ar and Kr are examples of inert gas ions that we use in this thesis helium (He) gas only. Because inert gas ions have a high chance of neutralising, ions scattered from deeper than the outermost atomic layer will be almost completely attenuated. When we detect only charged particles, we achieve surface sensitivity.

A schematic picture of ion backscattering at a surface is shown in Figure 3.14. LEIS primarily relies on elastic collisions between incoming ions and atoms on the surface. The scattering ion's energy after colliding with an atom on the surface can be described by equation

$$E_S = \left(\frac{\cos\theta + \sqrt{\left(\frac{M_S}{M_P}\right)^2 - \sin^2\theta}}{1 + \left(\frac{M_S}{M_P}\right)} \right)^2 E_P, \quad \left(\frac{M_S}{M_P}\right) \geq 1 \tag{10}$$

where E_P is the energy of the primary ion, E_S is the energy it has after scattering, M_P is the mass of the primary ion and M_S is the mass of the scattering surface atom, and θ is the angle through which the scattering takes place.

This equation indicates that if the mass of the surface atom (M_S) is above that of the primary ion (M_P), energy and momentum are transferred during scattering, enabling backscattering, which serves as the principal identifying mechanism in LEIS. If the mass ratio condition is not satisfied, forward scattering occurs. Similar to the behaviour of a bowling ball colliding with lighter pins rather than heavier ones, the lighter object re-

bounds upon impact.

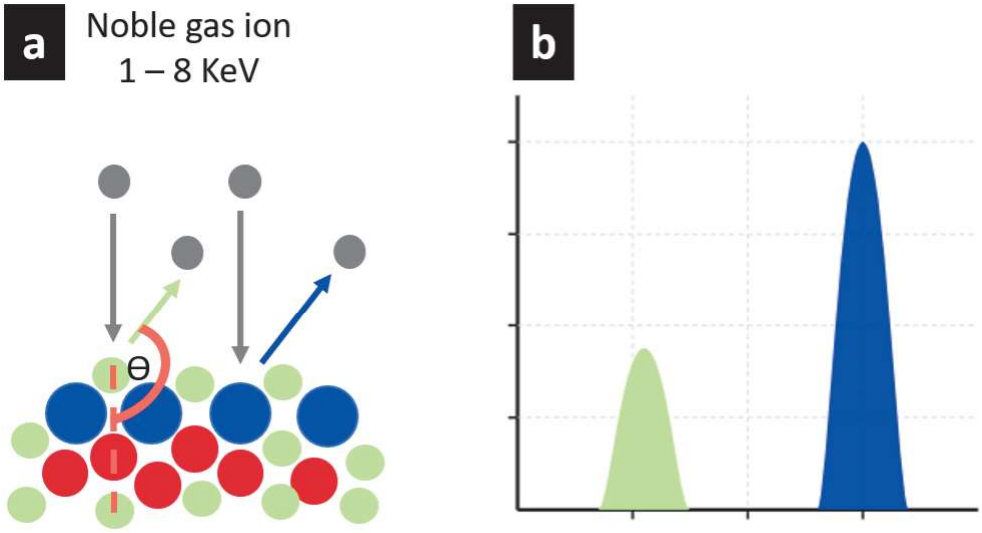


Figure 3.14: (a) The bombardment of a surface with three types of exposed atoms by noble gas ions. (b) LEIS signal corresponding to the surface on the left. Note that there is no LEIS signal from the 'red' atoms, which are deep in the surface. Reproduced and modified from [97].

Instrumentation

Qtac100 (commercial product) is a LEIS instrument with a double toroidal analyser (DTA). The Qtac100 is designed to operate at UHV conditions, essential for ensuring that ions have long mean free paths to the sample and minimising contamination. This advanced analytical instrument has been designed for high sensitivity and accuracy in determining the elemental composition of the outermost atomic layers of materials. Moreover, it allows an almost 360° azimuthal collection of backscattered ions, enhancing both sensitivity and specificity in analysis. This design proves useful as it allows for sampling a limited range of backscattering angles while obtaining a larger quantity of ions compared with typical hemispherical electron spectrometers used in XPS.

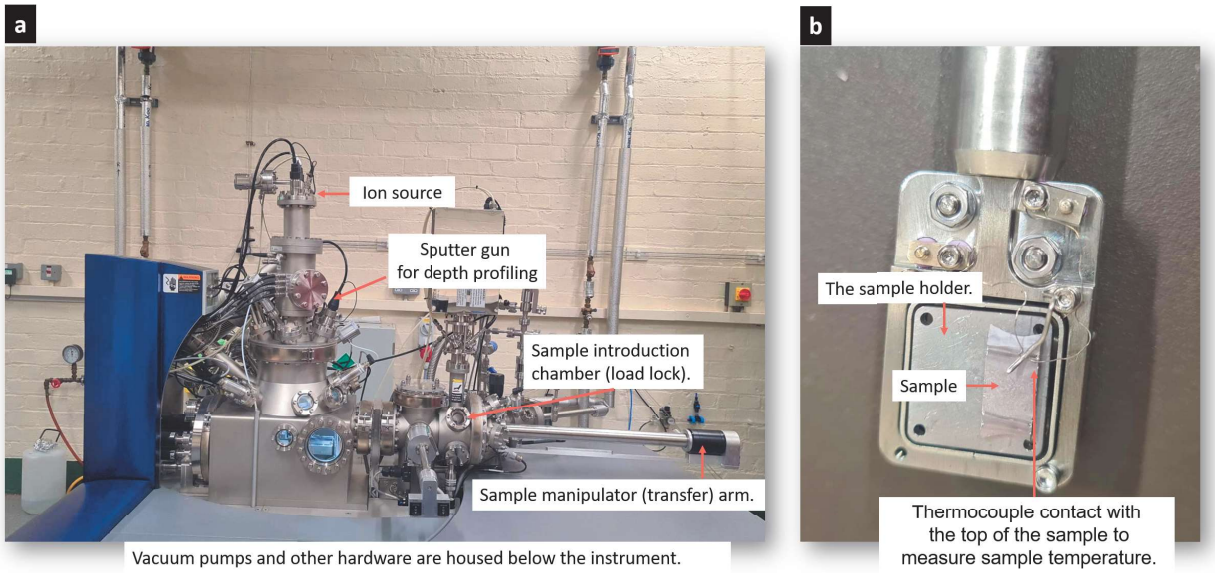


Figure 3.15: (a) LEIS instrument at the University of Liverpool used to produce the results for In_3Ni_2 samples. (b) The sample placed on the holder.

The machine's essential components include an ion source for emitting noble gas ions (He, Ne, or Ar) perpendicular to the sample, an ion gun to accelerate the ions before their interaction with the sample surface, an energy analyser located within the main chamber, and the ability to include a sputter gun for depth profiling, along with a double toroidal analyser (DTA). This component collects backscattered ions and is essential for determining their kinetic energy. The DTA has been designed to detect ions across a wide angular spectrum, allowing enhanced sensitivity and greater mass resolution relative to conventional analysers. Figure 3.15 illustrates the LEIS instrument used at the University of Liverpool.

3.4.3 Low Energy Electron Diffraction (LEED)

One surface-sensitive method is Low Energy Electron Diffraction (LEED), which involves reflecting an electron beam with low energy (50–500 eV) to determine the atomic structure of the surfaces of crystals.

It is commonly used in surface physics to image the reciprocal lattice and learn more

about how atoms are arranged on the surface, but it needs to be performed in ultra high vacuum. Clinton Joseph Davisson and Lester Halbert Germer conducted groundbreaking experiments in 1927, which led to the development of the electron diffraction technique. Their work demonstrated the wave nature of electrons, leading to the development of techniques such as LEED [99].

Physical Basis

Electron diffraction is a key tool for studying crystal structure. In fact, a crystal is defined as a material that exhibits a sharp, well-defined diffraction pattern. The Braggs were the first to use the coherent interference of photons with crystals to understand their structure, deriving what is now known as Bragg's law. Wavelengths that are smaller than or equivalent to the interatomic spacing between atoms and molecules at surfaces satisfy the atomic diffraction condition. This can be calculated using the de Broglie wavelength equations 11 and 12.

$$\lambda = \frac{h}{p} \tag{11}$$

$$\lambda_e = \sqrt{\frac{150.4}{E_k}} \tag{12}$$

where h is Planck's constant ($h = 6.63 \times 10^{-34}\,\mathrm{J \cdot s}$), m_e is the mass of the electron in kg, v is the velocity, and E_k is the kinetic energy of the electron. The diffraction of beams by crystals is described by Bragg in a simple equation 13.

$$n\lambda_{hkl} = 2d \sin\theta \tag{13}$$

where d is the spacing of the parallel atomic planes, λ is the wavelength of incident electrons and n is an integer representing the order of diffraction. hkl represents the Miller indices of the surface being investigated. θ is the angle between the incident beam and the

atomic plane.

Bragg's law is illustrated in Figure 3.16. It is clear that diffracted beams are observed when atoms in parallel planes constructively interfere with their reflections [99].

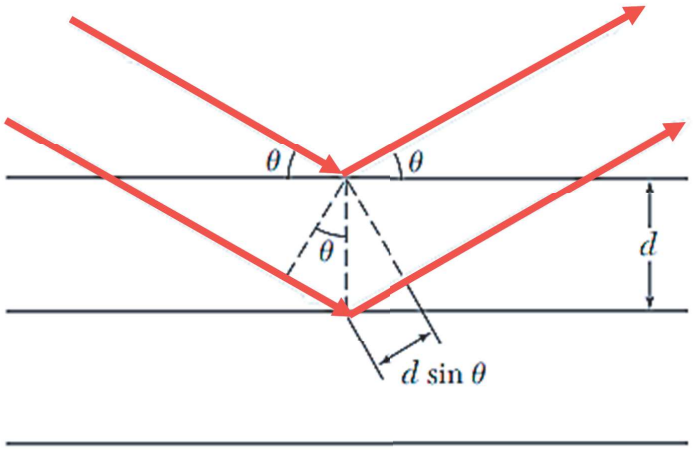


Figure 3.16: Illustrating Bragg's Law. Reproduced and modified from [99]

In addition to Bragg's law, Laue's law is an alternative to Equation 14 for diffraction. For diffraction to occur, the condition is that an incident electron with wave vector K_i and a scattered electron with wave vector K_d must satisfy:

$$\vec{K_d} = \vec{K_i} + \vec{g_{hkl}} \tag{14}$$

where K_i is the incident wave vector, K_d is the outgoing wave vector, and g_{hkl} is a reciprocal lattice vector; the magnitudes of both vectors are equal (elastic scattering). The reciprocal lattice is described by:

$$\vec{g_{hkl}} = h\vec{a^*} + k\vec{b^*} + l\vec{c^*} \tag{15}$$

where hkl are Miller indices, a^*, b^* and c^* are primitive translation vectors in reciprocal space, which can be written as:

$$
\begin{aligned}
\text{(3D)} \quad \vec{a}^* &= 2\pi \frac{\vec{b} \times \vec{c}}{\vec{a} \cdot (\vec{b} \times \vec{c})}, \\
\vec{b}^* &= 2\pi \frac{\vec{c} \times \vec{a}}{\vec{a} \cdot (\vec{b} \times \vec{c})}, \\
\vec{c}^* &= 2\pi \frac{\vec{a} \times \vec{b}}{\vec{a} \cdot (\vec{b} \times \vec{c})}
\end{aligned} \tag{16}
$$

$$
\begin{aligned}
\text{(2D)} \quad \vec{a}^* &= \frac{2\pi}{a \sin\theta}, \\
\vec{b}^* &= \frac{2\pi}{b \sin\theta},
\end{aligned}
$$

where θ represents the angle between the real-space lattice vectors $\vec{a}$ and $\vec{b}$ in a two-dimensional crystal, a, b: magnitudes of the real-space lattice vectors $\vec{a}$ and $\vec{b}$, and $\vec{a}^*$, $\vec{b}^*$: reciprocal lattice vectors.

The Ewald sphere principle can be employed to determine how many diffracted beams emerge from a crystalline surface at a given incident energy [100]. Diffraction occurs at all points in the reciprocal lattice that intersect with the surface of the Ewald sphere. In three-dimensional crystals, the reciprocal lattice consists of discrete points in space and diffraction arises when these points fall exactly on the surface of the Ewald sphere. In contrast, for two-dimensional systems, such as surfaces or thin films, the reciprocal lattice takes the form of rods (or lines) perpendicular to the surface plane. In this case, diffraction occurs when these rods intersect the Ewald sphere, leading to the appearance of diffraction spots.

Figure 3.17 clearly illustrates that weak reflections are associated with reciprocal lattice points that lie further from the Ewald sphere surface, whereas strong reflections, result in more intense diffraction spots, occur where reciprocal lattice points lie close to or directly on the Ewald sphere.

Moreover, changing the primary energy of the incident electron beam affects the magnitude of the wavevector k and hence the radius of the Ewald sphere. An increase in

energy expands the radius, allowing the Ewald sphere to intersect more reciprocal lattice features. As a result, the Ewald sphere may pass through stronger or weaker parts of the Bragg spots (in three-dimensional lattices) or through rods (in two-dimensional lattices), depending on the value of $\vec{k}$. Consequently, the intensity of each Bragg reflection varies with the beam energy, influencing the visibility and sharpness of the diffraction pattern.

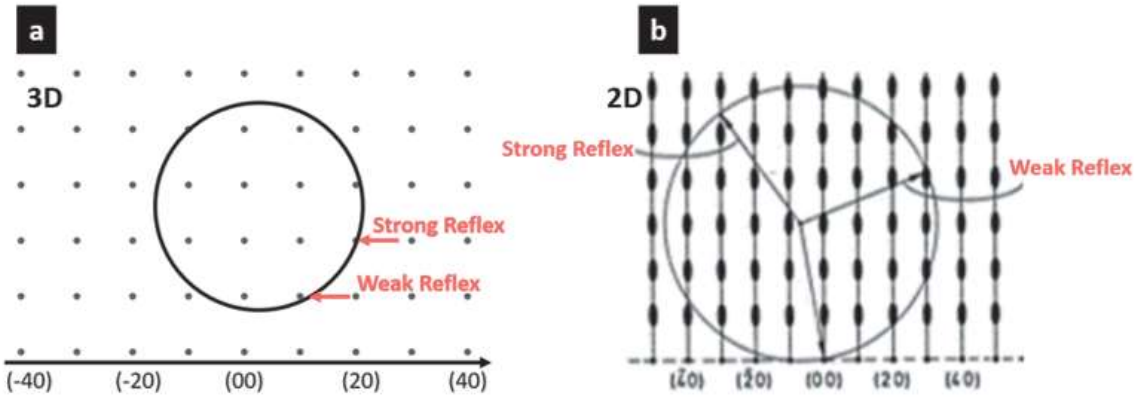


Figure 3.17: Ewald sphere representing diffraction in the reciprocal lattice (a) three dimensions

. (b) two dimensions [99].

Instrumentation

The LEED apparatus consists of an electron gun, a fluorescent screen and grids. The electron gun consists of a heated cathode and a set of focusing lenses that send electron beams at low energies to the surface of the sample.

Elastically and inelastically scattered electrons are accelerated from the material's surface and flow towards four different grids (known as retarding grids). The earthed grid is the first grid that is closest to the sample and it protects the phosphor screen from high voltages. To ensure that only elastically scattered electrons reach the detector, the outer grid is located near the sample , as are the inner grids. The second and third grids have a lower potential magnitude.

The elastically scattered electrons are detected by a fluorescence screen and a CCD camera as a result of emitted light when electrons strike the fluorescence screen, allowing for a real-time display of the diffraction pattern. The images can also be observed visually or through computer software. Figure 3.18 displays a schematic of a basic LEED system. This system is always contained within the UHV to preserve the required surface cleanliness.

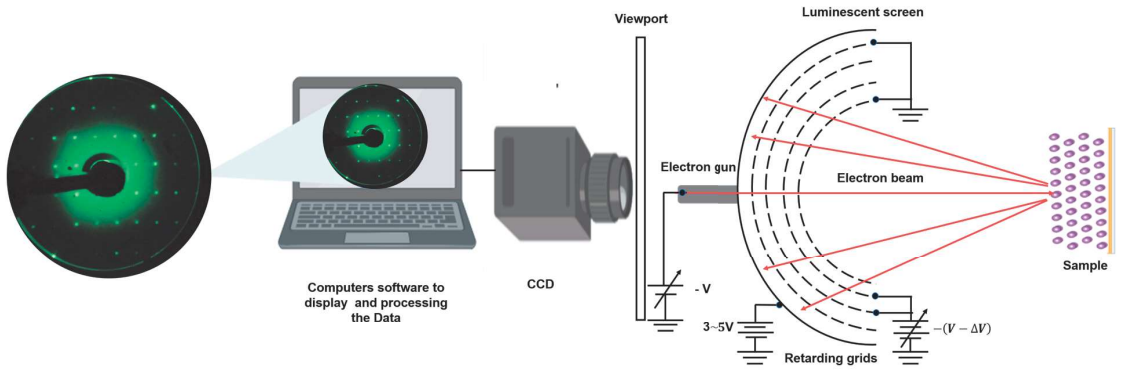


Figure 3.18: Schematic of the LEED apparatus, which is evacuated to ultra high vacuum. Reproduced and modified from [101].

A symmetric ordered surface may be seen using LEED patterns and compared to other methods, including 2D fast Fourier transformations of STM images. Before being placed in the STM chamber, LEED was used to confirm that the surface was clean and well ordered, as indicated by sharp points in the LEED pattern.

The In_3Ni_2 surface structure was investigated in this work by finding the lattice constants and comparing them to a model structure. The coherence length of this technique is of the order of 100 Å, meaning that surfaces that may be too rough for analysis with an STM can provide structural information through diffraction. LEED images provide the geometrical arrangement of the diffraction spots, along with the reciprocal lattice information. Besides background noise, spot brightness and sharpness can reveal information. In addition, LEED can detect surface reconstructions on samples.

3.4.4 Scanning Tunnelling Microscopy (STM)

STM is often used to characterise materials at the nanoscale. STM was invented by Dr Gerd Binnig and Dr Heinrich Rohrer in 1982 at IBM Zurich [101]. Both won the 1986 Nobel Prize in Physics for this discovery [101].

The main motivation behind the invention of the STM was the requirement for a device capable of nanoscale local spectroscopy. Also, it provides high resolution imaging of surfaces and has the ability to manipulate them, making it an important instrument for surface science research.

Scanning an atomically sharp tip across a surface allows for the detection of the electron density map of the surface. Electron density at the surface typically directly represents surface topology, however, any assumptions in this area must be made with careful consideration of extra factors [102].

Physical Basis

The physical basis of STM relies on the quantum tunnelling effect, which describes how electrons can pass through a potential barrier that separates a sample surface from a conductive tip by recording volt-ampere characteristics (VAC) of the tip–surface tunnelling contact at any point on a surface and investigating the local electronic properties of a sample.

In STM, a sharp metallic tip is brought within 5–10 Å of a conductive surface, causing the wave functions from the atom at the tip and the atom at the surface to overlap. When a voltage is applied, electrons can tunnel through the small gap between the tip and the surface. This tunnelling occurs because of the wave-like nature of electrons, which have a non-zero probability of existing on the other side of the barrier, even if they do not have enough energy to cross it classically. By measuring the tunnelling current or the z-axis position of the tip, an atomic level image of the surface may be obtained. The phenomenon known as quantum mechanical tunnelling occurs when a particle passes

through an energy barrier that is larger than the total energy of the particle.

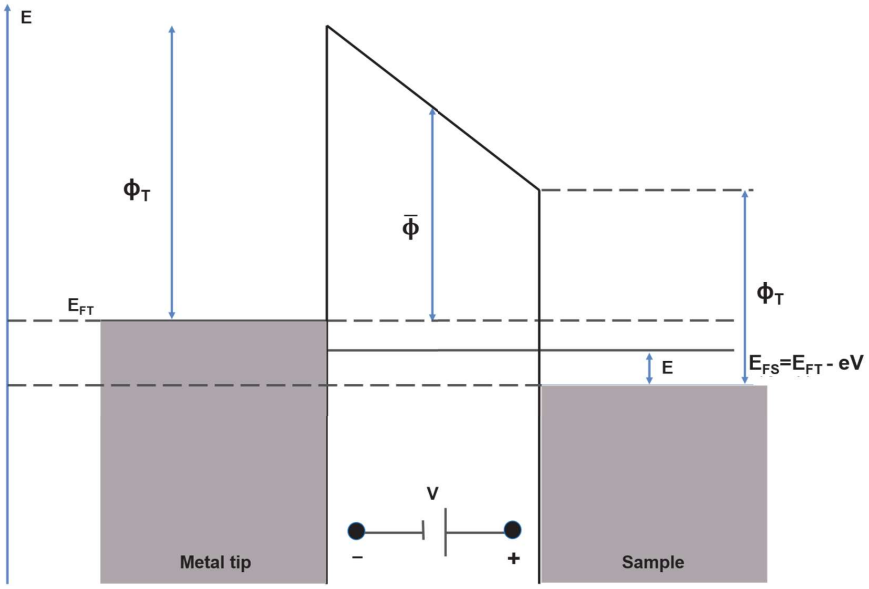


Figure 3.19: Schematic picture of the electron energy states in a tunnelling contact between STM metal tip and sample. Reproduced and modified from [103].

When a negative bias voltage is applied between the tip and surface leads to the situation where the tip becomes more negative compared to the surface. Consequently, electrons from the tip, which are at a higher energy, tunnel into the surface, probing the unoccupied states. On the other hand, the tip becomes more positive in comparison to the surface when a positive bias voltage is applied between them. As a result, electrons tunnel from the surface to the tip, probing the occupied states, as they naturally move from regions of higher to lower potential.

The quantum tunnelling process allows electrons to pass through the small gap between the tip and the surface, even though, classically, they would not have enough energy to surmount the potential barrier. As the tip scans across the surface, changes in the tunnelling current (j) provide electronic properties and atomic scale information about the material's surface. The surface local density of states (LDOS), the distance between the tip and surface (d) and the energy alignment between the tip and surface electronic states are the three variables that determine the tunnelling current.

Equation 17 illustrates an exponential correlation between j and d, indicating that a small change in the tip–sample distance, due to a protrusion or depression, would lead to a significant variation in the tunnelling current.

$$j = \frac{D(V)V}{d} \times \exp(-A\phi_b^{1/2}d) \tag{17}$$

Where, D(V) is the electron state densities of the tip and the sample, V is the bias voltage, d is the effective tunnelling gap, ϕ_b is the effective barrier height and A is a constant.

Instrumentation

The central part consists of a tip that is commonly made of tungsten or platinum–iridium alloys. The performance of the tip is greatly affected by its condition; for that reason, a sharp and stable tip is essential to produce topographical maps of surfaces with atomic resolution.

As seen in Figure 3.20, a mix of in situ preparation and ex situ production is used to make the tip itself atomically sharp. To make the tip itself atomically sharp, it is first introduced into UHV, then annealed to remove any gas before being placed under the microscope for cleaning. To enhance and remove any molecules or adsorbates detected by the tip, short voltage pulses can be applied to the tip. This method enables the maintenance of sharp, single tips. The tip height is held less than 1 nm away from the surface and it is adjusted via a feedback system in order to maintain a constant tunnelling current between the tip and the sample, adjusting the tip's height to generate accurate surface topography.

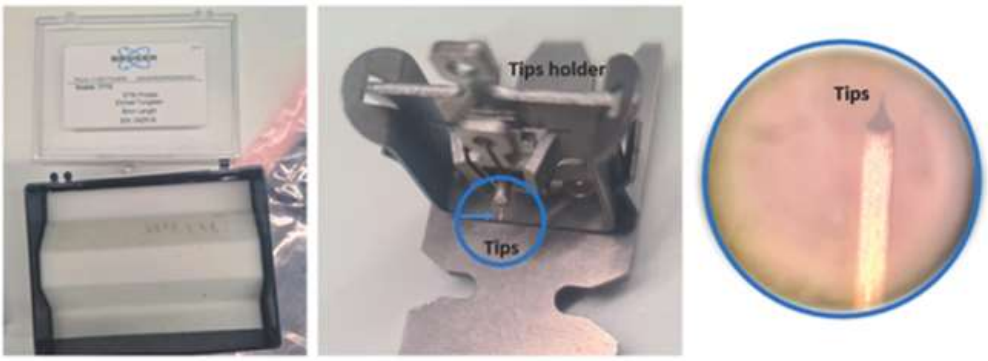


Figure 3.20: Metal tip and sample used in STM.

A piezoelectric scanner is responsible for moving the STM tip with high precision in three dimensions. Piezoelectric materials expand or contract when an electric voltage is applied, allowing for extremely fine control of the tip position. Precision in tip movement is controlled by piezoelectric scanners, which provide accuracy in three dimensions, crucial for mapping surface topographies. Also, high voltage amplifiers are used to drive the piezoelectric scanners. Computers and software are used to control the STM operation, collect data and generate images. The components of an STM device are shown in Figure 3.21.

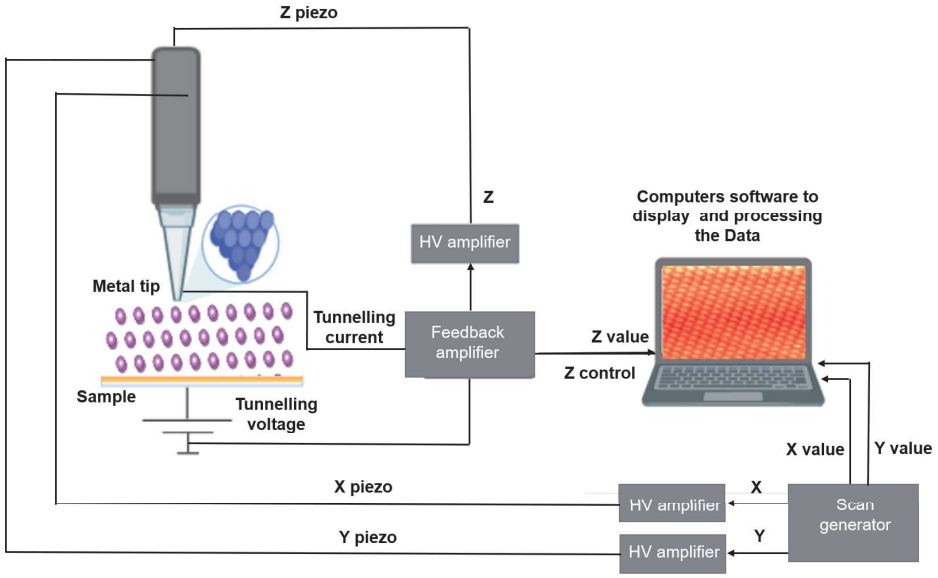


Figure 3.21: Schematic illustration of scanning tunnelling microscopy (STM). Reproduced and modified from [101].

There are two different modes of STM operation: constant current or constant height. The differences between these modes are depicted in Figure 3.22 (a–b). The most common method of obtaining STM images is through a constant current mode, in which a tip travels over the sample surface while the bias voltage and current are held constant [104]. The current and voltage are maintained constant while the x, y and z coordinates fluctuate with the movement of the scanning tip. Here we measure the voltage required to move the tip vertically in order to keep the tunnelling current constant; we need to calibrate the piezo voltage Z. A constant current gives images of the surface's electron density, which corresponds fairly closely to topographic images for certain materials [101].

In the constant current mode, the tip stays stationary while the sample is scanned and the tunnelling current is measured at different x and y positions [105]. When the sample's surface is smooth, this mode can be used. However, if the sample is rough or contains large particles, the tip may come into contact with the sample and cause damage to the surface [101].

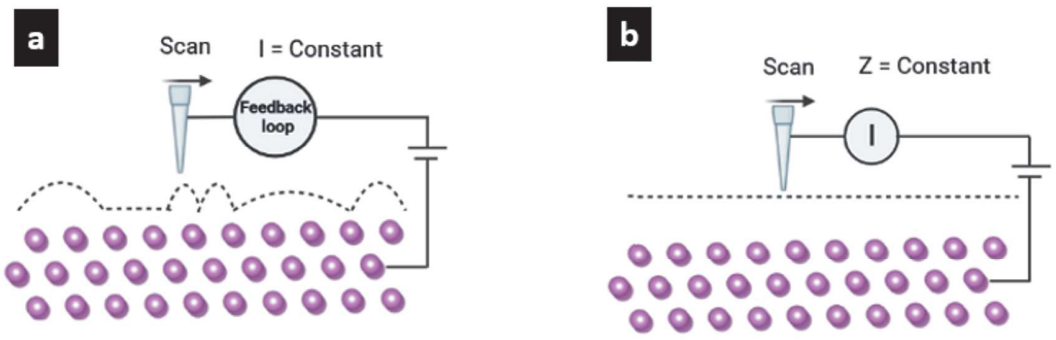


Figure 3.22: Operation of an STM in constant (a) current mode. (b) height mode. Reproduced and modified from [105].

Calibration.

In STM, image distortions can arise from various factors, including electronic noise, tip asymmetry and thermal drift, which can compromise the accuracy of atomic-scale mea-

surements. To address these distortions, a Highly Ordered Pyrolytic Graphite (HOPG) substrate is frequently used as a calibration standard due to its well-defined and regular crystalline lattice structure. HOPG's consistent hexagonal arrangement, with a known atomic spacing of 2.46 Å between adjacent carbon atoms, makes it an ideal reference for correcting distortions in STM images.

In this study, STM images of the HOPG surface were first obtained under the same experimental conditions used for imaging the In_3Ni_2 surface. These HOPG images, along with the theoretical model structure, were then used to calibrate the STM images of In_3Ni_2, allowing for the identification and correction of distortions (Figure 3.23). The distortions in the In_3Ni_2 STM images were compared to the ideal hexagonal lattice of HOPG, with any deviations from the expected atomic spacing corrected through a mathematical algorithm. This calibration process not only enhanced the accuracy of the In_3Ni_2 surface analysis but also contributed to the overall reliability and reproducibility of atomic-scale measurements in this study [106].

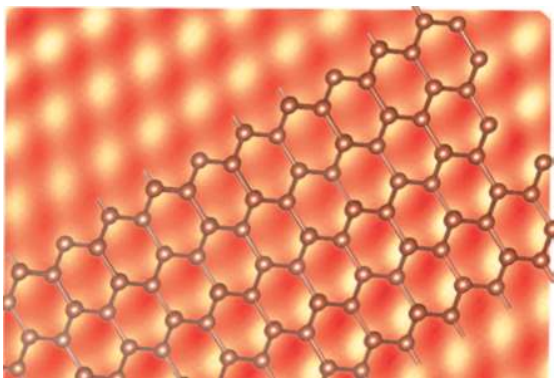


Figure 3.23: STM image of the HOPG surface after sputtering and annealing the surface to 216 °C, showing a (32 Å×35 Å scan area at
-0.785 V and 0.348 nA). The image is superimposed with a theoretical HOPG model, illustrating the alignment of the atomic structure and aiding in the calibration of the STM measurements.

Data collected in this investigation were processed using WSxM software. STM indicates distortions that can appear in the data that do not accurately represent any real surface features.

Plane levelling is used to correct data slopes that result from a tip-sample incline, using various levelling processes for atomically flat images or those featuring steps of differing heights as shown by Figure 3.24 (b). Scan line defects, which occur during the line-by-line capture of the image, and corrupted line faults, are removed using a scar removal process.

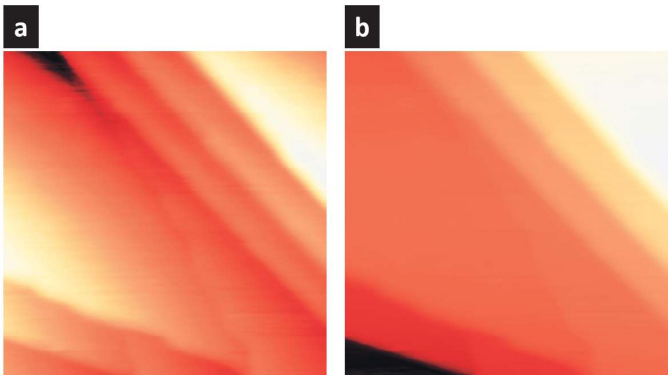


Figure 3.24: (a) STM image of the $In_3Ni_2(001)$ surface after sputtering and annealing the surface to 540 °C (750 Å×950 Å, +0.472 V, 0.448 nA). (b) STM image after correcting data slopes by plane levelling.

Drift correction was applied to the STM images to fix any drift that was seen using the expected surface symmetries. Once the STM data have been corrected, any drift measurements. can be directly extracted from the image. Line profiles, which measure the change in Z-axis height or tunnelling current along a given line, can be used to define step heights between terraces and other features. Another method to measure step heights is by using a height histogram (Figure 3.25 (a-b)).

Two additional image analysis methods frequently used to analyse STM images are Fast Fourier transform (FFT) and autocorrelation. Both allow us to quantify an image's inherent order, even if it's not obvious. By summing sine and cosine functions with various frequencies and amplitudes, an FFT may break down and convert an image into its harmonic components. Points in the Fourier domain, which represent these harmonic components, correlate with key frequencies present in the image of space as it actually exists. Like LEED patterns, bright spots in the Fourier domain where various frequencies overlap represent real-space repeating patterns. By using an inverse FFT to filter out these

high intensity points, we can see these characteristics in real space without the noise. It is common practice to integrate data from the FFT centre to avoid losing any actual surface information, although this requires careful consideration.

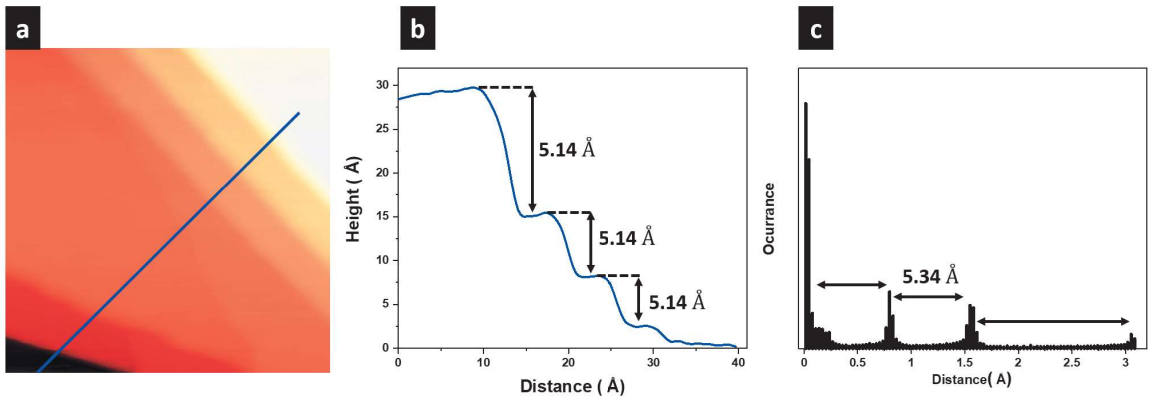


Figure 3.25: (a) STM image of the $In_3Ni_2(001)$ surface after sputtering and annealing the surface to 540 °C (750 Å×950 Å, +0.472 V, 0.448 nA). (b) Line profiles to measure the change in Z-axis height. (c) Height histogram to measure step heights.

4 | In_3Ni_2(001) Surface

4.1 Introduction

This chapter presents an investigation of the atomic structure, chemical composition, and oxidation behaviour of the In_3Ni_2(001) surface using a range of complementary techniques, including XPS, LEIS, LEED, and STM.

A series of sputtering and annealing cycles produced a clean, atomically ordered (001) surface. This work is the first comprehensive examination of the In_3Ni_2(001) surface using UHV methods.

XPS spectra provide information on the effects of air exposure, sputtering, and annealing on the surface composition of the In_3Ni_2(001) sample. The influence of varying annealing temperatures on the chemical composition of the surface is then analysed, along with compositional variations as a function of the scanning angle. Additionally, after sputtering and annealing at various temperatures, LEIS was used to investigate changes in the chemical composition within the surface's uppermost atomic layers.

The effect of sputtering and annealing at varying temperatures on LEED patterns is also examined. STM imaging is used to investigate the surface morphology and to identify the termination plane of the surface by comparing the STM images with a bulk atomic model. The oxidation behaviour of the In_3Ni_2(001) surface is studied through XPS, focusing on the shifts in binding energies of surface components, particularly indium (In) and nickel (Ni), as they interact with oxygen (O).

This section of the thesis is based on the work published in "Atomic Structure, Chemical Composition and Oxidation Behaviour of the (001) Surface of In_3Ni_2 Intermetallic Catalyst" by Alfahad *et al.* in Physical Review Materials [107]. To further investigate surface stability and complement the experimental findings, Emilie Gaudry from the Institute Jean Lamour, France, performed density-of-states calculations of surface energy, which will also be discussed in this chapter.

4.2 In_3Ni_2(001) Model Structure

Before discussing the experimental results, the crystal structure of the In_3Ni_2(001) surface is presented. Figure 4.1 (a) illustrates the unit cell of In_3Ni_2. The (001) surface is highlighted in yellow. The lattice parameters for the In_3Ni_2 unit cell are $a = b = 4.387$ Å, $c = 5.295$ Å, with angles $\alpha = \beta = 90^\circ$ and $\gamma = 120^\circ$ [107]. The structure is identical to the Al_3Ni_2 type, which is the trigonal space group P-3m1 [65].

A side view of the surface is shown in Figure 4.1 (b). The crystal structure can be described by stacking five atomic planes, labelled 0 to 4, within the unit cell. The separation between planes 0 and 3 is 3.417 Å, while the distance between planes 3 and 4 is 1.878 Å. The total distance, obtained by adding these separations, yields the lattice constant of 5.295 Å. These interplanar spacings were compared with the step heights observed in STM, allowing the identification of the bulk planes that terminate the surface.

The projections of the atomic model along the [001] direction are illustrated in Figure 4.1 (c). The outermost atomic layer is selected from five different atomic layers, as shown in Figure 4.1 (b). These structures are labelled surface models 0 to 4, representing different atomic layers on the surface [107].

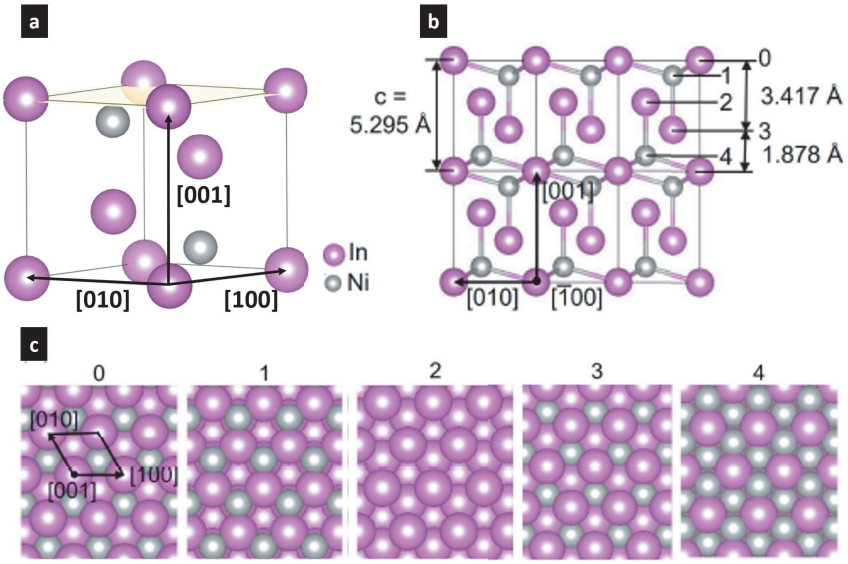


Figure 4.1: (a)The unit cell of the In_3Ni_2(001) surface, with the (001) plane highlighted in yellow. (b) Side view of the (001) surface, showing the stacking of five atomic planes, labelled 0 to 4, within the unit cell. The separations between specific planes are indicated. (c) Projection of atomic models along the [001] direction, where the outermost atomic layer is selected from five distinct layers (0 to 4) as shown in (b). High-symmetry directions are also marked [107].

4.3 Experimental Methods

The In3Ni2 single crystals were grown using the Czochralski method [108], as described in section 2.7. Subsequently, the sample surface (001) was cut using a wire saw that employed a 50 μm thick tungsten wire combined with boron carbide powder suspended in a glycerol solution to minimise material loss and prevent surface damage. Subsequently, the surface was polished with diamond paste, resulting in a reduction in the grain size to 0.25 μm.

The surface was then cleaned in a UHV chamber by performing several sputtering cycles with Ar^+ ions at an average drain current of approximately 6 μA for 30 minutes, followed by annealing at temperatures ranging from 300 °C to 560 °C for one to three hours. The cleaning process was repeated until a sharp LEED pattern was observable

from the surface. Temperature measurements for the XPS, STM, and LEED experiments were recorded using an optical pyrometer with an emissivity of 0.40. Since the emissivity of In3Ni2 was unknown, the value for NiCu was used [109].

In order to ensure accurate temperature measurements during surface analysis in the LEIS system, the emissivity setting of the optical pyrometer was calibrated using a thermocouple as a reference. The detailed experimental setup and instrumentation for this procedure have already been described in Chapter 3.3. The In3Ni2 sample was mounted such that both the thermocouple and the optical pyrometer could simultaneously measure the sample temperature within the LEIS chamber under UHV conditions.

Once surface preparation was completed, XPS measurements were also performed to ensure that the surface was free of contaminants. The prepared sample was then transferred to the STM chamber. Notably, the preparation chamber is vacuum-coupled to the XPS and STM chambers, with LEED instrumentation also in place, ensuring that the surface conditions remained unchanged during transfer. A room-temperature Omicron variable-temperature STM operating in constant-current mode was used for the STM imaging. The bias voltage ranged between 0.14 and 1.7 V, with a tunnelling current of 0.645 nA.

The LEIS experiment was carried out in the LEIS chamber, with surface cleaning conducted using the same procedure described previously. The surface temperature was measured with a thermocouple in direct contact with the sample. LEIS spectra were acquired from a (2×2) mm area employing a 3 keV He^+ beam with an ion dose of approximately 1×10^{14} ions cm^{-2}. He^+ ions with scattering energies ranging from 1800 to 2800 eV were collected to ensure an optimal signal-to-noise ratio, focusing on the surface peaks of Ni (approximately 2275 eV) and In (approximately 2575 eV). LEIS data were obtained using a commercial Qtac100 spectrometer (IonTOF), with the analysis carried out using Surface Lab 7 (IonTOF) [110].

XPS measurements were conducted at the Institute Jean Lamour using a non-monochromatic Al Kα source. For the oxidation process in UHV, a leak valve was used to introduce 99.999% pure oxygen gas, with the partial pressure maintained at approximately 1.333×10^{-6} mbar. Exposure was controlled by reaction time to 20 L, 300 L, 600 L, and 900 L at room temperature. Exposure was quantified in Langmuir units, where 1 L = 1.333×10^{-6} mbar·s. The freshly prepared surface was then exposed to 99.99% pure molecular hydrogen at room temperature. In the air exposure experiment, the surface was cleaned as previously described, removed from the UHV chamber, and left exposed to air for two days prior to XPS measurements. XPS data were analysed using the CasaXPS programme.

4.4 Results and Discussion

4.4.1 Chemical Composition Studied by XPS

Effect of Air Exposure, Sputtering and Annealing on Surface

The sample became contaminated with oxygen and other contaminants after prolonged exposure to air, prior to being transferred to the UHV chamber. XPS was used to identify both the constituent elements and any surface contaminants. XPS was also used to examine the effect of air exposure, sputtering, and annealing on the chemical composition of the surface.

As expected, the wide scan spectra showed the presence of In, Ni, C, and O on the surface following air exposure. However, after sputtering and annealing, the O 1s and C 1s peaks were no longer observed, with only the In and Ni peaks remaining. Figure 4.2 (a) illustrates the XPS wide scan spectra of the air-exposed, sputtered and annealed (001) surface at 560 °C for one hour. Figures 4.2 (b) and (c) present the XPS spectra that compare the binding energies of the core levels of In $3d_{5/2}$ and Ni $2p_{3/2}$, highlighting the effects of sputtering, air exposure, and the clean surface. The observed shifts to higher

binding energies of 0.4 eV in In and 0.35 eV in Ni occur after exposure to air, regardless of the elemental surface condition.

Thespectra of core levels of In, Ni, C and O are analysed using a convoluted Gaussian Lorentzian line shape with a Shirley-type background to determine the binding energies and peak areas for In and Ni. The peak positions of the annealed surface after fitting are marked by vertical dashed lines in Figure 4.2. The KLL peaks correspond to Auger electrons generated from the L shell due to the LET process, resulting from holes in the K shell.

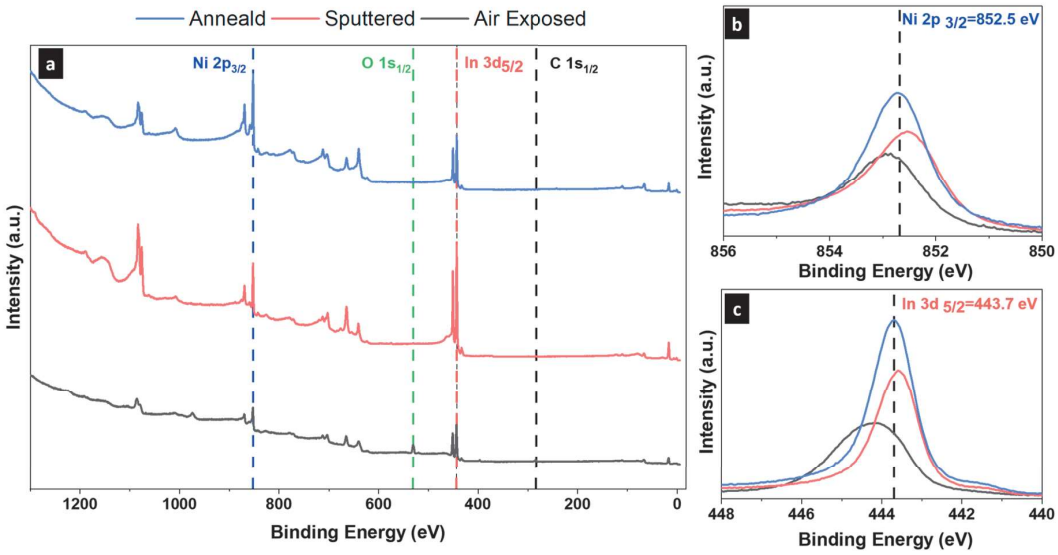


Figure 4.2: (a) XPS wide scan spectra of a clean In_3Ni_2(001) surface after exposure to air, sputtering, and annealing at 560 °C for one hour. (b) and (c) show XPS spectra comparing the binding energies of the core levels of In $3d_{5/2}$ and Ni $2p_{3/2}$, showing the effects of sputtering, air exposure, and the clean surface. The shifts to higher binding energies of 0.4 eV in In and 0.35 eV in Ni occur after air exposure, regardless of the surface elemental condition. Dashed lines indicate core levels of In, Ni, C and O.

After a single sputtering cycle, all surface contaminants were effectively removed. The peaks observed at approximately 443.7 eV and 852.6 eV correspond to pure In $3d_{5/2}$ and Ni $2p_{3/2}$, respectively. Following sputtering, the In peak shifted by approximately 0.1 eV to a lower binding energy, while the Ni peak shifted to a higher binding energy; the shift in In is within experimental error. Upon annealing the surface at 560 °C, no changes were

detected in the positions or shapes of the In and Ni peaks. However, the intensity of Ni decreases and the In intensity increases. We will discuss this change in intensities in the next section. In addition, the shift will be discussed in detail in Section 4.4.5. Table 4.1 provides a summary of these results, with the In and Ni core levels showing the metallic characteristics expected for the intermetallic compound.

Elemental	**Ni $2p_{3/2}$**	**In $3d_{5/2}$**
Elemental Binding Energy	852.5 eV [111]	443.7 eV [112]
Air Exposed Surface	852.8 eV	444.1 eV
Sputtered Surface	852.7 eV	443.7 eV
After Sputtered Annealed Cycles	852.5 eV	443.7 eV

Table 4.1: XPS data for In_3Ni_2(001) surface comparing the binding energies of the core levels of Ni $2p_{3/2}$ and In $3d_{5/2}$. Sputtering results in changes to the surface. Following two cycles, the peak positions represent the clean intermetallic compound.

Atomic Compositions Change as a Function of Sputtering and Annealing Temperatures

We investigated the atomic composition of the surface after sputtering and annealing at various temperatures to study the impact of these processes. The atomic composition of In and Ni was determined by analysing the integrated intensity (area under the curve) of the Ni $2p_{3/2}$ and In $3d_{5/2}$ peaks in the XPS spectra. These intensities were normalised by the photoionisation cross section, the inelastic mean free path of the photoelectrons, and the transmission function of the analyser, as detailed in Section 3.4.1.

Figure 4.3 illustrates how the chemical composition of the In_3Ni_2(001) surface varies as the annealing temperature increases from 300 °C to 560 °C. The bulk atomic percentage of In is 60%, but after sputtering, it reduces to approximately 37%. In contrast, there is an increase from 40% to 63% in the Ni atomic percentage, indicating that the sputtering process preferentially removes In, resulting in a higher surface concentration of Ni.

Several factors affect the preferential sputtering of elements in intermetallic compounds.

These include atomic weight, surface free energy, and bonding energy. An element with lower atomic weight, surface energy, and bonding energy is more likely to be preferentially sputtered [113, 114, 115]. Although atomic weight is not the main factor in this case, because In is heavier than Ni, the lower surface energy of In compared to that of Ni seems to be a contributing factor. This behaviour is consistent with observations in ZrNiAl and YNiAl, where a similar segregation occurs due to the lower surface energy of Ni [53].

Specifically, the surface free energy of a face-centred cubic (FCC) Ni close-packed surface is 2.011 J/m^2, while that of a body-centred tetragonal (BCT) In close-packed surface is 0.488 J/m^2 [116]. Therefore, we propose that the preferential sputtering of In can be attributed to its lower surface free energy.

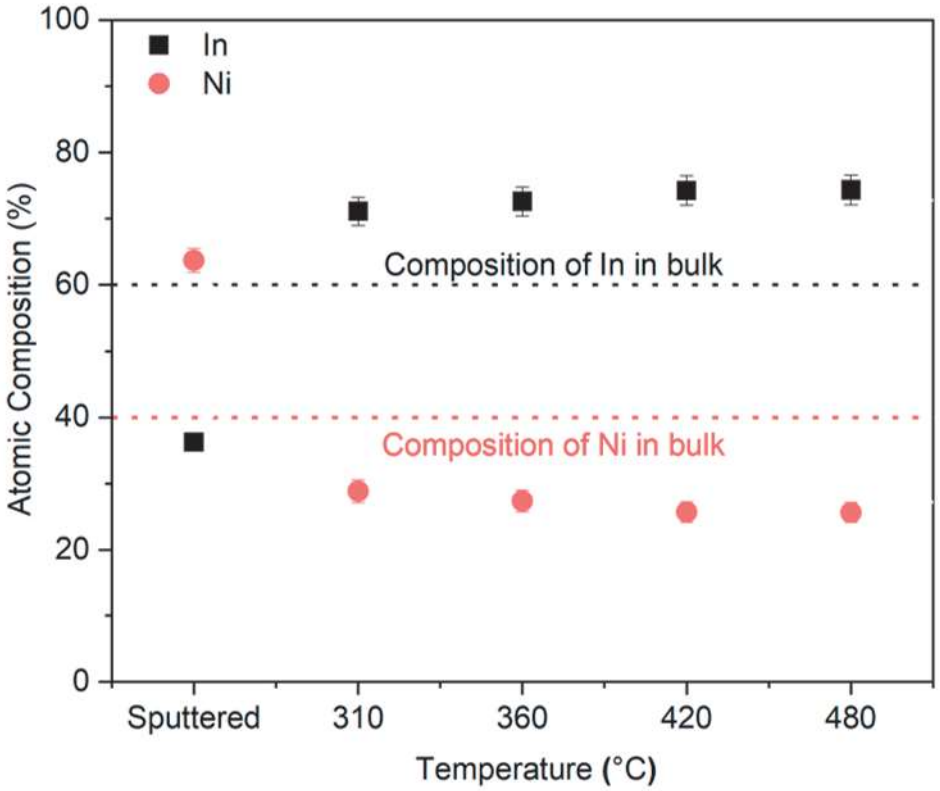


Figure 4.3: The surface chemical composition of the (001) surface after sputtering and annealing at various temperatures from 300 °C to 560 °C. Dotted lines indicate the In and Ni bulk compositions.

The In_3Ni_2(001) surface exhibits clear evidence of preferential In sputtering, which can be attributed to the large difference in surface free energy between In (0.488 J/m^2) and Ni (2.45 J/m^2). This behaviour is consistent with other intermetallic systems: Ga_3Ni_2(001) shows preferential Ga sputtering due to its lower surface free energy (0.661 J/m^2) relative to Ni, resulting in Ni enrichment [117], while InPd surfaces experience depletion of In from the (100), (110), and (111) surfaces for the same reason [60]. Similarly, in PdZn, Zn (0.989 J/m^2) preferentially sputters relative to Pd (1.92 J/m^2), leading to Pd-enriched surfaces [45]. These examples collectively illustrate that preferential sputtering is largely governed by differences in atomic surface free energy. A comparison of the surface free energies for these elements is provided in Table 4.2, highlighting the correlation between lower surface free energy and preferential sputtering.

Element	Surface Free Energy (J/m^2)
Pd (Palladium)	1.92
In (Indium)	0.49
Ga (Gallium)	0.66
Zn (Zinc)	0.99
Ni (Nickel)	2.01

Table 4.2: Surface free energies of selected elements [45, 116].

Following annealing of the surface at 300 °C, the atomic percentage of In increases to approximately 71%, remaining constant as the sample temperature increases further to 560 °C. In contrast, the atomic percentage of Ni decreases to around 29% and remains stable as the annealing temperature increases to 560 °C. This change in atomic composition indicates that In segregates to the surface when it is annealed at higher temperatures.

Surface segregation is influenced by several factors, including surface free energy, atomic radius, and bonding energy of the constituent elements [114]. Elements with lower binding energy, larger atomic radius, and lower surface energy are more likely to segregate to the surface. Compared to Ni, In has a lower surface free energy, as previously

mentioned, and a larger atomic radius [118]. Therefore, we suggest that In segregation is primarily driven by its larger atomic radius and lower surface free energy relative to Ni [119].

In comparison, the $Ga_3Ni_2(001)$ surface exhibits a similar trend in surface segregation, where Ga preferentially segregates to the surface at increased temperatures [117]. In the Ga_3Ni_2 sample, the atomic radius and surface free energy of Ga relative to Ni also contribute to the segregation behaviour, with Ga having a larger atomic radius and lower surface energy being key factors for its segregation. This behaviour in Ga_3Ni_2 supports our results for In segregation in the $In_3Ni_2(001)$ surface, further illustrating the importance of atomic characteristics in surface segregation during annealing. This behaviour is similar to that observed for InPd, which undergoes a change from Pd-rich to In-rich terminations upon annealing at high temperatures [60].

Atomic Compositions As Function of Scanning Angles

XPS spectra were recorded from the surface that had been annealed to examine the distribution of In and Ni on the surface. The surface atomic composition was determined by accounting for the photoemission cross section, the inelastic mean free path of the photoelectrons, the transmission function of the analyser, and the integrated intensity of the In $3d$ and Ni $2p$ peaks in the XPS spectra. A detailed explanation of the calculation methodology for the surface atomic composition can be found in Section 3.4.1.

Despite variations in the grazing angle, the atomic composition remained consistent at angles of 0°, 15°, 30°, 45°, 60°, and 70°, with 70° being the highest angle, as illustrated in Figure 4.4. The atomic composition was 80% In and 20% Ni at the lowest grazing angle of 0°, and it changed by only 1% to 81% In and 19% Ni at the highest grazing angle of 70°. Between grazing angles of 15° to 60°, the In content decreased marginally by 1%, while Ni gradually increased by 1%. This suggests a uniform distribution of In across the surface, as any concentration increase in the topmost layer would have been expected to correlate

with an increase in the grazing angle.

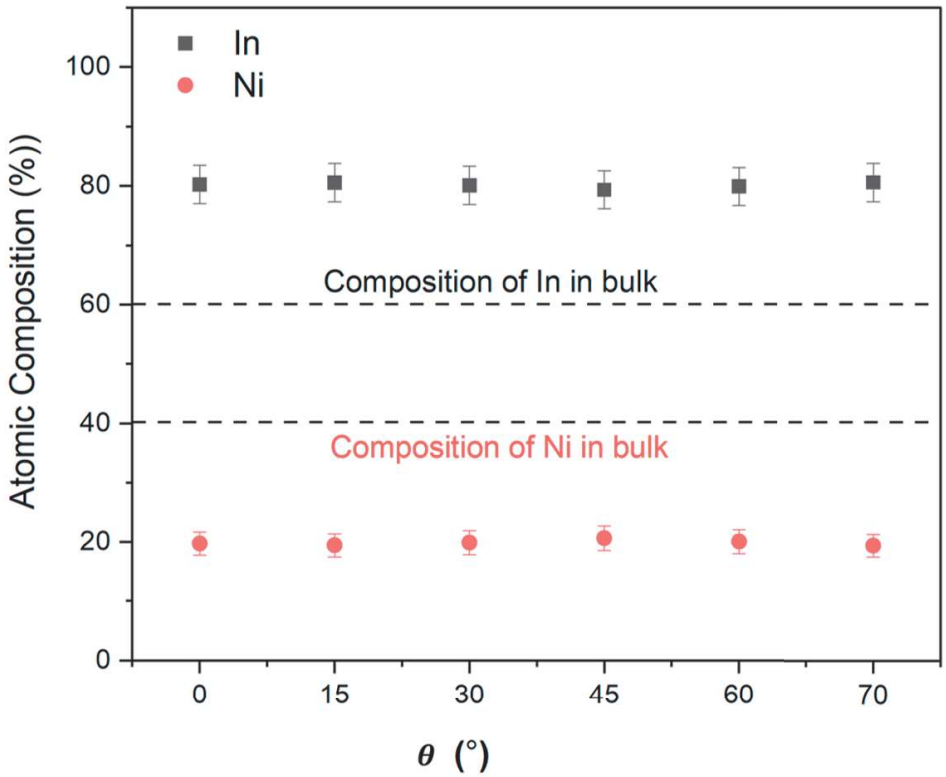


Figure 4.4: The surface chemical composition of the (001) surface after sputtering and annealing at 356 °C with various scan angles from 0 to 70°. Dotted lines indicate the In and Ni bulk composition. θ is the angle between the surface and the X-ray beam.

4.4.2 Elemental Information Studied by LEIS

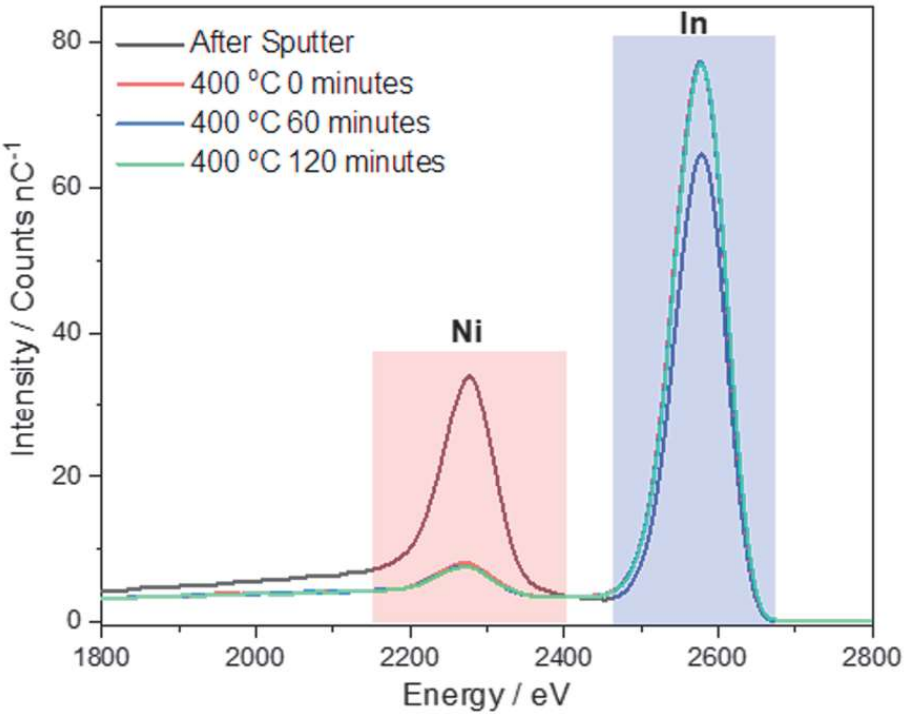
Low energy ion scattering (LEIS) measurements were performed on the surface following multiple cycles of sputtering and annealing to investigate the elemental composition of the topmost atomic layer [97]. Unlike XPS, which provides insight into the chemical composition of several atomic layers, LEIS specifically provides information on the topmost surface layer. A 1 keV Ar^+ beam was used to sputter a (2×2) mm^2 area of the surface. Initially, the sample was sputtered until the LEIS spectra stabilised with increasing sputter dose, which signified the removal of surface layers and revealing the bulk crystal structure.

The sample treatment followed a procedure similar to that in our XPS experiments. The surface was first cleaned by annealing at 400 °C for one hour, followed by a two-hour cooling period to room temperature. The sample was then exposed to the sputter beam for 30 minutes (total ion dosage = 3.0×10^{15} Ar^+ ions), with subsequent LEIS spectra (depth profile) recorded for the surface. After this, the sample was annealed at 400 °C for 15 minutes, and LEIS spectra were obtained over the next two hours as the temperature stabilised.

Annealing Time Dependent

Figure 4.5 compares the LEIS spectra obtained after sputtering and annealing at 400 °C for various periods. The peak at approximately 2275 eV is attributed to Ni, while the peak at approximately 2575 eV is attributed to In. The results clearly indicate that sputtering leads to a significant decrease in the intensity of the In peak, accompanied by a marked increase in the Ni peak.

However, annealing at 400 °C subsequently causes the surface to become much richer in In, and a significant reduction in the Ni signal intensity is observed. These observations indicate preferential surface segregation of In during the annealing treatment. Furthermore, the intensities of In and Ni remained stable during annealing for different durations, indicating that the surface composition became independent of the annealing time.



4

Figure 4.5: LEIS spectra recorded from the $In_3Ni_2(001)$ surface after sputtering and annealing at 400 °C for 2 hours using a 3 keV He^+ beam. The energy ranges for each surface peak highlighted correspond to the upper and lower limits used for the baseline subtraction.

Sputtering (Depth Profile)

Furthermore, we investigated the effect of the sputter ion dose (depth profile) and the annealing of the surface at various temperatures up to 480 °C on the variation of In and Ni intensities. The surface was freshly prepared by sputtering and annealing at 400 °C for one hour, followed by cooling to room temperature. LEIS spectra were then recorded with different ion doses. Initially, the intensity of In was higher than that of Ni, which caused the surface composition to resemble the bulk material. However, with increasing ion dose, the intensity of In decreased, indicating preferential sputtering of In.

This observation aligns with the XPS results, which also show preferential sputtering of In. Subsequently, the intensities of In and Ni reached a saturation point due to the formation of a clean surface, as shown in Figures 4.6 (a) and (c).

Annealing Temperatures dependent

Furthermore, LEIS spectra for In and Ni were recorded after annealing of the surface at various temperatures, up to 480 °C, with one hour of annealing at each temperature and no cooling between steps. To quantify the intensities, the baseline was subtracted using a two-point linear subtraction over the energy ranges highlighted in Figure 4.5, and the remaining signal, attributed to surface scattering from Ni and In, was integrated.

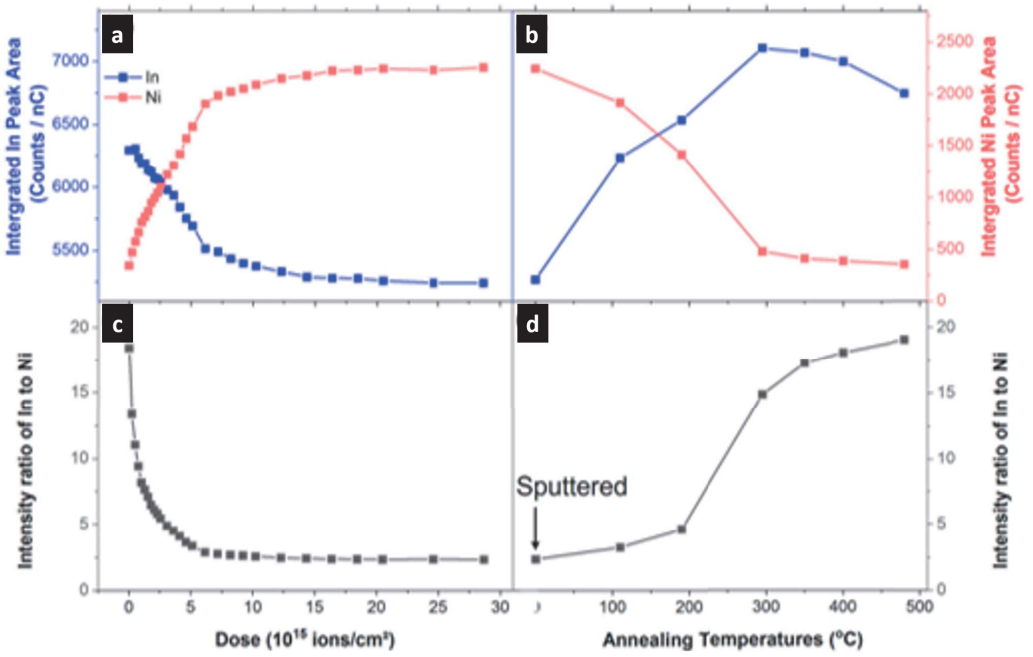


Figure 4.6: (a) The change in the integrated In and Ni intensities in LEIS from the In_3Ni_2(001) surface with sputtering at varying ion doses . (b) After annealing the sputtered surface at varying temperatures. (c) and (d) show the ratio of In to Ni intensities after the corresponding treatments (a, b) [107].

Variations in the intensities of In and Ni as a result of these treatments were analysed. From 295 °C to 480 °C, the intensity of In increased, while the intensity of Ni decreased with increasing annealing temperature. Since LEIS spectra were taken *in situ*, the signal accurately reflects the surface density. As the crystal expands with increasing temperature, it is reasonable to expect a decrease in surface density during annealing, as shown in Figure 4.6 (b). With an increase in temperature to 480 °C, the intensity of both In and

Ni decreased. However, the ratio of In to Ni intensities increased with the annealing temperature, as depicted in Figure 4.6 (d).

4.4.3 Atomic Structure Studied by LEED and STM

LEED

LEED patterns were recorded from the surface after sputtering and annealing at various temperatures ranging from 300 °C to 560 °C, within an energy range of 10–120 eV, using a digital charge-coupled device (CCD) camera coupled with a computer-controlled data acquisition system. No LEED patterns were observed from the surface after annealing at temperatures below 300 °C, indicating that the temperature was insufficient to induce surface ordering. However, after annealing the surface at 310 °C, a (1×1) LEED pattern with hexagonal symmetry was observed with low background intensity, suggesting long-range surface order.

The LEED pattern showed hexagonal symmetry, corresponding to the unit cell of the surface expected from the bulk. The two reciprocal lattice vectors, $|\vec{b} * 1|$ and $|\vec{b} * 2|$, are labelled in Figure 4.7 (a). These lattice constants were determined by comparing the LEED patterns from In_3Ni_2(001) with those of Ag(100) obtained on the same instrument at an energy of approximately 60 eV. The lattice constants derived from the LEED data in real space were $|\vec{b} * 1| = |\vec{b} * 2| = 4.5 \pm 0.2$ Å, which are in good agreement with the expected value for the bulk surface termination, 4.387 Å, as shown in Figure 4.1 (a). Thus, the surface LEED pattern is classified as (1×1).

Effect of Annealing Temperature and Beam Energies

The surface exhibits a (1×1) LEED pattern within the temperature range of 360 to 520 °C, indicating that there is no surface reconstruction or phase transition within these temperature ranges, as shown in Figure 4.7 (a–f).

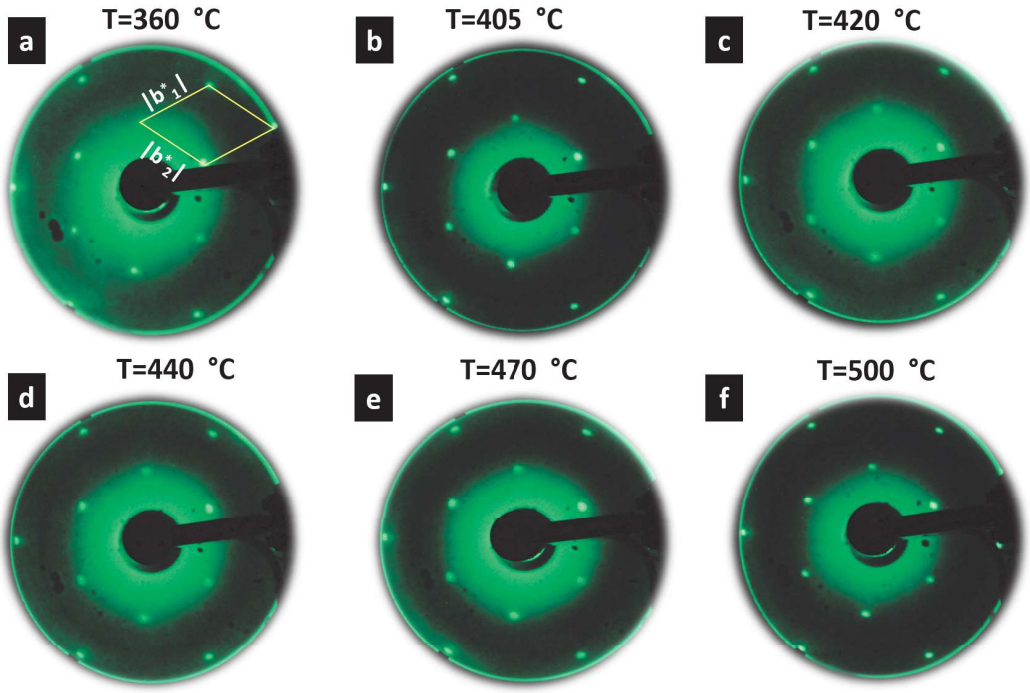


Figure 4.7: (1×1) LEED patterns from the (001) surface at a beam energy of 45 eV after being freshly prepared by sputtering and annealing at different temperatures: (a) annealing at 360 °C. (b) annealing at 405 °C. (c) annealing at 420 °C. (d) annealing at 440 °C. (e) annealing at 470 °C. (f) annealing at 500 °C.

Figure 4.8 (a–h) shows the LEED patterns of the surface after annealing at 360 °C with various beam energies from 10 eV to 100 eV. As expected, only the intensity of the spots changes with varying beam energies, while the pattern itself remains unchanged.

In comparison, LEED studies on Ga_3Ni_2(001) show similar behaviour in terms of surface ordering. The (001) surface typically exhibits a (1×1) LEED pattern at room temperature, which can remain stable over a range of temperatures and beam energies [117]. For example, the intensity of the diffraction spots from Ga3Ni2(001) may also change with beam energy, but the symmetry and general structure of the LEED pattern tend to remain consistent, similar to the observations in this study.

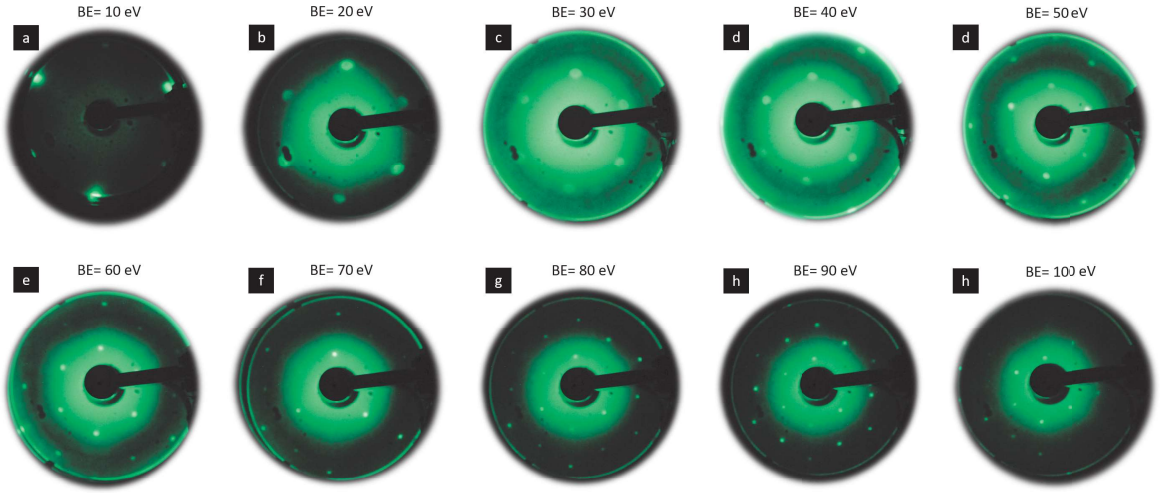


Figure 4.8: LEED patterns of the (001) surface after preparation by sputtering and annealing at 360 °C with beam energies: (a) 10 eV. (b) 20 eV. (c) 30 eV. (d) 40 eV. (e) 50 eV. (f) 60 eV. (g) 70 eV. (h) 80 eV. (i) 90 eV.

Surface Reconstruction induced by Hydrogen

The (1×1) LEED pattern becomes unstable at UHV pressures of 1×10^{-10} mbar. Under these conditions, the surface undergoes significant changes, forming a more complex reconstruction in less than an hour after cleaning. Figure 4.9 (a) shows a well-defined (1×1) LEED pattern after the surface has been freshly prepared by sputtering and annealing at 420 °C. In contrast, Figure 4.9 (b) illustrates a notable alteration in the LEED pattern after leaving the sample for 30 minutes, with the formation of a rectangular reconstruction c(2$\sqrt{3}$×4) with three distinct domains rotated 120° relative to one another. The same transformation is observed after annealing the surface at 470 °C, as shown in Figures 4.9 (c) and (d).

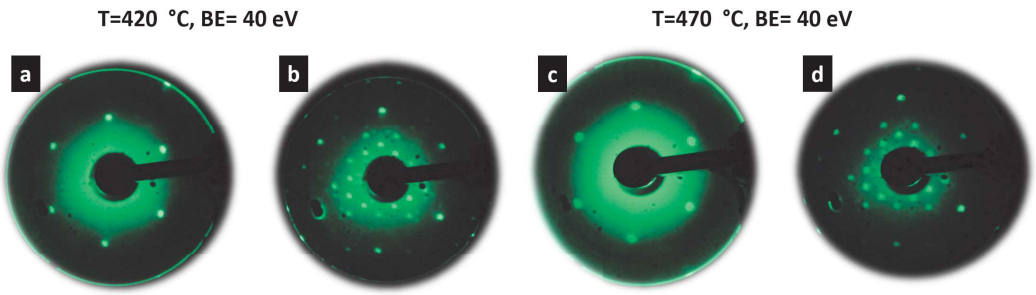


Figure 4.9: LEED patterns illustrating the bulk-type structure characteristic of the (001) clean surface with beam energy = 40 eV after (a) fresh preparation of the surface with annealing temperature = 420 °C. (b) After leaving the sample for 30 minutes. (c) fresh preparation of the surface with annealing temperature = 470 °C. (d) Leaving the sample for 30 minutes.

The observed surface reconstruction in In3Ni2(001) is likely induced by residual gases present in the vacuum chamber. To further investigate this, the Titanium Sublimation Pump (TSP) was activated following surface preparation and annealing at 560 °C. During this process, the chamber pressure was briefly increased to 1×10^{-5} mbar, as the TSP releases gases accumulated in the chamber, primarily hydrogen. Consequently, the surface reconstruction is most likely triggered by hydrogen released from either the TSP or the residual gases in the chamber, which influence the surface structure.

After firing the TSP, a c($2\sqrt{3}\times4$) structure with three distinct domains, each rotated 120° relative to the others, was observed in the LEED pattern (Figure 4.10 (b)). The expected positions of the LEED spots for a single domain and the triple-domain c($2\sqrt{3}\times4$) structure, which indicates the relationship between the substrate and the reconstruction, are shown in Figures 4.10 (c) and (d). Annealing the sample to approximately 200 °C restored the (1×1) LEED pattern. Hydrogen, a primary contaminant in UHV systems, is likely the key factor in this reconstruction process.

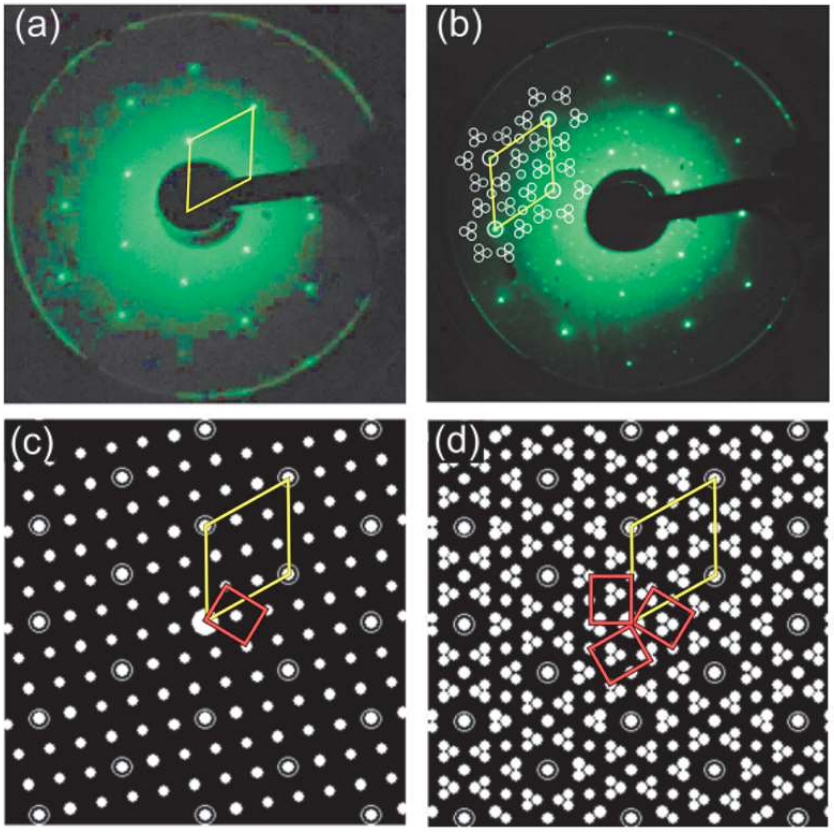


Figure 4.10: (a) LEED pattern from the freshly prepared $In_3Ni_2(001)$ surface, showing a (1×1) structure. (b) LEED pattern from the same surface after firing the Titanium Sublimation Pump, demonstrating the three domains of the c(2$\sqrt{3}$×4) rectangular reconstruction. A section of the pattern is superimposed with the positions expected for the three domains. Both patterns were taken at 100 eV beam energy. (c) The positions of LEED spots expected for a single-domain c(2$\sqrt{3}$×4) reconstruction, where solid circles represent the position of the reconstruction spots, while open circles denote the position of (1×1) spots. (d) The positions of the three-domain c(2$\sqrt{3}$×4) LEED pattern rotated by 120°from each other. Yellow represents the unit cell of the (1×1) structure, whereas that of the c(2$\sqrt{3}$×4) domains is marked by red rectangles [107]. The patterns in (c) and (d) were produced by LEEDpat, which is a software program used to reproduce the experimentally observed LEED pattern using specified parameters [120].

Following the TSP firing, we performed XPS analyses on the surface. On the basis of the results of the XPS analysis, it can be concluded that no additional gases are present on the surface, as only In and Ni are detected by XPS. Since hydrogen cannot be detected by XPS, we assume that the reconstruction is caused by hydrogen, not by other gases. The surface showed the (1×1) structure after being freshly prepared, dosed with 30 L of hy-

drogen, and subsequently measured for the LEED pattern to confirm that hydrogen is the cause of the reconstruction. Consistent with observations after TSP firing, as mentioned earlier, this hydrogen dose does in fact reproduce the c($2\sqrt{3} \times 4$) reconstruction.

This behaviour was not observed on the Ga3Ni2(001) surface, where no reconstruction occurred even after repeated TSP firings, and the surface remained unchanged after 48 hours [117]. In contrast to InPd surfaces, where reconstructions are temperature-dependent, the In3Ni2(001) surface exhibits notable stability during annealing, with reconstruction related to hydrogen exposure rather than annealing effects [60].

We obtained LEED patterns from various parts of the surface. We found a (1×1) surface structure following fresh preparation, and a c($2\sqrt{3}\times4$) rectangular reconstruction after leaving the sample for 30 minutes before taking measurements from most areas of the surface. Only at the edge of the surface did we observe additional spots appearing with low spot intensity compared to the substrate spots, indicating the presence of facets. As illustrated in Figure 4.11 (a–c), the LEED patterns were obtained from the edge of the sample surface after annealing at 440 °C with the selected beam energy, where some of the extra spots are marked by red circles. It is clear that these extra spots move in the opposite direction to the substrate spots' movement with changing beam energy. However, the quality of LEED from these facets is insufficient for further investigation of their structure.

The quality of the sample was assessed, including the potential presence of miscuts, by recording back-reflection Laue X-ray diffraction patterns from various regions of the surface. Most of the sample exhibited a Laue pattern consistent with a single-crystal In3Ni2 with a (001) orientation. However, a small part of the sample showed a polycrystalline In3Ni2 pattern. The edges of the sample produced a faint Laue pattern, which made it difficult to conclusively determine whether the facets observed in the LEED patterns were a result of surface miscuts.

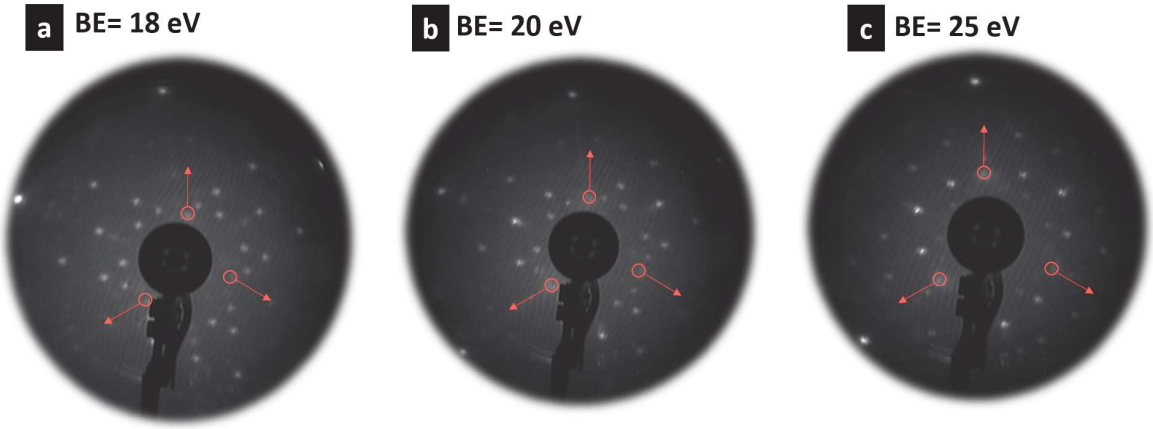


Figure 4.11: LEED patterns of the clean (001) surface recorded at varying beam energies: (a) 18 eV. (b) 20 eV. (c) 25 eV. Faceted diffraction spots, highlighted with red circles, shift outward as the beam energy increases.

The surface crystallographic characteristics were determined using the Laue backscattering method. The diffraction pattern shown in Figure 4.12 (a–b) reveals a series of well-defined, symmetrically positioned dots surrounding a centre point. This pattern indicates a highly ordered atomic arrangement and confirms the presence of a single-crystalline structure. The symmetry and arrangement of the diffraction spots correspond to the (001) orientation of the crystal lattice, indicating the fundamental periodicity of the atomic planes. Figure 4.12 (b) indicates that the diffuse ring pattern observed corresponds to a polycrystalline structure at the edge of the surface.

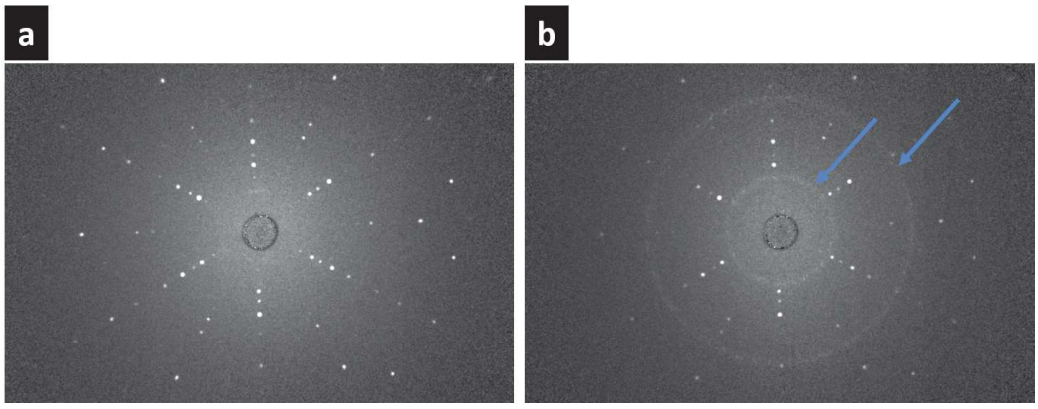


Figure 4.12: (a) Representative Laue back-scattering image taken from the centre of the surface reflecting the symmetry expected from the bulk. (b) Laue back-scattering image from the edge of the sample showing a diffuse ring.

STM

Following LEED experiments, STM images were acquired after annealing the surface at temperatures ranging from 420 °C to 560 °C for a duration of 1 to 3 hours, and the sample was then transferred to the STM. The STM was operated at room temperature in constant-current mode, with a tunnelling current of approximately 0.645 nA and a bias voltage between -0.86 V and 1.6 V to record the STM images.

The (001) surfaces displayed distinct stepped terraces after annealing for two and three hours at temperatures around 530 °C. These terraces were found to be flat, with approximate dimensions of up to 900 $\times$ 900 Å. Furthermore, large-scale scans of the crystal were often successfully performed, as the flat regions allowed for atomic resolution, enabling detailed characterisation of the surface structure.

Figure 4.13 (a) shows an STM image obtained after annealing at 540 °C for two hours, which reveals large, flat terraces. The step height was determined from the height distribution in the vicinity of the steps, with the results being corroborated by line scans. As shown in Figure 4.13 (b), the step heights are distributed along the blue arrow in Figure 4.13 (a), which highlights the steps. Similarly, the step height corresponds to the difference between the peak positions in the histogram, as illustrated in Figure 4.13 (c).

To ensure statistical reliability, more than 100 steps were analysed using STM images from different regions of the surface. The distribution of step heights is presented in the histogram shown in Figure 4.13 (d). The step height most frequently observed was found to be 5.2 $\pm$ 0.3 Å, or a multiple of this value. In some cases, steps of 5.2 Å were observed to split into two smaller steps with heights of 3.5 $\pm$ 0.2 Å and 1.7 $\pm$ 0.3 Å, as depicted in Figure 4.13 (a).

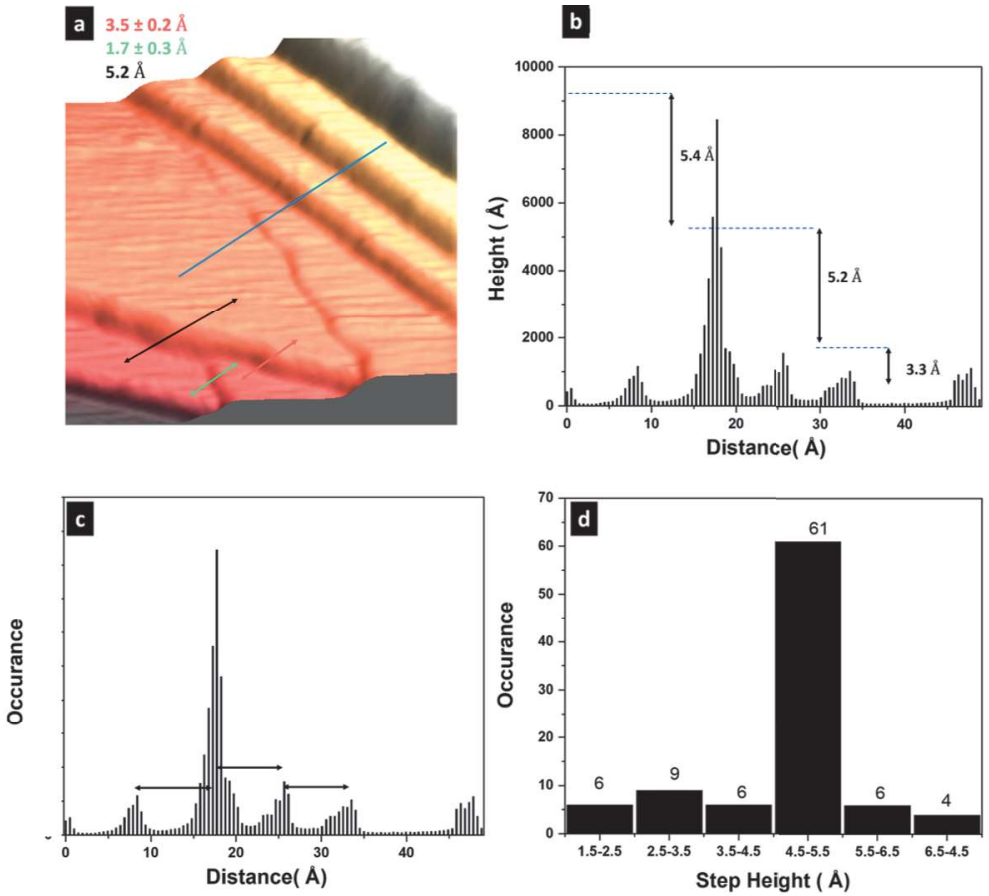


Figure 4.13: (a) STM image taken from the In_3Ni_2(001) surface after several cycles of sputtering and annealing at 540 °C (750 Å×950 Å, +0.472 V, 0.448 nA), demonstrating steps of different heights. (b) Height distribution along a blue line in (a) crossing the steps. Step heights are given. (c) The histogram of height distribution in the vicinity of the steps. (d) The histogram of steps that were analysed from STM images taken from different regions of the surface.

As discussed previously in the LEED section, the surface quickly undergoes reconstruction, which makes it difficult to detect the (1×1) structure by STM. Upon transferring the sample from the preparation chamber to the STM chamber, the surface undergoes reconstruction. According to LEED results, three domains exhibiting the c($2\sqrt{3}$×4) reconstruction should be present in the STM images. Figures 4.14 (a–c) show examples of the three distinct domains on separate terraces. These domains are rotated by 120° with respect to each other and do not coexist on the same terrace. Bright features form rectangular central unit cells with dimensions of $2\sqrt{3}$a and 4a. This observation is consistent with the

c($2\sqrt{3}\times4$) reconstruction, as shown in Figures 4.14 (a–c), and is further corroborated by the model structure in Figures 4.14 (d), (e), and (f). For high-resolution STM imaging, we typically measure a (200×200) Å region of the surface, within which only one domain is visible. The surface consistently exhibits the structure and morphology mentioned above described above.

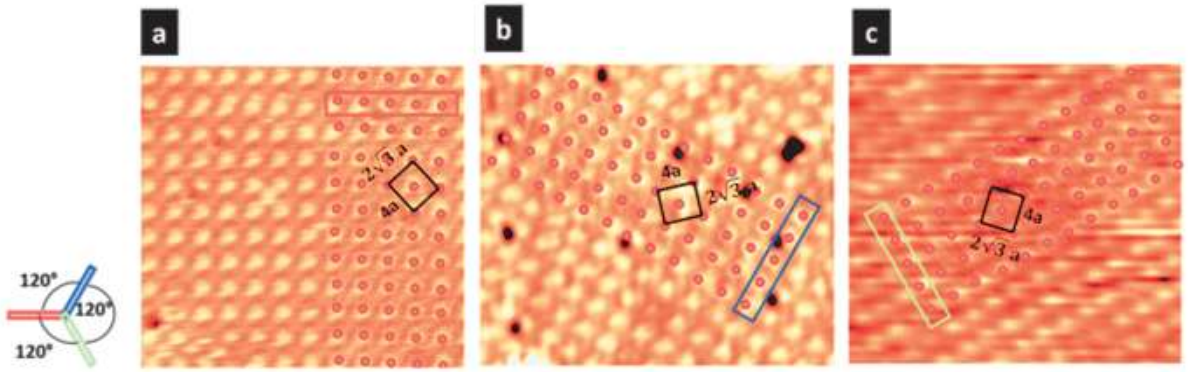


Figure 4.14: STM images of the In_3Ni_2(001) surface showing three domains of c($2\sqrt{3}\times4$) rect structure, rotated by 120° relative to one another. Unit cells are indicated by black rectangles. A model structure depicting a high-resolution STM image, where red spheres represent bright protrusions observed in STM, whereas the grid represents the unit cells of the (1×1) structure. A c($2\sqrt{3}\times4$) rect unit cell is shown by a black rectangle.(a) The image is rotated by 0°. (b) The image is rotated by 120°. (c) The image is rotated by 240°.

In addition to the predominant c($2\sqrt{3}\times4$) structure, the c($3\times\sqrt{3}$) reconstruction was also observed in STM images. The region under observation was insufficiently large to produce a detectable LEED pattern. The step height associated with the c($3\times\sqrt{3}$) reconstruction was measured to be 2.6 ± 0.1 Å, which does not correspond to the separation of atomic planes along the [001] direction. Furthermore, the surface became diffuse after prolonged annealing, indicative of increased roughness, which further complicates STM imaging.

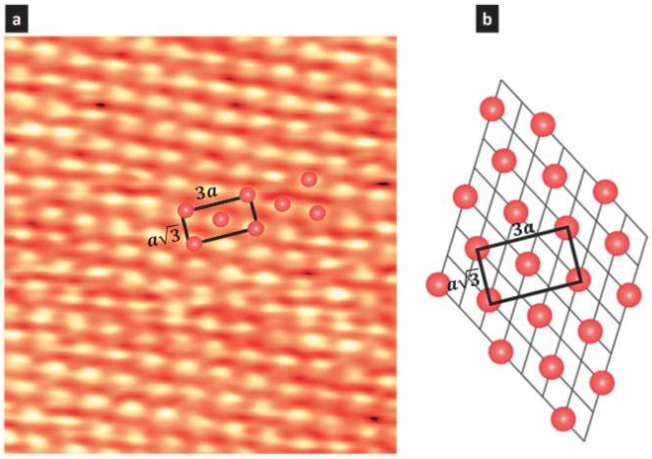


Figure 4.15: (a) STM images of the $In_3Ni_2(001)$ surface showing three domains of $c(3\times\sqrt{3})$ structure. The unit cell is indicated by a black rectangle. (b) A model structure, where red spheres represent bright protrusions observed in STM, and the grid represents the unit cells of the (1×1) structure. A $c(3\times\sqrt{3})$ unit cell is shown by a black rectangle.

4.4.4 Identification of Surface Termination

In this section, possible surface terminations are discussed based on multiple factors, including surface model analysis, surface energy calculations, and comparison with STM images and LEIS data.

Figure 4.1 (c) indicates that the surface could terminate in one of the following models: 0, 1, 3, or 4. Model 2 is ruled out because it places the upper layer of In atoms in such a way that the incoming He^+ ions cannot reach the Ni subsurface, thus preventing a clearly defined surface Ni peak. However, we observed a well-defined peak of Ni in LEIS.

The surface energy calculations rule out models 1 and 4, as their surface energies are much higher [107]. Therefore, only models 0 and 3, with the lowest surface energies, are consistent with both experimental and computational results, suggesting that these are plausible surface terminations (Figure 4.16).

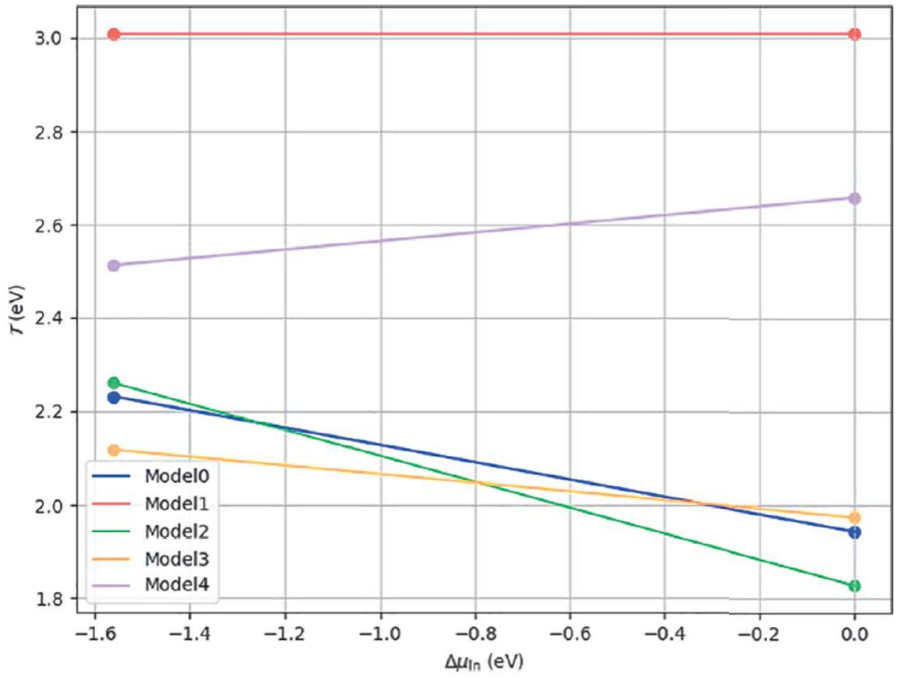


Figure 4.16: Variation of total energy (τ) as a function of the chemical potential of In ($\Delta\mu_{\mathrm{In}}$) for the five model surfaces presented in Figure 4.1 (c). Refer to the main text for definitions of total energy (τ) and $\Delta\mu_{\mathrm{In}}$, representing the In chemical potential in the In-rich regime [107].

Additionally, a comparison between the theoretical surface models and the STM images reveals that step heights correspond to the distance between model planes 0 and 3. This suggests that these planes define the termination of the surface, reinforcing the validity of these models. In both models 0 and 3, the distance between neighbouring In atoms in the top layer is 4.387 Å. In addition, the distance between an In atom in the top layer and a Ni atom in the layer below is 2.639 Å for model 0 and 2.777 Å for model 3. These values indicate that In and Ni are bonded to each other, which would likely enhance the stability of the crystal surface.

Further support for the identification of surface termination models 0 and 3 comes from density functional theory (DFT) calculations conducted by collaborators in this study, which also ruled out the terminations for surface models 1 and 4. The findings are consistent with previous studies on binary intermetallics, such as Zn–Pd, where surface termi-

nations involving both components are found to be more stable than those with a single element, as detailed by Lowe *et al.* (2024) [45]. Thus, surface models 0 and 3 are identified as the most stable terminations, with In–Ni bonding likely contributing to the observed surface stability.

4.4.5 Oxidation Behaviour

The oxidation behaviour of the surface was examined by XPS. The surface was cleaned by sputtering and annealing, followed by exposure to 20 L of oxygen, after which XPS measurements were performed. Subsequently, the surface was re-cleaned and subjected to varying oxygen doses of 300, 600, and 900 L, with XPS spectra acquired following each exposure. Moreover, following the cleaning process, the surface was exposed to air, and XPS spectra were obtained for comparison with those recorded from the oxygen-exposed surface.

Figures 4.17 (a–c) present the XPS spectra for In $3d$, Ni $2p$, and O $1s$ on surfaces that were cleaned, exposed to oxygen, and exposed to air. As oxygen exposure increases, shoulders develop at higher binding energies for the three core levels. Figures 4.17 (d) and (e) show the In $3d_{5/2}$ and Ni $2p_{3/2}$ spectra, with the intensity of each spectrum normalised between 0 and 1, which emphasises the appearance of the shoulder feature.

The shoulders observed in the spectra are attributed to the formation of In and Ni oxides. The peaks and shoulders in the O $1s$ spectra correspond to pure oxygen, oxide, and Ni hydroxide, respectively. A more detailed analysis of oxide formation will be presented later. Upon exposure of the (001) surface to air, the Ni $2p_{3/2}$ shoulder remains unchanged (Figure 4.17 (e)), while the In $3d_{5/2}$ shoulder becomes more prominent. Additionally, the shoulder in the O $1s$ spectra emerges as the dominant feature after exposure to air.

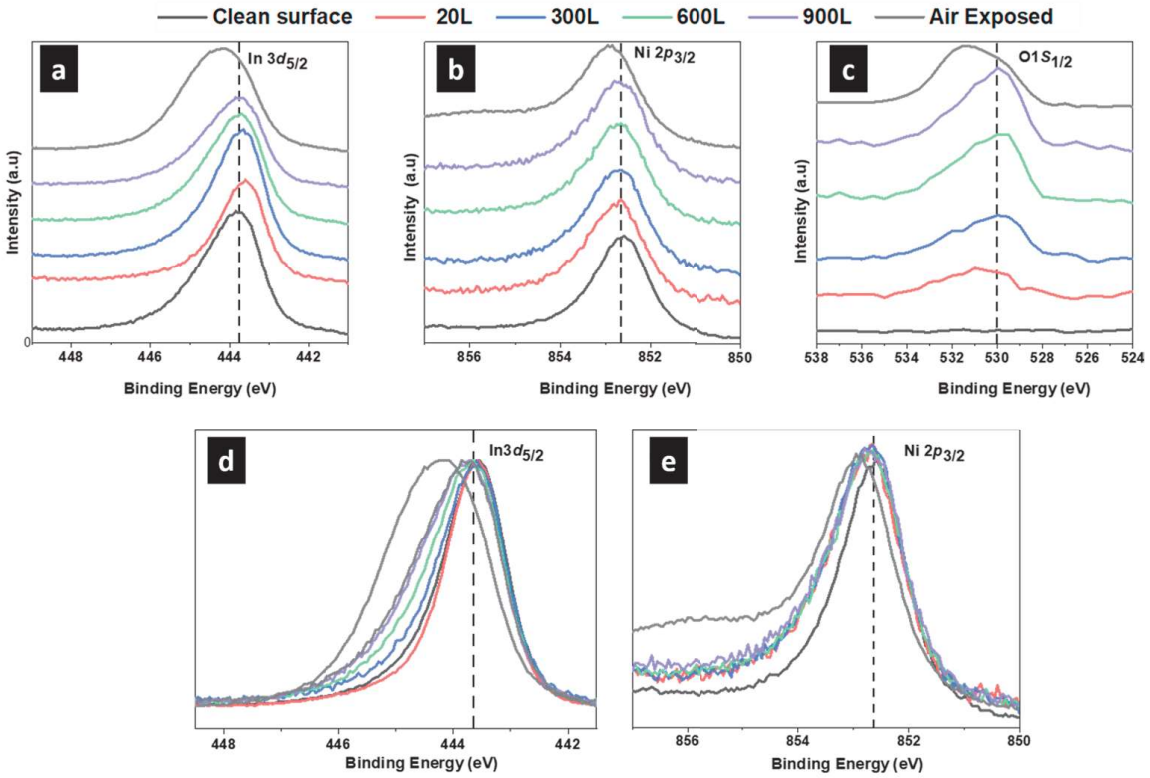


Figure 4.17: (a) to (c) XPS spectra of the clean (after annealing at 560 °C), oxygen exposed, and air exposed (001) surface of In_3Ni_2(001) (a: In 3d, b: Ni 2p, and c: C 1s). Oxygen exposure ranged from 20-900 L. (d, e) In $3d_{5/2}$ and Ni $2p_{3/2}$ spectra, respectively, after normalizing the minimum and maximum intensity between 0 and 1, illustrating the development of a shoulder at higher binding energies. The dotted, dashed, and dash dotted lines at 530.2 eV, 531.0 eV, and 531.6 eV in (c) correspond to the positions of the oxide, pure oxygen, and Ni hydroxide peaks, as reported in the literature [99, 121, 122]. The dotted lines in (c) indicate the positions of the oxide peaks, while the dashed lines in all other spectra correspond to the core level positions of the respective elements from the clean surface [107].

The spectra were fitted using a Shirley background along with a combination of asymmetric Gaussian and Lorentzian functions to extract the positions and intensities of the peaks and shoulders. Figures 4.18 and 4.19 (a–c) illustrate examples of the fitting procedure applied to the In $3d_{5/2}$ and Ni $2p_{3/2}$ spectra for clean and oxygen-exposed surfaces. The fitting model assumed a 60% Gaussian and 40% Lorentzian contribution. The positions of all the peaks presented in this thesis are derived from this approach, with an estimated error of approximately $\pm$ 0.1 eV in peak position.

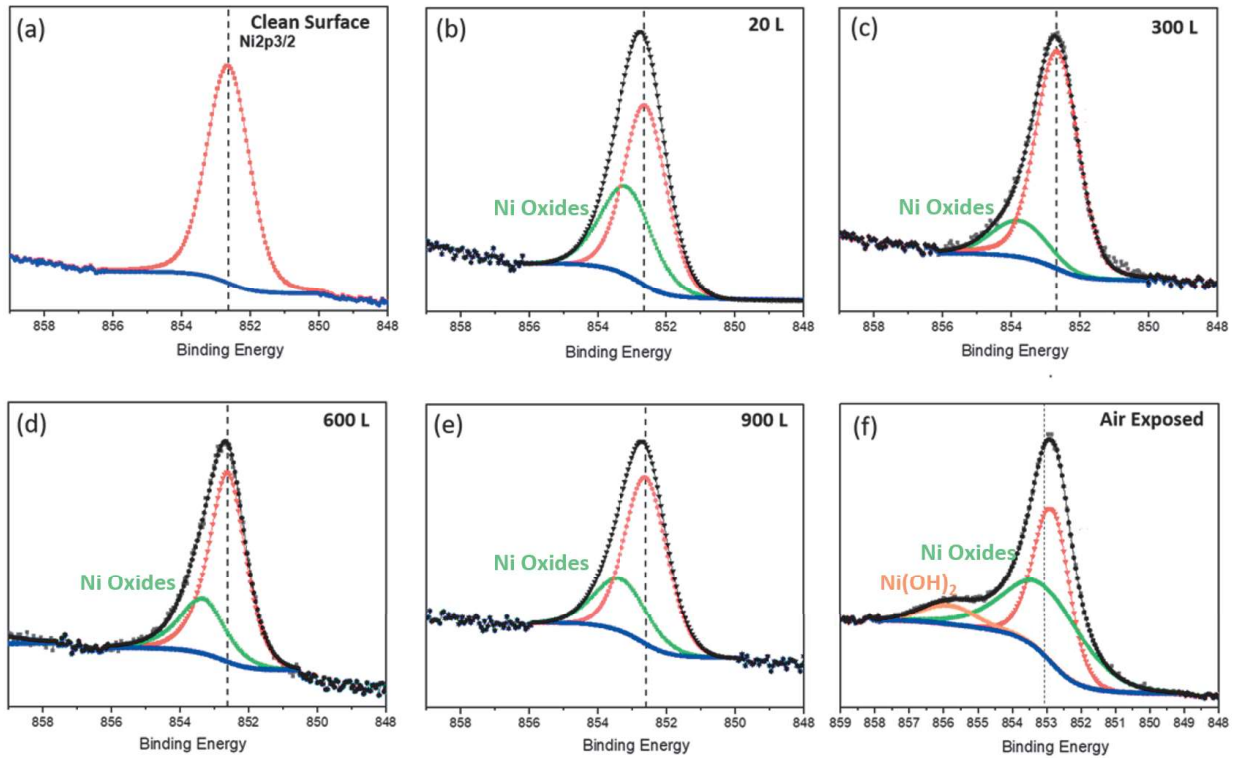


Figure 4.18: Ni $2p_{3/2}$ XPS spectra of the In_3Ni_2(001) surface after cleaning the surface through sputtering and annealing at 560 °C, with increasing oxygen exposure (20 L, 300 L, 600 L, and 900 L) and after air exposure. Vertical dashed lines in all spectra correspond to the core-level position of clean Ni $2p_{3/2}$.

For the clean surface, the In $3d_{5/2}$ and Ni $2p_{3/2}$ spectra can be fitted with single peaks at 443.6 eV and 852.5 eV, respectively, as shown in Figures 4.19 (a) and 4.18 (a). These peaks are attributed to intermetallic In and Ni. Given the proximity of these peaks to the binding energies of elemental In [112] and Ni [111], and taking into account the experimental energy resolution, it is not possible to definitively determine whether charge transfer occurs between In and Ni in the In_3Ni_2 intermetallic.

For the surface exposed to oxygen, the In $3d_{5/2}$ spectra can be fitted with two peaks, as shown in Figure 4.19 (b–f). The dominant peak at 443.6 eV corresponds to the intermetallic In (pure In in In_3Ni_2), while a smaller peak at 444.7 eV, appearing as a shoulder, is shifted to a higher binding energy by 1.1 e. This shift is indicative of the formation of In_2O_3 on the surface [112].

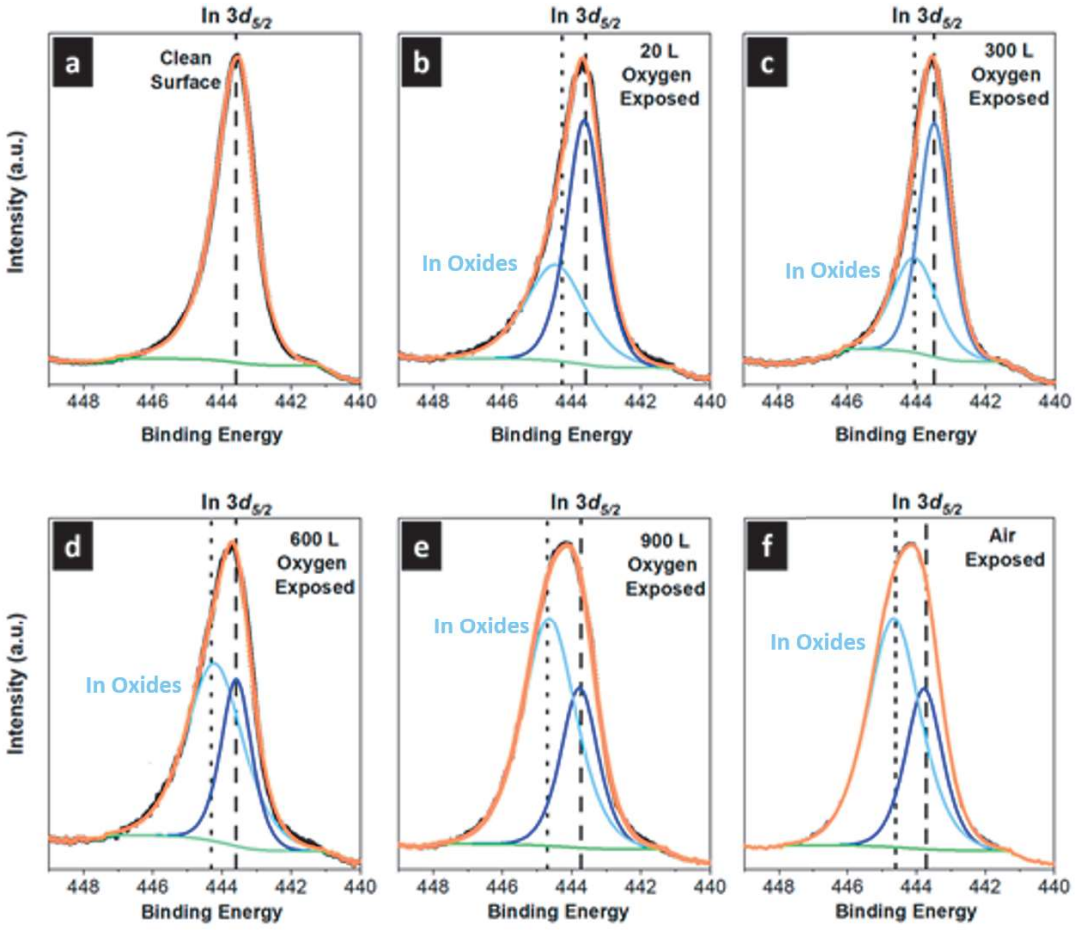


Figure 4.19: In $3d_{5/2}$ XPS spectra of the In_3Ni_2(001) surface after cleaning the surface via sputtering and annealing at
560 °C and with increasing oxygen exposure (20 L, 300 L, 600 L, and 900 L) and after air exposure. Vertical dashed lines in all spectra correspond to the core-level position of clean In $3d_{5/2}$.

On the surface exposed to air, the oxide peak becomes more prominent than the pure In peak, suggesting a higher concentration of In_2O_3 relative to pure In. In contrast, the oxygen-exposed surface under the dosing conditions employed ($\leq$ 900 L) exhibits a greater proportion of pure In. For the Ni $2p_{3/2}$ spectra, two peaks are observed: one at 852.5 eV corresponding to intermetallic Ni, and another at 853.6 eV corresponding to NiO, similar to the behaviour observed for the In $3d_{5/2}$ spectra. This shift is consistent with previous studies, which indicate that the NiO peak shifts to a higher binding energy by 1.1 eV above the pure Ni peak [111].

The intermetallic Ni peak remains more intense than the In peak on the air-exposed surface, implying that Ni is more prone to oxidation than In. This observation is further supported by the oxygen exposure experiments. As shown in Figure 4.19 (d), the intensity of the In_2O_3 shoulder progressively increases with exposure to oxygen. However, the NiO shoulder reaches saturation after 20 L of oxygen exposure (Figure 4.18 (e)). Additionally, a broad peak at 855.5 eV (indicated by an arrow in Figure 4.18 (e)) emerges following air exposure. This peak is identified as $Ni(OH)_2$, as evidenced by the observed peak shift of 3.0 eV, which matches previously reported data [111].

A qualitative analysis of the surface chemical composition was performed after cleaning, oxygen exposure, and air exposure treatments. The chemical composition was determined by evaluating the intensities of the In $3d_{5/2}$, Ni $2p_{3/2}$, O $1s$, and C $1s$ peaks after fitting the curves (areas under the curves), while also considering the photoemission cross sections of the respective elements. Potential influences, including instrumental response and the inelastic mean free path of the photoelectrons, were considered and excluded from the analysis. The surface composition following each treatment is illustrated in Figure 4.20.

As expected, only In and Ni are identified on the clean surface. Upon exposure to oxygen, additional peaks corresponding to pure oxygen and oxides, along with those for In and Ni, emerge. Following exposure to air, peaks associated with hydroxide and carbon are detected, in addition to the species identified on the oxygen-exposed surface. From the clean surface to the surface exposed to 900 L of oxygen, the proportion of pure In decreases from approximately 74% to approximately 27%, while the content of pure Ni decreases from approximately 28% to 6%. During the same exposure conditions, the fraction of oxidised In increases, reaching approximately 7% for 900 L exposure, and oxidised Ni increases to about 2% under the same exposure conditions, reflecting the decrease in the pure In and Ni content.

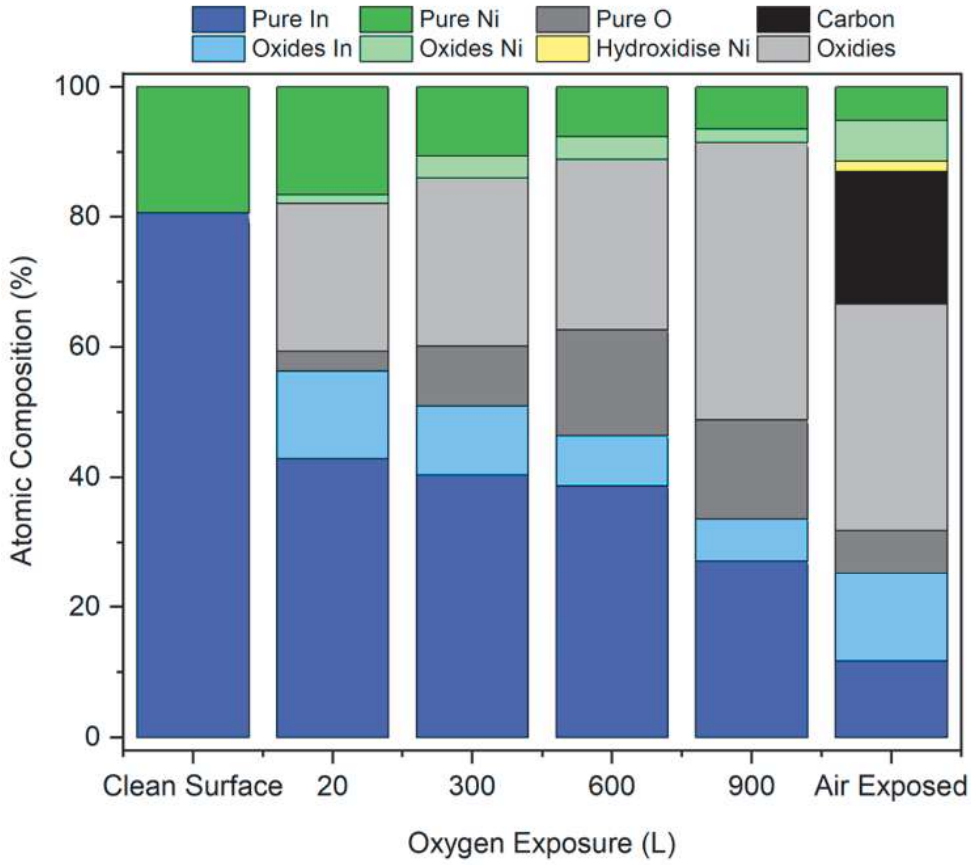


Figure 4.20: Chemical composition of the Ni_3In_2(001) surface after annealing at 560 °C and increasing oxygen exposure (20–900 L). The atomic composition of the clean and air-exposed surfaces is also provided for comparison. The composition was determined from the In $3d_{5/2}$, Ni $2p_{3/2}$, O $1s_{1/2}$, and C $1s_{1/2}$ XPS peaks.

4.5 Summary

For the first time, the atomic structure, chemical composition, and oxidation behaviour of the (001) surface of In_3Ni_2 was comprehensively investigated using a combination of techniques, including XPS, LEIS, STM, and LEED.

Both XPS and LEIS results demonstrated that sputtering preferentially removes In from the surface, while annealing facilitates the segregation of In from the bulk to the surface. This preferential sputtering and surface segregation behaviour is attributed to the lower surface free energy of In compared to that of Ni.

LEED analysis revealed that the surface retains a (1×1) symmetry, with the identification of a three-domain c($2\sqrt{3} \times 4$) rectangular structure. The formation of these surface structures is influenced by exposure to ambient hydrogen in the experimental chamber, as well as hydrogen introduced from external sources.

A comprehensive analysis integrating the step height distribution observed through STM, the intensity distribution from LEIS, and surface energy calculations indicates that the outermost surface layer comprises In atoms bonded to Ni atoms. This observation suggests that the stability of the surface may stem from the formation of intermetallic bonds. Furthermore, the presence of catalytically active Ni atoms on the surface, spatially isolated from one another, is expected to enhance the catalytic properties of the material.

5 | $In_3Ni_2(2\bar{1}0)$ Surface

5.1 Introduction

This chapter details the atomic structure, chemical composition, and oxidation characteristics of the $In_3Ni_2(2\bar{1}0)$ surface. The study involved the use of several surface-sensitive techniques, such as XPS, LEIS, LEED, and STM. Several sputtering and annealing cycles were used to obtain a clean and well-ordered surface. All treatments and measurements were performed under UHV conditions to prevent surface contamination throughout the experiments.

The chemical composition of the $In_3Ni_2(2\bar{1}0)$ surface was examined using XPS spectra to determine the effects of air exposure, sputtering, and annealing. Compositional changes as a function of different annealing temperatures and the influence of the grazing angle on the chemical composition were also investigated. Furthermore, elemental information of the uppermost atomic layers of the surface was obtained using LEIS after sputtering and annealing at various temperatures.

The impact of sputtering and annealing at varying temperatures on LEED patterns was also studied. STM imaging was used to analyse the surface morphology and identify the termination plane by comparing the obtained images with a bulk atomic model.

Moreover, the oxidation behaviour of the $In_3Ni_2(2\bar{1}0)$ surface was investigated using XPS. This involved investigating the variations in the binding energies of surface components, namely In and Ni, in response to differing oxygen interactions.

5.2 $In_3Ni_2(2\bar{1}0)$ Model Structure

The analysis and discussion of the experimental results will be carried out following the detailed description of the atomic structure of the In_3Ni_2 $(2\bar{1}0)$ surface.

Figure 5.1 (a) illustrates the bulk unit cell of In_3Ni_2, where the $(2\bar{1}0)$ surface is highlighted in yellow. The crystal lattice parameters are given as $a = b = 4.387$ Å, $c = 5.295$ Å, with angles $\alpha = \beta = 90^\circ$ and $\gamma = 120^\circ$ [107]. The structure of In_3Ni_2 is identical to the Al_3Ni_2 type and belongs to the trigonal space group P-3m1 [65], as further illustrated in Figure 2.12 (a).

In Figure 5.1 (b) presents a side view of the surface, where identical atomic planes composed of a mixture of In and Ni are arranged in an ordered stacking pattern that forms the overall crystal structure. The inter planar distance between consecutive atomic layers is 2.19 Å, which is half of the lattice constant, a = 4.39 Å.

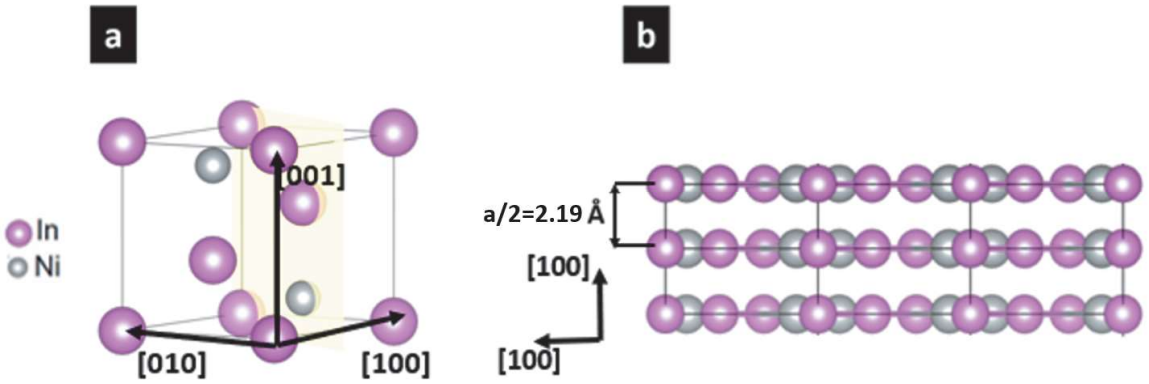


Figure 5.1: (a) The unit cell of In_3Ni_2, with the $(2\bar{1}0)$ plane highlighted in yellow. (b) Side view of the $(2\bar{1}0)$ surface, showing the stacking of three atomic layers of In and Ni within the unit cell.

5.3 Experimental Methods

The Czochralski method, detailed in Section 2.7, was used to grow high-quality single crystals of the In_3Ni_2 sample [108]. Once grown, the sample was sliced along the $(2\bar{1}0)$

surface and polished using diamond paste with a grain size successively reduced to 0.25 μm.

The $(2\bar{1}0)$ surface was subsequently cleaned under UHV conditions through multiple sputtering cycles using an Ar^+ ion beam. Each cycle involved 30 minutes of exposure at an energy of 2 keV, with a pressure of 2.5×10^{-5} mbar and a drain current of around 6 μA. Following sputtering, the sample was annealed at temperatures ranging from 300 °C to 560 °C for a duration of one to five hours.

For XPS, STM, and LEED experiments, the surface temperature was monitored using an optical pyrometer set with an emissivity of 0.40, consistent with that previously used for the (001) surface. In the LEIS system, the optical pyrometer was calibrated against a thermocouple under UHV conditions to ensure accuracy. The In_3Ni_2 sample was positioned to enable simultaneous temperature readings from both the pyrometer and the thermocouple during analysis.

Calibration involved adjusting the emissivity setting of the pyrometer until its readings aligned with those of the thermocouple over a range of temperatures. Initial findings indicated that emissivity values between 0.40 and 0.50 yielded reasonable agreement, prompting further refinement within this interval. An emissivity of 0.48 was identified as providing the most consistent match and was subsequently used for all optical pyrometry measurements in this study, as detailed in Chapter 3.3. It is important to note that the temperature measurements reported in this chapter, based on an emissivity of 0.40, are approximately 11 degrees lower than the more accurate calibrated values.

The surface cleaning process was repeated until a well-defined LEED pattern was clearly observed, confirming the successful preparation of the surface. XPS analysis was then used to verify the complete removal of contaminants, thereby confirming the effectiveness of the cleaning procedure. Finally, the freshly prepared sample was transferred to the STM chamber for further measurements.

We used an Omicron variable temperature STM that operated at room temperature in constant-current mode for STM imaging. A surface bias voltage ranging from -1.8 V to +1.8 V was applied, and the tunnelling current was maintained at 0.645 nA. The atomic-resolution imaging of the surface therefore offered detailed insights into its atomic arrangement and topography.

LEIS measurements were performed within a dedicated UHV chamber, where the surface cleaning process was independently repeated to prepare the sample specifically for this analysis. The LEIS spectra were acquired on a surface area of approximately 2 mm$\times$2 mm using a 3 keV He^+ ion beam, with an ion dose of approximately $\times 10^{14}$ ions cm^{-2}. The experimental parameters were carefully optimised to achieve a high signal-to-noise ratio for the characteristic surface peaks of Ni (approximately 2275 eV) and In (approximately 2575 eV). Data acquisition was carried out using a commercial Qtac100 spectrometer (IonTOF), and the spectra were processed and analysed using the Surface Lab 7 software suite (IonTOF) [110]. All LEIS experiments were conducted at the Low Energy Ion Scattering Facility, University of Liverpool.

The Czochralski method, detailed in Section 2.7, was used to grow high-quality single crystals of the In_3Ni_2 sample [108]. Once grown, the sample was cut along the $(2\bar{1}0)$ surface and polished using diamond paste with a grain size successively reduced to 0.25 μm.

The $(2\bar{1}0)$ surface was subsequently cleaned under UHV conditions through multiple sputtering cycles using an Ar^+ ion beam. Each cycle involved 30 minutes of exposure at an energy of 2 keV, with a pressure of 2.5×10^{-5} mbar and a drain current of around 6 μA. Following sputtering, the sample was annealed at temperatures ranging from 300 °C to 560 °C for a duration of one to five hours.

For XPS, STM, and LEED experiments, the surface temperature was monitored using an optical pyrometer set with an emissivity of 0.40, consistent with that previously used for the (001) surface. In the LEIS system, the optical pyrometer was calibrated against a thermocouple under UHV conditions to ensure accuracy. The In_3Ni_2 sample was po-

sitioned to enable simultaneous temperature readings from both the pyrometer and the thermocouple during analysis.

For surface oxidation studies, XPS data were obtained at the Institut Jean Lamour using a non-monochromatic Al K_α X-ray source. To induce oxidation, a leak valve was used to introduce 99.999% pure oxygen gas into the UHV system, with the partial pressure controlled at approximately 1.333×10^{-6} mbar. The exposure time, together with the controlled pressure, defined the total exposure, which was measured in Langmuir units (L), where 1 L = 1.333×10^{-6} mbar·s. For the air exposure experiment, the sample was first cleaned following the standard procedure, then removed from the UHV chamber and exposed to air for approximately 10 days before being reintroduced into the system for XPS measurements. The XPS data were analysed using the CasaXPS programme, which provided detailed chemical and electronic insights into the surface after oxidation.

5.4 Results and Discussion

5.4.1 Chemical Composition Studied by XPS

Effect of Air Exposure, Sputtering and Annealing on Surface

The sample was contaminated with oxygen and other contaminants when exposed to air before being transferred to the UHV chamber. To assess the chemical response of the surface to air exposure and to evaluate the effectiveness of the cleaning procedure, we used XPS after sputtering and annealing the surface.

Figure 5.2 (a) shows the XPS wide scan spectra for the $(2\bar{1}0)$ surface after air exposure, sputtering, and annealing at 560 °C for one hour, with the peaks of the corresponding components marked by vertical dashed lines. The KLL peaks, associated with Auger electrons, are produced from the L shell as a result of electron transitions. Figures 5.2 (b) and (c) present the characteristic peaks corresponding to In $3d_{5/2}$ and Ni $2p_{3/2}$.

The XPS spectrum following air exposure reveals a distinct O 1*s* peak, indicating the presence of surface oxygen contamination. To remove this contamination and restore the clean surface, three successive cycles of sputtering and annealing were performed under UHV conditions. Subsequently, the O 1*s* signal was no longer detectable in the wide scan spectrum, confirming the effective removal of surface oxygen. The resulting spectrum displayed only the characteristic core-level peaks of In and Ni, indicating a successful restoration of the surface composition.

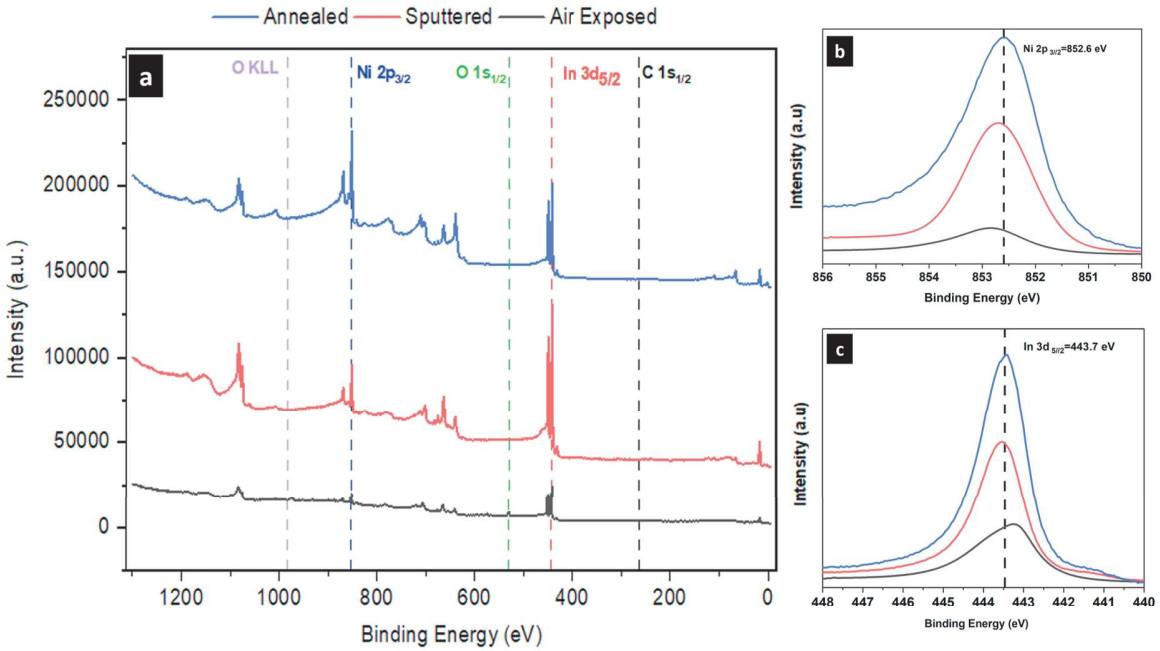


Figure 5.2: (a) XPS wide scan spectra of a clean $In_3Ni_2(2\bar{1}0)$ surface after sputtering and annealing the surface at 560 °C for an hour, and no oxygen or carbon contamination was detected. (b) and (c) XPS spectra comparing the binding energies of the core levels of In $3d_{5/2}$ and Ni $2p_{3/2}$ showing the effect of sputtering, air exposure, and the clean prepared surface.

As discussed previously in Chapter 4, the spectra were analysed over the energy range from 0 to 1200 eV, with particular emphasis on the core levels of In, Ni, and O. To accurately determine the binding energies and peak areas for In and Ni, a Gaussian-Lorentzian convoluted line shape was employed in conjunction with a Shirley-type background sub-

traction. A summary of the binding energies for the In $3d_{5/2}$ and Ni $2p_{3/2}$ core levels is presented in Table 5.1. Further discussion of the peak profiles will be provided in Section 5.4.4.

Element	Ni $2p_{3/2}$	In $3d_{5/2}$
Element Binding Energy	852.5 eV [111]	443.7eV [112]
Air Exposed Surface	852.9 eV	444.5 eV
Sputtered Surface	852.6eV	443.6 eV
After Sputtered Annealed Cycles	852.6 eV	443.5 eV

Table 5.1: Binding energies of the Ni $2p_{3/2}$ and In $3d_{5/2}$ core levels for the $In_3Ni_2(2\bar{1}0)$ surface measured by XPS after exposure to air, following sputtering, and after cleaning by sputtering and annealing. Core-level positions of elements are also given for comparison.

Atomic Composition Changes As Function of Sputtering and Annealing Temperature

Atomic composition of the surface was determined after sputtering and annealing at various annealing temperatures. The integrated intensity (area under the curve) of the Ni $2p_{3/2}$ and In $3d_{5/2}$ peaks in the XPS spectra was used to determine the atomic composition of In and Ni. The photoionisation cross section, the inelastic mean free path of photoelectrons, and the analyser's transmission function were used to normalise these intensities, as described in Section 3.4.1.

Analysis of the In $3d_{5/2}$ and Ni $2p_{3/2}$ XPS spectra for the In_3Ni_2 surface revealed a compositional change following sputtering (Figure 5.3). The bulk atomic percentage of In is approximately 60%, however after sputtering, this value decreases to around 55%. Conversely, the atomic percentage of Ni increases from 40% to approximately 45%. This reduction in In content, accompanied by a corresponding enrichment in Ni, indicates that the sputtering process preferentially removes In from the surface, resulting in an excess of Ni at the surface.

The preferential sputtering observed in intermetallic compounds can be influenced by several factors, including atomic mass, surface free energy, and bonding energy. Elements with lower atomic mass, reduced surface free energy, and weaker bonding strength are generally more susceptible to preferential sputtering [113, 114, 115, 123]. In this surface, atomic mass is not the dominant factor, as In is heavier than Ni. However, a comparison of surface free energies indicates that In possesses a lower surface free energy than Ni, which likely contributes to its preferential removal during the sputtering process.

The surface free energy of a face-centred cubic (FCC) Ni surface is higher than that of a body-centred tetragonal (BCT) In surface, with values of 1.31 J/m^2 and 0.488 J/m^2, respectively [116]. These values highlight the tendency of In to be preferentially sputtered due to its lower surface energy. Similar behaviour has been observed in the binary alloy Ga_3Ni_2(2=10) surface, where, after sputtering, Ga and Ni are present in almost equal atomic compositions, with Ga constituting 45

During surface annealing at 300 °C, the atomic percentage of In increases to approximately 76%, while the Ni decreases to 24%. This composition significantly exceeds the bulk concentration of In, particularly at such a relatively low annealing temperature. Further annealing at high temperatures, up to approximately 550 °C, results in no significant changes to the atomic composition, indicating that the surface has attained a state of compositional saturation. These observations suggest that annealing facilitates the segregation of In from the bulk to the surface. Surface segregation in alloys refers to the enrichment of one component at the surface relative to the bulk, a phenomenon well documented in the literature [124], and clearly evident in Figure 5.3.

The forces behind surface segregation in alloys are primarily attributed to differences in surface properties between the constituent elements, including surface free energy, atomic radius, and bonding energy [114]. Elements characterised by lower binding energy, larger atomic radius, and lower surface energy tend to preferentially segregate to the surface. In comparison to Ni, In exhibits a lower surface free energy and a larger atomic

radius, as previously discussed and supported in the literature [118]. Accordingly, it is proposed that the observed surface segregation of In is predominantly governed by these factors, namely its larger atomic size and lower surface energy relative to Ni [119]. Similar behaviour involving preferential segregation has also been reported for the Ga_3Ni_2(2=10) surface [117].

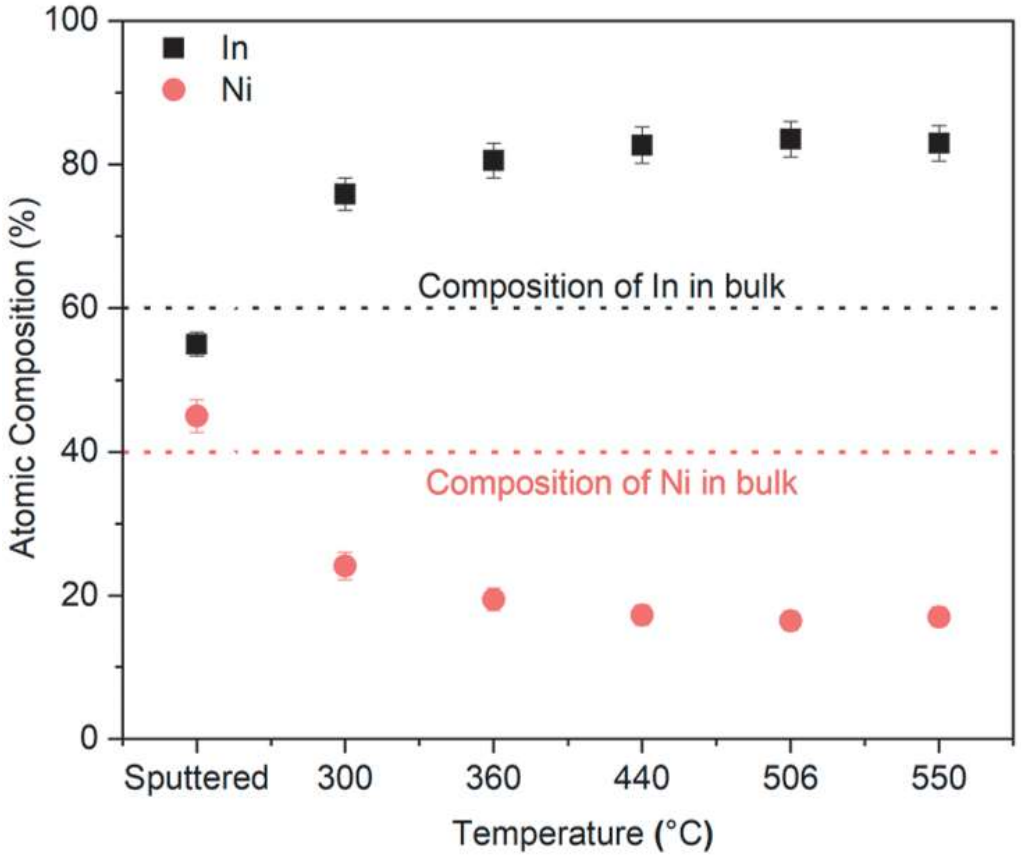


Figure 5.3: Surface chemical composition of the $(2\bar{1}0)$ surface after sputtering and annealing at temperatures ranging from 300 °C to 550 °C. Dotted lines indicate the bulk composition of In and Ni. θ is an angle between the surface and X-ray.

Atomic Composition as Function of Scanning Angles

The distribution of In on the $(2\bar{1}0)$ surface was examined by obtaining XPS spectra from the surface after annealing it at 530 °C at various angles: 30°, 40°, 50°, and 60°. The atomic composition of the surface is shown in Figure 5.4. The highest angle that could be further

tilted without releasing the sample from the manipulator was 70°.

As the grazing angle increases from 30° to 60°, the atomic composition of In and Ni remains unchanged. The concentration of In would be expected to increase with the grazing angle if it were only present in the topmost layer.

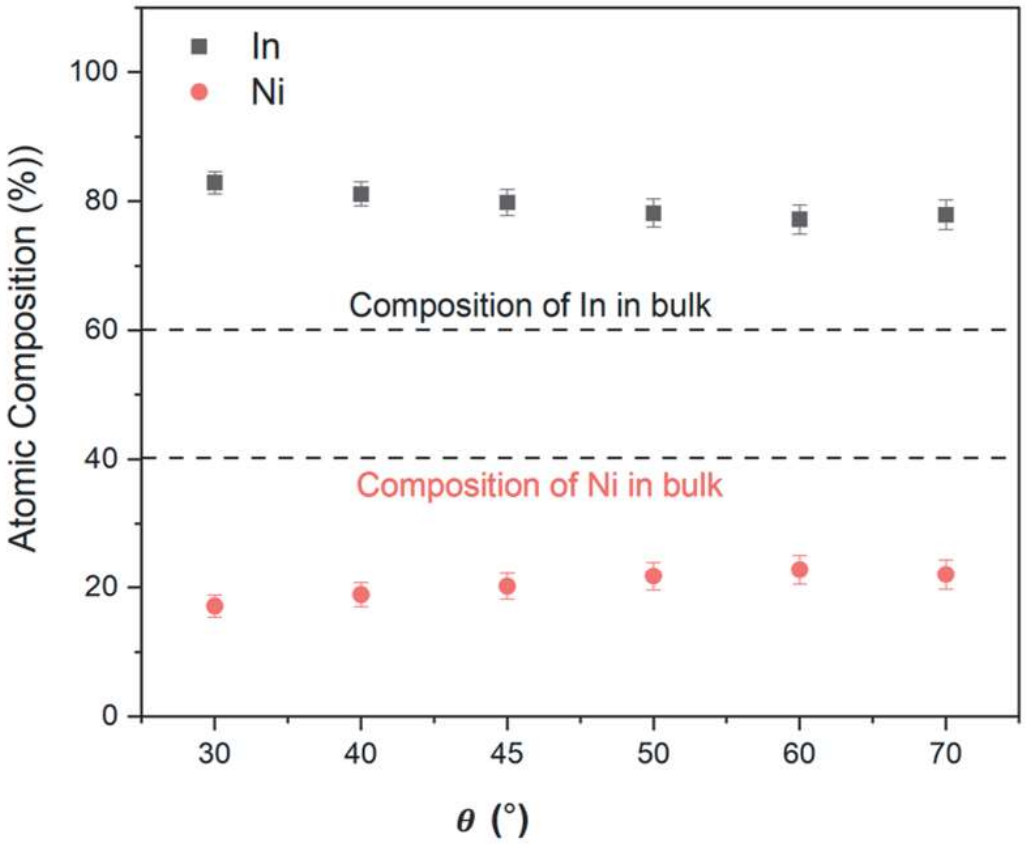


Figure 5.4: Surface chemical composition of the $(2\bar{1}0)$ surface determined by XPS after sputtering and annealing at 560 °C, measured at various scan angles from 30° to 70°. Dotted lines indicate the bulk composition of In and Ni.

5.4.2 Elemental Information Studied by LEIS

We used LEIS to obtain elemental information about the crystal's topmost atomic layer after cleaning the surface by sputtering and annealing at temperatures ranging from 200 °C to 480 °C, whereas XPS provided information on the chemical composition over several atomic layers of the surface. This complementary use of LEIS and XPS enabled a comprehensive characterisation of both the surface and near-surface regions of the sample.

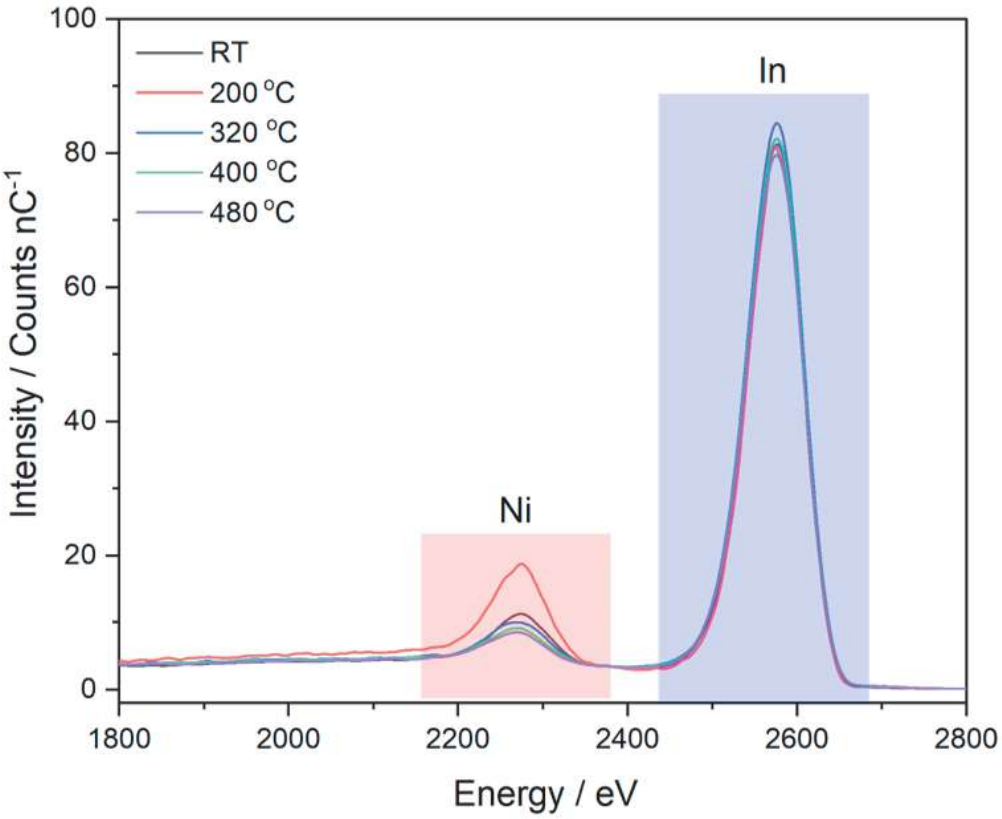


Figure 5.5: LEIS spectra obtained from the $In_3Ni_2(2\bar{1}0)$ surface after cleaning the surface by sputtering and annealing at selected temperatures for one hour, employing a 3 keV He^+ ion beam. The highlighted energy regions associated with each surface peak indicate the limits used for background correction.

Initially, the sample was freshly prepared through two cycles of sputtering and annealing. Sputtering was performed using a 1 keV Ar^+ ion beam directed over a (2×2) mm area. The sputtering process was continued until the LEIS spectra stabilised, indicating that surface contaminants had been completely removed. Following sputtering, the sample was annealed at 400 °C for 45 minutes and then cooled to room temperature over two hours. Subsequently, the surface was subjected to an additional 30-minute exposure to the sputter beam, resulting in a total ion dose of 2.28×10^{15} Ar^+ ions, and annealed at 480 °C temperature. After surface preparation, LEIS spectra were acquired to determine the composition of the topmost atomic layer.

Figure 5.5 presents LEIS spectra illustrating the effects of sputtering and annealing at

varying temperatures on the surface composition of $In_3Ni_2(100)$. Annealing up to 480 °C led to a marked increase in the In signal and a reduction in the Ni signal, suggesting a temperature-dependent redistribution of surface atoms.

Sputtering (Depth Profile)

The effect of Ar^+ ion sputtering dose (depth profiling) on the surface intensities of In and Ni was systematically examined. Following surface preparation with sputtering and annealing at 400 °C for one hour, the sample was cooled to room temperature, and LEIS spectra were recorded.

The evolution of LEIS intensity for In and Ni peaks as a function of increasing ion dose is presented in Figure 5.6 (a). To determine the spectral intensities, a two-point linear background subtraction was applied within the relevant energy ranges.

At the lowest sputtering dose, the In signal dominates, indicating an In-terminated top of the surface. With continued ion sputtering, a decrease in In intensity and an increase in Ni intensity were observed, suggesting preferential sputtering of In atoms. Upon reaching a high ion dose, both signals plateaued, signifying a steady-state surface composition, beyond which further sputtering had a negligible influence on the detected elements.

As shown in Figure 5.6 (c), the In-to-Ni intensity ratio was initially high, consistent with an In-rich surface following cleaning. However, with increasing sputtering, a decline in In intensity was noted, confirming the preferential removal of In. This observation was corroborated by XPS analysis, which also indicated selective sputtering of In. Eventually, both signals stabilised, indicating the formation of a compositionally stable surface.

Annealing Temperatures Dependent

Following annealing of the surface at each temperature between 200 °C and 480 °C for 45 minutes, LEIS spectra were collected to evaluate the surface composition of In and Ni. Figure 5.6 (b) displays the variation in signal intensities as a function of annealing

temperature. An increase in In intensity and a corresponding decrease in Ni intensity were observed up to approximately 320 °C, beyond which both signals showed a slight decline despite further temperature increases. This behaviour is attributed to thermally induced reduction in surface atomic density caused by lattice expansion at high temperatures from 340 °C to 480 °C. The spectra were acquired *in situ*, ensuring an accurate assessment of the surface composition. Figure 5.6 (d) shows that the In/Ni intensity ratio increases with temperature, indicating preferential surface segregation of In during thermal treatment.

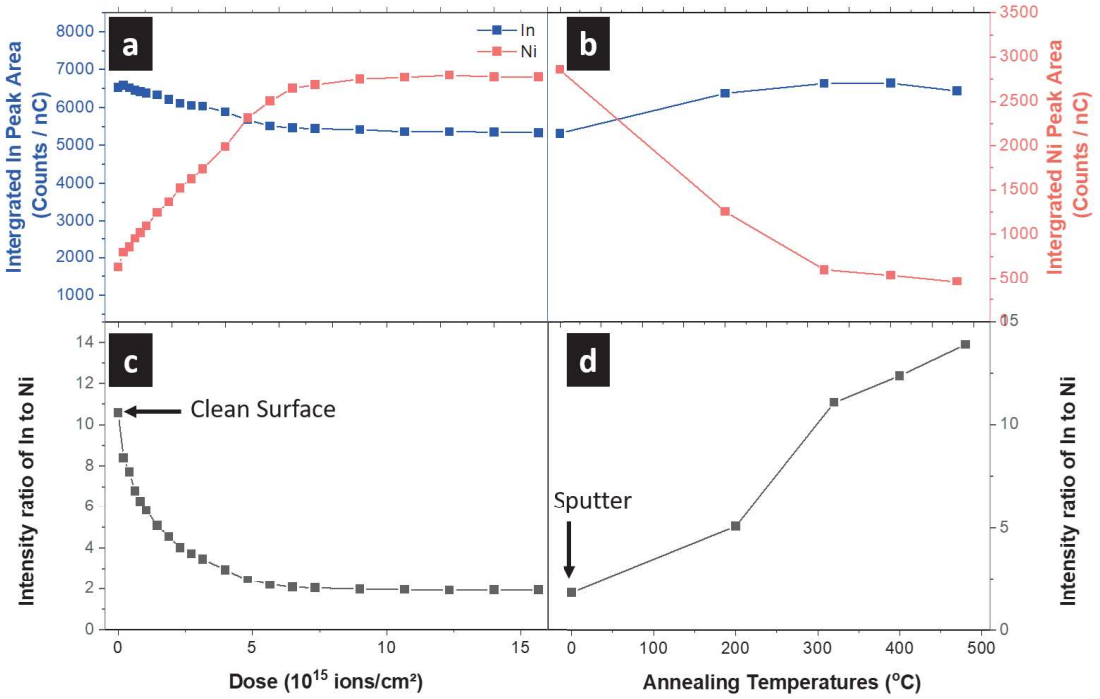


Figure 5.6: (a) The variation in the integrated In and Ni intensities in LEIS from the In and Ni $(2\bar{1}0)$ surface due to sputtering at different ion doses. (b) Annealing at various temperatures, along with the In to Ni intensity ratio following the respective treatments (c, d).

5.4.3 Atomic Structure Studied by LEED and STM

After sputtering and annealing the surface up to 500 °C, LEED patterns were obtained using a computer-controlled data collection system and a charge-coupled device (CCD)

camera within an energy range of 10–140 eV.

A temperature lower than 330 °C was insufficient to achieve surface ordering, so there were no LEED patterns visible from the surface.

After annealing the surface at 340 °C, a (1×1) LEED pattern with rectangular symmetry was observed, corresponding to the surface unit cell expected from the bulk. Long-range surface order with low background intensity indicates a high-quality structural surface.

To determine the lattice parameters of the $In_3Ni_2(2\bar{1}0)$ surface, we used the Ag (100) surface as a calibration reference. Specifically, the two reciprocal lattice vectors, $|b^*{}_1|$ and $|b^*{}_2|$, extracted from the LEED patterns of the $In_3Ni_2(2\bar{1}0)$ surface were compared with those obtained from an Ag(100) surface. Both LEED patterns were acquired using the same experimental setup and an incident electron beam energy of approximately 60 eV, ensuring consistency in the measurement conditions and allowing for accurate calibration of the lattice constants.

The bulk values predicted for the $In_3Ni_2(2\bar{1}0)$ surface are $|b_1| = 5.295$ Å and $|b_2| = 7.690$ Å. From the LEED measurements, the corresponding lattice constants determined in real space were $|b_1| = 5.21 \pm 0.2$ Å and $|b_2| = 7.58 \pm 0.2$ Å, which are in good agreement with the theoretical values. These results confirm that the observed LEED pattern corresponds to a (1×1) surface structure.

Effect of Annealing Temperature and Beam Energies

Figure 5.7 (a-f) demonstrates that there is no evidence of surface reconstruction or phase transitions, as the surface consistently exhibits a (1×1) pattern within the temperature range of 360 to 520 °C. The (1×1) pattern remains stable when placed at a UHV pressure of 10^{-10} mbar. This behaviour is similar to observations on PdGa(111) ZnPd, and InNi(110)surfaces, which also maintain unreconstructed [38, 45, 60].

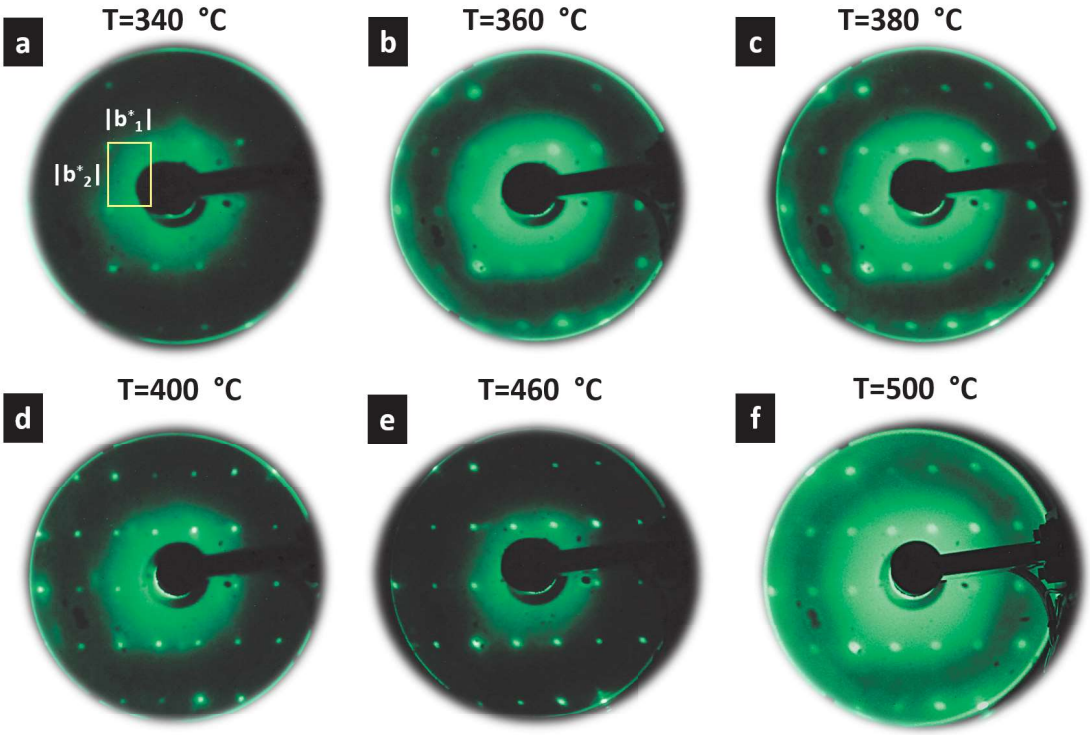


Figure 5.7: (1×1) LEED patterns from $(2\bar{1}0)$ surface at beam energy 45 eV after freshly prepared by sputtering and annealing at (a) 340 °C. (b) 360 °C. (c) 380 °C. (d) 400 °C. (e) 460 °C. (f) 500 °C.

After each preparation cycle (sputtering and annealing), LEED patterns were recorded for a range of beam energies, from 10 to 140 eV. In particular, following annealing of the surface at 500 °C, well-defined LEED patterns were observed over the beam energy range of 15 eV to 135 eV, indicating the order of the surface and the presence of a crystalline surface structure. Figure 5.8 (a–f) illustrates the LEED pattern of the surface at selected beam energies; the symmetry pattern remains unchanged at different beam energies.

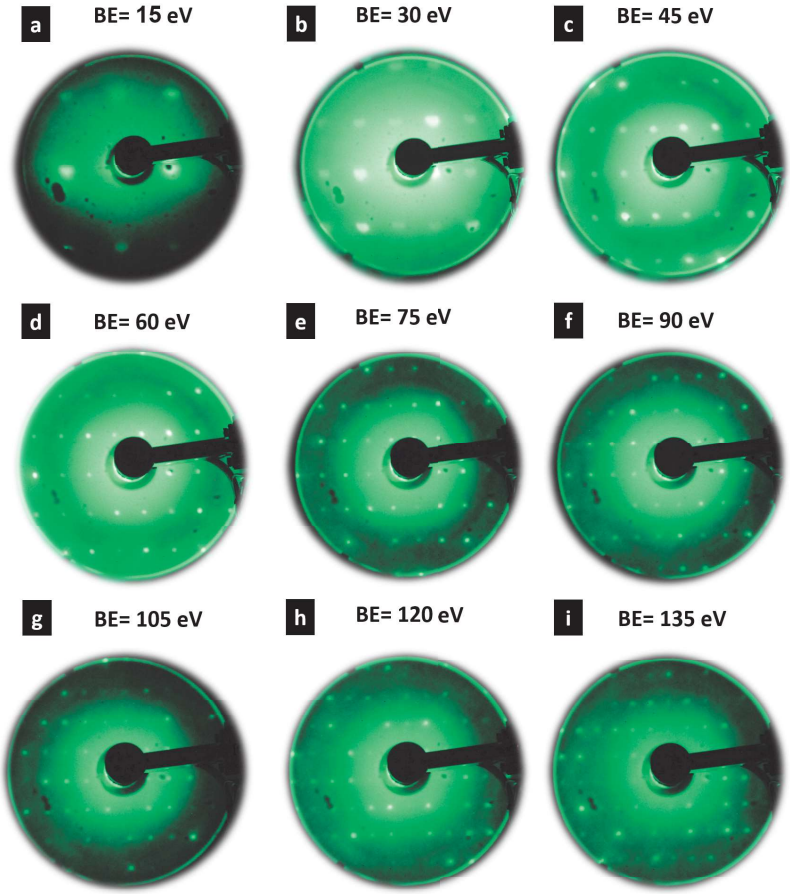


Figure 5.8: LEED patterns of the $(2\bar{1}0)$ surface after annealing at 500 °C, recorded at beam energies: (a) 15 eV, (b) 30 eV, (c) 45 eV, (d) 60 eV, (e) 75 eV, (f) 90 eV, (g) 105 eV, (h) 120 eV, and (i) 135 eV.

In comparison, LEED studies on $Ga_3Ni_2(2\bar{1}0)$ show different behaviour in terms of surface ordering. The $(2\bar{1}0)$ surface typically exhibits a (1×1) LEED pattern after annealing the surface at low temperatures around 320 °C, which cannot remain stable at high annealing temperatures; there is a (2×2) LEED pattern after annealing the surface at higher temperatures around 522 °C [117]. Furthermore, the intensity of the spots in $Ga_3Ni_2(2\bar{1}0)$ also changes with the beam energy, but the symmetry and overall structure of the LEED pattern tend to remain consistent, similar to the observations in this study.

The experiment was repeated by sputtering in Ar^+ for 30 minutes, then annealing for 2 hours at 400 °C. A LEED pattern from most parts of the surface remains unchanged,

but at the edge of the surface, there are additional low-intensity spots, as marked by red circles, moving in the opposite direction to the substrate spot movement with different beam energies, attributed to facets (Figure 5.9). However, the quality of LEED from these facets is insufficient for further examination of their direction and structure.

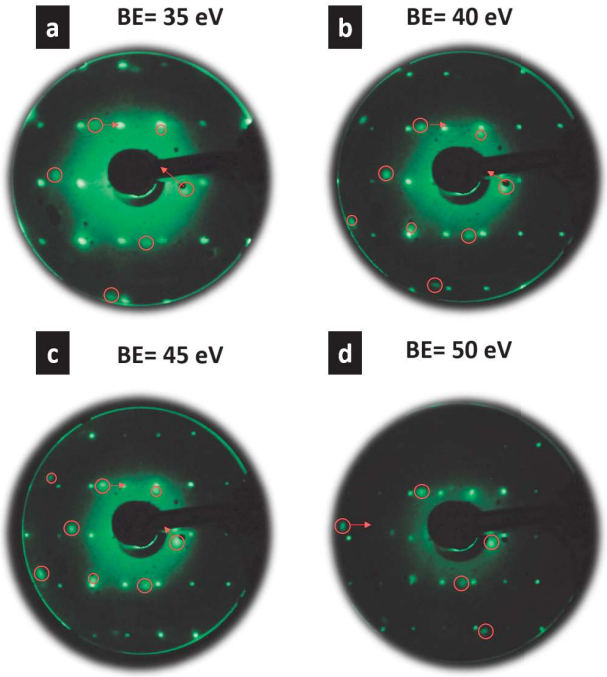


Figure 5.9: LEED patterns of the clean $In_3Ni_2(2\bar{1}0)$ surface recorded at different electron beam energies: (a) 35 eV. (b) 40 eV. (c) 45 eV. (d) 50 eV. Faceted diffraction spots, indicated by red circles, exhibit a downward shift with increasing beam energy.

We examined the sample quality by measuring back-reflection Laue X-ray diffraction from various surface regions. The main part of the sample exhibits a Laue pattern characteristic of a single crystal with $In_3Ni_2(2\bar{1}0)$ orientation. However, at the edge of the sample, a polycrystalline In_3Ni_2 structure is observed, as shown in Figure 5.10. The sample edges generated a weak Laue pattern. Because of this, we were unable to confirm whether the facets are due to a miscut of the surface.

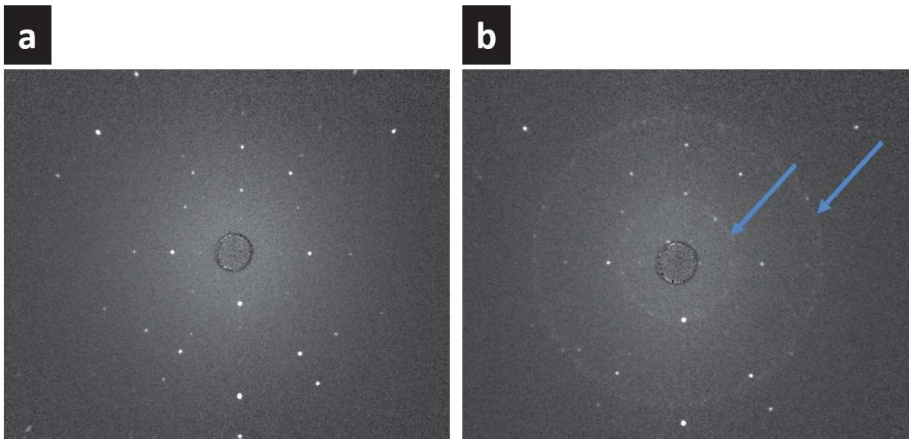


Figure 5.10: (a) Representative Laue back scattering image taken from the most part of the surface reflecting the symmetry expected from the bulk. (b) Laue back scattering image from the edge of sample showing a diffuse rings.

STM

Following the acquisition of LEED data, the surface was annealed at various temperatures ranging from 420 to 540 °C for durations between one and five hours. Subsequently, STM measurements were performed. The STM was operated in constant-current mode at room temperature, with a tunnelling current of approximately 0.645 nA and a bias voltage varying between -1.8 V and +1.8 V.

No step-terrace morphology appeared until annealing at 530 °C. At that temperature, well-defined flat step terraces were apparent. Most of the $(2\bar{1}0)$ surfaces showed a large area of stepped terraces after annealing at temperatures above 550 °C. Terraces with dimensions of up to 1500 Å$\times$1500 Å have been identified.

Figure 5.11 (a) presents an STM image taken after annealing at 540 °C, revealing large flat terraces. The step height is determined from a histogram of the height distribution near the steps, and the findings are confirmed by line scans. The distribution of step heights along the blue arrow in Figure 5.11 (a) is shown in Figure 5.11 (b). The step height can be defined as the difference between the nearest peak positions in the histogram (Figure 5.11 (c)).

We used STM images acquired from various surface regions to examine over 80 steps, enhancing statistical reliability. As demonstrated in Figure 5.11 (d), the most commonly observed step height is 2.3 $\pm$ 0.02 Å, which is half the value of the lattice constant, a = 4.39 Å.

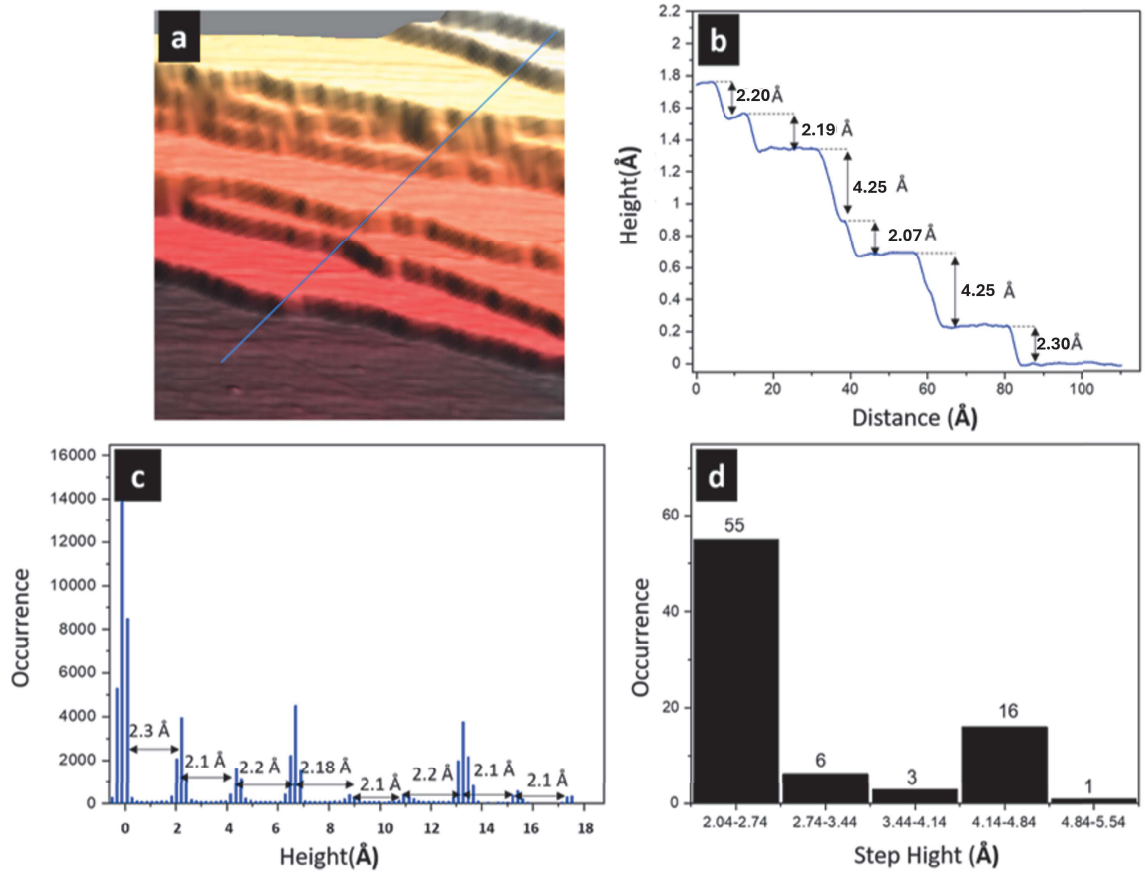


Figure 5.11: (a) STM image taken from the $In_3Ni_2(2\bar{1}0)$ surface after several cycles of sputtering and annealing (a) At 540 °C , (875 Å$\times$1127 Å, + 0.510 V, 0.448 nA), demonstrating steps of different heights. (b) Height distribution along a blue line in (c) Crossing the steps. Steps heights are given. (d) The histogram of height distribution in the vicinity of the steps.

The structure of the clean $(2\bar{1}0)$ surface was deduced from atomic-resolution STM images of typical areas measuring 180 Å$\times$180 Å and 300 Å$\times$300 Å taken at a variety of bias voltages, from -1.8 V to +1.8 V. Figures 5.12 (a) and (b) provide high-resolution STM images of the structure. Two lattice constants have been determined from line profiles. The separations along the [001] and [120] directions are $|b_1| = 7.72 \pm 0.04$ Å and $|b_2| = 5.23$

$\pm$ 0.2 Å, respectively. The lattice constants obtained from the STM measurements were found to be compatible with those of $In_3Ni_2(2\bar{1}0)$, measuring 5.29 Å and 7.69 Å (Figures 5.12 (d)). The FFT of Figure 5.12 (b) is depicted in Figure 5.12 (c), confirming the rectangular symmetry. We used the FFT pattern to calculate the characteristics of the real-space unit cell, $|b_1| = 7.21 \pm 0.04$ Å and $|b_2| = 5.60 \pm 0.2$ Å. A yellow rectangle represents the unit cell of the surface. The FFT pattern of the STM image is very similar to the LEED patterns, confirming that the structure of the $(2\bar{1}0)$ surface is (1×1).

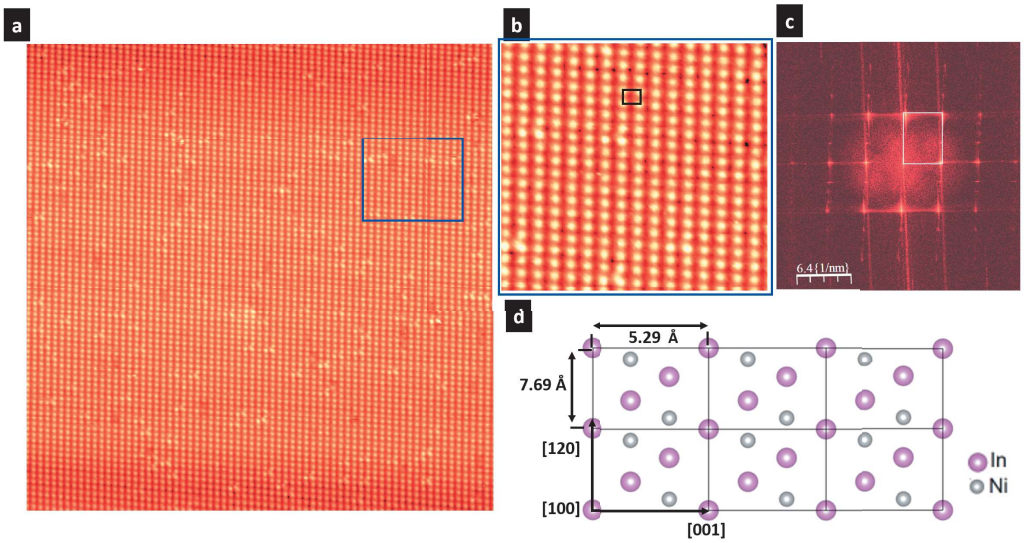
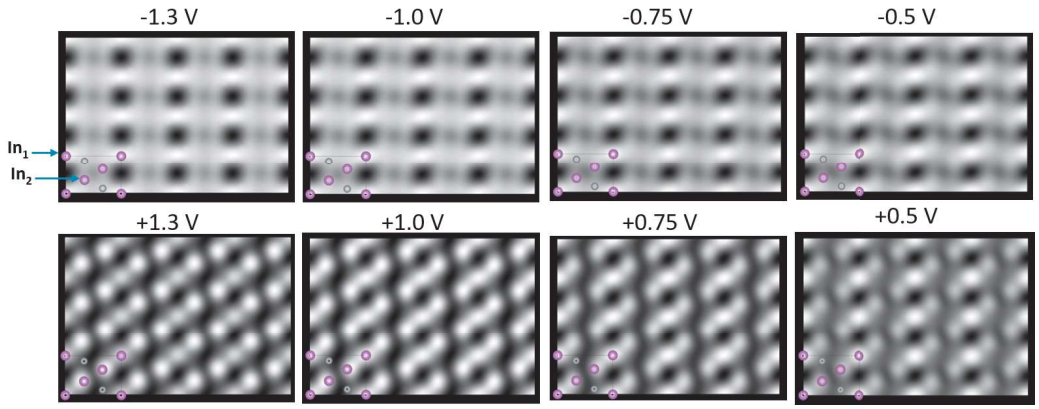


Figure 5.12: (a) and (b) STM images of In_3Ni_2 $(2\bar{1}0)$ surface showing atomic resolution after sputter and annealing it at 560 °C (500 Å × 500 Å, - 1.8 eV, 0.645 nA). (b) STM images (120 Å × 120 Å, - 1.8 eV, 0.645 nA). (c) The FFT pattern of Figure (b) shows a rectangle pattern. (d) The top view of $In_3Ni_2(2\bar{1}0)$ surface.

The effect of the bias voltage on the contrast of atomic sites In_1, In_2 and Ni on the $(2\bar{1}0)$ surface is clearly illustrated in the local density of states, which is calculated by E. Gaudry [125] and quantified in the accompanying contrast table in Figure 5.13. Across the bias range from -1.3 V to +1.3 V, a systematic evolution in site-specific contrast is observed, reflecting changes in the local density of states (LDOS) in each image.



Bias Voltage	In_1	In_2	Ni
-1.3 V	High	Low	Low
-1.0 V	High	Low	Low
-0.75 V	High	Low	Low
-0.5 V	High	Low	Zero
+0.5 V	High	Low	Zero
+0.75 V	High	High	Zero
+1.0 V	Low	High	Zero
+1.3 V	Low	High	Zero

Figure 5.13: Bias dependent STM images and corresponding local density of states (LDOS) contrast table for the In_3Ni_2 $(2\bar{1}0)$ surface [125]. The figures shows STM images at bias voltages ranging from –1.3 V to +1.3 V, highlighting the bias induced contrast variation of In_1, In_2, and Ni atomic sites within the model surface unit cell. The labelled sites (In_1, In_2) are marked for reference. The bottom panel summarises the observed relative contrast levels at each atomic site as a function of applied bias voltage, serving as a qualitative proxy for site specific LDOS. High and Low denote strong and weak contrast respectively, while zero indicates no observable contribution at that site [106].

At negative bias voltages (-1.3 V to -0.5 V), the In_1 site, which is located at the corner of the bulk model, consistently appears with high contrast, while the In_2 site, which is in the middle of the bulk model, exhibits low contrast. This indicates a higher occupied LDOS at In_1 compared to In_2 within this energy range. The Ni site demonstrates low contrast at more negative biases (-1.3 to -0.75 V), but transitions to zero contrast at -0.5 V, suggesting a depletion of the occupied LDOS as the Fermi level is approached.

As the bias is shifted to positive values (+0.5 V to +1.3 V), the contrast behaviour of In_1 and In_2 reverses. In_1 becomes low in contrast, while In_2 becomes more clear at +1 V and +1.3 V. This inversion suggests that the unoccupied LDOS is greater at In_2 than at In_1 within the positive bias range. Although the Ni site consistently maintains zero contrast throughout all positive bias voltages, there is a negligible contribution to the unoccupied LDOS within this range. In particular, the contrast is similar for In_1 and In_2 around +0.75 V, with both becoming bright.

We now compare LDOS calculations with STM images across a range of bias voltages to investigate the voltage-dependent surface characteristics of the $In_3Ni_2(2\bar{1}0)$ surface. All measurements were performed in specific surface regions with consistent tip conditions, ensuring the reliability of contrast and resolution comparisons across different tunnelling biases. Four distinct STM images with atomic characteristics were identified between -1.8 V and +1.8 V. By overlapping the structural unit cell model with the STM images, we were able to identify features related to individual atoms.

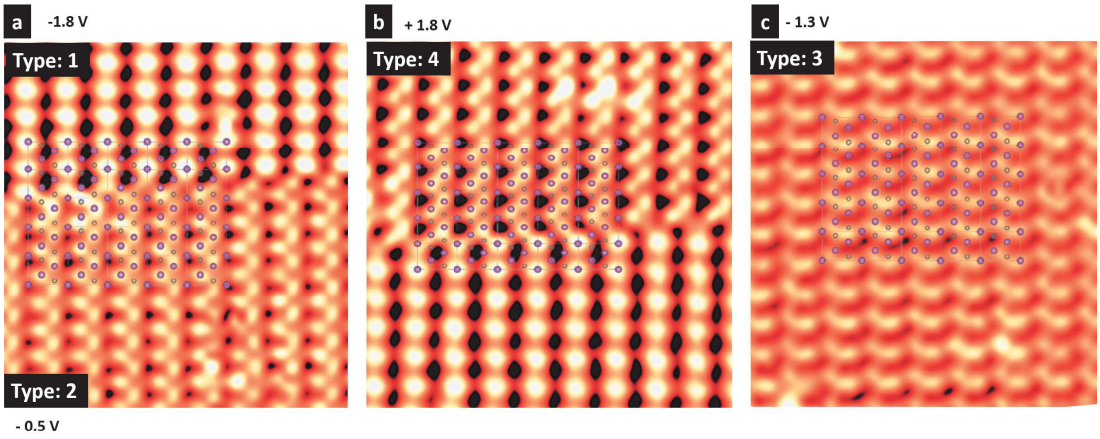


Figure 5.14: STM images of the In_3Ni_2 $(2\bar{1}0)$ surface under different bias voltages, overlaid with the atomic model of the surface structure. (a) Image at -1.8V, highlighting enhanced contrast at In_1 atoms, consistent with a higher local density of occupied states. while image at -1.8 V, where contrast shifts to In_2 atoms, reflecting enhanced unoccupied states at these sites. Ni atoms remain relatively low in contrast under both conditions, indicating a minimal contribution to the LDOS near the Fermi level. (b) STM image at +1.8V, highlighting enhanced contrast at In_1 atoms, consistent with a higher local density of occupied states and low contrast at In_2 atoms. (c) STM image at -1.3V, highlighting enhanced contrast at In_1 In_2 and Ni atoms.

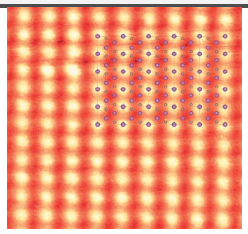
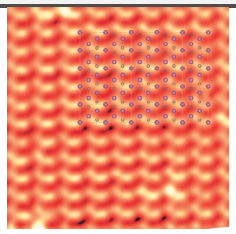
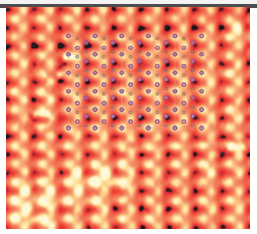
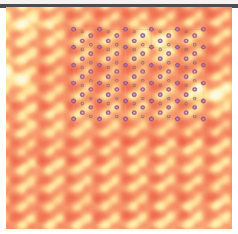
Type	1	2
Bias Voltage	$-1.8\,\mathrm{V} \leq V \leq -1.4\,\mathrm{V}$	$-1.3\,\mathrm{V} \leq V \leq -0.5\,\mathrm{V}$
Figure		
Type	**3**	**4**
Bias Voltage	$-0.4\,\mathrm{V} \leq V \leq +0.9\,\mathrm{V}$	$+1\,\mathrm{V} \leq V \leq +1.8\,\mathrm{V}$
Figure		

Table 5.2: STM image of the In_3Ni_2 $(2\bar{1}0)$ surface overlaid with the atomic model of the surface structure.

Figure 5.15 and Table 5.2 representative STM images of the In_3Ni_2 $(2\bar{1}0)$ surface in the bias voltage range of $-1.8\,\mathrm{V} \leq V \leq -1.4\,\mathrm{V}$, $-1.3\,\mathrm{V} \leq V \leq -0.5\,\mathrm{V}$, $-0.4\,\mathrm{V} \leq V \leq +0.9\,\mathrm{V}$, and $+1\,\mathrm{V} \leq V \leq +1.8\,\mathrm{V}$ each STM images in the different bias voltage overlaid with atomic structural models.

STM images under negative bias for the sample ranging from –1.8 V to –1.4 V are shown in Figure 5.2 (a), where enhanced contrast is observed predominantly at the In_1 sites. This corresponds to a higher local density of occupied states at these positions, while Ni sites remain weakly resolved due to their negligible LDOS near the Fermi level, which is in agreement with the trends summarised in the LDOS contrast table. Under positive bias from +1.0 V to +1.8 V, the contrast shifts significantly towards the In_2 atoms, reflecting their increased contribution to the unoccupied states. Figure 5.2 (b), recorded at intermediate bias voltages between –0.4 V and +0.9 V, reveals sustained brightness at the In_1 positions, reinforcing the predominance of these sites in the tunnelling current within

this range. Finally, Figure 5.2 (c) displays a STM image under near zero bias conditions, where contrast across the In_2 and Ni is reduced.

This finding is consistent with previous observations on PdZn surfaces where limited atomic contrast was observed on the (110) facet and bias dependent STM imaging revealed that Pd 4d states near the Fermi level dominated the tunnelling current [45]. Our study on In_3Ni_2 surfaces similarly demonstrates strong bias dependent contrast between In_1 and In_2 atoms, attributable to their distinct local densities of states (LDOS). In both systems, one element (Pd or In) primarily contributes to the tunnelling current. This behaviour is in good agreement with our LDOS calculations, as illustrated in Figure 5.15.

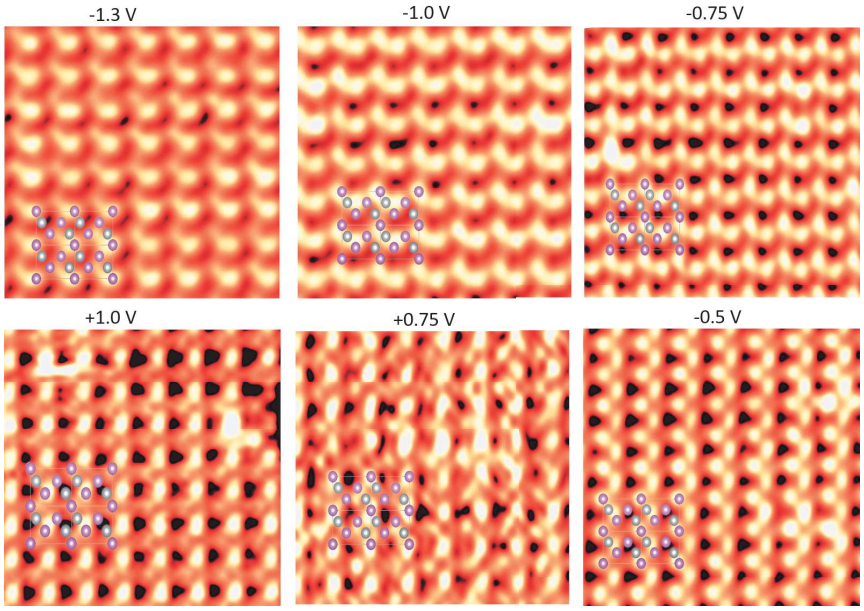


Figure 5.15: STM images of the $(2\bar{1}0)$ surface with various voltage bias (a) At $-1.8\,\mathrm{V} \leq V \leq -1.4\,\mathrm{V}$.(b)At $-1.3\,\mathrm{V} \leq V \leq -0.5\,\mathrm{V}$. (c) At $-0.4\,\mathrm{V} \leq V \leq +0.9\,\mathrm{V}$(d).

5.4.4 Oxidation Behaviour

We have investigated surface oxidation using the introduction of varying amounts of oxygen gas, with a purity of 99.999%, into UHV via a leak valve. Before cleaning, the sample was exposed to air for a duration of 10 days, after which XPS spectra were obtained. Subsequently, the surface was cleaned using Ar^+ sputtering followed by annealing at a high

temperature of approximately 560 °C. Then, 300 to 900 L of oxygen were dosed, and the results were examined using XPS.

XPS spectra for the In $3d_{5/2}$, Ni $2p_{3/2}$, and O $1s$ core levels on the surface under different conditions (cleaned, oxygen-exposed, and air-exposed) are presented in Figures 5.16(a–c). Upon exposure to controlled doses of oxygen, minor changes are observed in the In $3d_{5/2}$ and O $1s$ core level spectra, indicating limited surface oxidation, while there is no change in the Ni $2p_{3/2}$ core level spectra. However, after air exposure, a shift in the In $3d_{5/2}$ and O $1s$ core level spectra is evident, particularly in the increased broadening of the oxide-related features. These spectral changes clearly reflect a higher degree of surface oxidation in the air-exposed samples compared to those exposed solely to oxygen under vacuum conditions.

The detailed spectral evolution is further illustrated in Figures 5.16 (d–f), where the intensities of the In $3d_{5/2}$, Ni $2p_{3/2}$, and O $1s$ core level spectra have been normalised between 0 and 1 to highlight the development of shoulder features associated with oxidation. In particular, the shoulder appearing on the In $3d_{5/2}$ and Ni $2p_{3/2}$ peaks is clearly observed, providing compelling evidence of In and Ni oxide formation. These observations are corroborated by the O $1s$ spectra, which display characteristic peak shapes and shoulder positions corresponding to both oxygen and oxide species. A comprehensive analysis of these spectral features provides insight into the stepwise oxidation process that occurs at the surface.

Notably, following exposure of the $In_3Ni_2(2\bar{1}0)$ surface to air, the shoulder features in the In $3d_{5/2}$, Ni $2p_{3/2}$, and O $1s$ spectra become the dominant features (Figure 5.16 (d–f)), confirming extensive oxidation at the surface. Furthermore, clear shifts in the binding energies of the In $3d_{5/2}$ and O $1s$ peaks are observed, to 444.5 eV and 531 eV, respectively. These shifts provide evidence for the formation of oxidised species. For Ni $2p_{3/2}$, there is no clear binding energy shift, but an additional peak appears, related to Ni oxides.

Figure 5.15 and Table 5.2 present representative STM images of the In_3Ni_2 $(2\bar{1}0)$ surface

in the bias voltage ranges of $-1.8\,\mathrm{V} \leq V \leq -1.4\,\mathrm{V}$, $-1.3\,\mathrm{V} \leq V \leq -0.5\,\mathrm{V}$, $-0.4\,\mathrm{V} \leq V \leq +0.9\,\mathrm{V}$, and $+1\,\mathrm{V} \leq V \leq +1.8\,\mathrm{V}$, with each STM image at different bias voltages overlaid with atomic structural models.

STM images under negative bias for the sample ranging from –1.8 V to –1.4 V are shown in Figure 5.2 (a), where enhanced contrast is observed predominantly at the In_1 sites. This corresponds to a higher local density of occupied states at these positions, while Ni sites remain weakly resolved due to their negligible LDOS near the Fermi level, which is in agreement with the trends summarised in the LDOS contrast table. Under positive bias from +1.0 V to +1.8 V, the contrast shifts significantly towards the In_2 atoms, reflecting their increased contribution to the unoccupied states.

Figure 5.2 (b), recorded at intermediate bias voltages between –0.4 V and +0.9 V, reveals sustained brightness at the In_1 positions, reinforcing the predominance of these sites in the tunnelling current within this range.

Finally, Figure 5.2 (c) displays an STM image under near-zero bias conditions, where contrast across the In_2 and Ni sites is reduced.

This finding is consistent with previous observations on PdZn surfaces, where limited atomic contrast was observed on the (110) facet and bias-dependent STM imaging revealed that Pd 4d states near the Fermi level dominated the tunnelling current [45]. Our study on In_3Ni_2 surfaces similarly demonstrates strong bias-dependent contrast between In_1 and In_2 atoms, attributable to their distinct local densities of states (LDOS). In both systems, one element (Pd or In) primarily contributes to the tunnelling current. This behaviour is in good agreement with our LDOS calculations, as illustrated in Figure 5.15.

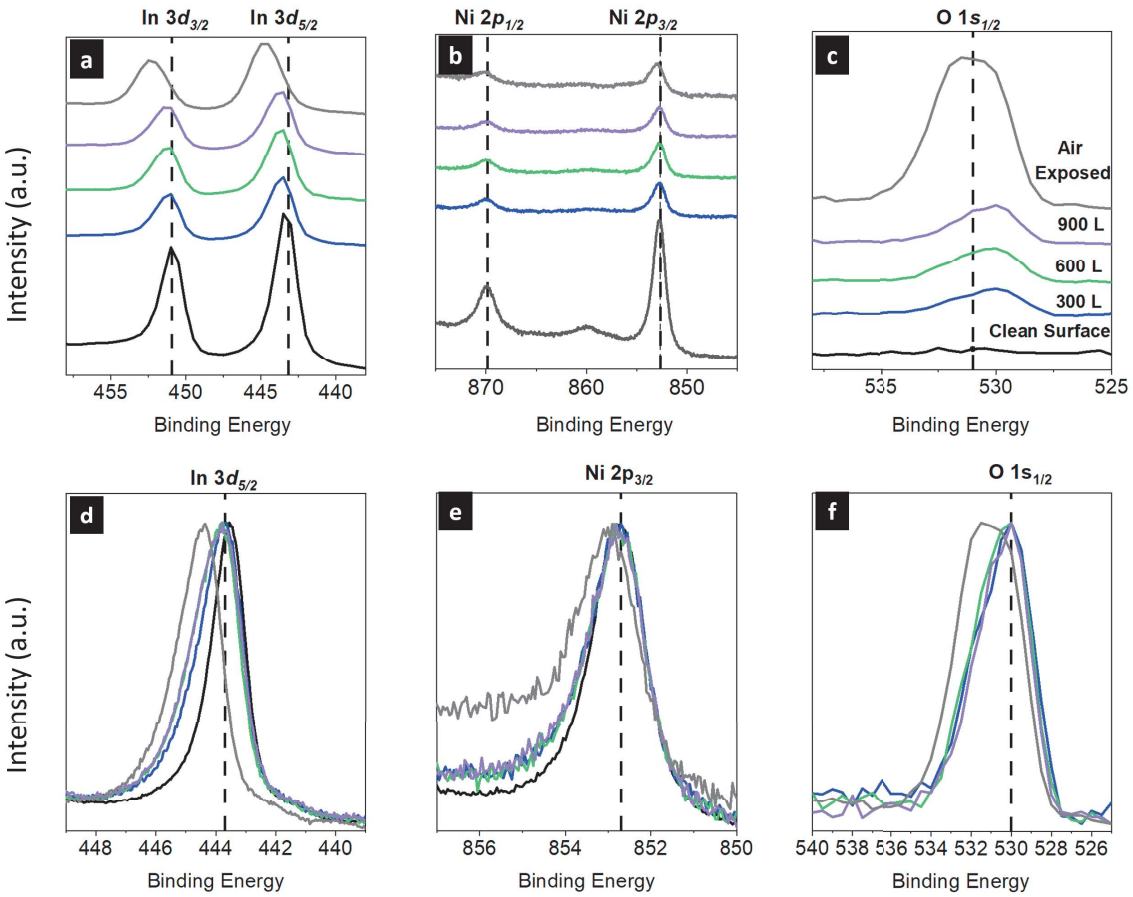


Figure 5.16: (a) to (c) XPS spectra from clean (after annealing at 560 °C), oxygen exposed and air exposed of $In_3Ni_2(2\bar{1}0)$ surface (a: In 3*d*, b: Ni 2*p*, and c: O 1*s*). Oxygen exposure was from 300 L-900 L. (d,e) In $3d_{5/2}$ and Ni $2p_{3/2}$ spectra, respectively, after normalizing minimum and maximum intensity between 0 and 1, illustrating the development of a shoulder at higher binding energy . The dotted, dashed, and dash dotted lines at 530.2 eV, 531.0 eV, and 531.6 eV in (f) correspond to the positions of the oxide, pure oxygen, and Ni oxide peaks, as reported in the literature [121, 122] respectively. The dashed lines in (c) marks the positions of the core levels of the respective elements from the clean surface.

The spectra were analysed by applying a Shirley background subtraction combined with a fitting procedure that employed asymmetric Gaussian–Lorentzian line shapes to accurately determine the peak positions and intensities, including shoulder features. The fitting model used a composite line shape comprising 40% Gaussian and 60% Lorentzian contributions to best represent the spectral profiles. Representative fitting procedures for the In $3d_{5/2}$ and Ni $2p_{3/2}$ core level spectra are illustrated in Figures 5.17 (a–e) and 5.18

(a–e), respectively. Throughout this thesis, all reported peak positions were obtained using this fitting methodology. The estimated uncertainty in the peak positions is approximately $\pm$ 0.1 eV.

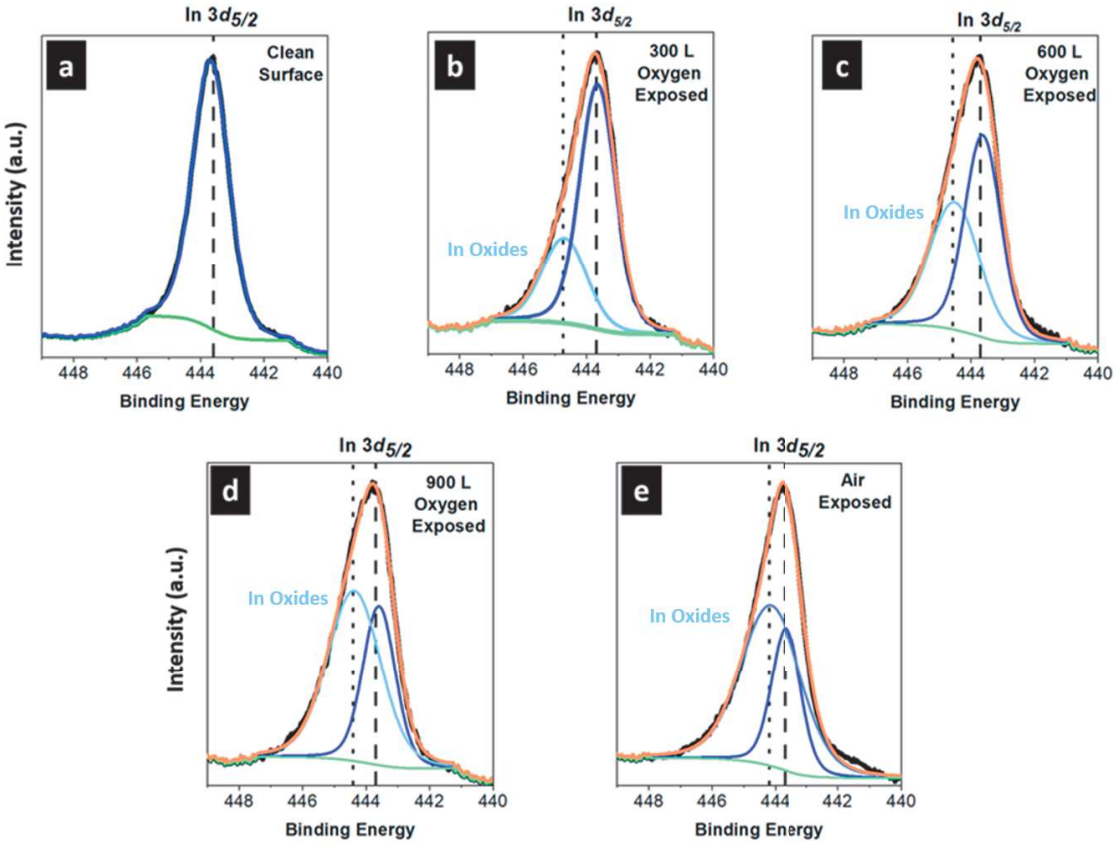


Figure 5.17: XPS spectra of the $In_3Ni_2(2\bar{1}0)$ surface after air exposure and cleaning of the surface by sputtering and annealing at 560 °C and with increasing oxygen exposure (300 L-900 L). Vertical dashed lines in all spectra correspond to the core level position of clean In $3d_{5/2}$.

The In $3d_{5/2}$ and Ni $2p_{3/2}$ core levels appear as single peaks at binding energies of 443.6 eV and 852.5 eV, respectively, on the clean surface, as shown in Figure 5.17 (a) and Figure 5.18 (a). These peak positions closely match those reported for In [112] and Ni [111].

The XPS spectra shown in Figures 5.17 (b–e) depict the evolution of the In $3d_{5/2}$ core level with increasing oxygen exposure, highlighting the chemical change from pure In to In oxide. After exposure to 300 L of oxygen (Figure 5.17 (b)), an additional compo-

nent appears at a higher binding energy (444.6 eV), attributed to In_2O_3 [112]. The oxide peak increases during 600 L and 900 L exposures (Figures 5.17 (c) and (d)), exhibiting a significant increase in intensity compared to pure In, which indicates increased surface oxidation. In the sample exposed to air (Figure 5.17 (e)), the oxide component dominates the spectrum, and the pure In peak is markedly reduced, indicating significant oxidation. The spectral changes indicate a transition from pure In to In_2O_3 with increasing oxygen exposure, characterised by a systematic increase in the intensity of the oxide peak and an associated decrease in the pure In peak.

The XPS spectra presented in Figures 5.18 (b–f) illustrate the evolution of the Ni $2p_{3/2}$ core level as a function of increasing oxygen exposure, providing evidence for the coexistence of pure Ni and Ni oxide species on the surface. Upon exposure to 300 L of oxygen (Figure 5.18 (b)), an additional peak emerges at a higher binding energy of approximately 854.1 eV, which is characteristic of NiO formation [111]. With further oxygen exposure of 600 L and 900 L (Figures 5.18 (c) and (e)), the intensity of the NiO-related peak increases, accompanied by a concurrent reduction in the pure Ni peak, indicating progressive surface oxidation. In the case of the air-exposed sample (Figure 5.18 (f)), the NiO peak remains present but is largely unchanged in intensity. In particular, a new feature appears at a binding energy of approximately 855.5 eV, which is attributed to the formation of nickel hydroxide $Ni(OH)_2$ [111], suggesting further surface modification due to prolonged air exposure.

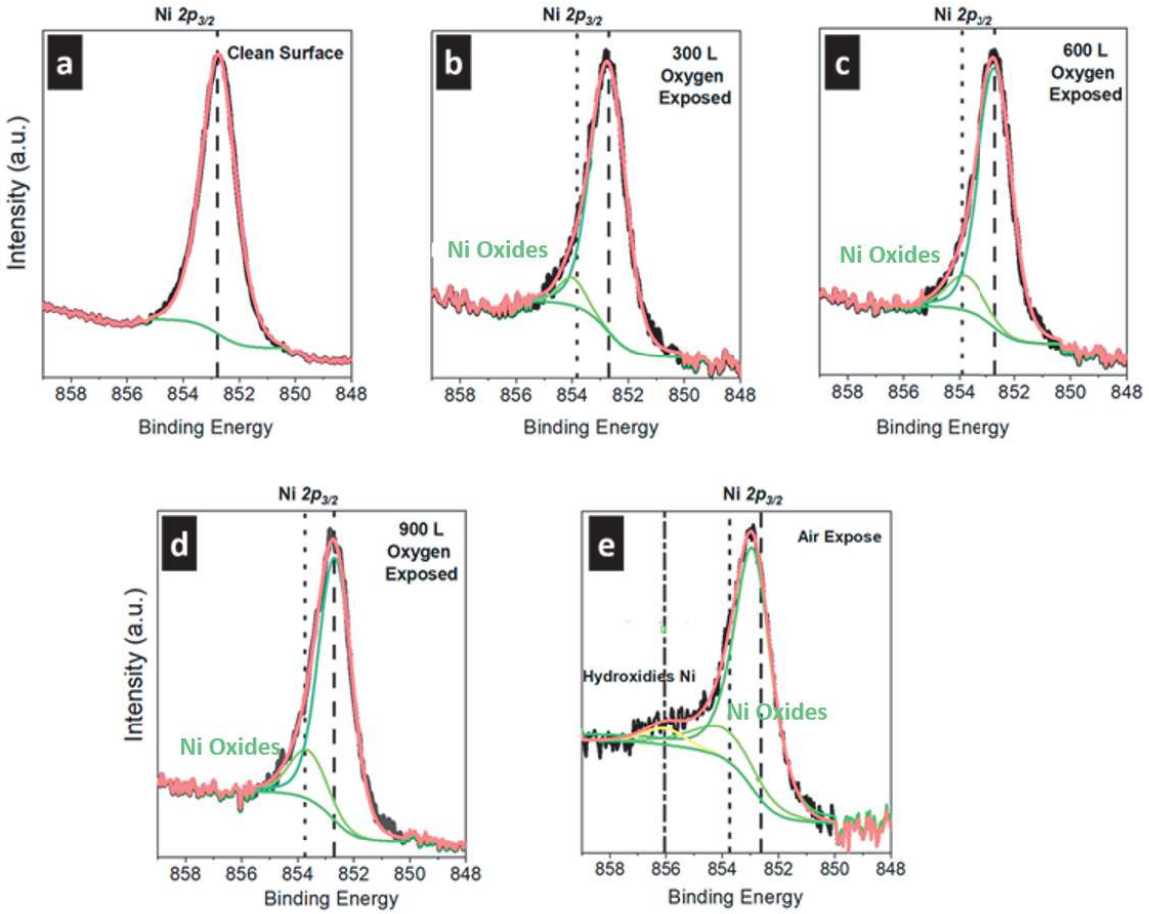


Figure 5.18: XPS spectra of the $In_3Ni_2(2\bar{1}0)$ surface after air exposed and clean the surface by sputtering and annealing it at 560 °C and with increasing oxygen exposure (300 L-900 L). Vertical dashed lines in all spectra correspond to the core level position of clean Ni $2p_{3/2}$.

Following surface cleaning and exposure to oxygen and air, the chemical composition is qualitatively analysed by examining the intensities of the In $3d_{5/2}$, Ni $2p_{3/2}$, and O $1s_{1/2}$ core levels via peak fitting (area under the curve) and normalisation using their respective photoemission cross sections. Additional effects, such as the inelastic mean free path of photoelectrons and instrumental response, have been accounted for and removed. The resulting surface composition after each treatment is presented in Figure 5.19.

As expected, only In and Ni are detected on the clean surface. Upon exposure to oxygen, O and its oxides appear alongside In and Ni. In contrast, air-exposed surfaces

additionally exhibit the presence of nickel hydroxide. The intensity of In decreases significantly, from approximately 78% on the clean surface to around 11% following exposure to 900 L of oxygen. Similarly, the proportion of pure Ni decreases from 22% to 5% under the same conditions. This reduction in metallic components coincides with an increase in oxidised In to approximately 23% at 900 L, while oxidised Ni remains relatively low, at around 4%, indicating significant oxidation of In and only limited oxidation of Ni.

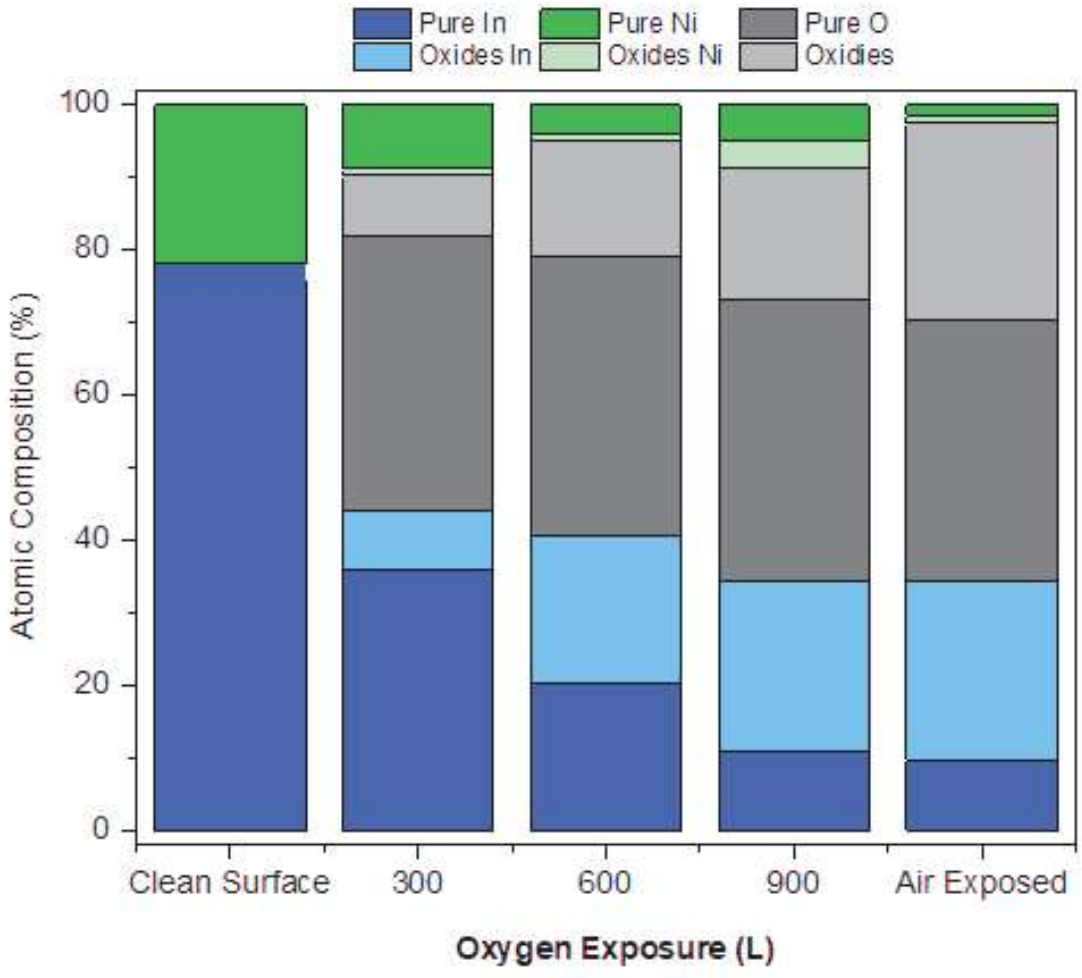


Figure 5.19: The chemical composition of the $In_3Ni_2(2\bar{1}0)$ surface after annealing at 560 °C and with increasing oxygen exposure (300 L-900 L). The atomic composition of the clean and air exposed surfaces is also given for comparison. The composition was determined from the In $3d_{5/2}$, Ni $2p_{3/2}$, and O $1S_{1/2}$ XPS peaks.

5.5 Summary

The atomic structure, chemical composition, and oxidation behaviour of the $(2\bar{1}0)$ surface of In_3Ni_2 were investigated for the first time using a combination of techniques, including XPS, LEIS, STM, and LEED.

Surface cleanliness and chemical composition were verified by XPS after sputtering and annealing. Both XPS and LEIS data revealed that sputtering preferentially removes In from the surface, while annealing promotes the segregation of In from the bulk to the surface. This behaviour is attributed to the lower surface free energy of In compared with Ni.

To further understand the atomic structure of the crystal surface, STM and LEED measurements were performed. The LEED pattern and STM images confirm a (1×1) surface structure.

STM images are influenced by the applied bias voltage, with individual atomic species In_1, In_2, and Ni exhibiting distinct contrast behaviours. At negative biases ranging from –1.8 V to –0.75 V, In_1 shows high contrast, whereas In_2 and Ni are observed with low contrast. At higher positive bias voltages, Ni atoms are not visible, In_1 appears with reduced contrast, and In_2 displays significantly higher contrast. These observations highlight the significant role of bias voltage in atomic detection and contrast variations.

XPS analysis revealed progressive oxidation following exposure to oxygen and air. Oxide species were formed, while the signals corresponding to metallic In and Ni decreased markedly. These changes confirm the onset of surface oxidation and the associated chemical transformation.

6 | In_3Ni_2 (100) Surface

6.1 Introduction

This chapter presents the atomic structure, surface composition and oxidation behaviour of the In_3Ni_2(100) surface, investigated using a variety of surface-sensitive techniques, including XPS, LEIS, LEED and STM. To obtain a clean and well-ordered surface, the sample was cleaned by repeated cycles of argon ion sputtering followed by annealing. All preparation and characterisation procedures were performed under UHV conditions to maintain contamination to a minimum and ensure the reliability of the surface analysis.

The chemical composition of the In_3Ni_2(100) surface was investigated through XPS to assess the effects of air exposure, sputtering , and annealing. Variations in surface composition were evaluated as a function of annealing temperature and photoelectron emission angle to gain insight into depth-dependent chemical composition changes. In addition, the elemental composition of the outermost atomic layers was characterised using LEIS, following sputtering and annealing at selected temperatures.

Surface crystallography was examined using LEED after sputtering and annealing at different temperatures. STM was used to investigate the surface termination and study the surface morphology.

In addition, the oxidation behaviour of the In_3Ni_2(100) surface was also studied by XPS, with emphasis on the changes in binding energy in the In and Ni core levels induced by various oxygen exposures.

6.2 In_3Ni_2 (100) Model Structure

The crystallography of the In_3Ni_2(100) surface is first described to provide the crystal structure for the experimental study. Figure 6.1 (a) shows the unit cell of In_3Ni_2 with the (100) crystallographic plane highlighted in yellow. The unit cell is characterised by lattice parameters $a = b = 4.387$ Å and $c = 5.295$ Å, with interaxial angles $\alpha = \beta = 90°$ and $\gamma = 120°$ [107]. Structurally, In_3Ni_2 conforms to the Al_3Ni_2 prototype and crystallises in the trigonal space group $P-^3m1$ [65].

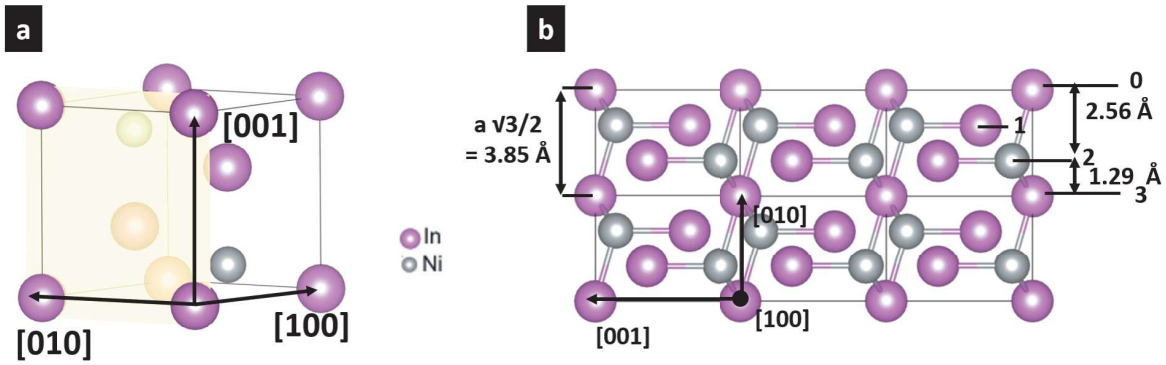


Figure 6.1: (a) The unit cell of the In_3Ni_2(100) surface, with the (100) plane highlighted in yellow. (b) Side view of the (100) surface, showing the stacking of four atomic planes, labelled 0 to 3, within the unit cell. The separations between specific planes are indicated.

Figure 6.1 (b) illustrates a side view of the In_3Ni_2(100) surface showing four atomic planes marked from 0 to 3. The vertical separations of planes 0 and 2 are 2.54 Å, while planes 2 and 3, as well as planes 0 and 1, are separated by 1.27 Å. A lattice parameter of 3.84 Å is represented by the sum of these interplanar lengths. By comparison of these structural dimensions with step heights obtained from STM images, the particular crystallographic planes in the surface termination could be identified.

6.3 Experimental Methods

This section describes the experimental procedures used to prepare and characterise the In_3Ni_2(100) single crystal surface. It was grown using the Czochralski pulling technique, as previously introduced in Section 2.7. The (100) crystallographic plane was precisely oriented and sectioned using a wire saw, utilising a 50 μm tungsten wire in combination with boron carbide particles suspended in glycerol. This method was chosen to mitigate material loss and prevent surface deformation. The resulting surface was mechanically polished using diamond paste to a grain size of 0.25 μm to achieve a smooth surface.

Cleaning of the sample surface in UHV involved cycles of argon ion sputtering at an average drain current of approximately 6 μA for 30 minutes per cycle and annealing the surface to temperatures ranging from 300 °C to 560 °C for durations between one and three hours. The cleaning cycles were repeated until the appearance of a sharp, well ordered LEED pattern was observed.

An optical pyrometer was used to monitor the surface temperature during XPS, STM and LEED characterisations. In the absence of a known emissivity value for In_3Ni_2, a reference value of 0.40 based on NiCu was initially applied, as suggested in the previous literature [109]. For calibration, temperature readings from the pyrometer were cross-referenced with those from a thermocouple in direct contact with the sample under UHV conditions. This procedure, identical to the one used for all In_3Ni_2 surfaces (refer to Section 3.3), resulted in a final calibrated emissivity of 0.48.

The sample was transferred to the STM chamber after XPS confirmed that the surface was clean and free of contamination. The STM, an Omicron variable temperature model operated at room temperature in constant current mode, was used to image the surface morphology and atomic structure. Tunnelling parameters were varied over a bias voltage range from -1.8 V to +1.8 V and a set current of 0.645 nA.

LEIS measurements were conducted on surfaces prepared using the same sputtering

and annealing approach. Temperature measurements during LEIS were taken using a thermocouple affixed directly to the sample. Spectra were collected from a surface area of (2×2) mm^2 using a 3 keV He^+ ion beam, with an ion dose of approximately 1×10^{14} ions/cm^2. Ion scattering energies were recorded between 1800 eV and 2800 eV to optimise the signal-to-noise ratio. The Ni and In peaks were located around 2275 eV and 2575 eV, respectively. Data acquisition was performed using a Qtac100 LEIS instrument (IONTOF GmbH, Germany) and analysis was carried out with the SurfaceLab 7 software package [110].

Further XPS measurements were performed at the Institut Jean Lamour using a non-monochromatic Al Kα X-ray source. To study oxidation behaviour under controlled UHV conditions, molecular oxygen (purity 99.999%) was introduced via a precision leak valve, maintaining a pressure of approximately 1.333×10^{-6} mbar. Oxygen exposure was modulated through dosing time to achieve dosages of 300 L, 600 L and 900 L, with 1 Langmuir (L) defined as 1.333×10^{-6} mbar·s.

In addition to controlled UHV oxidation, the surface reactivity to air exposure was also evaluated. Following the final surface cleaning, the sample was removed from the vacuum chamber and exposed to laboratory air for a duration of ten days before the XPS analysis was performed. All photoelectron spectra were processed using the CasaXPS software suite to determine chemical shifts and variations in elemental composition.

6.4 Results and Discussion

6.4.1 Chemical Composition Studied by XPS

Effect of Air Exposure, Sputtering and Annealing on Surface

XPS was used to determine the chemical composition of the In_3Ni_2(100) surface, identifying both the constituent elements and any surface contaminants. In addition, XPS was

used to investigate the effects of air exposure, sputtering and annealing on the chemical composition of the surface.

Figure 6.2 (a) presents the wide scan XPS spectra obtained under three sequential conditions: air exposure, after sputtering and after annealing. The core level spectra of In, Ni, C and O were analysed using a Gaussian-Lorentzian convolution, combined with a Shirley background, to accurately determine the binding energies and peak areas of In and Ni. The fitted peak positions for the annealed surface are indicated by vertical dashed lines in Figure 6.2. Additionally, the KLL Auger peaks observed in the spectra arise from electron transitions within the L shell, resulting from the filling of vacancies in the K shell.

The sample was contaminated with oxygen and other contaminants after being exposed to air for a long time, around 10 days. The wide scan XPS spectra of the $In_3Ni_2(100)$ surface identified peaks corresponding to In, Ni, C and O, indicative of surface contamination. However, after sputtering followed by annealing of the surface under UHV conditions, the O 1s and C 1s peaks were no longer detectable, confirming effective surface cleaning.

Figures 6.2 (b) and (c) compare the core level binding energies of In $3d_{5/2}$ and Ni $2p_{3/2}$, respectively, between different surface treatments. Exposure to air results in a binding energy increase of approximately 0.1 eV for In and 0.05 eV for Ni. The observed variation in the In and Ni peaks is within the margin of experimental uncertainty.

Subsequent annealing at 560 °C resulted in no observable changes in the binding energies or shapes of the In and Ni core levels; however, there was a change in the In peak position by 0.2 eV. The implications of these intensity variations will be explored in the following section (Section 3.4.1), and a more detailed discussion of the observed binding energy shifts is provided in Section 6.4.5. A summary of these findings is presented in Table 6.1.

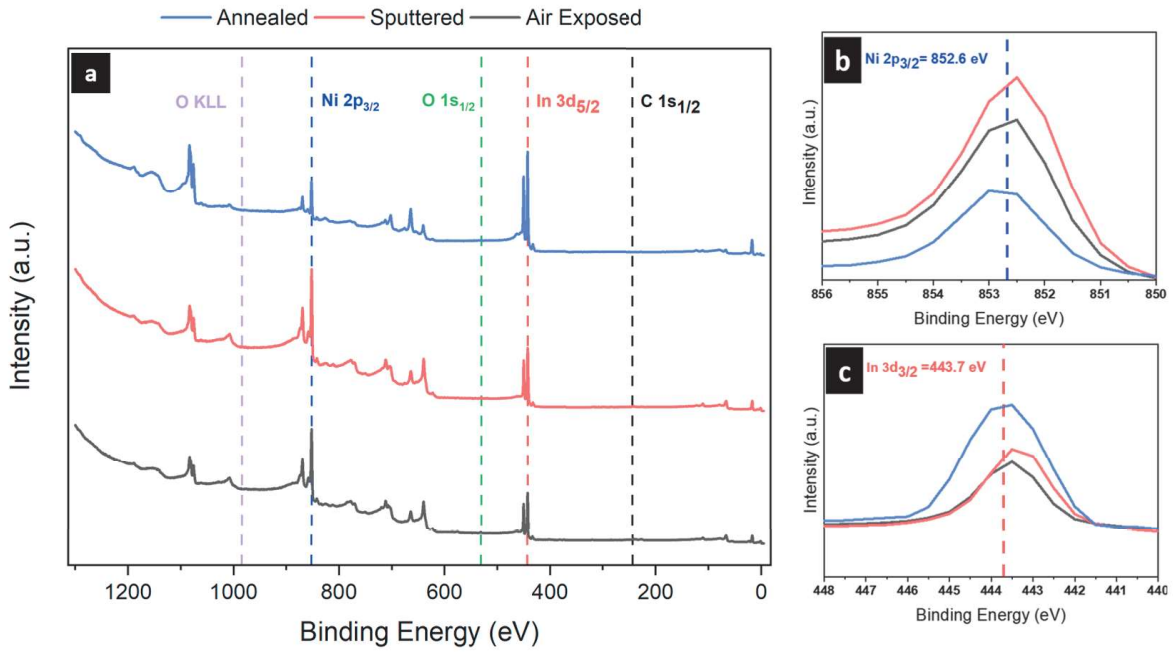


Figure 6.2: (a) XPS wide scan spectra obtained from the $In_3Ni_2(100)$ surface under three distinct conditions: air exposure, following sputtering and after annealing at 560 °C for one hour. No oxygen or carbon contamination were detected after cleaning the surface by sputtering and annealing. (b) and (c) High resolution XPS spectra illustrating the core level binding energies of In $3d_{5/2}$ and Ni $2p_{3/2}$, respectively. These spectra demonstrate the influence of air exposure and surface treatment on peak positions.

Elemental	**Ni $2p_{3/2}$**	**In $3d_{5/2}$**
Elemental Binding Energy	852.5 eV [111]	443.7 eV [112]
Air Exposed Surface	852.6 eV	443.65 eV
Sputtered Surface	852.6 eV	443.5 eV
After Sputtered Annealed Cycles	852.7 eV	443.7 eV

Table 6.1: XPS data for $In_3Ni_2(100)$ surface comparing the binding energies of the core levels of Ni $2p_{3/2}$ and In $3d_{5/2}$. Following three cycles, the peak positions represent the clean intermetallic compound.

Atomic Compositions Changes as a Function of Sputtering and Annealing Temperatures

To investigate the effects of sputtering and annealing at various temperatures on the surface chemical composition, a comprehensive XPS -based quantification of elemental constituents was performed. In and Ni concentrations were determined from the integrated intensities of the spectral peaks In $3d_{5/2}$ and Ni $2p_{3/2}$. These intensities were corrected by factors that account for the photoionisation cross section, the inelastic mean free path of the photoelectrons and the transmission function of the analyser, as described in Section 3.4.1.

Figure 6.3 presents the changes in the chemical composition of the $In_3Ni_2(100)$ surface as a function of the annealing temperature, ranging from 300 °C to 560 °C. Although the bulk structure corresponds to 60% In, the sputtering analysis reveals a notable decrease in the surface In concentration to approximately 43%. However, Ni the concentration increases to around 57%, suggesting that sputtering preferentially depletes In from the surface.

As discussed in Chapters 6.4.1 and 5.4.1, there are a number of factors that impact the preferential sputtering of an ICM. These include atomic mass, surface free energy and atomic bonding. Elements with lower atomic mass, reduced surface energy and weaker atomic bonds are more prone to preferential sputtering [113, 114, 115, 123]. Although atomic mass is not the primary factor in this surface, given that In is heavier than Ni, a comparison of the surface free energies indicates that In has a lower surface free energy than Ni. Specifically, the surface free energy of a face centred cubic (FCC) Ni surface is higher than that of a body centred tetragonal (BCT) In surface, with respective values of 1.31 J/m^2 and 0.488 J/m^2 [116].

This preferential sputtering is attributed to In's relatively lower surface energy. A similar phenomenon of preferential sputtering has been noted in the $Ga_3Ni_2(100)$ surface, where, following sputtering, the atomic compositions of Ga and Ni are nearly identical,

with each element representing approximately 50% of the surface composition [117]. This aligns with the preferential sputtering behaviour previously discussed and with the consistency of the results from all three surfaces under sputtering. This behaviour has already been addressed in Chapters 4.4.1 and 5.4.1.

Upon annealing at a temperature of 300 °C, a significant redistribution of surface atoms is observed. Specifically, the atomic concentration of In on the surface increases to about 74%, whereas that of Ni decreases to about 26%. This surface composition is significantly higher than the equivalent bulk concentration, even at this very low annealing temperature. Subsequent annealing cycles induce only minor changes in the atomic composition, indicating that a steady state or saturation condition has been reached at the surface.

This behaviour indicates that the annealing process promotes the thermally driven migration of In atoms from the bulk to the surface, a phenomenon consistent with surface segregation. In the context of alloy systems, surface segregation refers to the tendency of one component to preferentially accumulate at the surface, thereby altering the surface composition relative to the bulk [124], as shown in Figure 6.3.

Surface segregation is influenced by various factors, including surface free energy, atomic radius and the bonding energy of the components [114]. Elements that have less binding energy, a larger atomic radius and less surface energy tend to segregate to the surface. As previously observed, In has a lower surface free energy and a larger atomic radius than Ni [118]. Thus, we suggest that In segregation is mostly governed by its larger atomic radius and lower surface free energy compared to Ni [119]. Comparable patterns of preferential segregation have also been observed on the Ga_3Ni_2(100) surface under similar annealing conditions [117].

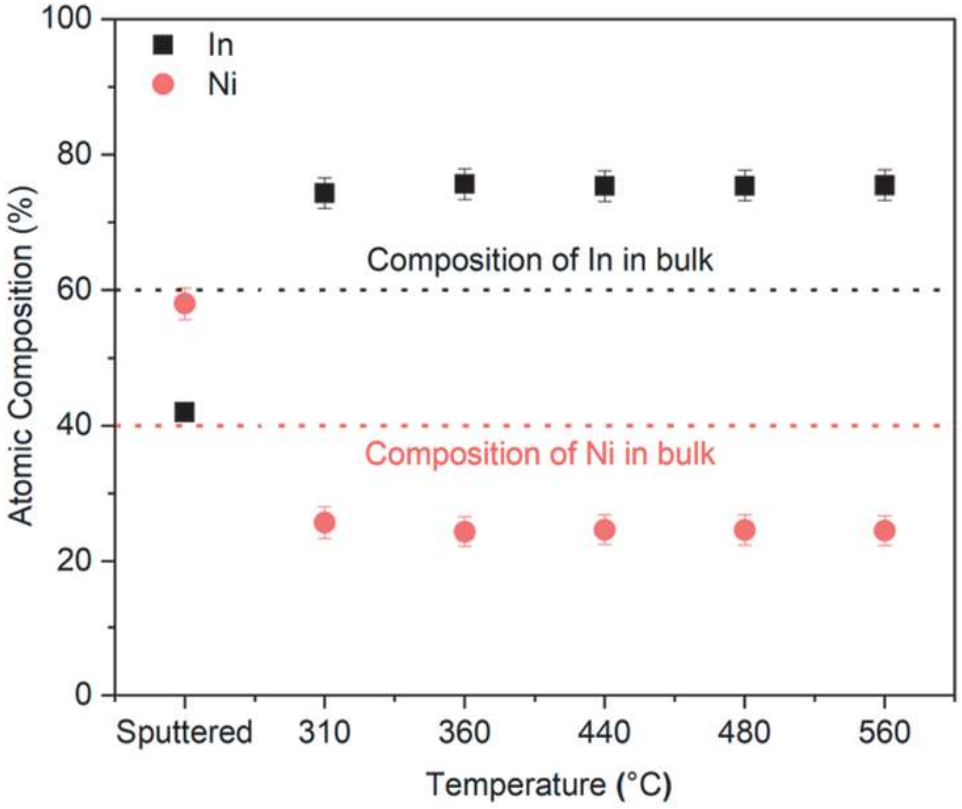


Figure 6.3: The surface chemical composition of the (100) surface after sputtering and annealing at various temperatures from 300 °C to 560 °C. Dotted lines across the top indicate the In and Ni bulk composition.

Atomic Compositions a Function of Scanning Angles

After annealing the surface at 560 °C, XPS spectra were recorded at grazing angles of 0°, 10°, 15°, 20°, 30°and 40° to investigate the distribution of In and Ni on the (100) surface. The resulting atomic composition is shown in Figure 6.4. It is worth noting that rotations beyond 40° were not feasible without losing the sample from the manipulator.

Across the range of grazing angles from 0° to 40°, the atomic composition remains relatively constant, with the In and Ni concentrations remaining unchanged. If In were confined to the surface layer, an increase in concentration would be anticipated as the grazing angle increases.

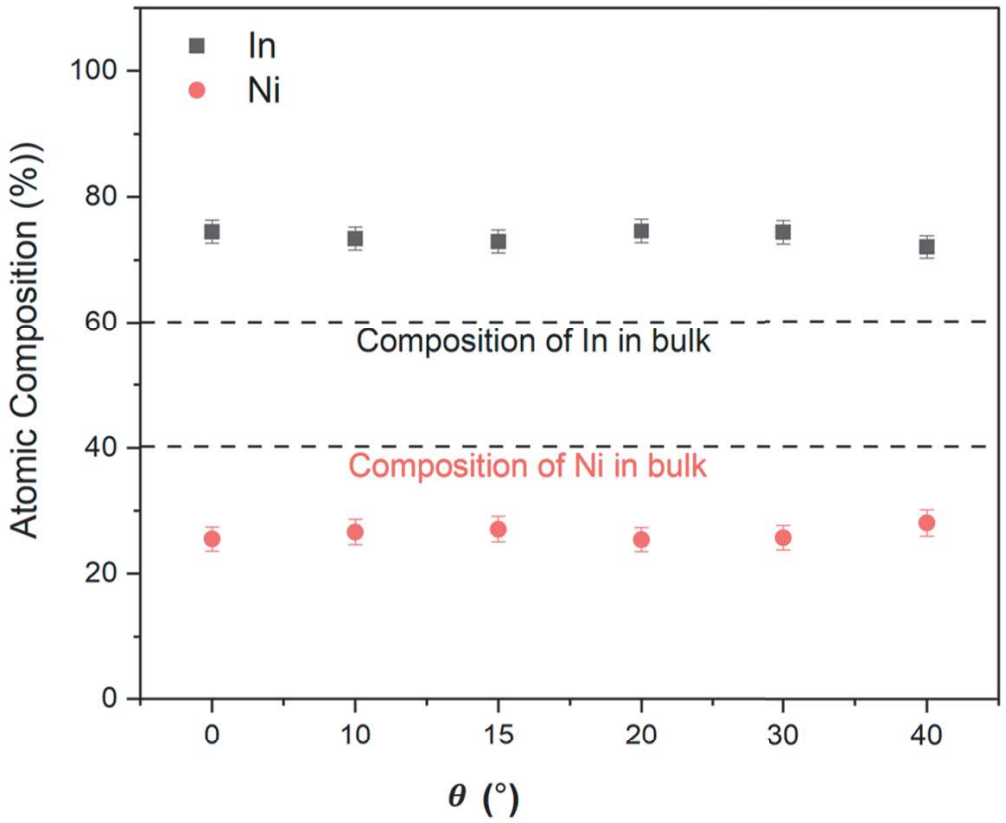


Figure 6.4: The surface chemical composition of the (100) surface determined by XPS with various scan angles from 0 to 40°. Dotted lines across the top indicate the In and Ni bulk composition. θ is an angle between the surface and X-ray.

6.4.2 Elemental Information Studied by LEIS

LEIS was used to identify the elemental composition of the crystal's topmost atomic layer. Prior to LEIS measurements, the sample was prepared by two cycles of sputtering and annealing to ensure a clean surface. Sputtering was carried out using a 1 keV Ar^+ ion beam over a (2×2) mm area, continuing until stabilisation of the LEIS signal indicated that surface contaminants had been effectively removed. The sample was then annealed at 400 °C for 45 minutes and subsequently cooled to room temperature for two hours.

After the surface was annealed to higher temperatures, up to 480 °C, LEIS spectra were acquired. Figure 6.5 shows LEIS spectra from sputtering and annealing at different temperatures that induced clear changes in the relative intensities of In and Ni after annealing

to 480 °C. With increasing temperature, the In peak gradually intensified, while the Ni peak diminished, indicating a temperature-dependent redistribution of surface atoms.

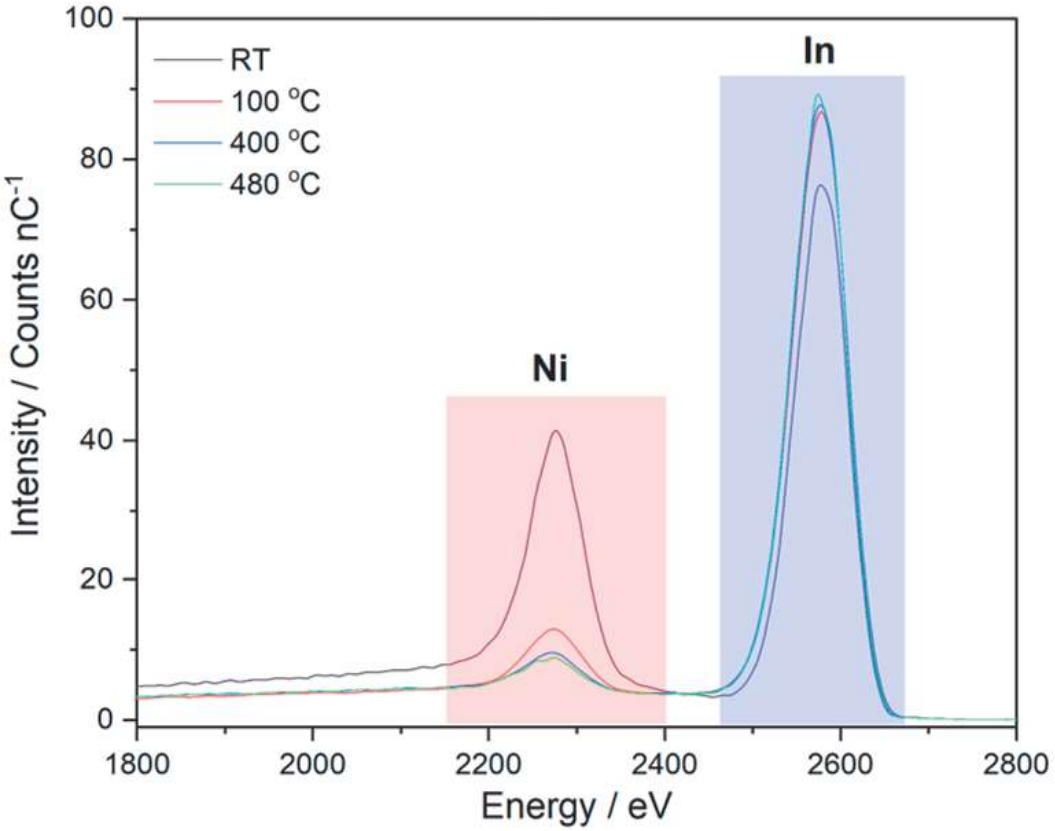


Figure 6.5: LEIS spectra recorded from the $In_3Ni_2(100)$ surface after sputtering and annealing at different temperatures for 1 hour using a 3 keV He^+ beam. The energy ranges for each surface peak highlighted correspond to the upper and lower limits used for the baseline subtraction.

Sputtering (Depth Profile)

We investigated how varying Ar^+ ion doses (depth profiling) affected the relative surface concentrations of In and Ni. The sample was prepared by sputtering and annealing at 400 °C for one hour, then allowed to cool to room temperature. LEIS spectra were subsequently recorded at different ion dose levels to monitor surface composition changes.

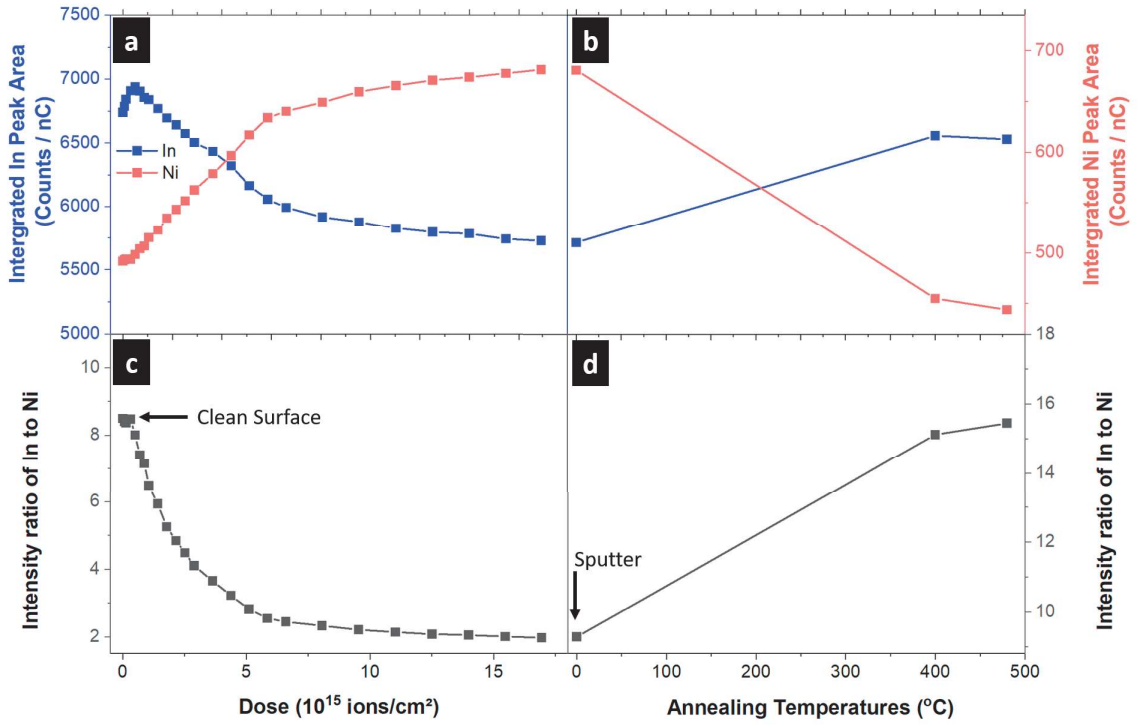


Figure 6.6: Integrated LEIS intensities of In and Ni from the In_3Ni_2 (100) surface (a) as a function of increasing Ar^+ ion dose and (b) sputtering annealing at selected temperatures 400 °C and 480 °C. (c) and (d) display the corresponding In/Ni peak intensity ratios, highlighting compositional shifts induced by sputtering and annealing.

Figure 6.6 (a) presents the variation in LEIS peak areas for In and Ni as a function of increasing ion exposure. To quantify the spectral intensities, a two-point linear background subtraction was applied across the relevant energy ranges. The integrated peak areas, following background correction, represent the surface contributions from In and Ni atoms, thereby enabling the evaluation of the surface composition at each stage. After surface cleaning using argon, a noticeable reduction in the In signal is observed, likely due to contamination from the sputtering gun filament. At the lowest ion dose, the In peak is substantially more intense than that of Ni, indicating a surface predominantly terminated by In. As ion exposure increases, the In signal decreases while the Ni signal increases, suggesting preferential sputtering of the In atoms. Beyond a certain sputtering dose, both signals stabilise, indicating that the surface has reached a steady-state composition, with

further ion exposure having little effect on the detected elemental distribution.

The In-to-Ni intensity ratio is shown in Figure 6.6 (c). The initial ratio is high, reflecting a surface enriched in In. As sputtering progresses, the ratio decreases sharply, confirming preferential sputtering of In. This trend continues until the ratio stabilises, signalling the formation of a consistently clean and compositionally steady surface.

Annealing Temperatures dependent

After sputtering and annealing at 400 °C, the LEIS data in Figure 6.6 (b) show a noticeable increase in the In peak intensity with a corresponding reduction in the Ni signal. This shift suggests that In atoms begin to migrate toward the surface during moderate thermal treatment, while Ni becomes less prominent at the topmost atomic layer. Upon further annealing to 480 °C, the In signal continues to increase slightly and the Ni peak declines. This behaviour is indicative of surface segregation, where In preferentially accumulates at the surface with increasing temperature.

The evolution of the In-to-Ni intensity ratio, shown in Figure 6.6 (d), supports this interpretation. The ratio increases slightly between 400 °C and 480 °C, confirming a growing surface enrichment of In relative to Ni.

6.4.3 Atomic Structure Studied by LEED and STM

LEED patterns were obtained from the surface using a computer-controlled data collection system and a digital charge-coupled device camera, after sputtering at temperatures ranging from 360 °C to 500 °C and within an energy range from 10 to 120 eV. After annealing the surface at temperatures below 350 °C, no LEED patterns were visible, indicating that the temperature was not high enough to produce a well-ordered surface. After annealing at 360 °C, the surface displays a (1×1) LEED pattern with sharp spots and long-range surface order with low background intensity, suggesting a stable surface.

The LEED patterns of In_3Ni_2(100) and Ag(100) are compared in this study using the

same equipment and a beam energy of around 60 eV. The expected value for the terminated bulk surface is 4.39 Å and 5.29 Å. The lattice constants calculated from the LEED data in real space, $|b_1| = 4.5 \pm 0.2$ Å and $|b_2| = 5.2 \pm 0.2$ Å, agree with this.

Effect of Annealing Temperature and Beam Energies

The LEED patterns were obtained after each preparation cycle, i.e. sputtering and annealing the surface from 360 °C to 500 °C. There is only a (1×1) structure and no evidence of surface reconstruction or phase transitions, as shown in Figure 6.7 (a-f). This behaviour is consistent with the stable, unreconstructed surfaces reported for PdGa(111), NiAl(110) and ZnPd [38, 45].

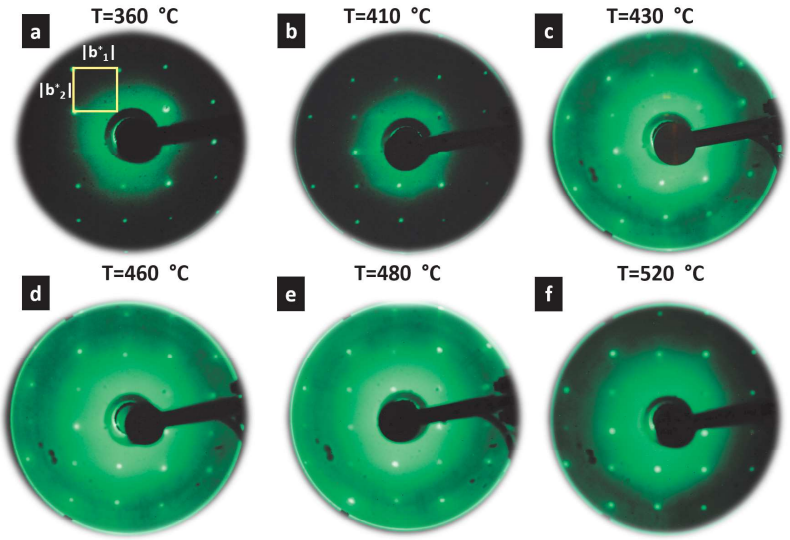


Figure 6.7: (1×1) LEED patterns at beam energy 45 eV after (a) Annealing at 360 °C. (b) Annealing at 410 °C. (c) Annealing at 430 °C. (d) Annealing at 460 °C. (e) Annealing at 480 °C.(f) Annealing at 520 °C.

In addition, LEED patterns were obtained for a range of beam energies from 10 to 140 eV after annealing the surface at 500 °C using selected beam energies. Figure 6.8 (a-f) shows the LEED pattern of the surface that is not affected by the different beam energies. The (1×1) pattern remains stable when the system is maintained at a UHV pressure of 10^{-10} mbar. In this case, the surface does not exhibit any phase transition or

reconstruction.

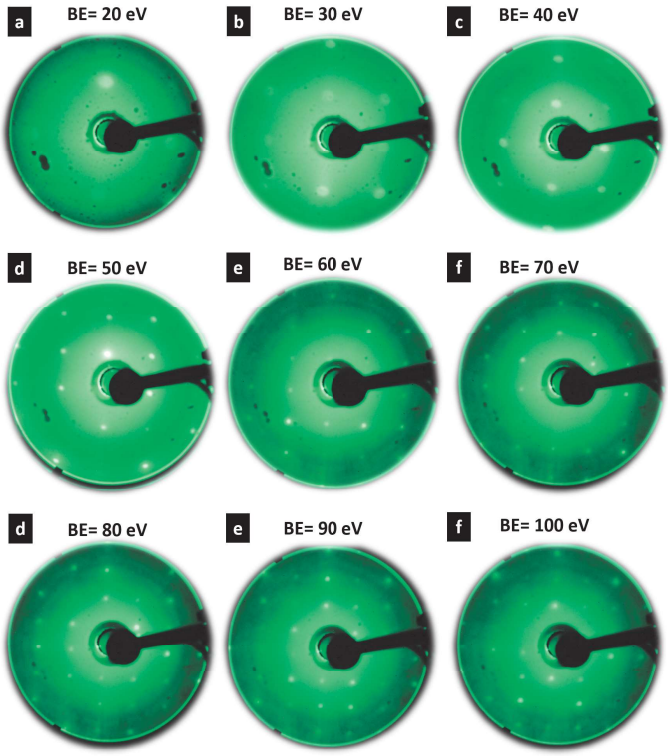


Figure 6.8: LEED patterns of the surface after annealing at 460 °C (a) Beam energy 20 eV. (b) Beam energy 30 eV. (c) At beam energy 40 eV. (d) Beam energy 50 eV. (e) Beam energy 60 eV. (f) Beam energy 70 eV. (g) Beam energy 80 eV. (h) Beam energy 90 eV.

The experiment was repeated at the edge of the sample after a 30 minute sputtering process using Ar^+ ions, followed by annealing at 400 °C for two hours. The resulting LEED pattern showed no notable change in the primary surface structure. However, additional low-intensity diffraction spots highlighted by yellow circles were observed. These features moved in the opposite direction to the movement of the substrate spots as the electron beam energy was varied, indicating the presence of surface facets. Similar features were previously identified on the (001) and $(2\bar{1}0)$ surfaces. However, the LEED diffraction pattern of these facets lacked sufficient clarity to allow a detailed analysis of their crystallographic orientation or structural properties.

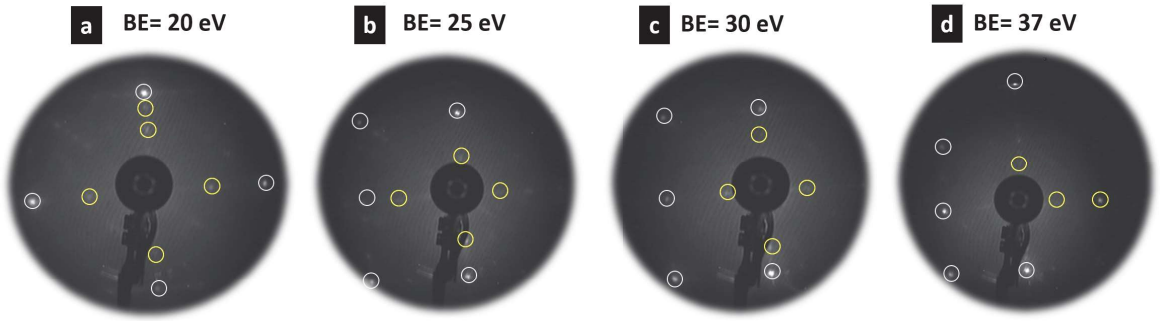


Figure 6.9: LEED patterns illustrating the facets structure characteristic of (100) clean surface with different beam energy (a) 30 eV. (b) 40 eV. (c) 45 eV.(d) 50 eV. The diffraction spots from the facet are marked by yellow circle.

The structural quality of the sample was evaluated using Laue X-ray diffraction back reflection measurements across different surface regions. Most of the sample showed a clear Laue pattern with no evidence of miscut (Figure 6.10 (a)), confirming the single crystalline nature of the In_3Ni_2 surface oriented along the (100) plane and indicating high crystallographic quality.

In contrast, measurements near the sample's edges revealed two Laue rings (Figure 6.10 (b)), indicating a polycrystalline structure in these regions. This suggests that the grains belong to the same phase, with a uniform chemical composition and crystal structure, although their crystallographic axes are slightly misoriented relative to each other.

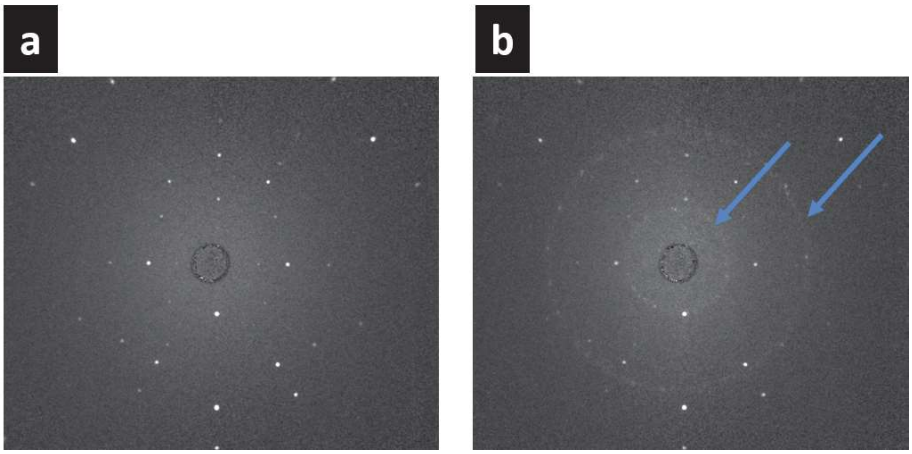


Figure 6.10: (a) Representative Laue back scattering image taken from the most part of the surface reflecting the symmetry expected from the bulk. (b) Laue back scattering image from the edge of sample showing a diffuse rings,indicated by polycrystalline.

STM

STM images were taken from the surface after annealing at 420 °C to 540 °C for periods ranging from one to three hours. STM images were obtained in constant current mode, maintaining a tunnelling current near 0.645 nA and employing a bias voltage adjustable within the range of -1.8 V to +1.8 V.

Steps and terraces were not detected until surface annealing at 450 °C, where clearly defined flat terraces first emerged. After annealing at temperatures above 550 °C for 150 minutes, most (100) surfaces displayed large stepped terrace regions. Terrace sizes were observed to reach dimensions as large as 1200 $\times$ 1200 Å.

Figure 6.11 (a) displays the STM image obtained after annealing at 550 °C, highlighting the presence of flat atomic terraces. The step heights observed in the image were quantitatively evaluated through line profile analysis and the results align with those predicted by the corresponding bulk crystal structure. Figure 6.11 (b) illustrates the distribution of the step heights along the blue arrow in Figure 6.11 (a).

To enhance statistical confidence, more than 144 surface steps were analysed using STM images acquired from multiple surface regions. As illustrated in Figure 6.11 (c), the predominant step height measured is 3.75 $\pm$ 0.03 Å. This value corresponds closely to $a\frac{\sqrt{3}}{2}$ Å, indicating consistency with the bulk lattice constant.

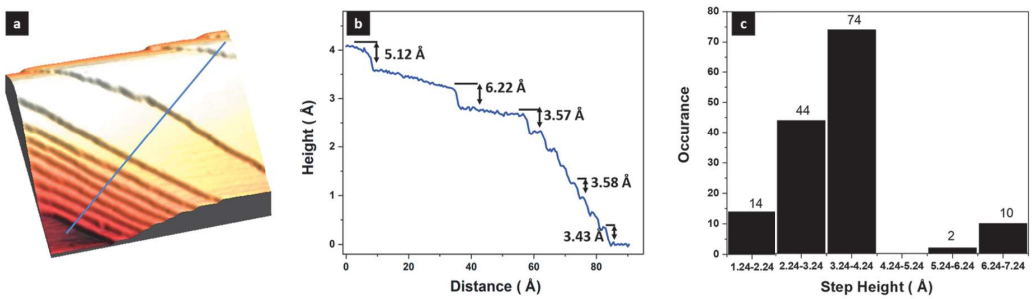


Figure 6.11: STM images of the In_3Ni_2(100) surface following multiple sputtering and annealing cycles. (a) Height distribution recorded at 530 °C over an area of 800 Å× 650 Å, with a sample bias of +0.7 Vand a tunnelling current of 0.457 nA, showing surface steps of varying heights. (b) Height profile extracted along the blue line indicated in (a). (c) Histogram representing the distribution of step heights near the observed steps.

High-resolution STM images of the freshly prepared surface are shown in Figures 6.12 (a-b). Line profile analysis reveals two distinct lattice spacings along the crystallographic directions [001] and [010], with measured periodicities of $|b_1| = 4.42 \pm 0.1$ Å and $|b_2| = 5.30 \pm 0.2$ Å, respectively. These values closely match the known lattice parameters of the $In_3Ni_2(100)$ surface, which are 4.39 Å and 5.29 Å. Most of the STM image, covering a large portion of the surface, shows no reconstruction, as illustrated in Figure 6.12 (c).

A similar behaviour is observed for the $PdGa(\bar{1},\bar{1},\bar{1})$ surface, which also exhibits a well-ordered, unreconstructed (1×1) hexagonal lattice with atomically flat terraces and uniform step heights, as confirmed by LEED and STM analyses [38].

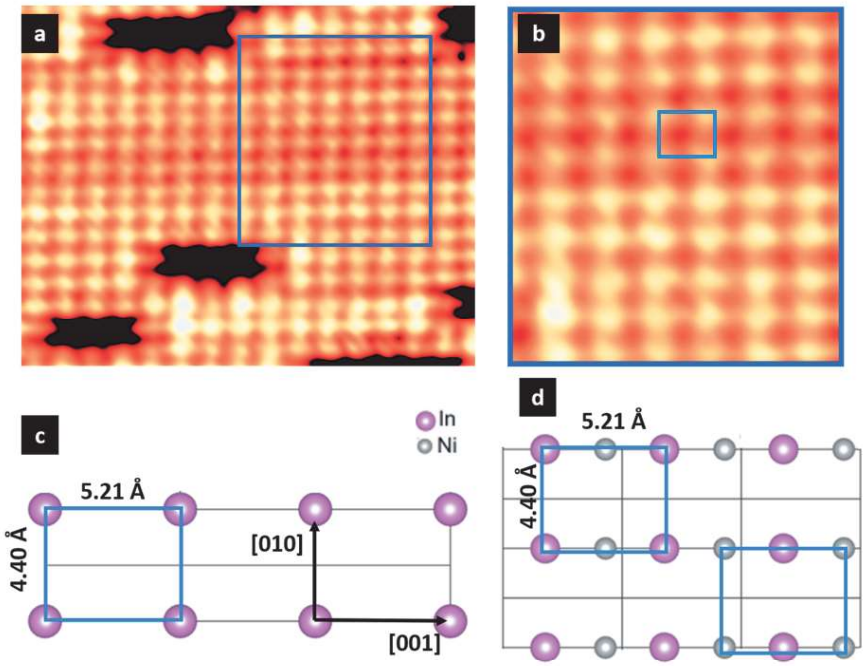


Figure 6.12: (a) STM images of $In_3Ni_2(100)$ surface showing atomic resolution after sputter and annealing at 550 °C (100 Å × 100 Å, - 0.5 eV, 0.645 nA). (b) STM image (4 Å × 3.5 Å, 0.5 eV, 0.645 nA). (c) and (d) Top view of (100) surface.

To investigate the bias-dependent surface characteristics of the $In_3Ni_2(100)$ surface, STM imaging was performed over a range of applied sample biases. All images were acquired from comparable surface regions under consistent tip conditions, thus maintaining

uniform image contrast and ensuring high atomic resolution for reliable comparison. A systematic analysis of the STM images recorded between –1.8 V and +1.8 V, as used for the $(2\bar{1}0)$ surface, reveals a bias dependence in both contrast and atomic-scale visibility, as shown in Figures 6.13 (a–f).

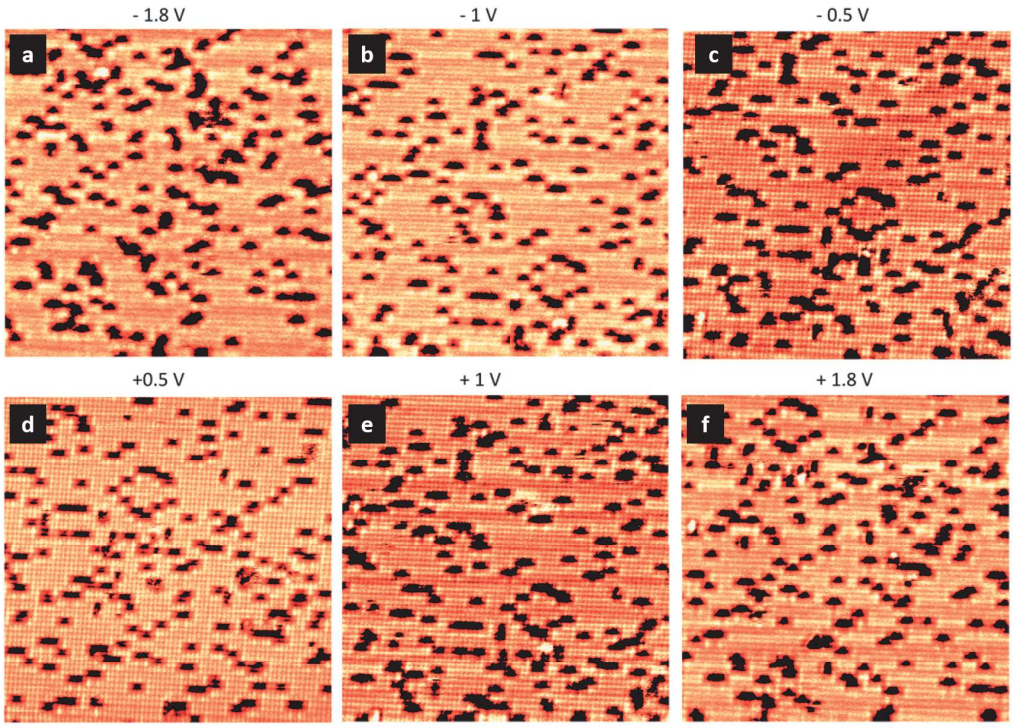


Figure 6.13: STM images showing atomic resolution (300 Å× 300 Å, 0.645 nA) after annealing (100) surface at 550 °C with different bias voltages (a) -1.8 eV. (b) -1 ev. (c) -0.5 eV. (d) +0.5 eV. (e) +1 eV. (f) +1.5 eV.

Figures 6.14 (a–f) provide a zoomed-in view of the same surface area at different voltage biases, highlighting the effect of tunnel conditions on the resultant contrast and resolution. At a significant negative bias (approximately –1.8 V, Figure 6.14 (a)), the atomic scale appears rather unclear; however, with a slightly reduced negative bias (approximately –1.0 V, Figure 6.14 (b)), these characteristics become more defined, with bright protrusions becoming increasingly discernible. As the bias approaches –0.5 V (Figure 6.14 (c)), the atomic resolution further enhances, revealing sharper periodicity and increased structural visibility. At near-zero to slightly positive bias voltages (approximately +0.5 V,

Figure 6.14 (d)), the atomic lattice becomes highly pronounced, suggesting a more accurate representation of the actual surface topography. At a moderate positive bias (around +1.0 V, Figure 6.14 (e)), atomic resolution remains evident. At the highest positive bias studied (+1.8 V, Figure 6.14 (f)), the STM images display reduced contrast.

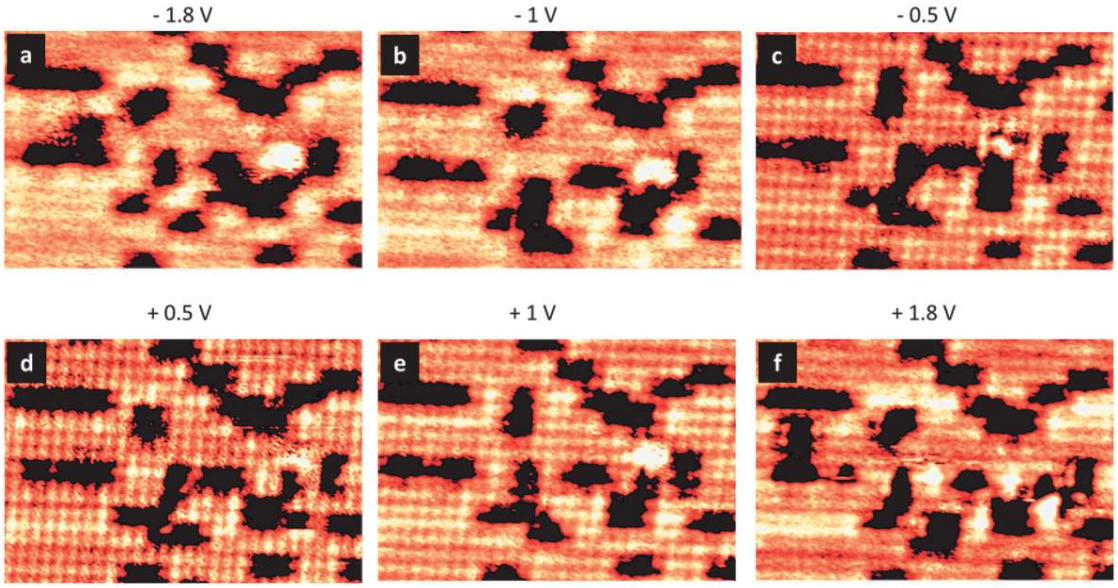


Figure 6.14: STM images showing atomic resolution (116 Å× 78 Å, 0.645 nA) after annealing (100) surface at 550 °C with different bias voltages (a) -1.8 eV. (b) -1 ev. (c) -0.5 ev. (d) +0.5 ev. (e) +1 ev. (f) +1.5 ev.

Additionally, high-quality STM images were obtained at the edge of the surface following sputtering and annealing of the surface at 550 °C, revealing well-defined step heights and atomic resolution across various regions of the sample (Figure 6.15). In particular, the measured step height of 2.1 $\pm$ 0.1 Å differs from previous results and does not correspond to any known interplanar spacing within the bulk (100) crystallographic structure (Figure 6.15 (b)). Moreover, the lattice constants of around 5 $\pm$ 0.1 Å and 10 $\pm$ 0.2 Å do not correspond to the unit cell dimensions. This suggests the presence of slightly different surface orientations of the same crystalline phase or impurity phases.

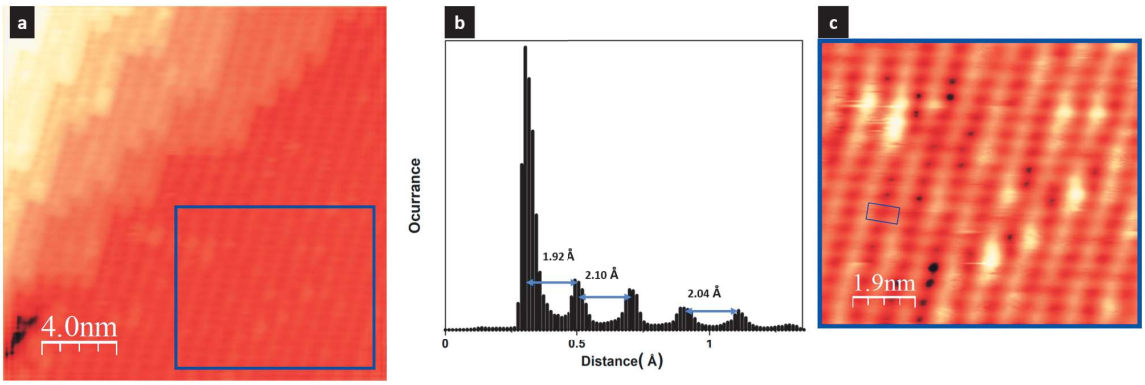


Figure 6.15: (a) STM images from the sample edge showing atomic resolution (200 Å× 200 Å, +1.8 V, 0.645 nA) after annealing (100) surface at 550 °C. (b) -1 ev. (c) STM images showing atomic resolution (86 Å× 83 Å, +1.8 V, 0.645 nA).

6.4.4 Identification of Surface +

In this section, possible surface terminations are investigated by considering a range of factors, including surface model analysis, comparisons with STM images, and LEIS data.

Figure 6.16 presents four possible surface termination configuration models 0, 1, 2 and 3, with models 0 and 3 being structurally equivalent. Each model depicts atomic positions within the crystal lattice, projected along the [100] direction, starting from the corresponding surface layer. Comparison with experimental STM images reveals a surface periodicity of approximately 5.29 $\pm$ 0.2 Å and 4.40 $\pm$ 0.1 Å, indicating the presence of a single atomic species, In or Ni, at the surface. Moreover, there is no voltage bias dependence in the STM contrast, which further supports this interpretation, suggesting that only one element contributes to the tunnelling current. These observations align more closely with model 0, in which a single atomic species, In, forms the outermost layer. To further investigate surface terminations, Emilie Gaudry from Institut Jean Lamour, France [125], performed density of states calculations, which support these results.

Further support for this conclusion is provided by LEIS measurements, which support the assignment of model 0 as the preferred surface termination. As shown in Figure 6.6

(b), the significantly higher detected intensity of In compared to Ni indicates that In dominates the outermost atomic layer. The relatively low Ni signal is attributed to the partial penetration of He^+ ions into subsurface layers, resulting in limited detection of the underlying Ni atoms, as shown in Figure 6.16. A similar interpretation has been reported for the (001) surface (Figure 4.1), where a comparable termination sequence of In above Ni was identified, specifically In in the top layer and Ni below.

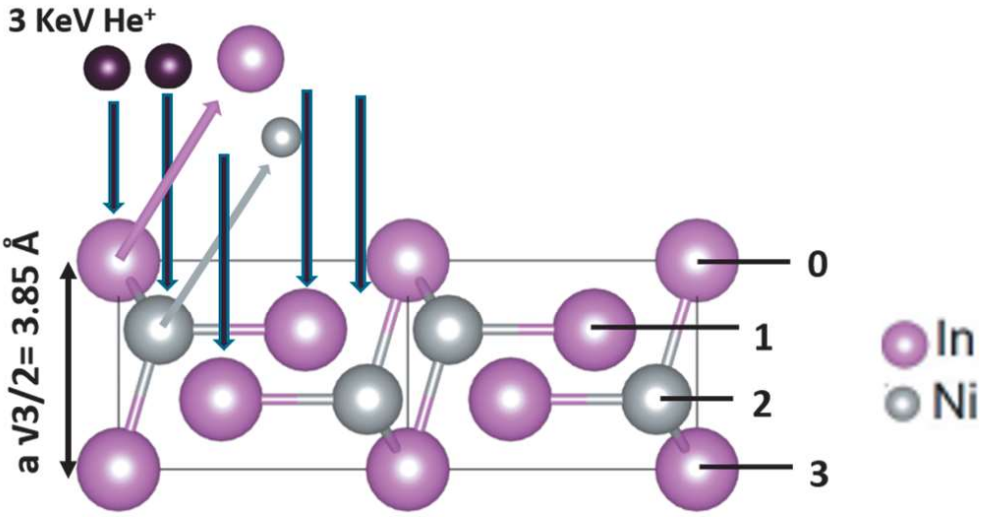


Figure 6.16: Side view of the $In_3Ni_2(100)$ surface, showing the stacking of four atomic planes, labelled 0 to 3, within the unit cell of the surface.

Models 1 and 2 are ruled out based on LEIS data, as their presence would result in He^+ ions striking both In and Ni atoms located in the same plane, leading to a markedly high Ni signal, an effect not observed experimentally.

Further validation was carried out by analysing the LEIS intensities of In and Ni in relation to the chemical composition. However, accurate conversion of these intensities into compositional values is inherently difficult. To overcome this, we used the LEIS intensity from the $(2\bar{1}0)$ surface, because the surface termination of this surface is known, as a reference. The In/Ni LEIS intensity from this surface is 14.9. We calculated the chemical composition and expected In/Ni for each layer 0, 1, 2, 0+1, 1+2.

By comparing In to Ni LEIS intensity ratios with those predicted by known crystallographic models, a direct correlation was established. As shown in Table 6.2, the In/Ni ratio obtained from the (100) surface closely corresponds to that of the $(2\bar{1}0)$ reference surface, providing strong support for model 0+1 as the most accurate description of the (100) surface termination.

Layer	Chemical Composition	In/Ni Ratio Expected Based on (100) Surface
0	In_1Ni_0	0
1	InNi	9.2
2	InNi	9.2
0+1	In_2Ni	18.53
1+2	In_2Ni_2	9.2

Table 6.2: Layer, chemical compositions and expected In-Ni ratio expected from(100) surface.

6.4.5 Oxidation Behaviour

The oxidation behaviour of the (100) surface was investigated using XPS. Initially, the surface was exposed to air for a period exceeding 10 days, after which XPS spectra were recorded. The sample was cleaned by sputtering followed by annealing at temperatures up to 560 °C, and the resulting spectra were compared to those obtained from the air-exposed surface. Subsequently, the surface was cleaned and exposed to controlled oxygen doses of 20 L, 300 L, 600 L and 900 L, with XPS measurements performed after each exposure to monitor changes in the chemical composition of the surface.

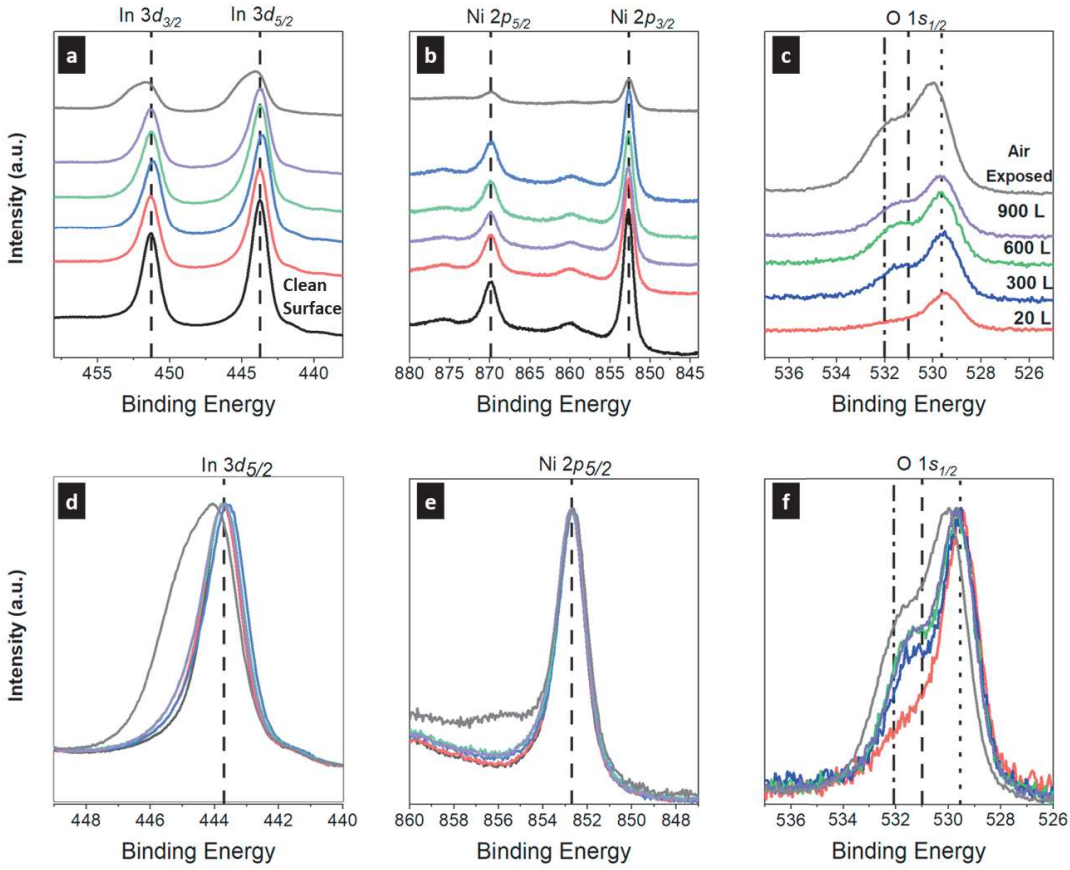


Figure 6.17: (a) to (c) XPS spectra of the clean (after annealing at 560 °C), oxygen exposed and air exposed of $In_3Ni_2(100)$ surface (a: In 3*d*, b: Ni 2*p* and c: O 1*s*). Oxygen exposure ranged from 20-900 L. (d, e, f) In $3d_{5/2}$, O $1S_{1/2}$ and spectra, respectively, after normalising the minimum and maximum intensity between 0 and 1, illustrating the development of a shoulder at higher binding energies. The dotted, dashed and dash dotted lines at 530.2 eV, 531.0 eV and 853.6 eV in (c) correspond to the positions of the oxide, pure oxygen and Ni oxide peaks, as reported in the literature [99, 121, 122]. The dotted lines in (c) indicate the positions of the oxide peaks, while the dashed lines in all other spectra correspond to the core level positions of the respective elements from the clean surface.

Figures 6.17 (a–c) display the XPS spectra corresponding to the core levels of In 3*d*, Ni 2*p* and O 1*s* for surfaces that were cleaned, exposed to oxygen and exposed to air. With increasing oxygen exposure, the In and O core level spectra exhibit the development of shoulder features at higher binding energies. In contrast, the Ni 2*p* core level does not show significant variation between the different oxygen exposures. Figures 6.17 (d–e)

present the In $3d_{5/2}$ and Ni $2p_{3/2}$ spectra, respectively, with their intensities normalised between 0 and 1. This normalisation highlights the emergence of shoulder features in the In and O spectra, while showing the relative invariance of the Ni peak.

The shoulder features observed in the XPS spectra are attributed to the formation of In oxides. In the Ni $2p_{3/2}$ spectra, the main peak corresponds to pure Ni, and there are no clear shoulders compared to the In and O peaks. Following air exposure, the Ni $2p_{3/2}$ spectra remained unchanged, as shown in Figure 6.17 (e), indicating that no oxidation of Ni occurred under these conditions. In contrast, the In $3d_{5/2}$ shoulder becomes more significant and the O $1s_{1/2}$ spectra increase in intensity, with the shoulder feature emerging as the dominant peak, reflecting the enhanced oxidation state of In and oxygen species on the surface.

The XPS spectra were fitted using a Shirley background in combination with a mixed line shape composed of asymmetric Gaussian and Lorentzian functions to accurately determine the peak and shoulder positions and their respective intensities. Figures 6.18 and 6.19 (a–f) show the In $3d_{5/2}$ and Ni $2p_{3/2}$ spectra with fitting for both the clean and oxygen-exposed surfaces. All peak positions reported in this thesis were extracted using this fitting method, with an estimated uncertainty of approximately ± 0.1 eV. Throughout the analysis, a line shape consisting of 40% Gaussian and 60% Lorentzian character was used.

Indium Core Level

As shown in Figure 6.18 (a), the In $3d_{5/2}$ spectrum of the clean surface is characterised by a single peak at 443.75 eV, consistent with pure In. This binding energy closely matches previously reported values for elemental In [112]. Upon exposure to oxygen in the range of 20 to 900 L, the In $3d_{5/2}$ spectra require two components to achieve an accurate fit, as illustrated in Figures 6.18 (b–f). The main peak at 443.75 eV remains attributable to pure In in the In_3Ni_2 surface, while an additional component appears at around 444.90 eV.

This higher binding energy feature, appearing as a shoulder and shifted by 1.1 eV, is attributed to the formation of In_2O_3 on the surface [112]. As the amount of oxygen increases, the oxide-related peak intensity increases, especially at 300, 600 and 900 L, indicating enhanced surface oxidation. Although pure In remains dominant under these controlled conditions, the systematic increase in intensity of the In_2O_3 peak reflects a gradual transformation of the surface composition.

In contrast, air exposure leads to a more significant oxidation effect. As shown in Figure 6.18 (f), the intensity of the oxide peak increases relative to the pure In peak, which signifies a higher surface concentration of In_2O_3. This suggests that air promotes more extensive oxidation than controlled oxygen dosing.

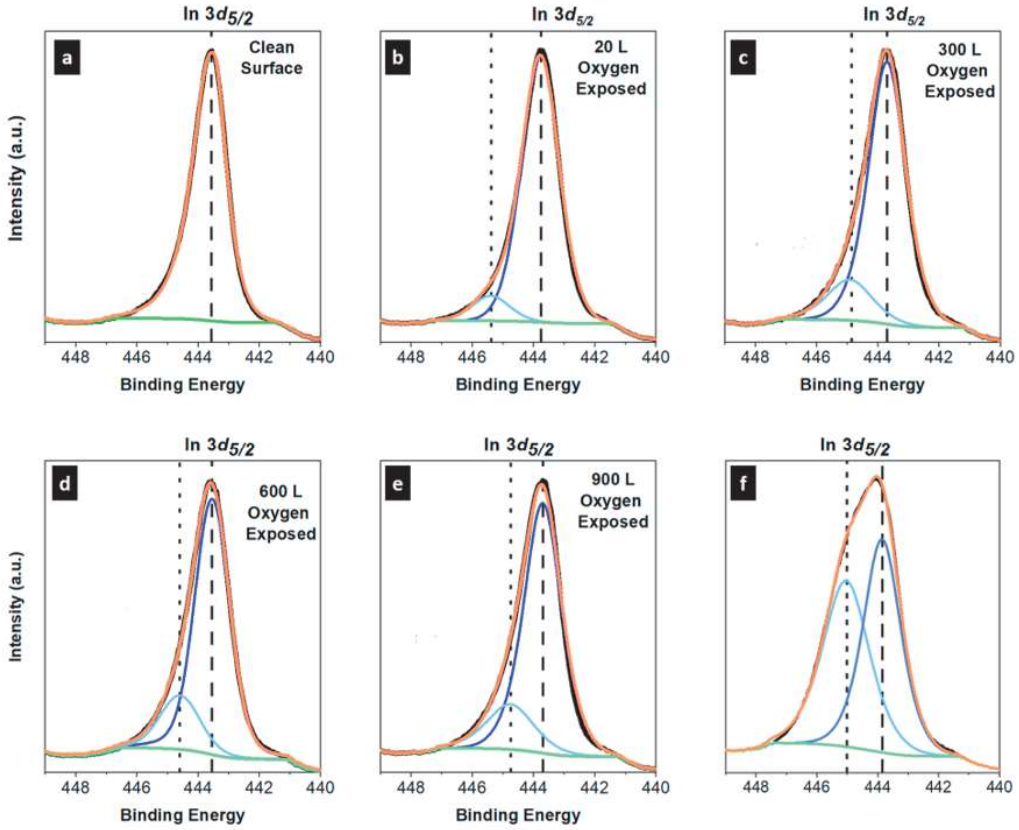


Figure 6.18: In $3d_{5/2}$ XPS spectra of the $In_3Ni_2(100)$ surface after cleaning the surface through sputtering and annealing at 560 °C, with increasing oxygen exposure (a) clean surface. (b) 20 L. (c) 300 L. (d) 600 L. (e) 900 L. (f) Air exposed. Vertical dashed lines in all spectra correspond to the core level position of the clean Ni $2p_{3/2}$, while vertical dot lines in all spectra correspond to the core level position of the oxidised In.

Nickel Core Level

For the clean surface, the Ni $2p_{3/2}$ spectrum can be fitted with a single peak at 852.5 eV, as shown in Figure 6.19 (a). This peak is attributed to pure Ni, with its binding energy closely matching that of pure Ni reported in the literature [111], within the limits of experimental resolution. The evolution of the Ni $2p_{3/2}$ core level with increasing oxygen exposure (20 L–900 L) is illustrated in Figures 5.18 (b–f). Across all exposure levels, the dominant feature remains consistent with pure Ni, indicating the persistence of unoxidised Ni at the surface. However, a subtle feature emerges at approximately 855.54 eV, particularly under air exposure, which is attributed to the formation of Ni hydroxide ($Ni(OH)_2$) [111]. This suggests minor surface oxidation of Ni, probably promoted by ambient conditions rather than controlled oxygen dosing.

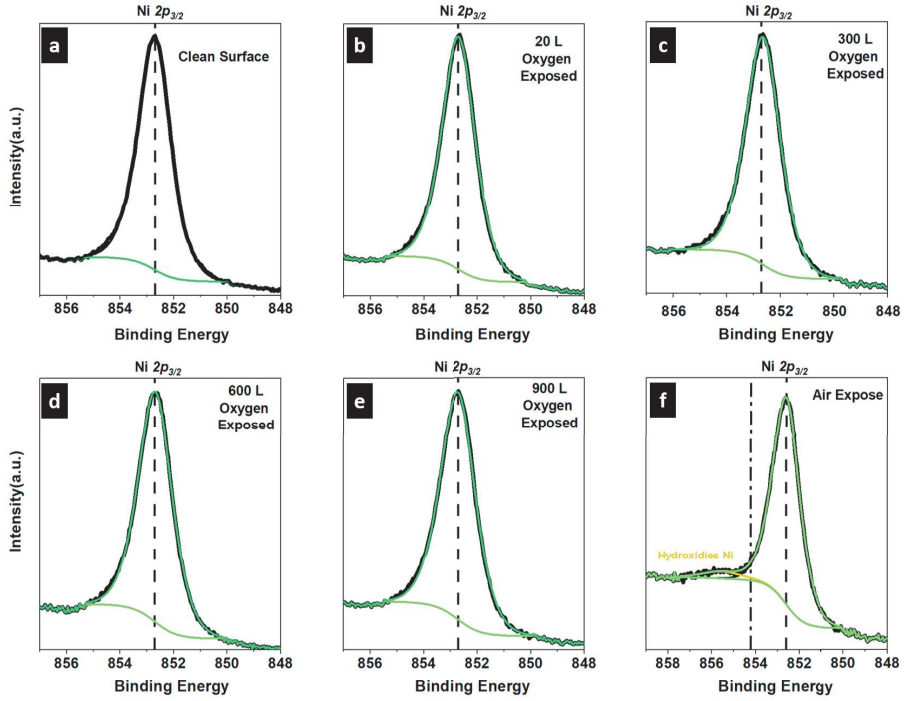


Figure 6.19: Ni $2p_{3/2}$ XPS spectra of the In_3Ni_2(100) surface after clean the surface by sputtering and annealing it at 560 °C and with increasing oxygen exposure (a) clean surface. (b) 20 L. (c) 300 L. (d) 600 L. (e) 900 L. (f) Air exposed. Vertical dashed lines in all spectra correspond to the core level position of the clean Ni $2p_{3/2}$, while vertical dash dot line in air exposed spectra correspond to the core level position of the Ni Hydroxide.

Oxygen Core Level

Figure 6.20 illustrates the evolution of the O $1s_{1/2}$ peak as the $In_3Ni_2(100)$ surface is exposed to increasing amounts of oxygen, ranging from 20 L to 900 L, as well as after air exposure. With an increase in oxygen dosage, the intensity of the peak associated with molecular oxygen decreases, while the contribution from oxidised species increases significantly. This trend indicates that the surface is gradually oxidising.

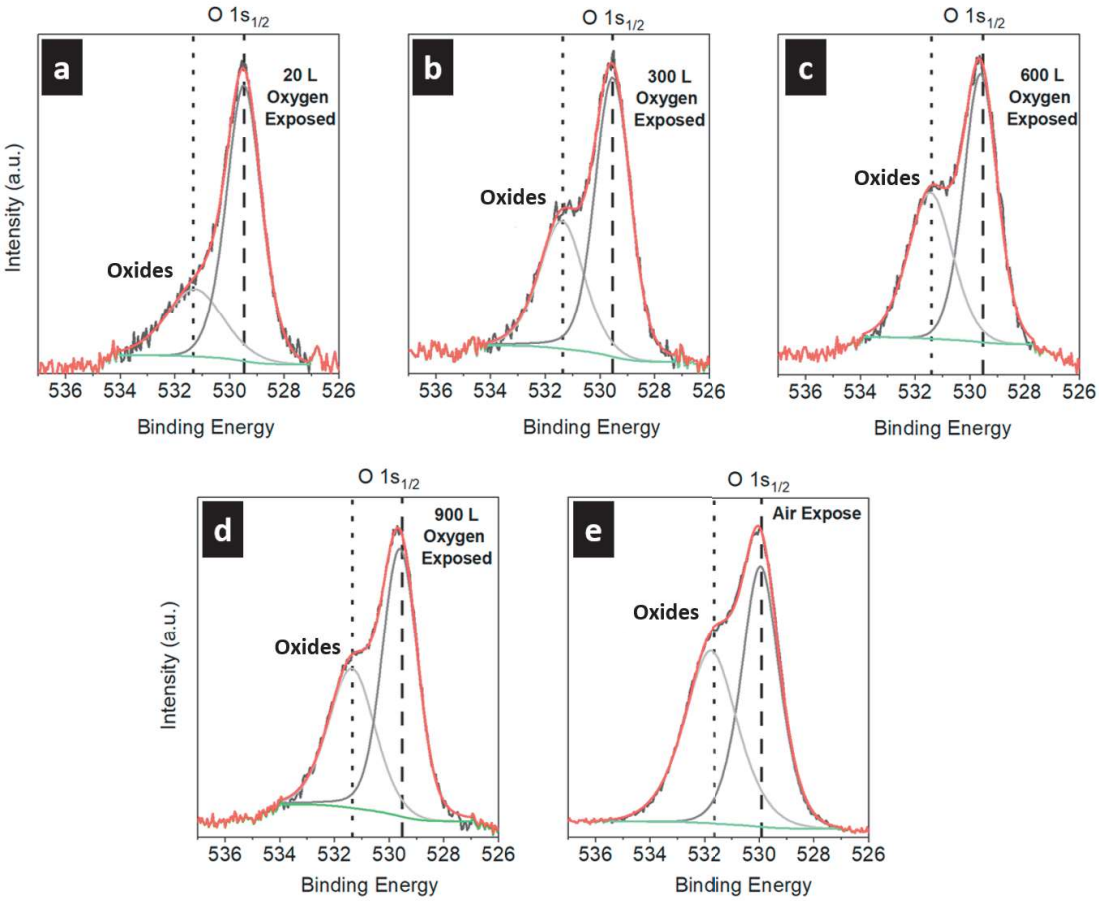


Figure 6.20: O $1s_{1/2}$ XPS spectra of the $In_3Ni_2(100)$ surface with increasing oxygen exposure (a) 20 L. (b) 300 L. (c) 600 L. (d) 900 L. (e) Air exposed. Vertical dashed lines in all spectra correspond to the core level position of the O $1s_{1/2}$, while Vertical dot lines in all spectra correspond to the core level position of the oxidised O.

Chemical Composition

Following surface cleaning and subsequent exposure to oxygen and air, the chemical composition was qualitatively assessed. Elemental chemical concentrations were estimated by analysing the fitted peak areas of In $3d_{5/2}$, Ni $2p_{3/2}$, O $1s$ and C $1s$ in the XPS spectra, normalised by their respective photoemission cross sections.

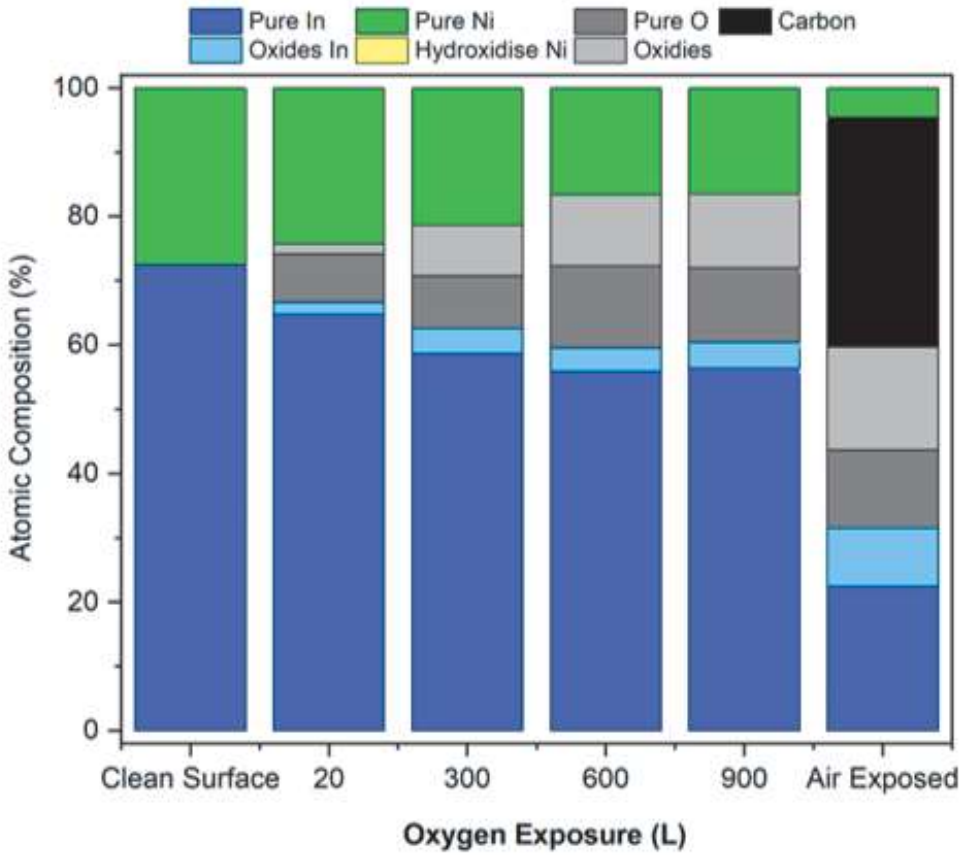


Figure 6.21: The chemical composition of the $In_3Ni_2(100)$ surface after annealing at 560 °C and with increasing oxygen exposure (20 L-900 L). The atomic composition of the clean and air exposed surfaces is also given for comparison. The composition was determined from the Ni $2p_{3/2}$, C $1S_{1/2}$ and O $1S_{1/2}$ XPS peaks.

A detailed compositional assessment indicates that the relative atomic percentage of pure In decreases from approximately 72% on the clean surface to 56% after exposure to 900 L of oxygen. The same trend is observed for Ni, with its concentration decreasing from 28% to around 17%. The proportion of oxidised In increases to approximately 4%,

while there is no presence of oxidised Ni, with only about 0.15% Ni hydroxide detected.

In addition, carbon contamination is apparent, with C 1*s* contributing around 36% after air exposure. The oxygen concentration, which comes mainly from surface oxides, increases to around 16%, indicating an increase in oxidation due to extended exposure conditions.

6.5 Summary

This work provides the first comprehensive characterisation of the (100) surface of In_3Ni_2, highlighting its atomic structure, surface composition and oxidation behaviour. Various techniques were used, including XPS, LEIS, STM and LEED analyses.

XPS and LEIS data reveal a preferential sputtering effect, in which In is more readily removed from the surface than Ni. Following annealing, In migrates from the bulk to the surface, a phenomenon attributed to its relatively lower surface free energy.

LEED patterns and STM imaging reveal a (1×1) surface symmetry, characterised by a well-defined rectangular arrangement. Although the central surface regions exhibited consistent agreement with this structure, deviations observed near the edges, such as changes in step height and atomic contrast, suggest differences in surface orientation or the presence of localised impurity phases.

Further insight was gained by correlating the observed step heights from STM, the LEIS signal intensity distributions and the density of states calculations with theoretical models based on the $(2\bar{1}0)$ surface. This integrated analysis supports a termination consisting of In atoms at the outermost layer, coordinated with underlying Ni atoms. The isolated presence of Ni sites at the surface is expected to contribute positively to the catalytic activity of the material.

7 | Comparative Study of In_3Ni_2 (001), (2$\bar{1}$0) and (100) Surfaces

7.1 Introduction

This chapter compares the results of the low-index surfaces of In_3Ni_2, namely the (001), (2$\bar{1}$0), and (100) surfaces, and explores how crystallographic orientation influences surface termination, composition, segregation behaviour, and reactivity. As discussed in Chapters 4, 5, and 6, all surfaces were prepared using similar cleaning procedures. This approach ensures that clean, well-ordered terminations are produced, thus enabling direct comparison between different orientations.

The (001), (2$\bar{1}$0), and (100) low-index surfaces each present distinct atomic terminations, which provide a clear comparison of how crystallographic orientation affects the composition and bonding between atoms. As shown in the side views of these three surfaces in Figure 7.1(a–c), the (001) surface can be characterised by alternating layers of In and Ni, forming a sequence of five atomic planes. In contrast, the (2$\bar{1}$0) surface consists of a stacking of identical planes with a mixed distribution of In and Ni atoms. The (100) surface exhibits either a stacking of In planes or mixed In–Ni planes.

The (001) and (100) surfaces exhibit terminations characterised by In atoms in the top layer that form bonds with Ni atoms in the subsequent layer, as detailed in Chapters 4.4, 5.4, and 6.4. In contrast, the terminating layer of the (2$\bar{1}$0) surface includes both In and Ni

atoms within the same layer.

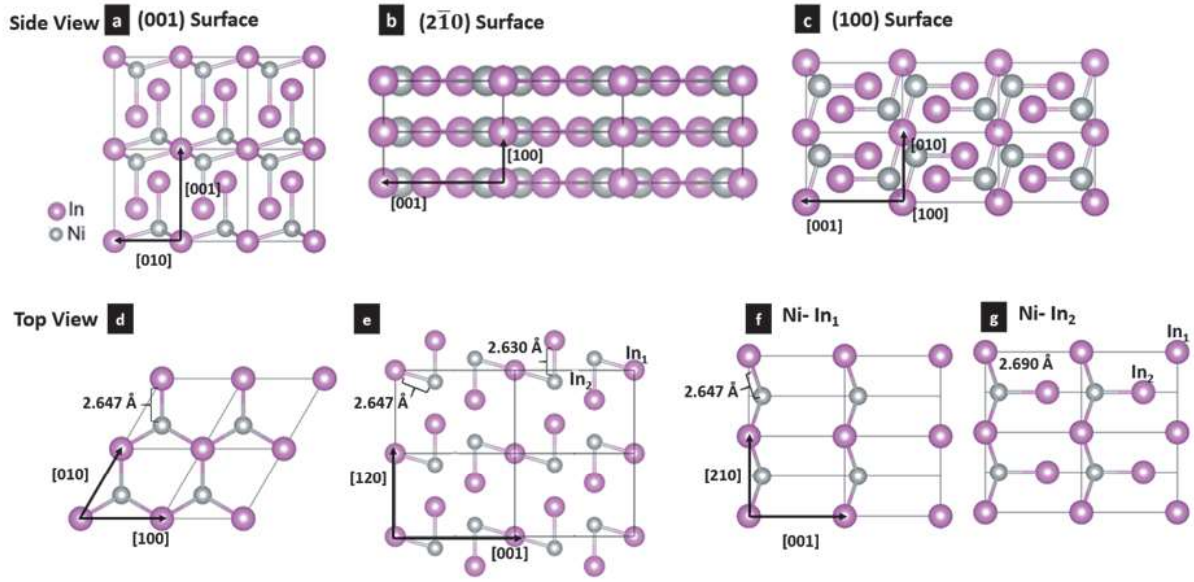


Figure 7.1: Side view representations of the In_3Ni_2 crystal structure along different crystallographic orientations, (a) (100) surface. (b) (2$\bar{1}$0) surface and (c) (001) surface. (d-g) The in-plane atomic structures of the terminating planes for the (001), (2$\bar{1}$0) and (100) surfaces. For the (001) and (100) surfaces, the atoms in the top two layers are considered, whereas for the (2$\bar{1}$0) surface, only the atoms in the top layer are considered. The bond-lengths between In and Ni atoms for each surface are also provided.

The length of the bond between the In_1 atom located at the corner of the unit cell and Ni atoms for three different surfaces is measured at approximately 2.673 Å (Figure 7.1 (f-g)). Considering the bond between the Ni and the In_2 atom within the unit cell, the shortest distance is observed for the (2$\bar{1}$0) surface at 2.630 Å, followed by the (100) surface at 2.690 Å. This observation indicates that the (100) surface exhibits the longest In_1–Ni interaction among the three orientations. The bond lengths are illustrated from top views of the surfaces in Figure 7.1 (d–g).

	(100) Surface	(001) Surface	(2$\bar{1}$0) Surface
Ni-In$_1$	2.673 Å	2.673 Å	2.673Å
Ni-In$_2$	2.690 Å		2.630 Å

Table 7.1: Bond lengths between In and Ni atoms in In_3Ni_2 for the (001),(2$\bar{1}$0) and (100) surface orientations. In_1 refers to the In atom located at the corner of the unit cell, while In_2 denotes the In atom within the cell interior.

Furthermore, the atomic densities of In_3Ni_2 vary with crystallographic orientation, reflecting differences in surface composition. These were determined from the top-view layers shown in Figure 7.1 (d–f) by counting the number of In and Ni atoms per unit area. Additionally, the atomic density of the (100) surface was calculated with the In_2 atoms excluded from the second layer.

As shown in Table 7.2, the (2$\bar{1}$0) surface exhibits the highest In surface density at 0.073 atoms/Å^2, while the (001) and (100) surfaces display densities of 0.059 atoms/Å^2 and 0.044 atoms/Å^2, respectively. As shown in Table 7.2, the (2$\bar{1}$0) surface exhibits the highest In surface density at 0.073 atoms/Å^2, which display densities of 0.059 atoms/Å^2 for (001) surface and 0.044 atoms/Å^2 for (100) surface.

In contrast, the (001) surface demonstrates a balanced distribution of In and Ni atoms, each contributing 0.059 atoms/Å^2, resulting in a total surface density of 0.118 atoms/Å^2. The (100) surface, while showing a similar uniform elemental distribution, exhibits the lowest overall atomic density at 0.088 atoms/Å^2. These variations in the densities of In and Ni per unit area provide a rational basis for surface reactivity, which will be discussed later.

7.2 Surface Orientation Dependent Chemical Composition

This section presents a comparative analysis of the differently orientated surfaces of In_3Ni_2. XPS provided information on both the surface and near-surface regions, providing insight into elemental distribution several nanometres beneath the surface. In contrast, LEIS, with

	(100) Surface	(001) Surface	(2$\bar{1}$0) Surface
In atoms / unit cell	1	1	3
Ni atoms / unit cell	1	1	2
Total atoms / unit cell	2	2	5
Unit cell area (Å^2)	22.924	17.172	40.964
In density (atoms/Å^2)	0.044	0.059	0.073
Ni density (atoms/Å^2)	0.044	0.059	0.049
Total density (atoms/Å^2)	0.088	0.118	0.122

Table 7.2: Calculated atomic density per unit cell for the (001), (100) and (2$\bar{1}$0) surfaces of In_3Ni_2.

its extreme surface sensitivity, quantified the elemental intensities of the outermost atomic layer, thus providing a direct measure of the surface termination.

7.2.1 XPS Study

As shown in Figure 7.2, the In/Ni XPS surface atomic composition ratios for the three surfaces were measured after sputtering and annealing at temperatures reaching approximately 560 °C. Sputtering resulted in a reduction in the In signal for all surfaces, indicating a preferential removal of In, with the effect being less notable for the (2$\bar{1}$0) surface compared with the (001) and (100) surfaces. This behaviour can be explained by the bond lengths between In and Ni atoms calculated from the top-view surface models (Figures 7.1 (d–f)). The Ni–In_2 bond is shortest on the (2$\bar{1}$0) surface at 2.630 Å, in contrast to 2.673 Å for both the (001) and (100) surfaces. Longer bonds generally indicate weaker atomic interactions, making In atoms on the (001) and (100) surfaces more weakly bound and therefore more prone to sputtering than those on the (2$\bar{1}$0) surface.

After annealing to 560 °C, all three surfaces exhibit an increased In to Ni ratio, indicat-

ing preferential In segregation. The $(2\bar{1}0)$ surface exhibits the highest segregation despite its shortest Ni–In_2 bond length of around 2.630 Å. This may suggest that the behaviour in In_3Ni_2 is governed by the surface geometry rather than by the bond length, as revealed in the views of the whole unit cell. As shown in Figure 7.1, the $(2\bar{1}0)$ surface has an open layer, while the (001) and (100) surfaces have more compact layered structures that partially shield the In subsurface, thus limiting segregation.

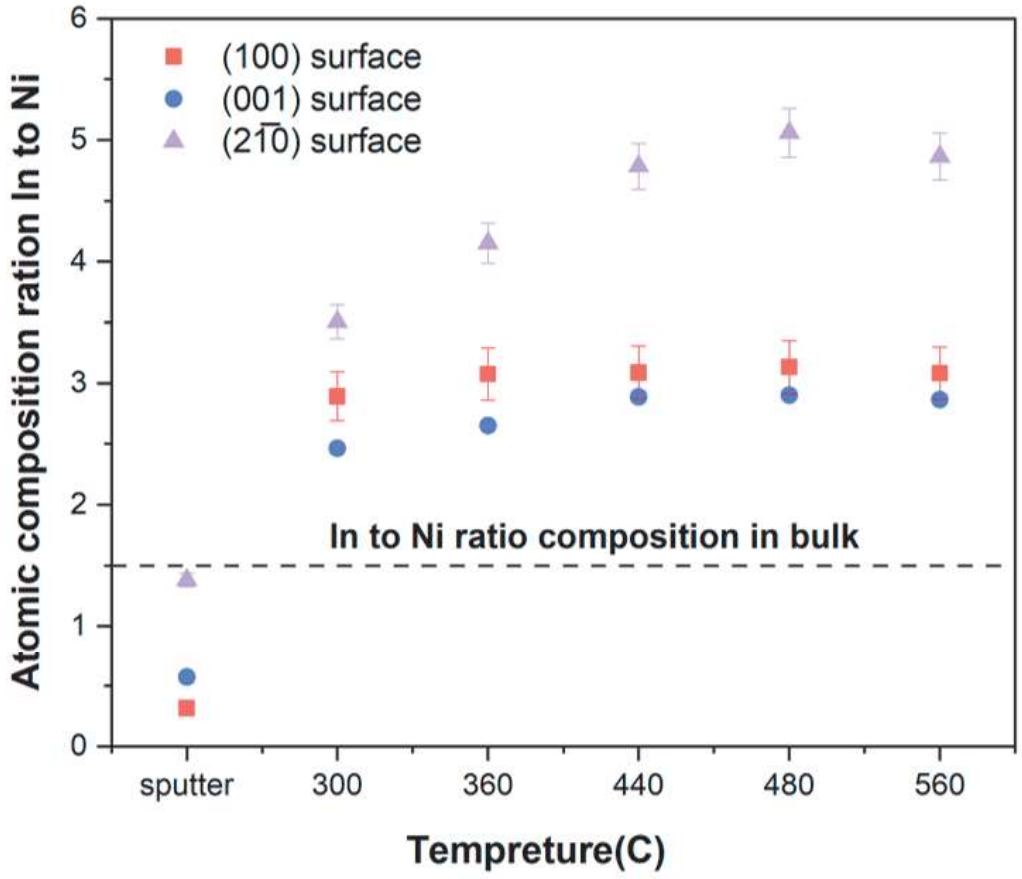


Figure 7.2: In/Ni atomic ratio on the In_3Ni_2 (100), $(2\bar{1}0)$ and (001) surfaces, as determined by XPS following sputtering and annealing at temperatures ranging from 360 °C to 560 °C. The data highlight the variation in surface composition as a function of both crystallographic orientation and annealing temperatures.

7.2.2 LEIS Study

Figure 7.3 illustrates the impact of sputtering and annealing on the surface chemical composition by presenting the intensity ratios of In and Ni LEIS for the (001), (100) and $(2\bar{1}0)$ surfaces. After sputtering, the In signal decreases significantly on all three surfaces, while the Ni signal dominates. This behaviour reflects the preferential sputtering of In, which results in Ni enrichment at the outermost layer of each surface. These findings are consistent with the XPS results.

Upon annealing the three surfaces to 480 °C, the intensity ratio of In to Ni increases significantly across all three crystallographic orientations, indicating In surface segregation to the topmost layer. All three surfaces exhibit an increased In to Ni ratio, consistent with the XPS results, which indicate preferential segregation of In after the surfaces are annealed to high temperatures. The (001) surface shows the highest ratio, indicating a larger surface concentration of In that causes surface segregation and a more In-rich termination. In contrast, the $(2\bar{1}0)$ surface exhibits the lowest concentration of In, which shows how the surface orientation affects segregation behaviour. The observed variation in surface composition after sputtering and annealing can be explained by examining the atomic arrangements of the (100), $(2\bar{1}0)$ and (001) surfaces, as illustrated in the crystal structure models provided (Figure 7.1).

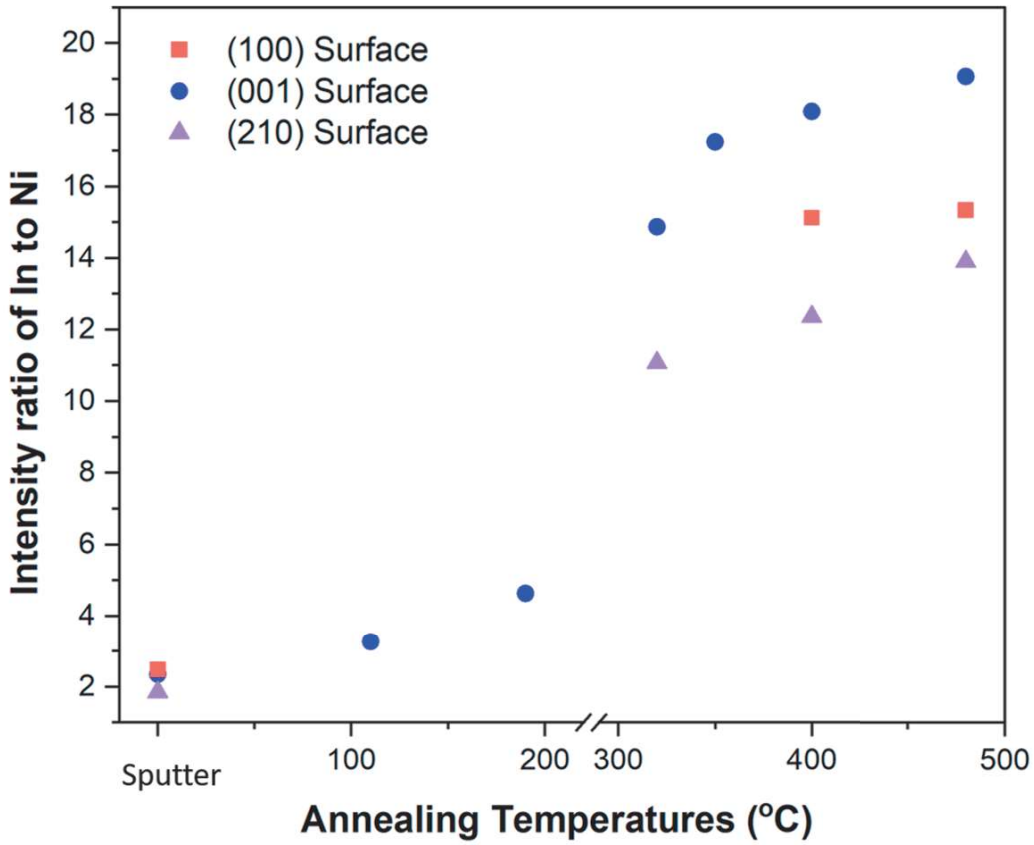


Figure 7.3: In/Ni intensity ratios obtained by LEIS for the In_3Ni_2 (001), (100) and (2$\bar{1}$0) surfaces following sputtering and annealing to 480 °C. These ratios reflect the elemental distribution at the outermost atomic layer.

To interpret these results, the number of In and Ni atoms was calculated for each surface based on the top-view structure of the ideal model (Figure 7.1 (d–g)). The (100) surface presents a ratio of 2:1, indicating twice as much In as Ni, followed by the (2$\bar{1}$0) surface with a ratio of 1.5:1. In contrast, the (001) surface shows an equal distribution of In and Ni (1:1). The measured In/Ni intensity ratios were then referenced to the (2$\bar{1}$0) surface. We chose this surface because it terminates with identical bulk planes of the known composition of In_3Ni_2. This surface yields a LEIS intensity ratio of 14.9. Based on this information, we estimated the In–Ni ratio for the other two surfaces, which are presented in Table 7.3 and compared with the experimentally observed ratio. The comparison revealed a clear correlation for the (100) surface. However, a discrepancy is observed for the (001) sur-

face, where the experimental ratio is much higher than estimated. We attribute this to surface reconstruction that may alter the atomic arrangement and, consequently, the surface composition. We note that, as discussed in Chapter 4.4, the (001) surface undergoes a reconstruction, whereas the other two surfaces remain bulk-terminated.

	(100) Surface	(001) Surface	(2$\bar{1}$0) Surface
Chemical Composition	In_2Ni	InNi	In_3Ni_2
Expected In/Ni Ratio from Model Structure	2:1	1:1	1.5:1
LEIS Intensity Ratio of In to Ni based on (2$\bar{1}$0) Surface	18.53	9.2	14.9
Measured LEIS Intensity Ratio of In to Ni	15.3	19.06	14.9

Table 7.3: Chemical compositions of the (100), (2$\bar{1}$0) and (001) surfaces and In to Ni ratio, the expected ratios are calculated from model structures, while the measured values are based on LEIS intensity ratios obtained from the (2$\bar{1}$0) surface.

7.3 Reactivity of Crystallographic Surfaces

The reactivity of crystalline materials is influenced by their crystallographic orientation, which determines the surface atomic density. Oxygen and hydrogen, both important in catalytic processes, show different behaviours on different crystal surfaces. Comparing the (100), (2$\bar{1}$0) and (001) surfaces provides a clear view of how the structure and composition of the surface affect their reactivity.

7.3.1 Surface Reactivity with Oxygen

All In_3Ni_2 surfaces were exposed to air for varying durations, approximately 10 days for the (001) and $(2\bar{1}0)$ surfaces and around 18 days for the (100) surface. However, both the (001) and (100) surfaces required only a single sputtering and annealing cycle to clean the surface. In contrast, the $(2\bar{1}0)$ surface exhibited a higher degree of contamination, as indicated by the O peak, requiring three subsequent cleaning cycles to achieve a higher degree of surface cleanliness.

In particular, XPS measurements revealed the rapid reappearance of the O peak on the $(2\bar{1}0)$ surface within 12 hours under UHV conditions, suggesting a higher reactivity towards oxygen. Consequently, this surface required an in situ cleaning cycle for each measurement to ensure accurate characterisation, a behaviour that was not observed for the other surfaces.

Following air exposure, the C $1s_{1/2}$ signal was detected on both the (100) and (001) surfaces. However, no significant C $1s_{1/2}$ signal was observed on the $(2\bar{1}0)$ surface, suggesting that the quantity present was insufficient for detection in the XPS spectrum. The presence of carbon, not being a basic component of the bulk material, is likely due to surface contamination introduced during sample preparation, possibly from the diamond paste utilised in surface polishing [45].

Indium Oxidation Behaviour

This section examines how the surface intensities of In and Ni vary with crystallographic orientation and evaluates the effect of oxygen exposure on surface composition. As shown in Figure 7.5, the $(2\bar{1}0)$ surface exhibits a higher ratio of oxidised In to metallic In compared with the (001) and (100) surfaces at all oxygen exposures, indicating that the $(2\bar{1}0)$ surface is more reactive. This behaviour can be attributed to differences in surface atomic density: the $(2\bar{1}0)$ surface has the highest In atomic density (0.073 atoms/Å^2), followed by the (001) surface (0.059 atoms/Å^2) and the (100) surface (0.044 atoms/Å^2). The increased

density on the $(2\bar{1}0)$ surface enhances the availability of reactive In sites for oxygen and results in oxidation. In contrast, lower In densities on the (001) and (100) surfaces result in comparatively reduced oxide formation.

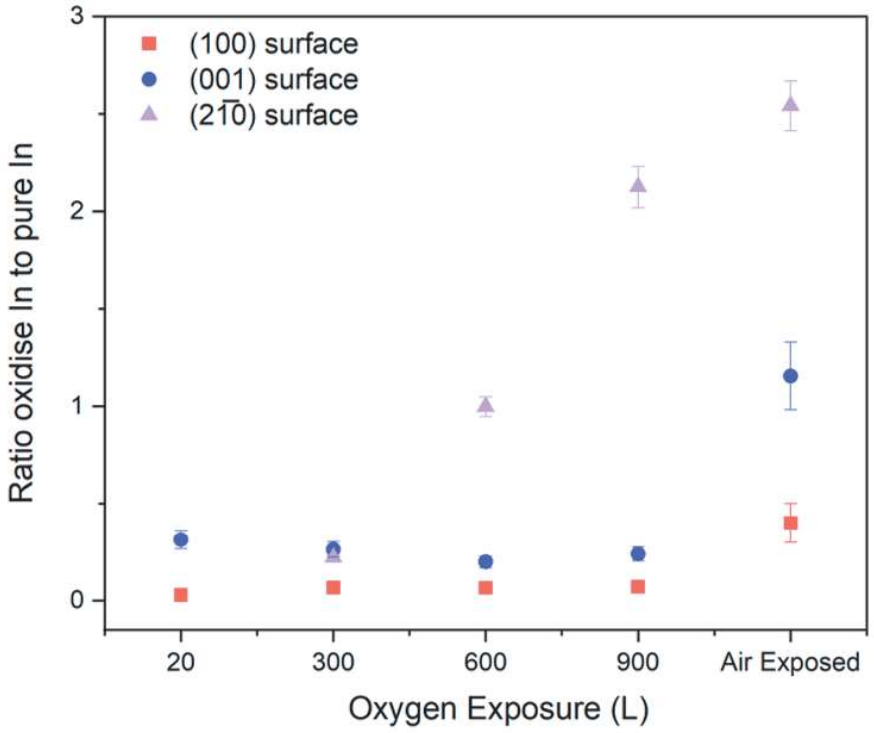


Figure 7.4: Ratio of pure In to In oxide on the $In_3Ni_2(100)$, $(2\bar{1}0)$ and (001) surfaces following exposure to air and oxygen doses ranging from 20 L to 900 L. The data illustrate the evolution of surface oxidation behaviour as a function of crystallographic orientation and oxygen exposure.

Nickel Oxidation Behaviour

The higher Ni oxide to pure Ni ratio observed for the (001) surface compared with the $(2\bar{1}0)$ surface across all oxygen exposures can be explained by differences in surface coordination, as illustrated in Figure 7.4. The (001) surface has a higher surface density of Ni atoms (0.059 atoms/Å^2) than the $(2\bar{1}0)$ surface (0.049 atoms/Å^2), which increases oxidation by providing more reactive sites per unit area. On the (100) surface of Ni, oxidation was minimal and did not produce a measurable signal, preventing reliable quantification

of oxide formation.

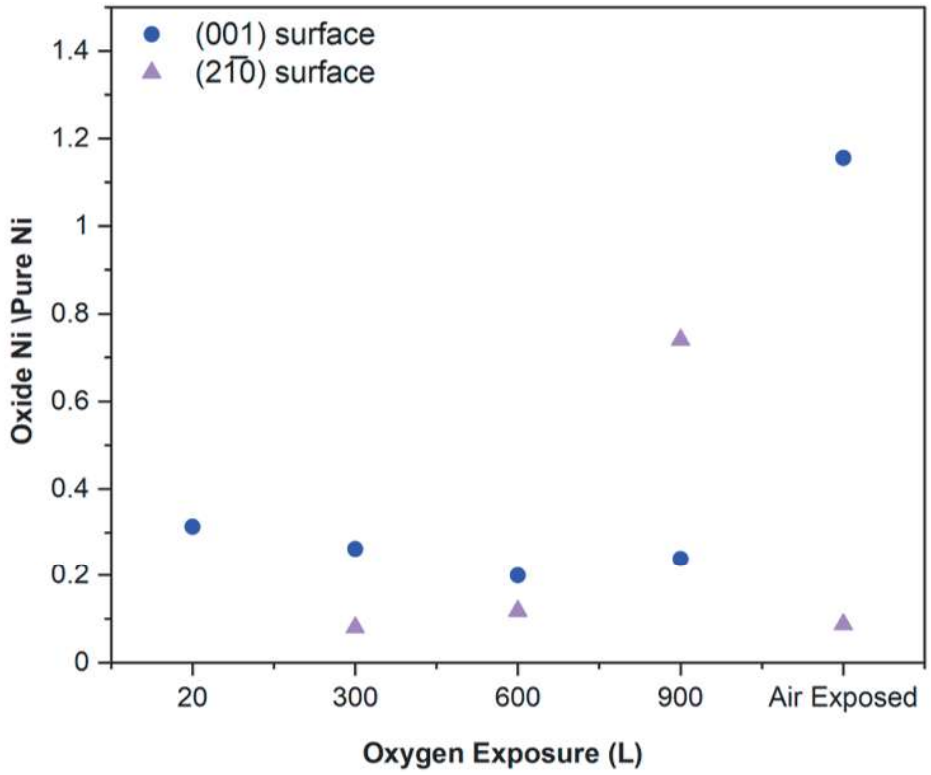


Figure 7.5: Ratio of pure nickel to nickel oxides on the $In_3Ni_2(2\bar{1}0)$ and (001) surfaces following air exposure and subsequent oxygen dosing ranging from 20 L to 900 L.

7.3.2 Surface Reactivity with Hydrogen

TThe (2$\bar{1}$0) surface was found to be more reactive to oxygen, while the (001) surface was shown to be more reactive to hydrogen than the (100) and (2$\bar{1}$0) surfaces. This tendency is caused by the fact that the (001) plane has a higher surface density of Ni atoms (0.059 atoms/Å^2) than the (2$\bar{1}$0) and (100) surfaces (0.049 and 0.044 atoms/Å^2, respectively). This means that there are more active sites for hydrogen adsorption and dissociation. The variations in surface atomic density and coordination are what make these low index surfaces respond differently to oxygen and hydrogen.

Similar behaviour has been reported for the AlNi(110) surface [61], which comprises the same Ni and Al terminations. Density functional theory (DFT) and surface science

studies reveal that molecular hydrogen adsorption is hindered by an activation barrier, whereas atomic hydrogen readily occupies the Ni–Ni bridge sites, restructuring the surface and eliminating its rippled relaxation. LEED and nuclear reaction analysis (NRA) indicate 0.5 monolayer coverage, producing a weak c(2×2) pattern and showing H-induced surface modifications (Figure 7.6(a)). The enhanced hydrogen reactivity of the (001) surface in this study is therefore consistent with the established role of Ni-rich sites and favourable surface geometries in promoting hydrogen binding and activation (Figure 7.6 (b–c)).

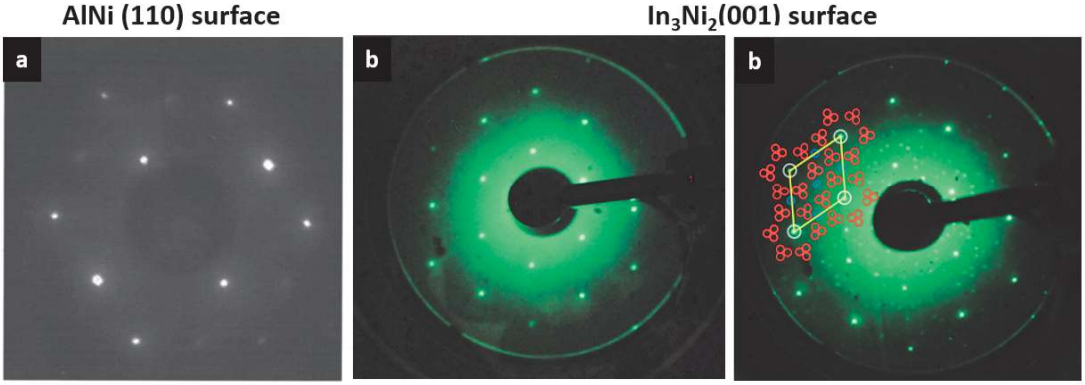


Figure 7.6: (a) LEED pattern of the AlNi(110) surface after exposure H [61]. (b) LEED pattern of the freshly prepared In_3Ni_2 (001) surface displaying a (1×1) structure. (c) LEED pattern of the same surface after firing of the TSP, revealing three domains of the c($2\sqrt{3} \times 4$) rectangular reconstruction.

7.4 Summary

In conclusion, we investigate the comparison of the (001), (100) and ($2\bar{1}0$) surfaces of In_3Ni_2, demonstrating that the crystallographic orientation surfaces of In_3Ni_2 determines surface termination, atomic arrangement, segregation behaviour and reactivity to oxygen and hydrogen. The (001) and (100) surfaces terminate with In atoms in the top layer that are bonded to Ni atoms in the second layer. The ($2\bar{1}0$) surface also terminates with In bonded with Ni, but both In and Ni are in the same layer. Similarly, the ($2\bar{1}0$) surface has

the highest In density, the (001) surface has a balanced In-Ni distribution and the (100) surface has the lowest overall atomic density. Each surface has different bond lengths and surface densities. These structural changes explain why bonding is different in various forms and help us to understand how surface reactivity depends on orientation.

XPS measurements demonstrate that sputtering mostly removes In from all surfaces. The impact is strongest on the (001) and (100) surfaces due to weaker Ni–In bonds. Annealing at 560 °C encourages In segregation on all surfaces, but segregation is more notable on the $(2\bar{1}0)$ surface, which is more open than the compact surfaces (001) and (100) that partially shield subsurface In.

LEIS measurements confirm these patterns, indicating In depletion after sputtering and enrichment after annealing at 480 °C. The (001) surface has the most In segregation, whereas the $(2\bar{1}0)$ surface has the least. These surfaces correspond to the ideal structural models , however, the (001) surface has a higher ratio of In to Ni than predicted, which may be related to surface reconstruction. We note that the (001) surface undergoes c$(2\sqrt{3}\times4)$ reconstruction upon exposure to residual hydrogen in the UHV chamber, whereas the other two surfaces remain (1×1).

Finally, the reactivity of these low index surfaces is strongly influenced by the surface atomic density and coordination. The $(2\bar{1}0)$ surface is more reactive to oxygen due to its higher In density, the (001) surface is more reactive to hydrogen due to its higher Ni density and the (100) surface shows minimal oxidation, without measurable signal.

8 | Conclusions and Outlook

Intermetallic compounds are of significant interest in catalysis and surface science because of their structural stability and tunable electronic properties. While the surfaces of some intermetallic compounds have been intensively studied, the surfaces of the specific systems presented in this thesis have not been previously investigated. A comprehensive understanding of their surface structure is important for catalysis, as the atomic structure, site specific bonding and surface terminations can influence chemical reactivity and selectivity.

This thesis investigates In_3Ni_2 intermetallic compound, with a focus on the (001), (100) and $(2\bar{1}0)$ surfaces. The study examines their atomic structure, surface termination, oxidation behaviour and hydrogen reactivity. A combination of surface sensitive techniques, including XPS, LEIS, STM and LEED, is used to investigate how crystallographic orientation affects surface termination, surface structure and chemical behaviour.

The $(2\bar{1}0)$ surface exhibits the highest In atomic density, while the (001) surface shows a balanced distribution of In and Ni and the (100) surface has the lowest In atomic density. Furthermore, the distribution of In and Ni within the topmost surface layer differs across various surfaces. These structural variations underpin differences in atomic bonding and provide a basis for understanding the orientation dependent surface reactivity.

Surface composition studies using XPS and LEIS revealed preferential sputtering of In due to its lower surface binding energy, with the degree of depletion depending on surface geometry. The highest In depletion upon sputtering is observed on the (001) and

(100) surfaces, whereas the $(2\bar{1}0)$ surface shows a smaller reduction in In signal, reflecting the weaker Ni–In bonding on the (001) and (100) surfaces, as consistently confirmed by both XPS and LEIS measurements. Following annealing, In segregation from the bulk is higher on the (001) surface, indicating that atomic arrangement, rather than bond length, is the primary factor influencing surface segregation.

LEED and STM analysis demonstrated that all three surfaces maintain a (1×1) symmetry, however, distinct orientation-dependent features are observed. The (001) surface, however, undergoes a three-domain $c(2\sqrt{3}\times4)$ reconstruction under hydrogen exposure in the UHV chamber, whereas the other two surfaces remain unchanged under the same conditions. Both LEED and STM reveal the $c(2\sqrt{3}\times4)$ reconstruction. The $(2\bar{1}0)$ surface exhibited bias-dependent variations in atomic contrast between In atoms located at the corner and inside the unit cell and Ni atoms, emphasising the influence of tunnelling conditions on STM imaging.

The measured step heights for the (001), $(2\bar{1}0)$ and (100) surfaces agree with those predicted by the bulk crystal structure. On the (001) surface, the main step height measured 5.2 ± 0.3 Å, with splits into sub-steps of 3.5 ± 0.2 Å and 1.7 ± 0.3 Å. The $(2\bar{1}0)$ surface had a major step height of 2.3 ± 0.02 Å, which is half of the bulk lattice constant. The observed step height of 3.75 ± 0.03 Å for the (100) surface closely corresponded to $a\frac{\sqrt{3}}{2}$.

The combined insights from STM, LEIS intensity distributions, DFT and surface energy calculations indicate that the (001) and (100) surfaces are characterised by In-terminated layers bonding to underlying Ni planes, while the $(2\bar{1}0)$ surface exhibits a mixed In–Ni top layer. This structural arrangement highlights the stability of intermetallic bonding, while also revealing spatially isolated Ni atoms at the surface, an arrangement considered especially valuable for catalytic performance.

The chemical reactivity with oxygen and hydrogen is influenced by surface atomic density and coordination. The $(2\bar{1}0)$ surface exhibits the highest In oxidation due to its greater In density, while the (001) surface shows higher Ni oxidation and reactivity toward

hydrogen, due to its higher Ni density. In contrast, the (100) surface demonstrates minimal reactivity to oxygen and hydrogen, consistent with its lower In atomic densities.

The findings establish clear correlations between crystallographic orientation, surface atomic structure and chemical reactivity, providing a fundamental understanding of intermetallic surface chemistry and guiding the rational design of In_3Ni_2 based catalytic materials.

Future Studies

This thesis provides significant insight into the surface structure and reactivity of In_3Ni_2. However, various limitations highlight opportunities for further research. In particular, the valence electronic structure was not directly measured. Ultraviolet photoelectron spectroscopy (UPS) could measure this, as it is highly sensitive to the valence band and states near the Fermi level, complementing XPS, which examines core level composition. UPS, combined with density of states calculations and STM simulations, would provide further assignment of surface terminations and contributions of In and Ni orbitals to surface stability and reactivity.

Combining these surface sensitive techniques with in situ or operando methods would clarify how In–Ni bonding affects catalytic activity and selectivity, thereby advancing the rational design of intermetallic catalysts. In addition, the interaction of In_3Ni_2 with organic molecules, such as C_{60} is an interesting area for further research. These investigations would help us understand how charge transfer occurs and how chemistry works at the interface. They would also give us a good idea of how useful In_3Ni_2 surfaces may be for hybrid electrical or catalytic applications.

Bibliography

[1] J. Westbrook, "Applications of intermetallic compounds," *MRS Bulletin*, vol. 21, no. 5, pp. 26–29, 1996.

[2] M. Armbrüster, R. Schlögl, and Y. Grin, "Intermetallic compounds in heterogeneous catalysis a quickly developing field," *Science and Technology of Advanced Materials*, 2014.

[3] A. Alvarez, A. Bansode, A. Urakawa, A. V. Bavykina, T. Wezendonk, M. Makkee, J. Gascon, and F. Kapteijn, "Challenges in the greener production of formates/-formic acid, methanol, and DME by heterogeneously catalyzed CO_2 hydrogenation processes," *Chemical Reviews*, vol. 117, no. 14, pp. 9804–9838, 2017.

[4] C. Quilis, N. Mota, E. Millán, B. Pawelec, and R. M. Navarro Yerga, "Application of intermetallic compounds as catalysts for the selective hydrogenation of CO_2 to methanol," *ChemCatChem*, vol. 16, no. 14, p. e202301496, 2024.

[5] M. Armbrüster, K. Kovnir, M. Friedrich, D. Teschner, G. Wowsnick, M. Hahne, P. Gille, L. Szentmiklósi, M. Feuerbacher, M. Heggen *et al.*, "A_l13Fe_4 as a low cost alternative for palladium in heterogeneous hydrogenation," *Nature Materials*, vol. 11, no. 8, pp. 690–693, 2012.

[6] M. Armbrüster, K. Kovnir, M. Behrens, D. Teschner, Y. Grin, and R. Schlögl, "Pd-Ga intermetallic compounds as highly selective semihydrogenation catalysts," *Journal of the American Chemical Society*, vol. 132, no. 42, pp. 14 745–14 747, 2010.

[7] K. Nozawa, N. Endo, S. Kameoka, A. Pang Tsai, and Y. Ishii, "Catalytic properties dominated by electronic structures in PdZn, NiZn, and PtZn intermetallic compounds," *Journal of the Physical Society of Japan*, vol. 80, no. 6, p. 064801, 2011.

[8] W. Sachtler, "Chemisorption complexes on alloy surfaces," *Catalysis Reviews—Science and Engineering*, vol. 14, no. 1, pp. 193–210, 1976.

[9] C. Schmetterer, H. Flandorfer, C. Lengauer, J.-P. Bros, and H. Ipser, "The system Ga–Ni: A new investigation of the Ga-rich part," *Intermetallics*, vol. 18, no. 2, pp. 277–285, 2010.

[10] M. Wencka, J. Kovač, V. C. Dasireddy, B. Likozar, A. Jelen, S. Vrtnik, P. Gille, H. J. Kim, and J. Dolinšek, "The effect of surface oxidation on the catalytic properties of Ga_3Ni_2 intermetallic compound for carbon dioxide reduction," *Journal of Analytical Science and Technology*, vol. 9, no. 1, pp. 1–10, 2018.

[11] C. Li, Y. Chen, S. Zhang, S. Xu, J. Zhou, F. Wang, M. Wei, D. G. Evans, and X. Duan, "Ni–In intermetallic nanocrystals as efficient catalysts toward unsaturated aldehydes hydrogenation," *Chemistry of Materials*, vol. 25, no. 19, pp. 3888–3896, 2013.

[12] D. Goodman, "Model catalysts: From extended single crystals to supported particles," *Surface Review and Letters*, vol. 2, no. 01, pp. 9–24, 1995.

[13] M. Argyle and C. Bartholomew, "Heterogeneous catalyst deactivation and regeneration: a review," *Catalysts*, vol. 5, no. 1, pp. 145–269, 2015.

[14] Y. Cui, Y. Liao, Y. Sun, W. Wang, J. Wu, W. Dai, and T. Huang, "Advanced XPS-based techniques in the characterization of catalytic materials: A mini-review," *Catalysts*, vol. 14, no. 9, p. 595, 2024.

[15] H. Brongersma, M. Draxler, M. De Ridder, and P. Bauer, "Surface composition analysis by low-energy ion scattering," *Surface Science Reports*, vol. 62, no. 3, pp. 63–109, 2007.

[16] M. Bowker and P. Davies, *Scanning Tunneling Microscopy in Surface Science, Nanoscience, and Catalysis*. John Wiley & Sons, 2009.

[17] J. Hagen, *Industrial Catalysis: A Practical Approach*. John Wiley & Sons, 2015.

[18] S. Van and A. Rutger, *Chemical Kinetics and Catalysis*. Springer Science & Business Media, 2013.

[19] H. Lüth, *Solid Surfaces, Interfaces and Thin Films*. Springer, 2001, vol. 4.

[20] K. Laidler, "The development of theories of catalysis," *Archive for History of Exact Sciences*, pp. 345–374, 1986.

[21] J. Wisniak, "The history of catalysis. From the beginning to Nobel prizes," *Educación química*, vol. 21, no. 1, pp. 60–69, 2010.

[22] M. Roberts, "Birth of the catalytic concept (1800-1900)," *Catalysis Letters*, vol. 67, no. 1, pp. 1–4, 2000.

[23] M. Bowker, "The basis and applications of heterogeneous catalysis," 1998.

[24] M. Ivanov, V. Berezutskii, M. Shevchenko, V. Kudin, and V. Sudavtsova, "Thermodynamic properties of binary In–Sn alloys," *Powder Metallurgy and Metal Ceramics*, vol. 54, no. 7, pp. 465–470, 2015.

[25] I. Chorkendorff and J. W. Niemantsverdriet, *Concepts of modern catalysis and kinetics*. Wiley-VCH, 2003.

[26] S. Pang, X. Dou, W. Zhao, S. Bai, B. Wan, T. Wang, and J.-H. Yang, "A review on the design strategies of copper-based catalysts for enhanced activity and stability in methanol reforming to hydrogen," *Nanomaterials*, vol. 15, no. 14, p. 1118, 2025.

[27] M. Armbrüster, "Intermetallic compounds in catalysis–a versatile class of materials meets interesting challenges," *Science and Technology of Advanced Materials*, vol. 21, no. 1, pp. 303–322, 2020.

[28] A. Dasgupta and R. Rioux, "Intermetallics in catalysis: An exciting subset of multimetallic catalysts," *Catalysis Today*, vol. 330, pp. 2–15, 2019.

[29] O. Jamie, "Researchers seek to revolutionize catalyst design with machine learning," 2019, accessed: 01-05-2025. [Online]. Available: https://www.che.psu.edu/news-archive/2019/janik-michael-machine-learning-grant.aspx

[30] K. Kovnir, M. Armbrüster, D. Teschner, T. Venkov, F. Jentoft, A. Knop-Gericke, Y. Grin, and R. Schlögl, "A new approach to well defined, stable and site isolated catalysts," *Science and Technology of Advanced Materials*, vol. 8, no. 5, p. 420, 2007.

[31] M. Friedrich, S. A. Villaseca, L. Szentmiklósi, D. Teschner, and M. Armbrüster, "Order-induced selectivity increase of $Cu_{60}Pd_{40}$ in the semi-hydrogenation of acetylene," *Materials*, vol. 6, no. 7, pp. 2958–2977, 2013.

[32] R. Meyer, Q. Zhang, A. Kryczka, C. Gomez, and R. Todorovic, "Perturbation of reactivity with geometry: how far can we go?" pp. 566–570, 2018.

[33] C. S. Spanjers, A. Dasgupta, M. Kirkham, B. A. Burger, G. Kumar, M. J. Janik, and R. M. Rioux, "Determination of bulk and surface atomic arrangement in Ni–Zn γ-brass phase at different Ni to Zn ratios," *Chemistry of Materials*, vol. 29, no. 2, pp. 504–512, 2017.

[34] G. K. Boreskov, *Heterogeneous Catalysis*. Nova Publishers, 2003.

[35] J. M. Thomas and W. J. Thomas, *Principles and practice of heterogeneous catalysis*. John Wiley & Sons, 2014.

[36] G. Ertl and H. Freund, "Catalysis and surface science," *Physics Today*, vol. 52, no. 1, pp. 32–38, 1999.

[37] BYJU'S, "Adsorption theory of heterogeneous catalysts," 2025,

accessed:02-05-2025. [Online]. Available: https://byjus.com/chemistry/adsorption-theory-heterogeneous-catalyst/

[38] D. Rosenthal, R. Widmer, R. Wagner, P. Gille, M. Armbrüster, Y. Grin, R. Schlögl, and O. Gröning, "Surface investigation of intermetallic PdGa (1 1 1)," *Langmuir*, vol. 28, no. 17, pp. 6848–6856, 2012.

[39] H. Zhou, X. Yang, L. Li, X. Liu, Y. Huang, X. Pan, A. Wang, J. Li, and T. Zhang, "PdZn intermetallic nanostructure with Pd–Zn–Pd ensembles for highly active and chemoselective semi hydrogenation of acetylene," *ACS Catalysis*, vol. 6, no. 2, pp. 1054–1061, 2016.

[40] J. Osswald, K. Kovnir, M. Armbrüster, R. Giedigkeit, R. Jentoft, U. Wild, Y. Grin, and R. Schlögl, "Palladium–gallium intermetallic compounds for the selective hydrogenation of acetylene: Part II: Surface characterization and catalytic performance," *Journal of Catalysis*, vol. 258, no. 1, pp. 219–227, 2008.

[41] K. Kovnir, M. Armbrüster, D. Teschner, T. Venkov, L. Szentmiklósi, F. Jentoft, A. Knop-Gericke, Y. Grin, and R. Schlögl, "In situ surface characterization of the intermetallic compound PdGa–A highly selective hydrogenation catalyst," *Surface Science*, vol. 603, no. 10-12, pp. 1784–1792, 2009.

[42] W. Liu, L. Li, S. Lin, Y. Luo, Z. Bao, Y. Mao, K. Li, D. Wu, and H. Peng, "Confined Ni-In intermetallic alloy nanocatalyst with excellent coking resistance for methane dry reforming," *Journal of Energy Chemistry*, vol. 65, pp. 34–47, 2022.

[43] K. Kovnir, M. Armbrüster, R. Schlögl, and Y. Grin, "Synthesis and Investigation of the Electronic Structure of Pd–Ga Intermetallic Compounds as Highly Selective Hydrogenation Catalysts," in *European Conference on Solid State Chemistry XI*, 2007.

[44] A. Pang Tsai, S. Kameoka, and Y. Ishii, "PdZn= Cu: Can an intermetallic compound

replace an element?" *Journal of the Physical Society of Japan*, vol. 73, no. 12, pp. 3270–3273, 2004.

[45] M. Lowe, A. Al-Mahboob, D. Ivarsson, M. Armbrüster, J. Ardini, G. Held, F. Maccherozzi, A. Bayer, V. Fournée, J. Ledieu *et al.*, "Atomic structure of different surface terminations of polycrystalline ZnPd," *Physical Review Materials*, vol. 8, no. 10, p. 105801, 2024.

[46] S. Dey and N. Mehta, "Oxidation of carbon monoxide over various nickel oxide catalysts in different conditions: A review," *Chemical Engineering Journal Advances*, vol. 1, p. 100008, 2020.

[47] H. Liu and D. He, "Recent progress on Ni-based catalysts in partial oxidation of methane to syngas," *Catalysis Surveys from Asia*, vol. 16, pp. 53–61, 2012.

[48] A. Tsipouriari, Z. Zhang, and E. Verykios, "Catalytic partial oxidation of methane to synthesis gas over Ni-based catalysts: I. Catalyst performance characteristics," *Journal of Catalysis*, vol. 179, no. 1, pp. 283–291, 1998.

[49] D. Costa, R. Gomes, C. Rodella, R. da Silva Junior, R. Frety, É. Neto, and S. Brandao, "Study of nickel, lanthanum and niobium-based catalysts applied in the partial oxidation of methane," *Catalysis Today*, vol. 344, pp. 15–23, 2020.

[50] L. Wang, S. Yamamoto, K. Hayashizaki, S.-i. Nagamatsu, S. Malwadkar, T. Sasaki, and Y. Iwasawa, "Selective synthesis of phenol from benzene with O_2 by switchover of the reaction pathway from complete oxidation to selective hydroxylation by NH_3 on Ir/β and Ni/β catalysts," *ChemCatChem*, vol. 7, no. 20, pp. 3248–3253, 2015.

[51] P. Lejcek, *Grain boundary segregation in metals*. Springer Science & Business Media, 2010, vol. 136.

[52] Y.-J. Song, S. Guo, P. Xia, F. Sun, Z.-X. Chen, S.-H. Yang, X.-Y. Zhang, and T. Zhang, "Development of supported intermetallic compounds: advancing the Frontiers of heterogeneous catalysis," *Nanoscale Horizons*, 2025.

[53] I. Jacob, M. Fisher, and Z. Hadari, "Segregation behavior of the intermetallic compounds ZrNiAl, YNiAl and UNiAl," *Solid State Communications*, vol. 60, no. 4, pp. 401–405, 1986.

[54] C. Li, Y. Chen, S. Zhang, J. Zhou, F. Wang, S. He, M. Wei, D. Evans, and X. Duan, "Nickel–Gallium intermetallic nanocrystal catalysts in the semihydrogenation of phenylacetylene," *ChemCatChem*, vol. 6, no. 3, pp. 824–831, 2014.

[55] Q. Feng, S. Zhao, Y. Wang, J. Dong, W. Chen, D. He, D. Wang, J. Yang, Y. Zhu, H. Zhu *et al.*, "Isolated single atom Pd sites in intermetallic nanostructures: high catalytic selectivity for semihydrogenation of alkynes," *Journal of the American Chemical Society*, vol. 139, no. 21, pp. 7294–7301, 2017.

[56] M. Klanjšek, A. Gradišek, A. Kocjan, M. Bobnar, P. Jeglič, M. Wencka, Z. Jagličić, P. Popčević, J. Ivkov, A. Smontara *et al.*, "PdGa intermetallic hydrogenation catalyst: an NMR and physical property study," *Journal of Physics: Condensed Matter*, vol. 24, no. 8, p. 085703, 2012.

[57] C. Spanjers, J. Held, M. Jones, D. Stanley, R. Sim, M. Janik, and R. Rioux, "Zinc inclusion to heterogeneous nickel catalysts reduces oligomerization during the semi hydrogenation of acetylene," *Journal of Catalysis*, vol. 316, pp. 164–173, 2014.

[58] M. Armbrüster, M. Behrens, K. Föttinger, M. Friedrich, É. Gaudry, S. Matam, and H. R. Sharma, "The intermetallic compound ZnPd and its role in methanol steam reforming," *Catalysis Reviews*, vol. 55, no. 3, pp. 289–367, 2013.

[59] F. Studt, I. Sharafutdinov, F. Abild-Pedersen, C. Elkjær, J. Hummelshøj, S. Dahl,

I. Chorkendorff, and J. K. Nørskov, "Discovery of a Ni-Ga catalyst for carbon dioxide reduction to methanol," *Nature Chemistry*, vol. 6, no. 4, pp. 320–324, 2014.

[60] M. McGuirk, J. Ledieu, É. Gaudry, M.-C. De Weerd, M. Hahne, P. Gille, D. Ivarsson, M. Armbrüster, J. Ardini, G. Held *et al.*, "The atomic structure of low index surfaces of the intermetallic compound InPd," *The Journal of Chemical Physics*, vol. 143, no. 7, p. 074704, 2015.

[61] A. Hanbicki, A. Baddorf, E. Plummer, B. Hammer, and M. Scheffler, "The interaction of hydrogen with the (110) surface of AlNi," *Surface Science*, vol. 331, pp. 811–817, 1995.

[62] H. Okamoto, "In-Ni (Indium-Nickel)," *Journal of Phase Equilibria*, vol. 20, no. 5, p. 540, 1999.

[63] M. Wencka, M. Pillaca, and P. Gille, "Single crystal growth of Ga_3Ni_2 by the czochralski method," *Journal of Crystal Growth*, vol. 449, pp. 114–118, 2016.

[64] J. Czochralski, "Ein neues verfahren zur Messung der kristallisationsgeschwindigkeit der Metalle," *Zeitschrift für Physikalische Chemie*, vol. 92, pp. 219–221, 1918.

[65] E. Hellner and Z. Metallkd, "Das system Nickel-Indium," *International Journal of Materials Research*, vol. 41, pp. 401–406, 1950.

[66] M. Krnel, P. Koželj, S. Vrtnik, A. Jelen, M. Wencka, P. Gille, and J. Dolinšek, "Anisotropic electrical, magnetic, and thermal properties of In_3Ni_2 intermetallic catalyst," *Zeitschrift für anorganische und allgemeine Chemie*, vol. 646, no. 14, pp. 1099–1104, 2020.

[67] A. Chambers, *Basic vacuum technology*. CRC Press, 1998.

[68] J. F. O'Hanlon, *A user's guide to vacuum technology*. John Wiley & Sons, 2003.

[69] J. Pendry, *Low energy electron diffraction: the theory and its application to determination of surface structure*. Academic Press, 1977, vol. 30, no. 2.

[70] K. Diels and R. Jaeckel, *Leybold Vacuum Handbook*. Elsevier, 2013.

[71] W. Umrath, "Fundamentals of vacuum technology," 1998.

[72] S. Ahmed, *Physics and engineering of radiation detection*. Academic Press, 2007.

[73] V. Pfeiffer, *The Vacuum technology book*. Pfeiffer Vacuum GmbH, 2013, vol. II.

[74] G. Attard and C. Barnes, "Surfaces," vol. 59, 1998.

[75] J. Venables, *Introduction to surface and thin film processes*. Cambridge university press, 2000.

[76] P. Hofmann, *Surface Physics*. Kindle Edition, 2013.

[77] K. Oura, V. Lifshits, A. Saranin, A. Zotov, and M. Katayama, *Surface science: an introduction*. Springer Science & Business Media, 2013.

[78] J. H. Moore, C. C. Davis, and M. A. Coplan, *Building scientific apparatus*. Cambridge University Press, 2009.

[79] Industrial Quick Search. (2025) Types and operating principles of vacuum pumps. [Online]. Available: https://www.iqsdirectory.com/articles/vacuum-pump.html

[80] P. Urban, Y.-C. Chen, and Y.-S. Wang, *Time resolved mass spectrometry: from concept to applications*. John Wiley & Sons, 2016.

[81] A. Vyas and W. Wong, "Teaching PVD magnetron sputtering technique for deposition of multilayer thin film coatings supported by simulation," *Journal of Materials Education*, vol. 39, no. 1-2, pp. 43–58, 2017.

[82] H. Ibach, *Physics of surfaces and interfaces*. Springer, 2006, vol. 12.

[83] M. Soriaga, "Ultra-high vacuum techniques in the study of single crystal electrode surfaces," *Progress in Surface Science*, vol. 39, no. 4, pp. 325–443, 1992.

[84] J. Vickerman and I. Gilmore, *Surface analysis: the principal techniques*. John Wiley & Sons, 2011.

[85] F. Stevie and C. Donley, "Introduction to x-ray photoelectron spectroscopy," *Journal of Vacuum Science & Technology A*, vol. 38, no. 6, 2020.

[86] A. Einstein, "Über einen die erzeugung und verwandlung des lichtes betreffenden heuristischen gesichtspunkt," *Annalen der Physik*, vol. 17, pp. 132–148, 1905.

[87] K. Siegbahn, "ESCA: Atomic, molecular and solid state structure studied by means of electron spectroscopy," *Nova Acta Regiae Societatis Scientiarum Upsaliensis*, vol. Series 4, Vol. 20, 1967.

[88] K. Kolasinski, "Experimental probes and techniques," *Surface Science: Foundations of Catalysis and Nanoscience*, pp. 51–114, 2012.

[89] B. Ratner and D. Castner, "Electron spectroscopy for chemical analysis," *Surface analysis–the principal techniques*, vol. 51, 2009.

[90] C. Tusche, Y.-J. Chen, C. Schneider, and J. Kirschner, "Imaging properties of hemispherical electrostatic energy analyzers for high resolution momentum microscopy," *Ultramicroscopy*, vol. 206, p. 112815, 2019.

[91] J. Végh, "The Shirley background revised," *Journal of Electron Spectroscopy and Related Phenomena*, vol. 151, no. 3, pp. 159–164, 2006.

[92] J. Scofield, "Hartree slater subshell photoionization cross sections at 1254 and 1487 eV," *Journal of electron spectroscopy and related phenomena*, vol. 8, no. 2, pp. 129–137, 1976.

[93] T. Shigeo, P. Cedric, and P. David, "Calculations of electron inelastic mean free paths. II. Data for 27 elements over the 50–2000 eV range," *Surface and Interface Analysis*, vol. 17, no. 13, pp. 911–926, 1991.

[94] S. Tanuma, C. Powell, and D. Penn, "Calculations of electron inelastic mean free paths. V. Data for 14 organic compounds over the 50–2000 eV range," *Surface and Interface Analysis*, vol. 21, no. 3, pp. 165–176, 1994.

[95] R. Lin, J. Xu, M. Wei, Y. Wang, Z. Qin, Z. Liu, J. Wu, K. Xiao, B. Chen, S. Park *et al.*, "All perovskite tandem solar cells with improved grain surface passivation," *Nature*, vol. 603, no. 7899, pp. 73–78, 2022.

[96] S. Fadley, J. Baird, W. Siekhaus, T. Novakov, and S. Bergström, "Surface analysis and angular distributions in x-ray photoelectron spectroscopy," *Journal of Electron Spectroscopy and Related Phenomena*, vol. 4, no. 2, pp. 93–137, 1974.

[97] C. Cushman, P. Brüner, J. Zakel, G. Major, B. Lunt, N. Smith, T. Grehl, and M. Linford, "Low energy ion scattering (LEIS): A practical introduction to its theory, instrumentation, and applications," *Analytical Methods*, vol. 8, no. 17, pp. 3419–3439, 2016.

[98] H. Brongersma, M. Draxler, M. De Ridder, and P. Bauer, "Surface composition analysis by low-energy ion scattering," *Surface Science Reports*, vol. 62, no. 3, pp. 63–109, 2007.

[99] C. Kittel and P. McEuen, *Introduction to solid state Physics*. John Wiley & Sons, 2018.

[100] G. Held, "Low energy electron diffraction crystallography of surfaces and interfaces," *Bunsen-Magazin*, vol. 12, no. 12, pp. 124–131, 2010.

[101] G. Lleopart, "STM: theory and research Applications," https://hdl.handle.net/2445/117496, 2017, accessed:25-08-2025.

[102] G. Binnig, H. Rohrer, C. Gerber, and E. Weibel, "7 $\times$ 7 reconstruction on Si (111) resolved in real space," *Physical Review Letters*, vol. 50, no. 2, pp. 120–123, 1983.

[103] K. Takeuchi, A. Suda, and S. Ushioda, "Local variation of the work function of cu (1 1 1) surface deduced from the low energy photoemission spectra," *Surface science*, vol. 489, no. 1-3, pp. 100–106, 2001.

[104] S. Hämäläinen, "Modification of the electronic structure of graphene by quantum confinement and molecular self-assembly," no. 150/2014, 2014.

[105] R. Pavan and A. Barron. (2021) Scanning tunneling microscopy. https://chem.libretexts.org/@go/page/55919. Accessed: 16-12-2022.

[106] M. Aketagawa and K. Takada, "Correction of distorted stm image by using a regular crystalline lattice and 2d fft," *Nanotechnology*, vol. 6, no. 4, pp. 105–110, 1995.

[107] A. Alfahad, V. Singh, E. Gaudry, J. Ledieu, V. Fournée, P. Gille, A. Gardner, P. Chalker, R. McGrath, and H. R. Sharma, "Atomic structure, chemical composition, and oxidation behavior of the (001) surface of Ni_2In_3 intermetallic catalyst," *Physical Review Materials*, vol. 9, no. 3, p. 035801, 2025.

[108] M. Wencka, M. Pillaca, and P. Gille, "Single crystal growth of Ga_3Ni_2 by the Czochralski method," *Journal of Crystal Growth*, vol. 449, pp. 114–118, 2016.

[109] Ennologic, "Ultimate emissivity table," https://ennologic.com/wp-content/uploads/2018/07/Ultimate-Emissivity-Table.pdf, 2018, accessed: 02-06-2025.

[110] I. GmbH, *Qtac100 spectrometer and surfaceLab 7 software*, Münster, Germany, 2023.

[111] R. Furstenau, G. McDougall, and M. Langell, "Initial stages of hydrogen reduction of NiO (100)," *Surface Science*, vol. 150, no. 1, pp. 55–79, 1985.

[112] Z. Detweiler, S. Wulfsberg, M. Frith, A. Bocarsly, and S. Bernasek, "The oxidation and surface speciation of indium and indium oxides exposed to atmospheric oxidants," *Surface Science*, vol. 648, pp. 188–195, 2016.

[113] L. Feldman and J. Mayer, "Fundamentals of surface and thin film analysis," *North-Holland, Elsevier Science Publishers*, 1986.

[114] C. Yuen, B. Ünal, D. Jing, and P. Thiel, "Weak bonding of Zn in an Al-based approximant based on surface measurements," *The Philosophical Magazine*, vol. 91, no. 19–21, pp. 2879–2888, 2010.

[115] P. Sigmund, "Theory of sputtering. I. sputtering yield of amorphous and polycrystalline targets," *Physical Review*, vol. 184, no. 2, pp. 383–416, 1969.

[116] L. Vitos, A. Ruban, H. Skriver, and J. Kollár, "The surface energy of metals," *Surface Science*, vol. 411, no. 1–2, pp. 186–202, 1998.

[117] O. Shedwick, "Surface chemical composition, atomic structure and oxidation of the Ga_3Ni_2 intermetallic catalyst," Ph.D. dissertation, University of Liverpool, 2024.

[118] S. O. T.O Owolabi, K.O Akande, "Estimation of the atomic radii of periodic elements using support vector machine," *International Journal of Advanced Information Science and Technology (IJAIST)*, vol. 28, no. 28, pp. 39–49, 2014.

[119] T. Owolabi, K. Akande, and S. Olatunji, "Support vector machines approach for estimating work function of semiconductors: addressing the limitation of metallic plasma model," *Applied Physics Research*, vol. 6, no. 5, pp. 122–132, 2014.

[120] K. Hermann and M. Van, "LEEDpat, version 4.1, utility," 2014. [Online]. Available: http://www.fhi-berlin.mpg.de/KHsoftware/LEEDpat/index.html

[121] J. Nugent, G. Simutis, R. Dhanak, R. McGrath, M. Shimoda, C. Cui, P. Tsai, and

H. Sharma, “Surface oxidation of the icosahedral Ag-In-Yb quasicrystal,” *Physical Review B*, vol. 82, no. 1, p. 014201, 2010.

[122] J. Chastain and R. King, “Handbook of X-ray photoelectron spectroscopy,” *Perkin-Elmer Corporation*, p. 221, 1992.

[123] R. Kelly and D. Harrison, “A summary of the theory of the preferential sputtering of alloys,” *Materials Science and Engineering*, vol. 69, no. 2, pp. 449–455, 1985.

[124] K. Eldressi, H. Eltawahni, M. Moradi, E. Twiname, and R. Mistler, “Energy effects in bulk metals,” in *Reference Module in Materials Science and Materials Engineering*. Elsevier, 2019.

[125] E. Gaudry, *Density of states calculations*, Institut Jean Lamour, Nancy, France, 2025, private communication.

List of Figures

2.1 Cyclic catalytic reaction: in a catalytic reaction, reactant molecules bind to the catalyst, where molecules A and B react, and the product P then separates from the catalyst, releasing it for use in the next cycle. Reproduced and modified from [25]. 8

2.2 Schematic representation of the Langmuir–Hinshelwood and Eley–Rideal mechanisms in heterogeneous catalysis. In the Langmuir–Hinshelwood pathway (a), both reactants are adsorbed onto the catalyst surface before reacting to form products. In the Eley–Rideal pathway (b), a gas-phase species reacts directly with an adsorbed surface species. The grey spheres represent catalyst surface atoms, whereas the coloured spheres indicate reactant species and intermediates [26]. 9

2.3 (a) An ordered intermetallic structure. (b) An alloy that lacks periodic order or well-defined site occupation [29]. 10

2.4 A schematic diagram 13

2.5 (1×1) LEED patterns after annealing the PdGa($\bar{1}\bar{1}\bar{1}$) surface with different beam energies (a) 40 eV. (b) 105 eV [38]. (c) STM images of the PdGa($\bar{1}\bar{1}\bar{1}$) surface after sputtering and annealing show (c) A highly terraced surface area (1000 Å × 1000 Å, −1 V, 0.5 nA). (d) atomic resolution of a smaller region (200 A × 200 Å, −2.5 V, 0.5 nA), with the FFT [38]. 20

2.6 (a) Bulk terminated structural models of the InPd(100) surface, illustrating terminations at either a pure In or pure Pd atomic plane. (b) LEED pattern of the InPd(100) surface exhibiting the p(4×4) reconstruction, recorded at a primary beam energy of 50 eV. The (1×1) reciprocal unit cell is outlined with a dashed line for reference. (c) STM image of the same p(4×4) structure, revealing quasi ordered square surface features (scan area, 15×15 nm^2, +1.8 V, 0.09 nA). (d) LEED pattern of the c($3\sqrt{2} \times \sqrt{2}$)R45° superstructure recorded at beam energy of 46 eV. (c) STM image (5×5 nm^2, +1.4 V, 0.25 nA) showing a single domain of the c($3\sqrt{2} \times \sqrt{2}$)R45° reconstruction, with both rectangular (solid line) and primitive (dashed line) unit cells superimposed [60]. 21

2.7 (a) Bulk terminated structure models of the InPd(110) surface, the unit cells corresponding to (110) surface reconstructions observed during sample preparation are illustrated and labelled. LEED patterns of the (b) (1×1), (c) (2×1), (d) c(4×2) phases observed on the InPd(110) surface, recorded at a consistent electron beam energy of 63 eV. The primitive reciprocal space unit cells for each surface phase are indicated by green solid lines. (e) STM image of the same surface, revealing linear atomic rows attributed to either In or Pa (9.4×9.4 nm^2, -1.5 V, 0.08 nA) [60]. 22

2.8 (a) Bulk terminated structural models of the (111) surface. LEED images, both taken at a primary beam energy of 50 eV, showing (b) the (1×1) phase and (c) the ($\sqrt{3} \times \sqrt{3}$)R30° superstructure on the InPd(111) surface. The reciprocal unit cells are marked by solid lines. (d) STM image (30×30 nm^2, +1.8 V, 0.09 nA) of the InPd(111)-($\sqrt{3} \times \sqrt{3}$)R30° phase [60]. 22

2.9 (a) LEED pattern of the clean InPd(111) surface recorded at beam energy of 68eV, exhibiting a (1×1) surface symmetry indicative of an unreconstructed termination under UHV conditions. (b) LEED pattern of the c$(3\sqrt{2}\times 3\sqrt{2})$R45° oxygen overlayer formed on the InPd(111) surface following exposure to 20 L of O_2 at 750 K, recorded at beam energy of 69 eV [60]. 23
2.10 Schematic of various PdZn surfaces. The (110), (101), (111) and (114) surfaces, observed by STM, contain both Zn and Pd atoms in or near the top surface layer. The (001) surface, which has not been observed, shows single element termination [45]. 24
2.11 Thermodynamic phase diagram for the In–Ni binary system [62]. 26
2.12 (a) A schematic of the Czochralski method [65]. (b) An image of the In_3Ni_2 single crystal that was grown using the Czochralski method, with the $3\bar{3}$ rotating axis pulled along [001] [66]. 28
2.13 Laue diffraction images obtained from the grown In_3Ni_2 crystal with the principal X-ray beam parallel to the three symmetrically different orientations indicated in the stereographic projection: (a) [100], (b) [001], (c) [$2\bar{1}0$]. . 29
2.14 The unit cell of the In_3Ni_2 surface. Ni atoms are structurally isolated from each other by In first neighbours. 30

3.1 Schematic of a rotary pump [79]. 37
3.2 (a) Schematic of a turbo molecular pump [79]. (b) Turbo molecular pump at the Surface Science Research Centre of the University of Liverpool. 38
3.3 Schematic of an ion pump [79]. 39
3.4 Schematic of a titanium sublimation pump [79]. 40
3.5 (a) Schematic of an ionisation gauge [67]. (b) An ionisation gauge at the Surface Science Research Centre of the University of Liverpool. 41
3.6 Ultra high vacuum chamber at the Surface Science Research Centre of the University of Liverpool used in this thesis. 42

3.7 Baking ultra high vacuum equipment at the Surface Science Research Centre of the University of Liverpool. 43
3.8 Mass spectrometer used in the Surface Science Research Centre of the University of Liverpool, which is used to indicate the elements inside the UHV chamber. 44
3.9 (a) Stainless steel sample holder cleaned by immersing it in methanol and an ultrasonic device for 15 minutes. (b) Sample attached to 45
3.10 Operational setup of an Ar^+ ion gun during the sputtering process. In this configuration, argon ions are accelerated under vacuum conditions and directed towards the target (sample surface), where they induce the controlled removal of surface atoms. This process is commonly used for surface cleaning in surface science. 48
3.11 Photoemission process in XPS. Reproduced and modified from [89]. 50
3.12 (a) An XPS spectrum taken from $In_3Ni_2(001)$ with the largest core level highlighted by a blue line for Ni and red lines for In. (b) Ni 2*p* core level. (c) In 3*d* core level. 52
3.13 The scanning angles between the detector and the X-ray affect the depth of the sample scanned by XPS: (a) at normal angle; (b) at 45°; (c) at 75°. Reproduced and modified from [95]. 55
3.14 (a) The bombardment of a surface with three types of exposed atoms by noble gas ions. (b) LEIS signal corresponding to the surface on the left. Note that there is no LEIS signal from the 'red' atoms, which are deep in the surface. Reproduced and modified from [97]. 57
3.15 (a) LEIS instrument at the University of Liverpool used to produce the results for In_3Ni_2 samples. (b) The sample placed on the holder. 58
3.16 Illustrating Bragg's Law. Reproduced and modified from [99] 60

3.17 Ewald sphere representing diffraction in the reciprocal lattice (a) three dimensions 62
3.18 Schematic of the LEED apparatus, which is evacuated to ultra high vacuum. Reproduced and modified from [101]. 63
3.19 Schematic picture of the electron energy states in a tunnelling contact between STM metal tip and sample. Reproduced and modified from [103]. . . 65
3.20 Metal tip and sample used in STM. 67
3.21 Schematic illustration of scanning tunnelling 67
3.22 Operation of an STM in constant (a) current mode. (b) height mode. Reproduced and modified from [105]. 68
3.23 STM image of the HOPG surface after sputtering and annealing the surface to 216 °C, showing a (32 Å×35 Å scan area at 69
3.24 (a) STM image of the In_3Ni_2(001) surface after sputtering and 70
3.25 (a) STM image of the In_3Ni_2(001) surface after sputtering and 71

4.1 (a)The unit cell of the In_3Ni_2(001) surface, with the (001) plane highlighted in yellow. (b) Side view of the (001) surface, showing the stacking of five atomic planes, labelled 0 to 4, within the unit cell. The separations between specific planes are indicated. (c) Projection of atomic models along the [001] direction, where the outermost atomic layer is selected from five distinct layers (0 to 4) as shown in (b). High-symmetry directions are also marked [107]. 74

4.2 (a) XPS wide scan spectra of a clean In_3Ni_2(001) surface after exposure to air, sputtering, and annealing at 560 °C for one hour. (b) and (c) show XPS spectra comparing the binding energies of the core levels of In $3d_{5/2}$ and Ni $2p_{3/2}$, showing the effects of sputtering, air exposure, and the clean surface. The shifts to higher binding energies of 0.4 eV in In and 0.35 eV in Ni occur after air exposure, regardless of the surface elemental condition. Dashed lines indicate core levels of In, Ni, C and O. 77

4.3 The surface chemical composition of the (001) surface after sputtering and annealing at various temperatures from 300 °C to 560 °C. Dotted lines indicate the In and Ni bulk compositions. 79

4.4 The surface chemical composition of the (001) surface after sputtering and annealing at 356 °C with various scan angles from 0 to 70°. Dotted lines indicate the In and Ni bulk composition. θ is the angle between the surface and the X-ray beam. 82

4.5 LEIS spectra recorded from the In_3Ni_2(001) surface after sputtering and annealing at 400 °C for 2 hours using a 3 keV He^+ beam. The energy ranges for each surface peak highlighted correspond to the upper and lower limits used for the baseline subtraction. 84

4.6 (a) The change in the integrated In and Ni intensities in LEIS from the In_3Ni_2(001) surface with sputtering at varying ion doses . (b) After annealing the sputtered surface at varying temperatures. (c) and (d) show the ratio of In to Ni intensities after the corresponding treatments (a, b) [107]. . 85

4.7 (1×1) LEED patterns from the (001) surface at a beam energy of 45 eV after being freshly prepared by sputtering and annealing at different temperatures: (a) annealing at 360 °C. (b) annealing at 405 °C. (c) annealing at 420 °C. (d) annealing at 440 °C. (e) annealing at 470 °C. (f) annealing at 500 °C. . 87

4.8 LEED patterns of the (001) surface after preparation by sputtering and annealing at 360 °C with beam energies: (a) 10 eV. (b) 20 eV. (c) 30 eV. (d) 40 eV. (e) 50 eV. (f) 60 eV. (g) 70 eV. (h) 80 eV. (i) 90 eV. 88

4.9 LEED patterns illustrating the bulk-type structure characteristic of the (001) clean surface with beam energy = 40 eV after (a) fresh preparation of the surface with annealing temperature = 420 °C. (b) After leaving the sample for 30 minutes. (c) fresh preparation of the surface with annealing temperature = 470 °C. (d) Leaving the sample for 30 minutes. 89

4.10 (a) LEED pattern from the freshly prepared In_3Ni_2(001) surface, showing a (1×1) structure. (b) LEED pattern from the same surface after firing the Titanium Sublimation Pump, demonstrating the three domains of the c(2$\sqrt{3}$×4) rectangular reconstruction. A section of the pattern is superimposed with the positions expected for the three domains. Both patterns were taken at 100 eV beam energy. (c) The positions of LEED spots expected for a single-domain c(2$\sqrt{3}$×4) reconstruction, where solid circles represent the position of the reconstruction spots, while open circles denote the position of (1×1) spots. (d) The positions of the three-domain c(2$\sqrt{3}$×4) LEED pattern rotated by 120°from each other. Yellow represents the unit cell of the (1×1) structure, whereas that of the c(2$\sqrt{3}$×4) domains is marked by red rectangles [107]. The patterns in (c) and (d) were produced by LEEDpat, which is a software program used to reproduce the experimentally observed LEED pattern using specified parameters [120]. 90

4.11 LEED patterns of the clean (001) surface recorded at varying beam energies: (a) 18 eV. (b) 20 eV. (c) 25 eV. Faceted diffraction spots, highlighted with red circles, shift outward as the beam energy increases. 92

4.12 (a) Representative Laue back-scattering image taken from the centre of the surface reflecting the symmetry expected from the bulk. (b) Laue back-scattering image from the edge of the sample showing a diffuse ring. 92
4.13 (a) STM image taken from the In_3Ni_2(001) surface after several cycles of sputtering and annealing at 540 °C (750 Å×950 Å, +0.472 V, 0.448 nA), demonstrating steps of different heights. (b) Height distribution along a blue line in (a) crossing the steps. Step heights are given. (c) The histogram of height distribution in the vicinity of the steps. (d) The histogram of steps that were analysed from STM images taken from different regions of the surface. 94
4.14 STM images of the In_3Ni_2(001) surface showing three domains of c($2\sqrt{3}\times4$) rect structure, rotated by 120° relative to one another. Unit cells are indicated by black rectangles. A model structure depicting a high-resolution STM image, where red spheres represent bright protrusions observed in STM, whereas the grid represents the unit cells of the (1×1) structure. A c($2\sqrt{3}\times4$) rect unit cell is shown by a black rectangle.(a) The image is rotated by 0°. (b) The image is rotated by 120°. (c) The image is rotated by 240°. 95
4.15 (a) STM images of the In_3Ni_2(001) surface showing three domains of c($3\times\sqrt{3}$) structure. The unit cell is indicated by a black rectangle. (b) A model structure, where red spheres represent bright protrusions observed in STM, and the grid represents the unit cells of the (1×1) structure. A c($3\times\sqrt{3}$) unit cell is shown by a black rectangle. 96
4.16 Variation of total energy (τ) as a function of the chemical potential of In ($\Delta\mu_{In}$) for the five model surfaces presented in Figure 4.1 (c). Refer to the main text for definitions of total energy (τ) and $\Delta\mu_{In}$, representing the In chemical potential in the In-rich regime [107]. 97

4.17 (a) to (c) XPS spectra of the clean (after annealing at 560 °C), oxygen exposed, and air exposed (001) surface of In_3Ni_2(001) (a: In $3d$, b: Ni $2p$, and c: C $1s$). Oxygen exposure ranged from 20-900 L. (d, e) In $3d_{5/2}$ and Ni $2p_{3/2}$ spectra, respectively, after normalizing the minimum and maximum intensity between 0 and 1, illustrating the development of a shoulder at higher binding energies. The dotted, dashed, and dash dotted lines at 530.2 eV, 531.0 eV, and 531.6 eV in (c) correspond to the positions of the oxide, pure oxygen, and Ni hydroxide peaks, as reported in the literature [99, 121, 122]. The dotted lines in (c) indicate the positions of the oxide peaks, while the dashed lines in all other spectra correspond to the core level positions of the respective elements from the clean surface [107]. 99

4.18 Ni $2p_{3/2}$ XPS spectra of the In_3Ni_2(001) surface after cleaning the surface through sputtering and annealing at 560 °C, with increasing oxygen exposure (20 L, 300 L, 600 L, and 900 L) and after air exposure. Vertical dashed lines in all spectra correspond to the core-level position of clean Ni $2p_{3/2}$. . 100

4.19 In $3d_{5/2}$ XPS spectra of the In_3Ni_2(001) surface after cleaning the surface via sputtering and annealing at 101

4.20 Chemical composition of the Ni_3In_2(001) surface after annealing at 560 °C and increasing oxygen exposure (20–900 L). The atomic composition of the clean and air-exposed surfaces is also provided for comparison. The composition was determined from the In $3d_{5/2}$, Ni $2p_{3/2}$, O $1s_{1/2}$, and C $1s_{1/2}$ XPS peaks. 103

5.1 (a) The unit cell of In_3Ni_2, with the $(2\bar{1}0)$ plane highlighted in yellow. (b) Side view of the $(2\bar{1}0)$ surface, showing the stacking of three atomic layers of In and Ni within the unit cell. 106

5.2 (a) XPS wide scan spectra of a clean $In_3Ni_2(2\bar{1}0)$ surface after sputtering and annealing the surface at 560 °C for an hour, and no oxygen or carbon contamination was detected. (b) and (c) XPS spectra comparing the binding energies of the core levels of In $3d_{5/2}$ and Ni $2p_{3/2}$ showing the effect of sputtering, air exposure, and the clean prepared surface. 110

5.3 Surface chemical composition of the $(2\bar{1}0)$ surface after sputtering and annealing at temperatures ranging from 300 °C to 550 °C. Dotted lines indicate the bulk composition of In and Ni. θ is an angle between the surface and X-ray. 113

5.4 Surface chemical composition of the $(2\bar{1}0)$ surface determined by XPS after sputtering and annealing at 560 °C, measured at various scan angles from 30° to 70°. Dotted lines indicate the bulk composition of In and Ni. 114

5.5 LEIS spectra obtained from the $In_3Ni_2(2\bar{1}0)$ surface after cleaning the surface by sputtering and annealing at selected temperatures for one hour, employing a 3 keV He^+ ion beam. The highlighted energy regions associated with each surface peak indicate the limits used for background correction. . 115

5.6 (a) The variation in the integrated In and Ni intensities in LEIS from the In and Ni $(2\bar{1}0)$ surface due to sputtering at different ion doses. (b) Annealing at various temperatures, along with the In to Ni intensity ratio following the respective treatments (c, d). 117

5.7 (1×1) LEED patterns from $(2\bar{1}0)$ surface at beam energy 45 eV after freshly prepared by sputtering and annealing at (a) 340 °C. (b) 360 °C. (c) 380 °C. (d) 400 °C. (e) 460 °C. (f) 500 °C. 119

5.8 LEED patterns of the $(2\bar{1}0)$ surface after annealing at 500 °C, recorded at beam energies: (a) 15 eV, (b) 30 eV, (c) 45 eV, (d) 60 eV, (e) 75 eV, (f) 90 eV, (g) 105 eV, (h) 120 eV, and (i) 135 eV. 120

5.9 LEED patterns of the clean $In_3Ni_2(2\bar{1}0)$ surface recorded at different electron beam energies: (a) 35 eV. (b) 40 eV. (c) 45 eV. (d) 50 eV. Faceted diffraction spots, indicated by red circles, exhibit a downward shift with increasing beam energy. 121

5.10 (a) Representative Laue back scattering image taken from the most part of the surface reflecting the symmetry expected from the bulk. (b) Laue back scattering image from the edge of sample showing a diffuse rings. 122

5.11 (a) STM image taken from the $In_3Ni_2(2\bar{1}0)$ surface after several cycles of sputtering and annealing (a) At 540 °C , (875 Å×1127 Å, + 0.510 V, 0.448 nA), demonstrating steps of different heights. (b) Height distribution along a blue line in (c) Crossing the steps. Steps heights are given. (d) The histogram of height distribution in the vicinity of the steps. 123

5.12 (a) and (b) STM images of In_3Ni_2 $(2\bar{1}0)$ surface showing atomic resolution after sputter and annealing it at 560 °C (500 Å × 500 Å, - 1.8 eV, 0.645 nA). (b) STM images (120 Å × 120 Å, - 1.8 eV, 0.645 nA). (c) The FFT pattern of Figure (b) shows a rectangle pattern. (d) The top view of $In_3Ni_2(2\bar{1}0)$ surface. 124

5.13 Bias dependent STM images and corresponding local density of states (LDOS) contrast table for the In_3Ni_2 $(2\bar{1}0)$ surface [125]. The figures shows STM images at bias voltages ranging from –1.3 V to +1.3 V, highlighting the bias induced contrast variation of In_1, In_2, and Ni atomic sites within the model surface unit cell. The labelled sites (In_1, In_2) are marked for reference. The bottom panel summarises the observed relative contrast levels at each atomic site as a function of applied bias voltage, serving as a qualitative proxy for site specific LDOS. High and Low denote strong and weak contrast respectively, while zero indicates no observable contribution at that site [106]. 125

5.14 STM images of the In_3Ni_2 $(2\bar{1}0)$ surface under different bias voltages, overlaid with the atomic model of the surface structure. (a) Image at -1.8V, highlighting enhanced contrast at In_1 atoms, consistent with a higher local density of occupied states. while image at -1.8 V, where contrast shifts to In_2 atoms, reflecting enhanced unoccupied states at these sites. Ni atoms remain relatively low in contrast under both conditions, indicating a minimal contribution to the LDOS near the Fermi level. (b) STM image at +1.8V, highlighting enhanced contrast at In_1 atoms, consistent with a higher local density of occupied states and low contrast at In_2 atoms. (c) STM image at -1.3V, highlighting enhanced contrast at In_1 In_2 and Ni atoms. 126

5.15 STM images of the $(2\bar{1}0)$ surface with various voltage bias (a) At $-1.8\,\mathrm{V} \leq V \leq -1.4\,\mathrm{V}$.(b)At $-1.3\,\mathrm{V} \leq V \leq -0.5\,\mathrm{V}$. (c) At $-0.4\,\mathrm{V} \leq V \leq +0.9\,\mathrm{V}$(d). . . 128

5.16 (a) to (c) XPS spectra from clean (after annealing at 560 °C), oxygen exposed and air exposed of $In_3Ni_2(2\bar{1}0)$ surface (a: In $3d$, b: Ni $2p$, and c: O $1s$). Oxygen exposure was from 300 L-900 L. (d,e) In $3d_{5/2}$ and Ni $2p_{3/2}$ spectra, respectively, after normalizing minimum and maximum intensity between 0 and 1, illustrating the development of a shoulder at higher binding energy . The dotted, dashed, and dash dotted lines at 530.2 eV, 531.0 eV, and 531.6 eV in (f) correspond to the positions of the oxide, pure oxygen, and Ni oxide peaks, as reported in the literature [121, 122] respectively. The dashed lines in (c) marks the positions of the core levels of the respective elements from the clean surface. 131

5.17 XPS spectra of the $In_3Ni_2(2\bar{1}0)$ surface after air exposure and cleaning of the surface by sputtering and annealing at 560 °C and with increasing oxygen exposure (300 L-900 L). Vertical dashed lines in all spectra correspond to the core level position of clean In $3d_{5/2}$. 132

5.18 XPS spectra of the $In_3Ni_2(2\bar{1}0)$ surface after air exposed and clean the surface by sputtering and annealing it at 560 °C and with increasing oxygen exposure (300 L-900 L). Vertical dashed lines in all spectra correspond to the core level position of clean Ni $2p_{3/2}$. 134

5.19 The chemical composition of the In $_3Ni_2(2\bar{1}0)$ surface after annealing at 560 °C and with increasing oxygen exposure (300 L-900 L). The atomic composition of the clean and air exposed surfaces is also given for comparison. The composition was determined from the In $3d_{5/2}$, Ni $2p_{3/2}$, and O $1S_{1/2}$ XPS peaks. 135

6.1 (a) The unit cell of the $In_3Ni_2(100)$ surface, with the (100) plane highlighted in yellow. (b) Side view of the (100) surface, showing the stacking of four atomic planes, labelled 0 to 3, within the unit cell. The separations between specific planes are indicated. 138

6.2 (a) XPS wide scan spectra obtained from the $In_3Ni_2(100)$ surface under three distinct conditions: air exposure, following sputtering and after annealing at 560 °C for one hour. No oxygen or carbon contamination were detected after cleaning the surface by sputtering and annealing. (b) and (c) High resolution XPS spectra illustrating the core level binding energies of In $3d_{5/2}$ and Ni $2p_{3/2}$, respectively. These spectra demonstrate the influence of air exposure and surface treatment on peak positions. 142

6.3 The surface chemical composition of the (100) surface after sputtering and annealing at various temperatures from 300 °C to 560 °C. Dotted lines across the top indicate the In and Ni bulk composition. 145

6.4 The surface chemical composition of the (100) surface determined by XPS with various scan angles from 0 to 40°. Dotted lines across the top indicate the In and Ni bulk composition. θ is an angle between the surface and X-ray. 146

6.5 LEIS spectra recorded from the In_3Ni_2(100) surface after sputtering and annealing at different temperatures for 1 hour using a 3 keV He^+ beam. The energy ranges for each surface peak highlighted correspond to the upper and lower limits used for the baseline subtraction. 147
6.6 Integrated LEIS intensities of In and Ni from the In_3Ni_2 (100) surface (a) as a function of increasing Ar^+ ion dose and (b) sputtering annealing at selected temperatures 400 °C and 480 °C. (c) and (d) display the corresponding In/Ni peak intensity ratios, highlighting compositional shifts induced by sputtering and annealing. 148
6.7 (1×1) LEED patterns at beam energy 45 eV after (a) Annealing at 360 °C. (b) Annealing at 410 °C. (c) Annealing at 430 °C. (d) Annealing at 460 °C. (e) Annealing at 480 °C.(f) Annealing at 520 °C. 150
6.8 LEED patterns of the surface after annealing at 460 °C (a) Beam energy 20 eV. (b) Beam energy 30 eV. (c) At beam energy 40 eV. (d) Beam energy 50 eV. (e) Beam energy 60 eV. (f) Beam energy 70 eV. (g) Beam energy 80 eV. (h) Beam energy 90 eV. 151
6.9 LEED patterns illustrating the facets structure characteristic of (100) clean surface with different beam energy (a) 30 eV. (b) 40 eV. (c) 45 eV.(d) 50 eV. The diffraction spots from the facet are marked by yellow circle. 152
6.10 (a) Representative Laue back scattering image taken from the most part of the surface reflecting the symmetry expected from the bulk. (b) Laue back scattering image from the edge of sample showing a diffuse rings,indicated by polycrystalline. 152

6.11 STM images of the In_3Ni_2(100) surface following multiple sputtering and annealing cycles. (a) Height distribution recorded at 530 °C over an area of 800 Å× 650 Å, with a sample bias of +0.7 Vand a tunnelling current of 0.457 nA, showing surface steps of varying heights. (b) Height profile extracted along the blue line indicated in (a). (c) Histogram representing the distribution of step heights near the observed steps. 153

6.12 (a) STM images of In_3Ni_2(100) surface showing atomic resolution after sputter and annealing at 550 °C (100 Å × 100 Å, - 0.5 eV, 0.645 nA). (b) STM image (4 Å × 3.5 Å, 0.5 eV, 0.645 nA). (c) and (d) Top view of (100) surface. . 154

6.13 STM images showing atomic resolution (300 Å× 300 Å, 0.645 nA) after annealing (100) surface at 550 °C with different bias voltages (a) -1.8 eV. (b) -1 ev. (c) -0.5 eV. (d) +0.5 eV. (e) +1 eV. (f) +1.5 eV. 155

6.14 STM images showing atomic resolution (116 Å× 78 Å, 0.645 nA) after annealing (100) surface at 550 °C with different bias voltages (a) -1.8 eV. (b) -1 ev. (c) -0.5 ev. (d) +0.5 ev. (e) +1 ev. (f) +1.5 ev. 156

6.15 (a) STM images from the sample edge showing atomic resolution (200 Å× 200 Å, +1.8 V, 0.645 nA) after annealing (100) surface at 550 °C. (b) -1 ev. (c) STM images showing atomic resolution (86 Å× 83 Å, +1.8 V, 0.645 nA). . . . 157

6.16 Side view of the In_3Ni_2(100) surface, showing the stacking of four atomic planes, labelled 0 to 3, within the unit cell of the surface. 158

6.17 (a) to (c) XPS spectra of the clean (after annealing at 560 °C), oxygen exposed and air exposed of In_3Ni_2(100) surface (a: In 3d, b: Ni 2p and c: O 1s). Oxygen exposure ranged from 20-900 L. (d, e, f) In $3d_{5/2}$, O $1S_{1/2}$ and spectra, respectively, after normalising the minimum and maximum intensity between 0 and 1, illustrating the development of a shoulder at higher binding energies. The dotted, dashed and dash dotted lines at 530.2 eV, 531.0 eV and 853.6 eV in (c) correspond to the positions of the oxide, pure oxygen and Ni oxide peaks, as reported in the literature [99, 121, 122]. The dotted lines in (c) indicate the positions of the oxide peaks, while the dashed lines in all other spectra correspond to the core level positions of the respective elements from the clean surface. 160

6.18 In $3d_{5/2}$ XPS spectra of the In_3Ni_2(100) surface after cleaning the surface through sputtering and annealing at 560 °C, with increasing oxygen exposure (a) clean surface. (b) 20 L. (c) 300 L. (d) 600 L. (e) 900 L. (f) Air exposed. Vertical dashed lines in all spectra correspond to the core level position of the clean Ni $2p_{3/2}$, while vertical dot lines in all spectra correspond to the core level position of the oxidised In. 162

6.19 Ni $2p_{3/2}$ XPS spectra of the In_3Ni_2(100) surface after clean the surface by sputtering and annealing it at 560 °C and with increasing oxygen exposure (a) clean surface. (b) 20 L. (c) 300 L. (d) 600 L. (e) 900 L. (f) Air exposed. Vertical dashed lines in all spectra correspond to the core level position of the clean Ni $2p_{3/2}$, while vertical dash dot line in air exposed spectra correspond to the core level position of the Ni Hydroxide. 163

6.20 O $1s_{1/2}$ XPS spectra of the In_3Ni_2(100) surface with increasing oxygen exposure (a) 20 L. (b) 300 L. (c) 600 L. (d) 900 L. (e) Air exposed. Vertical dashed lines in all spectra correspond to the core level position of the O $1s_{1/2}$, while Vertical dot lines in all spectra correspond to the core level position of the oxidised O. 164

6.21 The chemical composition of the In_3Ni_2(100) surface after annealing at 560 °C and with increasing oxygen exposure (20 L-900 L). The atomic composition of the clean and air exposed surfaces is also given for comparison. The composition was determined from the Ni $2p_{3/2}$, C $1S_{1/2}$ and O $1S_{1/2}$ XPS peaks. 165

7.1 Side view representations of the In_3Ni_2 crystal structure along different crystallographic orientations, (a) (100) surface. (b) $(2\bar{1}0)$ surface and (c) (001) surface. (d-g) The in-plane atomic structures of the terminating planes for the (001), $(2\bar{1}0)$ and (100) surfaces. For the (001) and (100) surfaces, the atoms in the top two layers are considered, whereas for the $(2\bar{1}0)$ surface, only the atoms in the top layer are considered. The bond-lengths between In and Ni atoms for each surface are also provided. 168

7.2 In/Ni atomic ratio on the In_3Ni_2 (100), $(2\bar{1}0)$ and (001) surfaces, as determined by XPS following sputtering and annealing at temperatures ranging from 360 °C to 560 °C. The data highlight the variation in surface composition as a function of both crystallographic orientation and annealing temperatures. 171

7.3 In/Ni intensity ratios obtained by LEIS for the In_3Ni_2 (001), (100) and $(2\bar{1}0)$ surfaces following sputtering and annealing to 480 °C. These ratios reflect the elemental distribution at the outermost atomic layer. 173

7.4 Ratio of pure In to In oxide on the In_3Ni_2(100), (2$\bar{1}$0) and (001) surfaces following exposure to air and oxygen doses ranging from 20 L to 900 L. The data illustrate the evolution of surface oxidation behaviour as a function of crystallographic orientation and oxygen exposure. 176

7.5 Ratio of pure nickel to nickel oxides on the In_3Ni_2(2$\bar{1}$0) and (001) surfaces following air exposure and subsequent oxygen dosing ranging from 20 L to 900 L. 177

7.6 (a) LEED pattern of the AlNi(110) surface after exposure H [61]. (b) LEED pattern of the freshly prepared In_3Ni_2 (001) surface displaying a (1$\times$1) structure. (c) LEED pattern of the same surface after firing of the TSP, revealing three domains of the c(2$\sqrt{3}\times 4$) rectangular reconstruction. 178

List of Tables

2.1 Summary of chemical reactions catalysed and key advantages of selected intermetallic compounds. 18

3.1 Classification of vacuum levels and their corresponding pressure ranges [68]. 32

3.2 Comparison of temperature measurements obtained from the thermocouple and the optical pyrometer at various emissivity settings. Emissivity values between 0.4 and 0.5, highlighted in blue, represent the most accurate correspondence between the two measurement methods. 47

3.3 Comparison of emissivity values measured using thermocouple and optical pyrometer techniques. The emissivity value of 0.48, highlighted in blue, shows the closest agreement between the optical pyrometer and thermocouple values; therefore, 0.48 is considered the most accurate emissivity. . . 47

4.1 XPS data for In_3Ni_2(001) surface comparing the binding energies of the core levels of Ni $2p_{3/2}$ and In $3d_{5/2}$. Sputtering results in changes to the surface. Following two cycles, the peak positions represent the clean intermetallic compound. 78

4.2 Surface free energies of selected elements [45, 116]. 80

5.1 Binding energies of the Ni $2p_{3/2}$ and In $3d_{5/2}$ core levels for the $In_3Ni_2(2\bar{1}0)$ surface measured by XPS after exposure to air, following sputtering, and after cleaning by sputtering and annealing. Core-level positions of elements are also given for comparison. 111

5.2 STM image of the In_3Ni_2 $(2\bar{1}0)$ surface overlaid with the atomic model of the surface structure. 127

6.1 XPS data for $In_3Ni_2(100)$ surface comparing the binding energies of the core levels of Ni $2p_{3/2}$ and In $3d_{5/2}$. Following three cycles, the peak positions represent the clean intermetallic compound. 142

6.2 Layer, chemical compositions and expected In-Ni ratio expected from(100) surface. 159

7.1 Bond lengths between In and Ni atoms in In_3Ni_2 for the (001),$(2\bar{1}0)$ and (100) surface orientations. In_1 refers to the In atom located at the corner of the unit cell, while In_2 denotes the In atom within the cell interior. 169

7.2 Calculated atomic density per unit cell for the (001), (100) and $(2\bar{1}0)$ surfaces of In_3Ni_2. 170

7.3 Chemical compositions of the (100), $(2\bar{1}0)$ and (001) surfaces and In to Ni ratio, the expected ratios are calculated from model structures, while the measured values are based on LEIS intensity ratios obtained from the $(2\bar{1}0)$ surface. 174

Appendix

Publications

A. Y. Alfahad, V. K. Singh, E. Gaudry, J. Ledieu, V. Fournée, P. Gille, A. M. Gardner, P. R. Chalker, R. McGrath, and H. R. Sharma, "Atomic structure, chemical composition, and oxidation behaviour of the (001) surface of In_2Ni_3intermetallic catalyst," Physical Review Materials, vol. 9, no. 3, p. 035801, 2025.

Future Publications

- A. Y. Alfahad, V. K. Singh, E. Gaudry, J. Ledieu, V. Fournée, P. Gille, A. M. Gardner, P. R. Chalker, R. McGrath, and H. R. Sharma, "The $(2\bar{1}0)$ Surface of In_2Ni_3: Atomic Structure, Composition, and Oxidation Behaviour".
- A. Y. Alfahad, V. K. Singh, E. Gaudry, J. Ledieu, V. Fournée, P. Gille, A. M. Gardner, P. R. Chalker, R. McGrath, and H. R. Sharma, "Surface Atomic Structure, Chemical Composition, and Oxidation Behaviour of In_2Ni_3 (100) Intermetallic Catalyst".

Conference Attendance

- ECMetAC ASCI Workshop, Online, 2023.
- Surface Structure and Chemical Composition of Intermetallic Compound In_3Ni_2, ECMetAC Days, Kranjska Gora, 2023.

- Studying the chemical structure of In_3Ni_2 Intermetallic compounds by Low Energy Ion Scattering (LEIS), ECMetAC ASCI Workshop, Online, 2024.
- Surface Structure of In_3Ni_2 Intermetallic Compound, Surface Science Day, Liverpool, 2022.
- Surface Structure of In_3Ni_2 Intermetallic Compound, ECMetAC Days, Split, 2022.
- Surface Structure of In_3Ni_2 Intermetallic Compound, Surface Science Day, Chester, 2023.
- Atomic Structure and Chemical Composition of the Surface of In_3Ni_2 $(2\bar{1}0)$ Intermetallic Catalyst, ECMetAC Days, Zagreb, 2024.
- Atomic Structure, Chemical Composition, and Oxidation Behaviour of the Low Index Surface of In_3Ni_2 Intermetallic Catalyst, ECMetAC Days, Zurich, 2025.

Research Visits

- Young Scientist Exchange, Institute for Jean Lamour, Nancy, France, May 2023.
- Young Scientist Exchange, Institute for Jean Lamour, Nancy, France, September 2024.

Awards

The Best Young Scientists' Presentation, ECMetAC Days, Kranjska Gora, 2023.